Physical and electrical characterization of CVD graphene devices : towards large scale and flexible graphene electronics

Joanna Njeim

Thesis submitted for the degree of Doctor
of Philosophy at Sorbonne University

ED 391: Sciences mécaniques, acoustique, électronique et robotique de Paris

Discipline: Engineering Science

Physical and electrical characterization of CVD graphene devices: towards large scale and flexible graphene electronics

By: **Joanna Njeim**

Jury members:

Nedjma Bendiab, Université Grenoble Alpes, Institut Néel, Reviewer
Costel-Sorin Cojocaru, Ecole Polytechnique, LPICM, CNRS, Reviewer
Stéphane Holé, Sorbonne Université ESPCI/LPEM, Examinator
Arianna Filoramo, CEA, Examinator
Emiliano Pallecchi, Université de Lille, IEMN, CNRS, Examinator
Ali Madouri, C2N, CNRS, Invited member
Zhuoxiang Ren, Sorbonne Université, L2E, Thesis supervisor
David Brunel, Sorbonne Université, L2E/GeePs, Thesis Co-supervisor

This is for my parents Roukoz and Siham Njeim

Acknowledgments

Firstly, I would like to express my sincere gratitude to the director of the L2E laboratory Prof. Aziz Benlarbi-Delai for welcoming me into the lab, and for my supervisor Prof. Zhuoxiang Ren for giving me this opportunity as well as always giving me new insights regarding my work.

Secondly, a huge thank you goes to the wonderful Chloe Hamel-Dellenbach for everything she has done for me during my three years of PhD.

I would also like to thank my thesis co-supervisor, Dr. David Brunel for his guidance and advice, and for having the patience to handle tough situations. It was hard and challenging but it taught us so much about ourselves, life, and of course about graphene; for that, I am extremely grateful. My sincerest thank yous goes to our collaborator Dr. Ali Madouri for his counsel throughout these three years.

I would like to thank everyone I met during these three years of research; whether in the L2E lab, in the GeePs lab, in the C2N lab, or during the conferences and summer school. Thank you all one by one as you have affected my life one way or another. A very special thank you goes out to my second family here in France. Christian A., Laurent, Kevin, Lydia, Mounir, Mandiaye, and Benjamin, for making me feel at home when I was feeling alone and away from everything familiar. You have been there for me during my ups and downs, and for all the drinks and shots we have had, the laughs and the love, thank you.

Some people have lived this journey with me all the way from Lebanon. Ayman, Pilo, Roy, Ryan, Youssef, Elige and Rachelle, I am forever grateful to every one of you for your support during my hardest times.

Thank you Chris, for every push and every motivating speech you have ever given me. Although you have taken the same path as I have, and have struggled just as much as I did, you were still there for me, every second of every day of every month of every year. No words will suffice to describe my gratitude; you're my hero.

Finally, I would like to dedicate my PhD thesis to the two people who struggled so much and gave up everything in order to see me stand where I am standing today. Mom and Dad, I love you very much, thank you for everything. I am forever grateful and thankful for having parents like you. As for my brother, Jad, a special thank you for the motivation. Seeing you be that passionate about your work has inspired me so much to acquire the same passion towards mine.

Last but not least, I would also like to dedicate this PhD thesis to a very special creature; my 9 year old handsome cat, Newton. I love you so much buddy! I am sorry for leaving you behind, it was something I had to do, but the idea of you kept me going during my worst days.

Contents

List of Figures

Abstract

Throughout these few years, graphene has been rapidly proven to be a very promising material in the field of flexible and communicating electronics. Moreover, the chemical vapor deposition technique has allowed the synthesis of large-scale graphene, making the commercialization of graphene-based devices possible. Nevertheless, the fabrication process has not quite been understood at every step in order to overcome the most fundamental challenges in this field. In this work, a step-by-step structural and chemical characterization has been performed to study the properties of CVD-grown graphene, and the most crucial steps have been tackled in order to pave the way for flexible RF graphene-based devices on parylene substrates. We have found that the common large-scale techniques have yet to yield homogeneous graphene properties on the same sheet which results in wafer-scale graphene-devices with different performances. This highlights the need to encapsulate graphene. Parylene C was studied as a potential substrate for graphene devices, and sub-60 nm gate lengths RF devices have been fabricated, showing that the parylene-graphene combination could indeed be a very propitious solution to obtaining reproducible device performance.

Résumé

Depuis une dizaine d'années, le graphène s'est rapidement révélé etre un matériau très prometteur dans le domaine de l'électronique flexible et communicante. Dans cette optique, la technique de dépot chimique en phase vapeur a permis la synthèse de graphène sur de grandes surfaces, rendant ainsi possible la commercialisation de dispositifs a base de graphène. Cependant, les procédés de fabrication ne sont pas tous clairement acquis a chaque étape afin de relever les défis les plus fondamentaux dans ce domaine. Dans ce travail de thèse, une caractérisation chimique et structurelle a été réalisée étape par étape afin d'étudier les propriétés du graphène CVD, et les étapes les plus importantes ont été abordées afin d'ouvrir la voie a des dispositifs RF flexibles a base de graphène sur du parylène. Nous avons constaté que les techniques classiques permettant l'obtention de grandes surfaces doivent encore fournir des propriétés d'homogénéité sur le meme feuillet. Cela met en évidence la nécessité d'encapsuler le graphène. Le parylène C a été étudié comme substrat potentiel pour les dispositifs a base de graphène et des dispositifs RF a des longueurs de grille inférieures a 60 nm ont été fabriqués, ce qui montre que la combinaison parylène/graphène pourrait constituer une solution trés propice a l'obtention de dispositifs avec des performances reproductibles.

Chapter 1

General Introduction

In electronics, the evolution of silicon technology is based on Moore's law which predicts that the number of transistors (the main element that composes the processors) per circuit of the same size would double every 24 months [1]. This is achieved by reducing the dimensions and improving the performance of these devices. However, this improvement in chip performance and the reduction in device size is reaching a nanometre-scale limit in which parasitic effects such as the quantum tunnel effect begin to appear. To solve this problem, several solutions have been considered, such as the introduction of new materials. III-V compound semiconductors [2] or carbon nanotubes [3], the search for a replacement material with comparable or even much higher performances than silicon, while being abundant, is a crucial step for the development of electronic technologies. In 2004, two physicists from the University of Manchester, Andre Geim and Konstantin Novoselov [4], isolated a two-dimensional material which they called graphene. The idea of graphene has existed for over 60 years, back when it was called 2D graphite. However, it was believed that this atom-thick material is thermodinamically unstable and thus cannot exist in real life. These two scientists however proved the existence of graphene. Using a Scotch-tape mechanical exfoliation technique, they were able to isolate it and transfer it onto a silicon dioxide (SiO_2) substrate. Due to its honeycomb structure, graphene presented extraordinary mechanical, optical, thermal and electronic properties [5]. This discovery opened a new path towards numerous applications including flexible, stretchable and bendable electronics such as flexible smartphones and screens, RFID chips, ultra-fast charging, as well as biomedical devices e.g. artificial skins, biomedical coatings *etc.*. These applications are emerging today with great force and require technological development beyond the silicon era. The outstanding properties of graphene could make this new miracle material the future of the electronics and medical industries.

Today, graphene-based devices in roughly every graphene-compatible application have been proven to be notably superior to other materials implemented for the same applications. Nevertheless, graphene technologies are still conditional to many fundamental challenges which restrict the commercialization of graphene devices. In reality, production-worthy devices must maintain the same record properties of the starting graphene, and it all begins at the synthesis of this two dimensional material. Many growth techniques exist today, yielding different "types" of graphene with distinctive properties for particular applications and purposes. However, the most industrially-compatible synthesis method today seems to be the chemical vapor deposition of graphene (CVD). The CVD yields wafer-scale graphene sheets on various metal substrates, and it only seems to be limited by the machine's chamber room, in which, in some cases, has succeeded in producing a 30-inch continuous graphene sheet. This seems very promising, and companies around the world have already commercialized graphene on metals and even graphene transferred on target substrates such as SiO_2, quartz and PET. However, the road to the industrialization of graphene devices is still under construction, for the synthesis of graphene is only the beginning. Other important challenges exist, particularly the graphene transfer. Today, the most common technique for transferring graphene is the PMMA-assisted wet transfer. Although many problems arise from this method, such as polymer residues and contamination via impurity particles, it is still the most appropriate mean for large-scale graphene transfer and thus it is still being used by a large community of scientists. Other drawbacks like the fabrication process are still very challenging. Lithography patterning, etching and lift off processes, as well as some inevitable characterization techniques continue to deteriorate the intrinsic properties of graphene, hampering by that the commercialization of graphene devices. Reproducibility is a key factor for electronics and every other industry. Today, this factor is still not achieved, since the crystalline quality of the same graphene layer differs from area to another within the same sheet.

Despite all these challenges, graphene still holds tremendous hope as a replacement for silicon technologies, and an unmatched miracle material for today's electronics industry. Immense research and funding around the world among which the Graphene Flagship comes first with its 1 billion euro budget demonstrate the immeasurable importance of graphene for the future of technology.

1.1 Objectives of this thesis

The objectives of this thesis are: (1) To synthesis graphene on clean and flat cm-large copper foils and transfer it onto target substrates. The copper foils are characterized via SEM, AFM and XPS before and after treatment to examine their surface morphology and chemical composition. The graphene is then transferred using two different copper etching solutions which are carefully analyzed via XPS in order to examine the effect of these solutions on the PMMA residues and the graphene quality. (2) To fabricate large-scale graphene-based field effect transistors and characterize the graphene channels via Raman spectroscopy, followed by an exhaustive study on the electrical properties of our CVD-grown graphene. Time dependence of the graphene's electrical properties are also presented, insisting on the need to encapsulate the graphene for long-term use. Preliminary results on graphene nanomesh are reviewed in this work and show promising findings. (3) To intensively discuss the critical steps towards wafer-scale production of time-independent flexible graphene RF transistors. This is achieved by fabricating thin graphene transistors with gate lengths below 60 nm on polymer substrates. These substrates are sensitive to what is normally harmless for silicon-based technologies such as high temperatures. Intensive XPS and AFM studies on these polymers will also be reviewed in this work, which will be concluded with the challenges of fabricating wafer-scale flexible electronics.

1.2 Thesis structure

This thesis presents the author's experimental and theoretical work on the development, characterization and understanding of every step of large-scale chemical vapor deposited graphene-based field effect transistors (GFETs), as well as the work towards the realization of flexible RF GFETs on parylene C substrates.

Chapter 1 announces a general introduction on the field of this work and presents the objectives and general structure of this thesis.

Chapter 2 introduces the reader to the basics of graphene including its fundamental properties. The graphene synthesis methods are also reviewed with heightened emphasis on the copper-based CVD approach. The most common transfer techniques are detailed, along with profound attention on the most popular graphene characterization technique: Raman spectroscopy. A survey on graphene electronics is briefly presented.

Chapter 3 summarizes the main experimental techniques used in this research. Structural characterization techniques such as atomic force microscopy, scanning electron microscopy and X-ray photoelectron microscopy are detailed. The graphene field effect transistors (GFETs) fabrication techniques including reactive ion etching (RIE), electron beam lithography (EBL), atomic layer deposition (ALD) and electron beam physical vapor deposition (EBPVD) are also presented.

Chapter 4 aims at understanding every step of the fabrication process of large-scale graphene devices in order to study the properties of CVD graphene. For that, large-scale-compatible fabrication techniques were chosen. This chapter demonstrates the optimization of the copper (Cu) growth substrate towards the synthesis of clean and flat monolayer graphene through a chemical mechanical polishing and annealing technique. The surface of the copper was further investigated using atomic force microscopy, and scanning electron microscopy X-ray photoelectron microscopy. A CVD-derived technique called the pulsed chemical vapor deposition is also presented, and the PMMA-assisted wet transfer is envisaged. An exhaustive study on the effect of the copper etching solution is discussed via XPS measurements. The fabrication process of hundreds of GFETs carried out in this work is discussed, and the Raman characterization of transferred graphene is thoroughly analyzed via Raman spectra and Raman mappings. Finally, the electrical characterization of the GFETs is intensively explored, where the mobility extraction method is detailed and the effect of air exposure on the graphene's electrical properties is presented. Preliminary results on graphene nanomesh are also presented in this chapter.

Chapter 5 describes the author's contribution in realizing flexible RF graphene-based devices. An introduction on the flexible substrate, parylene C, is presented alongside its deposition technique and a brief presentation of parylene C's properties. Structural and chemical characterization of parylene C substrates are also presented. A simulation of the optimized RF device design is demonstrated, as well as the fabrication process of these RF field effect transistors on parylene C, with sub 60 nm gate lengths. The effect of the oxide deposition method is exhaustively discussed, as XPS and AFM measurements are carried out in order to obtain a complete idea about this unexpectedly important step. The challenges of fabricating parylene C-based RF devices are thus tackled in this chapter.

This thesis will be concluded in Chapter 6 by summarizing the results and findings of this work, and lastly the perspectives are presented.

Chapter 2

Literature review

2.1 Retrospect on carbon

Carbon is one of the most important elements on earth. It is the fourth most abundant element in the universe and is indispensable for life on earth. It occupies the 6th position in the periodic table, and its ground state electronic configuration is 1s2 2s2 2p2. According to the Valence bond theory, since there are two unpaired electrons in the carbon atom, it should form two covalent bonds, resulting in a CH_2 molecule. However, experiments showed that CH_2 is highly reactive and cannot exist outside of a reaction. Instead, CH_4 was found to exist. This implies that the carbon should form four bonds, meaning that it must have four unpaired electrons. This means that hybrid orbitals must exist in order to have four electrons occupying the 2s and the 2p orbitals (that is 2s, 2px, 2py and 2pz, because the s orbital is a sphere centered at the nucleus and thus no orientation is needed, contrary to the p orbital which consists of two "lobes" oriented along a particular axis relative to the nucleus). In order to obtain CH_4, the carbon atom must hybridize (Hybridization is the act of combining atomic orbitals (s, p, d, f, etc) to form hybrid orbitals (sp, sp2, sp3). The hybridization of carbon is highly favorable because hybridized orbitals have lower energies than atomic orbitals, resulting in a more stable compound. The electron distribution in C orbitals is shown in figure 2.1 (a-b).

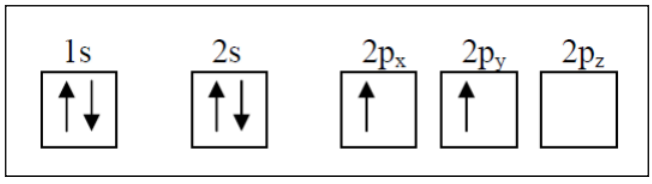

Figure 2.1: Electron distribution in the carbon orbitals. Adapted from [6].

Hybridization in a carbon atom comprises three cases:

- Two sp orbitals generated from s + p (one s and one p orbital)
- Three sp2 orbitals generated from s + p + p (one s and two p orbitals)
- Four sp3 orbitals generated from s + p + p + p (one s and three p orbitals)

The s and p atomic orbitals as well as the three hybrid orbitals are shown in figure 2.2.

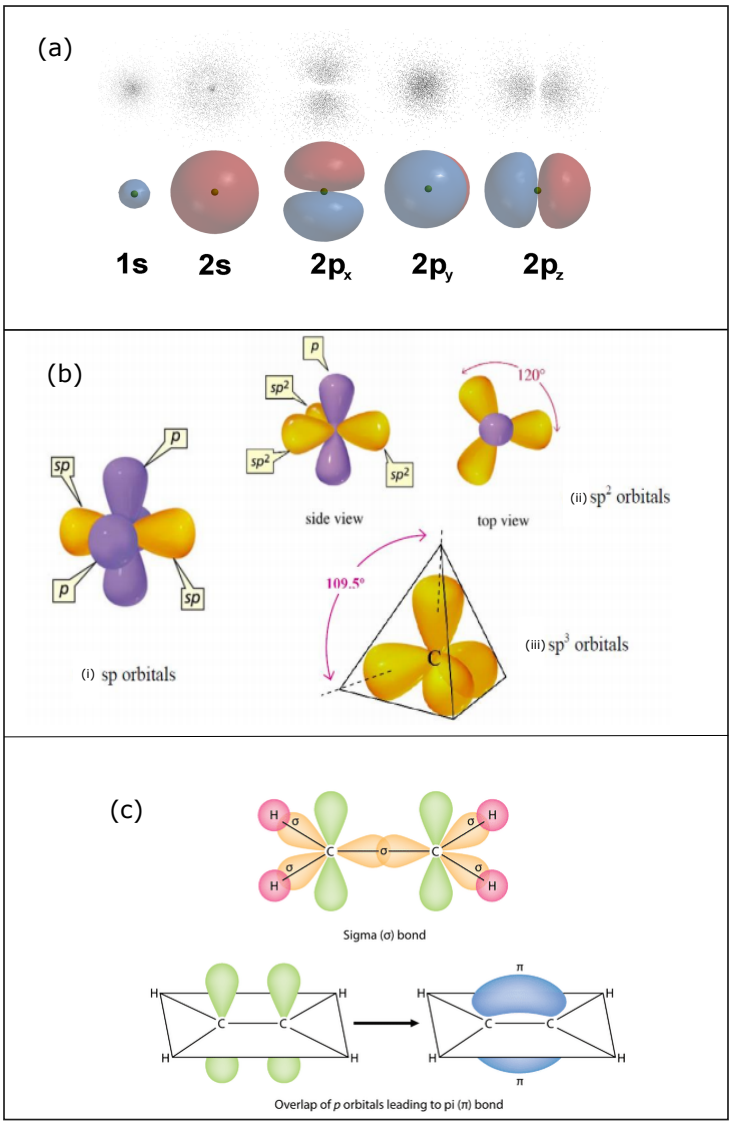

Figure 2.2: Schematic representation of (a) s and p atomic orbitals, (b) the spatial arrangement of orbitals in the carbon atom in the case of (i) sp, (ii) sp2 and (iii) sp3 hybridizations and (c) Sigma and Pi bonds in a ethylene molecule (C_2H_4). Adapted respectively from [7], [6] and [8].

The s orbital is a sphere centered at the nucleus, meaning that the electron is equally likely to be located in any direction from the nucleus. The p orbital consists of two "lobes" oriented along a particular axis relative to the nucleus, thus there are three orbitals named px, py and pz.

In the case of carbon atoms, the overlap of hybrid orbitals form sigma bonds, and un-hybridized p orbitals form pi bonds. An example of the two bonds is shown in figure 2.2 (c). In the case of the sp orbitals, two overlapped sp orbitals make strong frontal sigma (σ) bonds to an adjacent atom, whereas there are two weak lateral pi (π) bonds with neighboring p orbitals. Sp2 hybridization has a trigonal planar configuration which forms sigma bonds, and the pure p orbital forms a pi bond. Finally, sp3 lobes are oriented towards the vertexes of a regular tetrahedron. In this case, all the four orbitals are hybridized and form sigma bonds.

If we take the example of the four sp3 hybrid orbitals, they are called "degenerate orbitals", meaning that they all have the same energy. Lastly, every single bond (C-C) contains 1 sigma bond, every double bond (C=C) contains at least one sigma bond and one pi bond, and every triple bond contains 1 sigma bond and two pi bonds. Triple bonds are shorter and stronger than single bonds, which are longer and weaker, and sigma bonds are stronger than pi bonds.

Thanks to its valency, carbon possess various forms including ancient allotropes such as graphite and diamond, and relatively recent allotropes such as buckminsterfullerene, fullerene, carbon nanotubes, lonsdaleite, amorphous carbon, and graphene. These allotropes are resumed in figure 2.3.

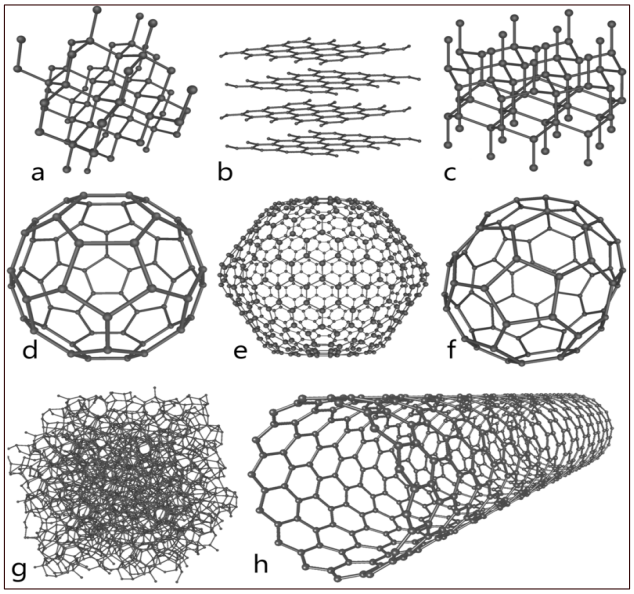

Figure 2.3: Structural representation of carbon allotropes: (a) Diamond, (b) Graphite, (c) Lonsdaleite, (d) C_{60} (Buckminsterfullerene), (e) C_{540} Fullerene, (f) C_{70} Fullerene, (g) Amorphous carbon, and (h) Single-walled carbon nanotube. Adapted from [9].

2.2 Graphene

Graphene is a two dimensional (2D) material consisting of sp2 hybridized carbon atoms periodically arranged in an hexagonal lattice. This one atomic layer of graphite is the basic structural element of other allotropes, including graphyne, carbon nanotubes, graphite and fullerenes [10]. Some examples are shown in figure 2.4.

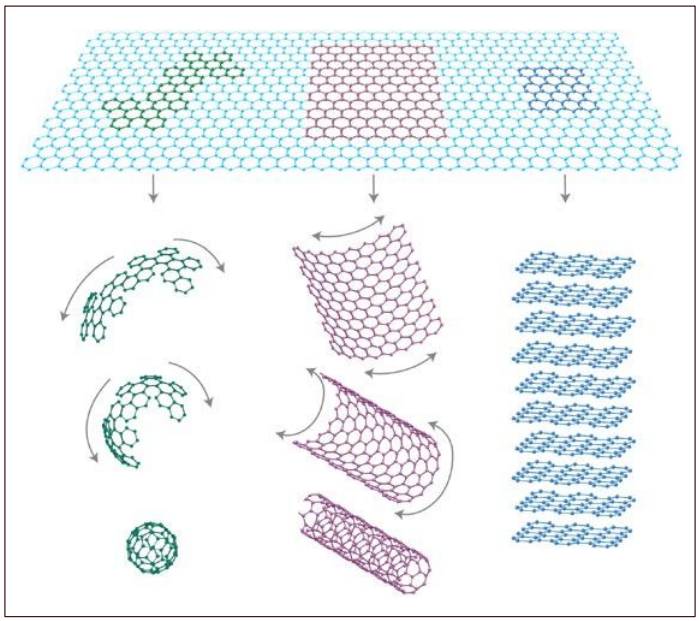

Figure 2.4: Mother of all graphitic forms. Graphene is a 2D building material for carbon materials of all other dimensionalities. It can be wrapped up into 0D buckyballs, rolled into 1D nanotubes or stacked into 3D graphite. Adapted from [11].

Since carbon atoms of graphene are bonded with sp2 hybridizations, these hybrid orbitals form strong in-plane sigma bonds (3 for each C atom). These strong bonds maintain the interatomic distance (a_c-a_c) of 0.142 nm (figure 2.5), which provides the graphene with outstanding mechanical properties. On the other hand, the un-hybridized p orbitals form one out of plane weak pi bond per carbon atom. The pi bonds hybridize together to form pi* bonds. Together, they are responsible for graphene's outstanding electronic properties due to the unpaired moving electrons.

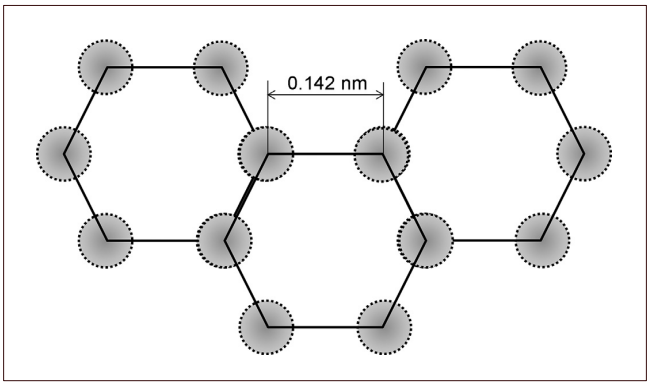

Figure 2.5: Hexagonal lattice of graphene. Adapted from [12]

2.2.1 Structure of Graphene

The unit cell of graphene's honeycomb lattice represented in figure 2.6 contains two geometrically different carbon atoms A and B. The unit vectors a_1 and a_2 that define this lattice are written as:

$$a_1 = \frac{a_{c-c}}{2}(3, \sqrt{3}) \tag{2.1}$$

$$a_2 = \frac{a_{c-c}}{2}(3, -\sqrt{3}) \tag{2.2}$$

where $a_c - a_c$ is the carbon-carbon bond length measuring 0.142 nm. Considering the reciprocal lattice definition $a_1 a_2 = b_1 b_2 = 2\pi$, the corresponding reciprocal lattice vectors b_1 and b_2 are found to be:

$$b_1 = \frac{2\pi}{3a_{c-c}}(1, \sqrt{3}) \tag{2.3}$$

$$b_2 = \frac{2\pi}{3a_{c-c}}(1, -\sqrt{3}) \tag{2.4}$$

Using these reciprocal lattice vectors, the Brillouin zone in the k-space can be constructed. This zone determines the k-vectors which allow to obtain independent solutions to the Schrdinger equation. The two vertices of the Brillouin zone K and K' are of utmost importance for the understanding of the physics of graphene and its properties. They are as following:

$$K = \frac{2\pi}{3a_{c-c}}(1, \frac{\sqrt{3}}{3}) \tag{2.5}$$

$$K' = \frac{2\pi}{3a_{c-c}}(1, -\frac{\sqrt{3}}{3}) \tag{2.6}$$

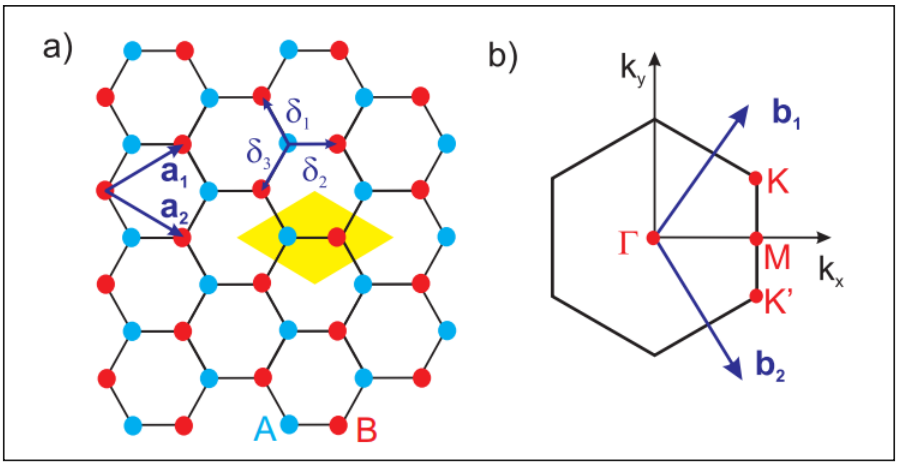

Figure 2.6: (a) Real space lattice of graphene. a_1 and a_2 are the two lattice unit (primitive) vectors and $\delta 1, \delta 2$ and $\delta 3$ are the nearest-neighbour vectors. The yellow rhombus represents the primitive unit cell. (b) The Brillouin zone of graphene with the Dirac points K and K' indicated and centered on Γ. The reciprocal lattice vectors b_1 and b_2 are also shown. Adapted from [13].

2.2.2 Graphene properties

Due to its honeycomb structure, one atom-thick graphene possesses extraordinary optical, mechanical, thermal and electronic properties. These properties make of graphene a very interesting material for optoelectronics, Excellent electrical [14] and thermal [15] conductivity, high mechanical strength [16], these properties make of graphene a very interesting material in electronics, optoelectronics, spintronics as well as in the biomedical industry.

2.2.3 Electronic properties of graphene

The π and the $\pi*$ bands, perpendicular to the σ bonds, are responsible for the transport properties of graphene. In fact, the electronic band structure of graphene, simulated using the tight binding approximation method [17] and depicted in figure 2.7 shows the conduction ($\pi*$) and valence (π) bands. These two intersect at six points of two different equivalences, named K and K′, the so-called Dirac point (also called the charge neutrality point (CNP)). As the band structure shows, the energy dispersion close to the Dirac points is linear with the momentum, being described by $E = hkv_F$. The parameter v_F is the Fermi velocity with its value of $v_F = c/300$, where c is the velocity of light in vacuum, and k is the wave vector. Indeed, the linear dispersion relation resembles to that of a photon, indicating that electrons and holes in the graphene behave like massless fermions. In theory, a zero effective mass leads to an infinite high charge carrier mobility. But in reality, graphene contains defects, phonons and a finite charge carrier concentration. These three limit

the transport of the charge carriers. Despite this drawback, graphene-based field effect transistors have showed mobilities up to 10 000 $cm^2/V.s$ for graphene on SiO_2 substrate at room temperature, as well as mobilities reaching 230 000 $cm^2/V.s$ for suspended graphene at 1.8K. These values are much higher than the regular Si-based transistor, where mobilities reach 1400 $cm^2/V.s$, which gives tremendous hope for the commercialization of graphene in the electronic industry. Another important point about charge transport in graphene is ambipolarity. In fact, due to graphene′s conical shaped-band structure, charge carriers in graphene can be continuously tuned by the external gate voltage. As figure 2.8 shows, under negative gate bias, the Fermi level drops below the Dirac point, introducing a significant population of holes into the valence band. Under positive gate bias, the Fermi level rises above the Dirac point, promoting a significant population of electrons into the conduction band. The ambipolarity of graphene has attracted much attention in the electronic industry, where high frequency FETs have been fabricated with cut-off frequencies reaching tens to hundreds of GHz. However this zero bandgap results in a low I_{on}/I_{off} ratio, implying that at a zero gate voltage, graphene still conducts electricity. This means that it cannot be turned off. This energy consuming disadvantage can however be overcome by opening a band gap in the graphene by several means, including epitaxially growing graphene on SiC, applying a perpendicular electric field to bilayer graphene and structuring the graphene monolayer into nanoribbons or nanomeshes, confining by that the graphenes charge carriers.

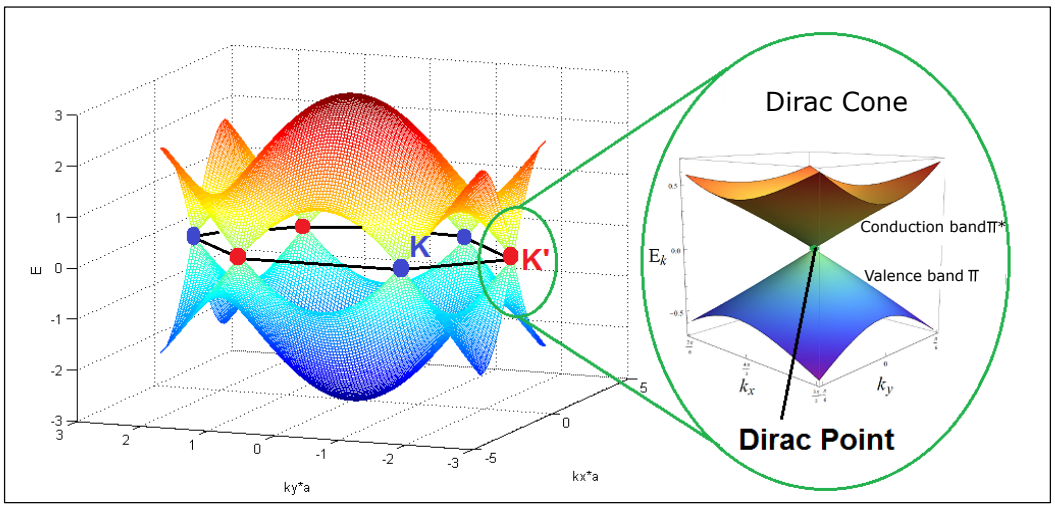

Figure 2.7: Electronic band structure of graphene in the first Brillouin zone. Adapted from [18]

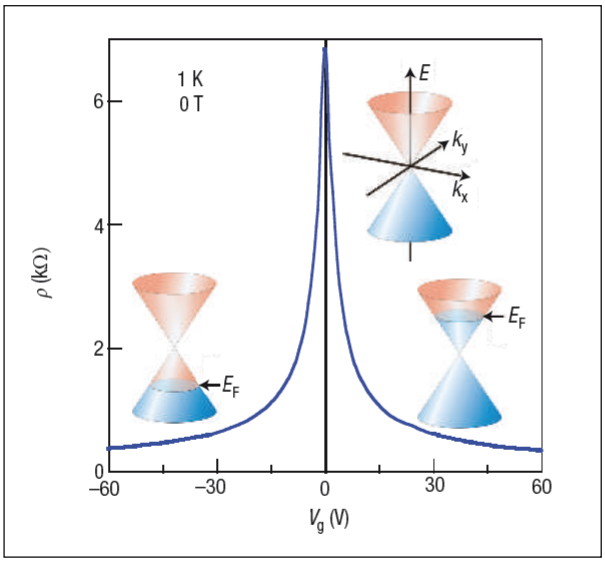

Figure 2.8: caption Adapted from [11]

2.2.4 Optical, mechanical and thermal properties of graphene

Three molecular and strong σ bonds maintaining a maximum link between the carbon atoms are the main reason for graphene's extraordinary mechanical, optical and thermal properties. When it comes to the optical properties, monolayer graphene disposes of a high optical transmittance of 97.7 % [19] making it almost transparent. This unique light absorption is almost constant within the visible range, and varies linearly with up to five graphene layers [19] as shown in figure 2.9 (a). Alongside graphene's high optical transmittance, its high conductivity make of it a promising candidate for transparent conductive electrodes, light emitting diodes (LEDs), photodetectors, ultrafast lasers and various photonic devices that require conducting and transparent thin films [19–23]. In addition to higher optical properties, graphene films have high mechanical strength, are flexible, and are chemically stable in comparison to traditional transparent conductive electrodes such as indium tin oxide (ITO) [20, 24, 25]. Although graphene films show relatively poor electrical conductivity owing to the structural defects [25] and high sheet resistance [26], the high crystalline quality of the graphene samples can be preserved by successfully transferring graphene sheets without inducing further defects, and the sheet resistance can be further reduced to the order of 100-200 Ω by chemical doping [26–28].

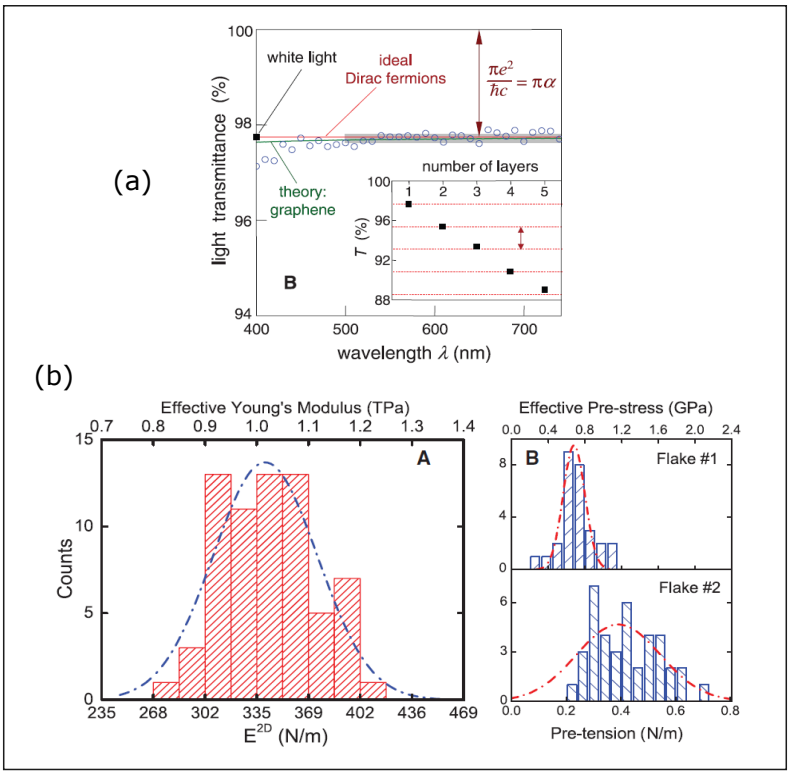

Figure 2.9: Optical, mechanical and thermal properties of graphene. (a). Adapted from (a) [19] and (b) [16].

On the other hand, graphene's mechanical properties hold record values, as its tensile strength is about 130 GPa [16] (which is 200 times higher than steel [23]), and its Young's Modulus measures approximately 1 TPa [16], as shown in figure 2.9 (b). Graphene's intrinsic strength, elasticity and high flexibility [16, 25, 26], alongside being very light (0.77 mg/m^2) motivates the use of graphene in a handful of applications such as stretchable and bendable electronics, automobile and airplane components, and have even allowed high expectations for exotic structures such as a space elevator [16, 23, 25, 26].

The thermal properties of graphene are also very significant. Its thermal conductivity is mainly contributed by the phonon transport, and measurements have showed a room temperature thermal conductivity of a single layer graphene of the order of $5300W/mK$ [15], exceeding the record values of diamond and carbon nanotubes. This outstanding thermal conduction property of graphene allow its integration in the electronic industry, especially for nanometer-scale silicon complementary metal-oxide-semiconductor (CMOS) technology as well as beyond CMOS devices. Other applications for graphene include optoelectronics and bioengineering, since graphene is proven to be an excellent material for thermal management and solving heat dissipation problems [15, 29]. Beyond its mechanical, optical and thermal properties, high quality defect-free graphene shows a chemical inertness and biocompatibility [30, 31].

2.3 Graphene growth techniques

Since the discovery of graphene in 2004, methods of obtaining graphene have boomed. Requirements for large-scale, low cost and even green processes have motivated the development of new techniques. However, different synthesis methods lead to different qualities and characteristics of the graphene produced, specifically tailored for target applications. Below are some of the most common methods of obtaining graphene.

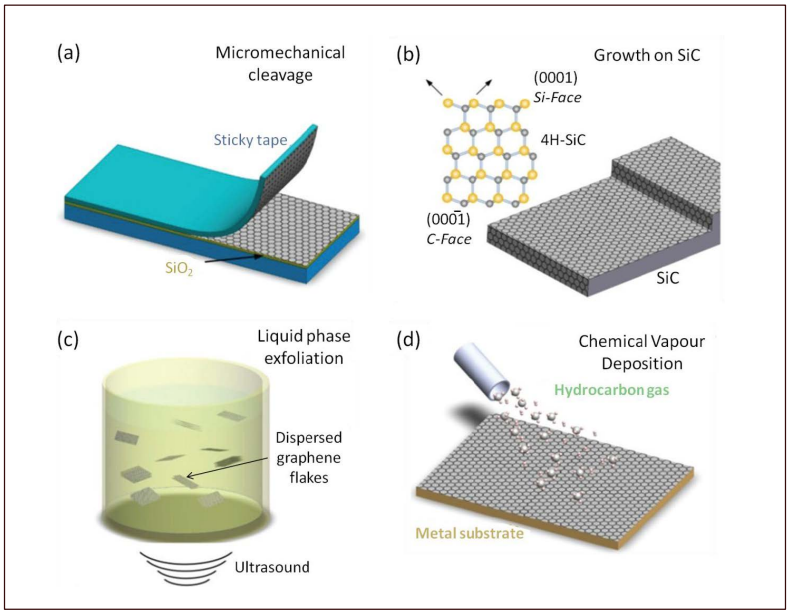

Figure 2.10: Common graphene synthesis methods: (a) Mechanical exfoliation (b) Epitaxial growth (c) Chemical exfoliation and (d) Chemical vapor deposition. Adapted from [23].

2.3.1 A little history

After the discovery of graphene in 2004, the research on this powerful material bloomed. The microcleaving of HOPG yielded high quality single layer graphene, however, this technique was difficult to scale up for applications. In the same year, Berger *et al.* [32] developed epitaxial graphene on 6H-SiC substrates, which principle relies on the thermal decomposition of SiC substrates upon annealing in high temperatures. The group's work resulted in a tri-layer graphene with a charge carrier mobility reaching 1100 $cm^2/(V.s)$ at 4K. A couple of years later, Berger *et al.* [33] managed to grow a single layer graphene on single crystal SiC, yielding a carrier mobility of 27000 $cm^2/(V.s)$. However, epitaxial growth was hard in achieving large graphene domains and the resulted graphene had a strong bonding with the substrate, which affected the electronic bonding of epitaxial graphene layers [34]. In 2007, Obraztov *et al.* [35] developed for the first time a CVD process to synthesize a few thin layers of graphite, with a thickness of 1.5 +- 0.5 nm on Ni substrates.

Shortly after, CVD growth of graphene on transition metals such as Ru [34], Ir [36, 37] and Ni [25, 38, 39] was quickly being developed and large-scale graphene was starting to give hope for postsilicon electronics. However, the graphene grown by these methods resulted in regions of graphene with different thicknesses since the synthesis is due to the carbon segregation on the surface of the metal and the precipitation of these atoms upon cooling. In 2009, Xuesong Li *et al.* [40] developed a CVD technique for growing continuous and 95 % single-layer graphene on centimeter-large copper foils. The technique yielded a graphene of high quality and an electron mobility of 4050 $cm^2/(V.s)$. To this day, the most widely used metal catalyst is copper. In fact, graphene is grown on Cu by a surface-catalyzed process rather than a precipitation process. Thus, upon decomposition of hydrocarbons, carbons become adatoms on the surface of the Cu and form graphene. Once the first layer of graphene is completed, there will be no room left for graphene to grow, hence, the process is self-limited.

2.3.2 Mechanical exfoliation

The Nobel prize-winning graphene exfoliation method A. Geim and K.S Novoselov firstly introduced to the world in 2004 [5], also called the Scotch tape method and micromechanical cleavage, is an easy technique of obtaining single and multilayer pristine graphene (figure 2.10 (a)). Thin sheets of graphite are peeled off of a highly-oriented pyrolytic graphite (HOPG) using adhesive tape, then thinned further into few-layer and monolayer graphene flakes with subsequent tape-to-tape peelings. Eventually, the sticky tape is pressed against the target substrate such as silicon dioxide and the graphene is "transferred" onto the substrate. This peeling process is possible due to weak bonds between the atomic planes of graphite, which renders the Van der Waals force between them to be not as strong as the force between graphite/graphene and the substrate. Thus, when the tape is lifted the interlayer bonds will break, leaving some amount of graphite/graphene on the substrate. Graphene obtained by mechanical exfoliation presents the best electronic properties (charge carrier mobility reaching ..) and the highest crystalline quality, however, the graphene flake size is limited by the single crystal grains in the starting HOPG, and is generally below the order of millimeters [41], which present a main drawback for large scale applications. Therefore, the graphene prepared in this method is generally used for the fundamental research and prototypical device fabrication.

2.3.3 Expitaxial growth

Epitaxial growth (figure 2.10 (b)) is a technique which principle relies on the thermal decomposition of SiC substrates upon annealing in high temperatures (above 1300°C) in a controlled argon atmosphere or in ultra high vacuum. Under high temperatures, the Si atoms sublimate and the carbon atoms reorganize to form graphene [32, 33]. The most commonly used forms of SiC are the 4H-SiC and the 6H-SiC.

The benefit of the epitaxial growth of graphene is its compatibility with the established SiC-technology

in power electronics. For instance, high frequency transistors have been fabricated from graphene grown on SiC with 100 GHz cut-off frequency which is twice higher than the Si transistors of the same gate length (40 GHz) [42]. Record breaking cut-off frequency of 427 GHz was reported by Cheng *et el.* in 2012 [43], however, the device suffered from large parasitic parameters and poor drain current saturation resulting in a low maximum oscillation frequency. The highest extrinsic frequencies on SiC were recorded by Yu *et al.* in 2017 [44] with an extrinsic cut-off frequency of 70 GHz and a maximum oscillation frequency of 120 GHz. Top gated transistors have also been demonstrated with charge carrier mobilities up to 5000 $cm^2/(V.s)$ [45]. Although higher mobilities have been achieved at 25K (29 000 $cm^2/(V.s)$) [46], the average mobility of graphene on SiC is usually between 2000 and 10000 $cm^2/(V.s)$ [47, 48].

However, the SiC-derived graphene generally contains a mixture of multi-layer graphene which prevents its potential use in applications where layer thickness uniformity is necessary. In addition, the high surface roughness of graphene obtained from this method limits the performance of graphene in determined applications [49]. Another disadvantage of the SiC technology is that the SiC wafers are expensive (around 325 USD for a 2-inch wafer).

2.3.4 Chemical exfoliation

The chemical exfoliation technique (figure 2.10 (c)) consists of producing graphene oxide (GO) through an oxygen-producing chemical reaction (sulfuric and/or nitric acid) within the layers of a graphite crystal that softens the van der Waals interactions. Then, the graphene oxide is exfoliated (the softened van der Waals interactions are broken) in-situ via ultrasonication. The result consists in graphene oxide sheets suspended in a colloidal solution, which are deposited on a substrate. To obtain pure graphene flakes, the oxide has to be removed in a reducing atmosphere using alkaline solutions, or applying hydrogen plasma, or hydrazine vapours or through heat treatments [50–53]. Although the final material should be graphene, partially oxidized flakes are also obtained because the reduction processes are not very efficient (C/O ratio of 17.2 [54]). Recent works such as [55] have successfully yielded 100 % of graphene using this technique, however, thicknesses of 10-35 nm were obtained. Liu *et al.* [56] have recently published an article on the chemical exfoliation of 100 % few-layer graphene (up to 5 layers) . Another major drawbacks include a produced graphene comprised of sp2-sp3 structures, which makes it of relatively low crystalline quality compared to other techniques, and the charge carrier mobility is a few hundreds of $cm^2/(V.s)$ [54]. However, the main advantages of this techniques are the possibility of obtaining very precise flake sizes as well as the high output of this technique, making it economically competitive. Chemical exfoliation is a very popular method used for the production of inks [57], powder coatings, composite materials [50, 58], and biological applications.

2.3.5 CVD growth substrate

Throughout the years, the CVD growth of graphene has been performed on multiple metals such as Ni, [25,38,39,59–63], Cu [26,40,63–68], Ru [34,69,70], Co [71,72], Ir [36,69,73,74], Fe [75], Au [76], Rh [77] and Pt [78–80]. However, the cost of the majority of these metals, as well as the difficulty in etching make of Ni and Cu the best candidates for graphene growth [63].

Ni possesses a high carbon solubility (0.9 at.% at 900°C [63]) , which translates into a segregation of carbon atoms from the bulk of the metal to its surface and a precipitation of these atoms upon cooling, generating by that a inhomogeneous graphene layers on the Ni surface [69, 81] . In contrast, Cu acquires a very low carbon solubility which allows carbon atoms to adsorb on the metal surface, which enables the synthesis of large-area single-layer graphene sheets. Thus, graphene is formed from the carbon gas source (hydrocarbon) which is decomposed by the catalytic Cu surface. The graphene growth stops automatically once the surface of the Cu is entirely covered by carbon atoms, hence it is a self-limited process [40,63,81] [40]. It is for this reason that Cu is the most used catalytic substrate for graphene growth.

2.3.6 Chemical vapor deposition of graphene on copper

Chemical vapor deposition (figure 2.10 (d)) is the process of growing graphene via high temperature decomposition of gaseous hydrocarbon precursors such as CH_4 or C_2H_2 on metal substrates such as Cu, Ni, Ru, Ir, *etc.* which are used as catalysts to assist the graphene formation. The reaction occurs in a growth chamber, typically under vacuum, alongside other gases such as argon and hydrogen, and under a well defined total pressure. The graphene film is thus formed on the substrate, while the gaseous by-products along with the un-reacted precursors are evacuated out of the reactor.

Figure 2.11 illustrates the standard CVD process:

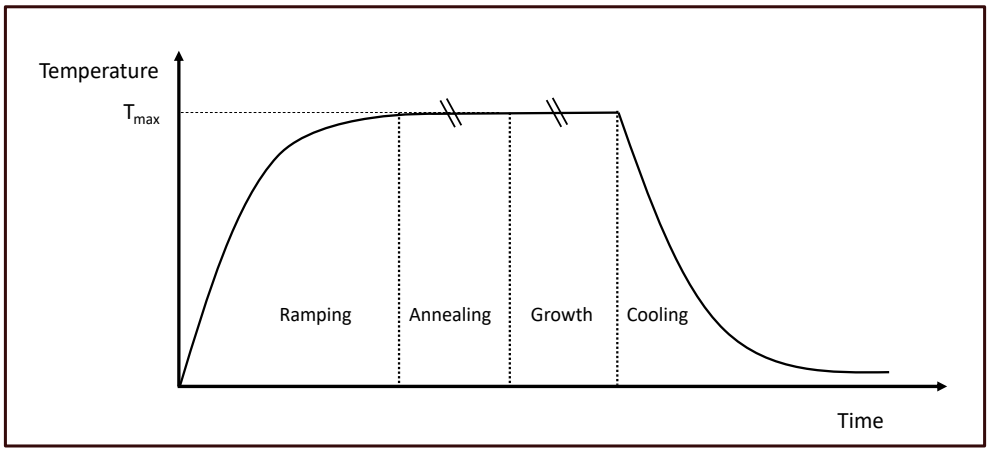

Figure 2.11: Schematic illustration of a standard CVD process.

After loading the substrate in the chamber room, the general steps for graphene growth are the following:

1. Ramping of the temperature until it reaches the desired value and maintaining it throughout the subsequent steps.

2. Annealing of the metal substrate, generally under Ar/H_2 flow in order to increase its grain size, smooth its surface and remove surface impurities.

3. Growth of graphene by injection and decomposition of the hydrocarbon (mainly CH_4) while keeping the Ar/H_2 flow stable, under precise partial and total pressures.

4. Cooling of the reactor until ambient temperature is reached and retrieving the graphene-coated substrate.

The growth parameters (temperature, partial and total pressures, carbon precursors, copper, CH_4/H_2 ratio, *etc.*) differ from lab to lab, and the results vary from a single-crystal graphene to a small-domain polyrystalline graphene film. However, even if these parameters were presumably the same, the as-grown graphene still diverges from lab to lab. It is for this reason that the growth of graphene on the atomic level has been investigated by a plethora of groups [69, 70, 82–86] in order to understand the atomic phenomena (adsorption, C attachment, *etc.*) that occurs during growth and link them to the nano-to-macroscopic growth parameters such as grain boundaries, substrate roughness and so on.

figure 2.12 shows the formation of graphene on copper surface:

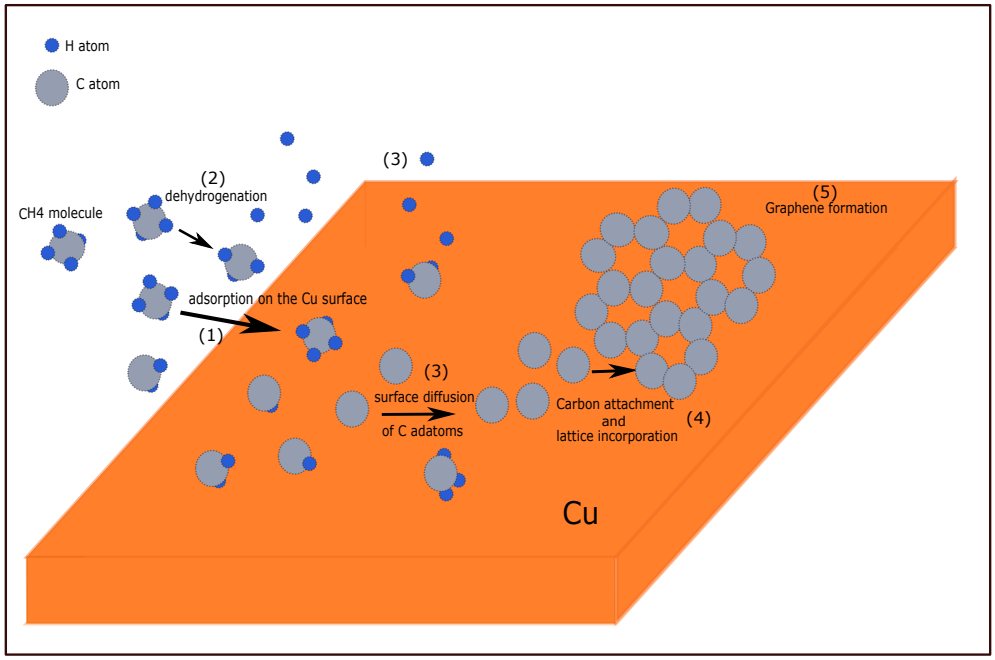

Figure 2.12: Schematic illustration of the growth kinetics on copper

The synthesis steps are:

1. CH_4 chemisorption on the Cu surface: when the methane enters the reactor, these molecules are adsorbed on the surface of the metal.

2. CH_4 partial dehydrogenation resulting in CH_x species (x=0,1,2,3). In fact, the dehydrogenation of CH_4 on Cu is endothermic, meaning that it is energetically unfavorable. Therefore, the diffusing C species on Cu are mainly CH_x (0¡x¡4) rather that atomic C [70, 82, 84–86]. Upon this breakdown, the concentration of the active C species on the Cu surface increases until it reaches a critical supersaturation where nucleation of graphene nuclei takes place.

3. Desorption of the dehydrogenated H and surface diffusion of the C adatom species.

4. C species attachment to the graphene domain edge and incorporation into the graphene lattice.

5. The nucleation and growth of the graphene nuclei deplete the adsorbed C species surrounding them, thus the C concentration is decreased to a level where the nucleation rate is negligible, while the growth of the graphene nuclei continues until all the C atoms on the surface of the Cu are consumed.

6. Graphene nuclei either coalesce to form a continuous film or, stop growing to reach a final incomplete coverage.

Graphene is formed from the crystallization of carbon adatoms. However, these adatoms, when on the surface of the Cu, have two options : either to desorb from the surface, or to attach to the graphene lattice to continue forming graphene. Kim *et al.* [83] found that the nucleation of graphene is the result of competition between the mobility of the C species and their desorption rate. They also found that for temperatures above 870°C, the desorption rate is significant compared to the mobility of the C atoms, which means that the nucleation rate is desorption-controlled. Therefore, the growth-limiting step here is the attachment of C adatoms to the graphene edges.

Zhang *et al.* [84] found that the dehydrogenation step is rate-limiting, since the synthesis of graphene can only happen when the dehydrogenation is complete. And since CH_y structures are more thermodynamically favorable to be formed than atomic C, the growth can happen at very late stages.

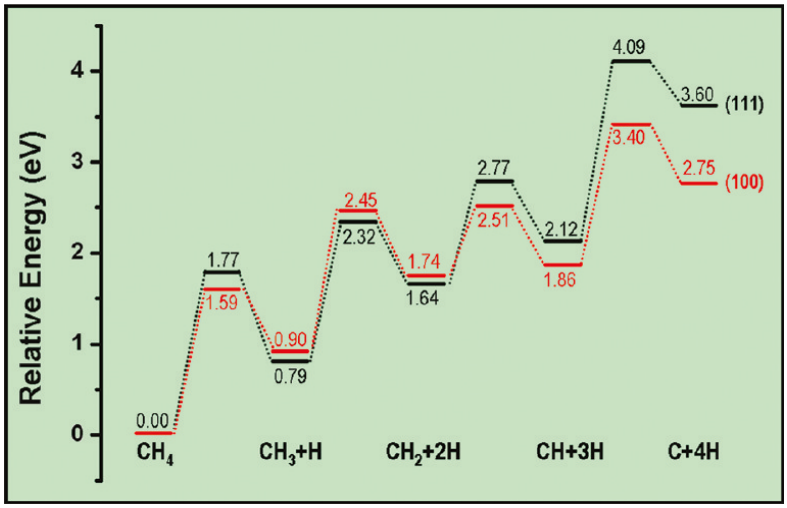

Figure 2.13: Energy profile of the dehydrogenation processes of CH_4 on Cu(100) and Cu (111). Adapted from [84]

Figure 2.13 illustrates the energy of dehydrogenation of the CH_4 molecules on each of Cu(100) and Cu(111). For both copper orientations, the atomic C is very thermodynamically unfavorable on the Cu surface.

All these contributions to the CVD growth of graphene have resulted in a wide comprehension of the synthesis process, and have opened a path for CVD to give rise to graphene with quality comparable to that of mechanically exfoliated graphene.

2.4 Graphene transfer

Since graphene is grown on a metal substrate, it is therefore necessary to transfer it onto dielectric substrates in order to fabricate electrically isolated devices. This step is called the graphene transfer. It represents the main drawback of CVD graphene since it does not preserve the quality of the as-grown graphene. For instance, the chemicals used to etch the growth substrate can introduce impurities into the graphene sheet which act as dopants, therefore changing its electronic properties. A second example is the deionized water used during the process that get trapped between the graphene and the substrate, eventually inducing cracks in the graphene sheet, making it noncontinuous and lowering its crystalline quality. Another drawback comes from the protection layer that is commonly used that can be hard to remove, leaving impurity particles on the graphene surface. Considering how the transfer step alters the intrinsic physical and electrical properties of graphene, it can prohibit its utilization in wafer-scale applications, especially in the electronic industry. Therefore, this step is very important in the graphene-based device industry and it has been in constant improvement over the past years. In this section, we will go back to the first groups who performed the graphene transfer, and we will talk about the different methods of transferring graphene as well as the main advantages and inconveniences of these methods.

2.4.1 A little bit of history

The first transfer of CVD grown graphene from copper foils to silicon dioxide substrates was performed by Xuesong Li *et al.* [40] in 2009. The group first spin coated poly(methyl methacrylate) (PMMA) or polydimethylsiloxane (PDMS) on the graphene film, serving as a mechanical support for graphene during the whole process, and then etched away the copper underneath using an iron nitrate solution ($Fe(NO_3)_3$) as the etchant. When the copper is completely dissolved, the support/graphene remaining film was "fished" onto SiO_2 substrates. This technique was a reproduction of a transfer firstly made by Alfonso Reina *et al.* [87] shown in figure 2.14 (a). This group deposited graphene on SiO_2 by microcleaving HOPG and then transferred it onto another SiO_2 substrate to prove the feasibility of this process. They spin coated PMMA on graphene and used a sodium hydroxide ($NaOH$) solution to detach the PMMA/Graphene film from the initial SiO_2 substrate. Then, they transferred the film onto another SiO_2 substrate. Finally, the PMMA was dissolved using a slow acetone flow. Much like Xuesong Li *et al.*, Alfonso Reina *et al.* carried out their transfer similarly to a method that has been previously reported on carbon nanotubes (CNTs) by Jiao *et al.* [88] (figure 2.14 (b)). This research group also used PMMA as a protection layer for carbon nanotubes and the resist was afterwards dissolved using either acetone or thermal decomposition at 300°C under Ar flow.

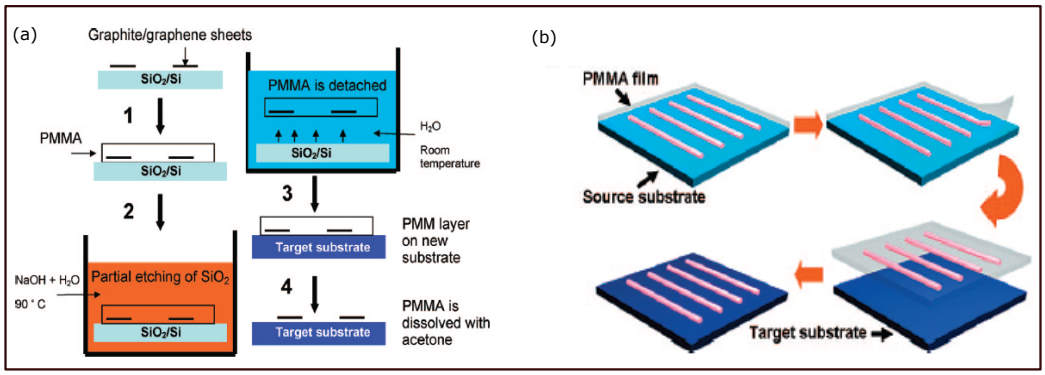

Figure 2.14: The transfer process of (a) microcleaved HOPG on SiO_2 and (b) carbon nanotubes. Adapted from [87, 88].

However, in the same year, Yu *et al.* [39] demonstrated a transfer technique on Ni using silicon rubber (polymerized siloxanes) as the media to transfer a 5 mm x 5 mm graphene sheet on a glass plate. The group covered the rubber with the glass plate to create a Ni/Gr/Rubber/Glass sandwich, and then performed a 24-hour cure in order to solidify the silicon rubber. Afterwards, the Ni was etched away using diluted nitric acid (HNO_3). The result of these previous works gave birth to a now very popular transfer process known as the PMMA-assisted wet transfer of graphene. To this day, this method of transferring graphene is still being used and modified and by a large group of researchers, each with their own recipe, due to its simplicity, rapidity and capability of transferring large graphene areas onto a very large collection of substrates.

2.4.2 PMMA-assisted wet transfer

Figure 4.10 summarizes the PMMA-assisted wet transfer process:

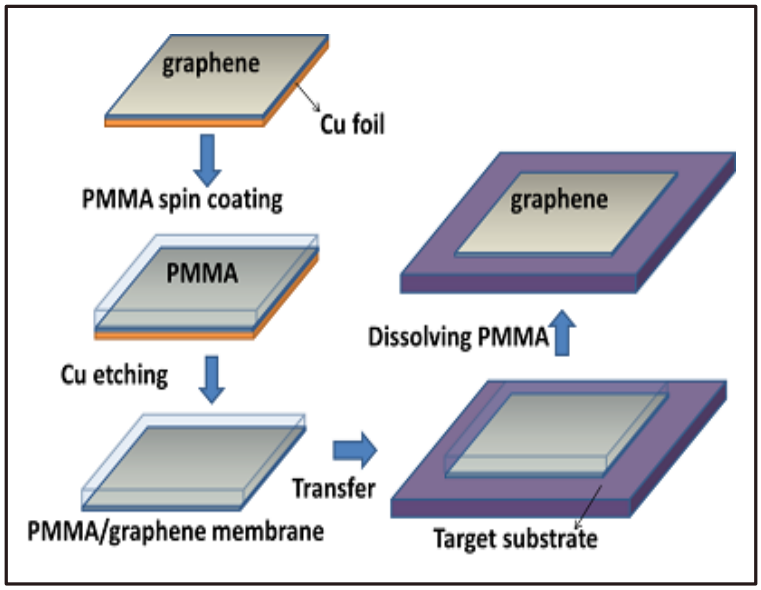

Figure 2.15: The PMMA-assisted transfer process. Adapted from [51].

Generally, there are 4 steps for this transfer technique:

1. PMMA is spin coated on the CVD-grown graphene on Cu as a support layer to avoid the rupture of the graphene druring the transfer.
2. The Cu is dissolved in a commercial copper etchant such as $FeCl_3$.
3. The graphene/PMMA stack is "fished" using the target substrate.
4. The PMMA is dissolved using acetone.

Copper can be etched using a wide collection of chemical solutions including HCl, $Fe(NO_3)3$, $FeCl_3$, $CuCl_2$, $(NH_4)_2S_2O_8$ or $Na_2S_2O_8$, HNO_3 [89–91]. All of these chemicals can efficiently remove Cu, however, not all of them are beneficial for the graphene transfer. This subject will be discussed in chapter 3.

2.5 Transfer techniques

A considerable amount of transfer techniques has branched out of this transfer process, and the labels are not exactly clear. Some groups prefer to categorize the transfer techniques as "wet or dry chemical transfer" [90], since all the graphene transfers involve the use of chemical solutions, others prefer the label "transfer with

and without supporting layers" [92] thus dividing the transfer between groups who use a supporting layer and those who do not, as the name suggests. Others simply say "wet and dry transfer" [93] depending on the environment in which the graphene touches the target substrate. Thus, there is no agreed-upon classification for the graphene transfer methods. Of course, recent studies include direct growth of graphene on dielectric substrates. However, this research area is still at its beginning. The direct growth of graphene film on an insulating substrate such as a SiO_2/Si wafer would be useful for this purpose, but current research efforts remain grounded at the proof-of-concept stage, where only discontinuous, nanometre-sized islands can be obtained [94]

The demand for large-scale, low cost and efficient transfer of CVD graphene to arbitrary substrates has led to the development of various optimized and upgraded PMMA techniques.

For example, a few months apart, the same group that has demonstrated the transfer of graphene on Cu in 2008, has improved this technique by adding a second layer of PMMA after the transfer on SiO_2 [20]. This helps dissolve the first layer by mechanically relaxing the underlying graphene in order to obtain a better adhesion with the substrate. This technique has been redefined by Barin *et al.* in 2014 [95], where it was shown that adding a second PMMA layer that is diluted enough, right after the transfer of the graphene onto the final substrate, helps dissolve the first PMMA layer, decreasing by that the polymer residues and consequently increasing the graphene quality. The group also studied the effect of annealing on the residues and found that a short period of time (5 min) is not sufficient enough to eliminate trapped water molecules between the PMMA/graphene and the target substrate, and long baking times (40 min) resulted in high amounts of residues on the graphene surface. However, a baking time of 25 minutes was found ideal and yielded relatively high hole mobility values between 1000 and 1200 $cm^2/(V.s)$. Both methods of using two PMMA layers are shown in figure 2.16.

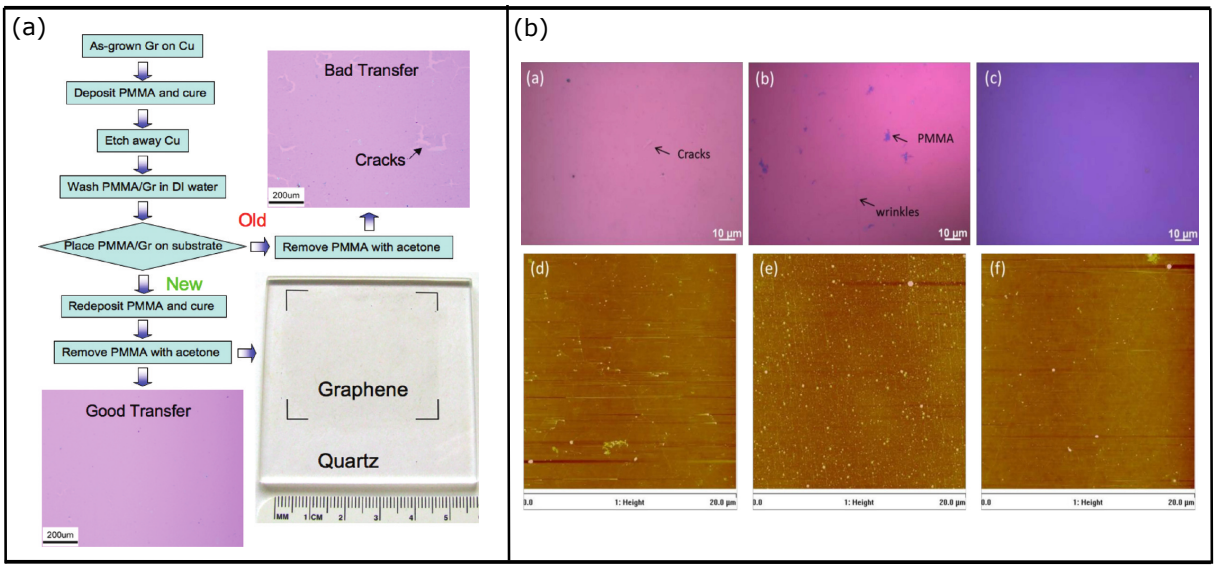

Figure 2.16: The transfer method using 2 layers of PMMA. (a) is the work of Li *et al.* [20] in which a second layer of PMMA was dropped on the initial spin-coated PMMA layer after the transfer on target substrates, which generated less cracks through a better PMMA/graphene-substrate contact. (b) is the work of Barin *et al.* [95] in which optical images (a-c) and AFM measurements (d-f) showed that a well diluted second PMMA layer can effectively reduce the polymer residues on graphene (c,f) in contrast to only one PMMA layer (a,d) and (b,e) 2 PMMA layers of the same concentration (4.5% anisole).

Recently, Kim *et al.* [96] have showed that using a low average molecular weight PMMA yields cleaner graphene with less polymer residues and thus less p-doping and improved charge carrier mobility.

Gorantla *et al.* [97] on the other hand demonstrated a low cost transfer technique that does not involve the etching of the metal substrate, offering the advantages of reusing it and of avoiding the doping of the graphene from the etching solution. The group coated the graphene with PMMA and then combined $NH_4OH + H_2O_2 + H_2O$ at 80°C to form vigorous bubbles which separated the PMMA/graphene from the Cu substrate, and transferred it onto arbitrary substrates and finally removed the PMMA using hot acetone vapor (100°C). Although this transfer process showed a small density of defects in the graphene sheets, it still offers many other advantages. The transfer process is shown in figure 2.17 (a).

For water-sensitive substrate, a similar transfer method has been reported by Ohotmo *et al.* [98], where the PMMA/graphene was detached from the copper substrate using a 12-hour intercalation of alkanethiol selfassembled monolayers (SAMs) at the graphene/Cu interfaces. In fact, the formation of SAMs releases the compressive strain of graphene induced by the metal substrate but however slightly n-dopes the graphene. This method is also economically competitive since the Cu substrates can be reused.

Gao *et al.* [99] on the other hand developed a face-to-face transfer method for wafer-scale graphene

films. This technique allows both the growth and transfer steps on one wafer, and is compatible with any size and shape of substrate, which is a huge advantage for large-scale commercialization of graphene-based electronic devices. The principle of this process relies on the capillary bridges formed between the graphene film and the underlying substrate during etching of the metal catalyst. In fact, the initial SiO_2/Si substrate is subjected to a nitridation pre-treatment, and 700 nm-thick copper is then sputtered on the substrate. Graphene is subsequently grown on the copper surface. Then, the graphene is coated with PMMA and the $PMMA/graphene/Cu/SiO_2/Si$ is immersed in an etching solution to remove the Cu. The nitridation pre-treatment of SiO_2/Si is a critical step in this process because it generates silicon oxynitride on the silicon wafer that decomposes during the CVD growth and forms bubbles during the Cu etching, which are essential for the formation of capillary bridges between the graphene and the underlying substrate. These bridges ensure that the graphene film remains attached to the substrate. Finally, the PMMA is removed with acetone and the sample is baked to completely evaporate the infiltrated water. This technique is very useful for rigid graphene devices, however, the current technological flow is aiming towards flexible electronics and other applications. The transfer process is shown in figure 2.17 (b). Although PMMA has been commonly used in the transfer process throughout all these years due to its advantages such as flexibility and mechanical support, PMMA has been experimentally proven to be difficult to remove from the graphene after transfer. It inevitably leaves residues on the surface of the graphene, which affect the overall quality and electronic properties of graphene [92, 100]. Various post-transfer procedures to reduce the PMMA residues have been made, such as high-temperature annealing in a mixture of H_2/Ar [101], laser treatment [102] and electrolyte cleaning [103]. However, current processes cannot fully remove the PMMA residues without introducing defects in the graphene film.

A well-known transfer technique on flexible substrate is the roll-to-roll technique reported by Bae *et al.* [26]. This technique is destined for large-scale growth and transfer of predominantly monolayer graphene on flexible substrates such as PET, for applications such as transparent electrodes. The process consists of growing graphene on a roll of copper foil inserted into a tubular quartz tube, as shown in figure 2.17 (c). After the growth, the graphene is attached to a thermal release tape by applying a soft pressure between two rollers. Then, the copper foil is etched using a commercial Ammonium persulfate solution ($(NH_4)_2S_2O_8$) and further cleaned in DI water. Afterwards, it is transferred to a flexible substrate (PET here) by inserting the graphene on the thermal release tape into the rollers, along with the target substrate and exposed to mild heat reaching 120°C. By doing this, the thermal release tape will be detached and the graphene will be transferred onto the target substrate. This technique demonstrate a great promise for flexible electronics, but however cannot be implemented in laboratories for further characterizations.

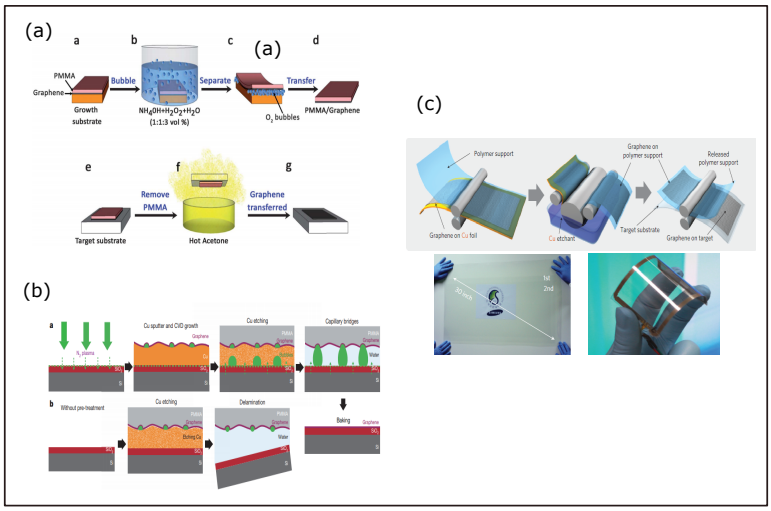

Figure 2.17: The transfer techniques using different methods: (a) The bubbling technique (b) Face to face transfer and (c) Roll to Roll transfer. Adapted respectively from [97], [99] and [26].

The work of K.S. Kim *et al.* [25] not only demonstrated CVD grown graphene on Ni, but also two transfer methods on rigid (SiO_2) and flexible ($PDMS$) substrates (figure 2.18 (a)). The two techniques are close in principle. Basically, a thin layer of 300 nm Ni is deposited on a SiO_2/Si substrate, and after graphene synthesis, the graphene is coated with a PDMS stamp and the Ni film is etched using a commercial Ni etchant such as $FeCl_3$. Thus, the PDMS/graphene membrane is then transferred onto SiO_2 substrates. In the other technique, the graphene is not coated by a support layer, and the $Ni/SiO_2/Si$ is etched using a HF/BOE solution for a long time. Since few-layer graphene is obtained on Ni, there is no need for a support layer because it is strong enough not to collapse under surface tension.

Much like PMMA, PDMS-assisted methods have inherent drawbacks, such as the introduction of adhesive residues and defects in the transferred graphene films which deteriorate the excellent electronic properties of graphene and restrict their applications in commercial devices [92, 104].

Recent works aim towards the replacement of PMMA/PDMS, one in order to obtain a clean graphene, and two, in order to lower the costs of the transfer process. For instance, a natural polymer, cellulose acetate [105] is extracted from seaweed, and has been proven to efficiently replace the PMMA/PDMS. Chen *et al.* [105] demonstrated two similar transfers, one using cellulose acetate (figure 2.18 (b)) and another one using the standard wet transfer including PMMA. They managed to show that by using this green polymer, fewer residues were found on the graphene sheet and graphene-based field effect transistors exhibited high mobilities 2 times higher than those for devices prepared with the standard wet transfer (1650 $cm^{-1}/(V.s)$ hole mobility using cellulose acetate compared to 450 $cm^{-1}/(V.s)$ using PMMA). In addition to carrier

mobility, the on-off ratio of the transferred graphene is found to be enhanced by 60% when the cellulose acetate assisted method as compared to the PMMA-assisted transfer. This technique could be useful for economic large-scale fabrication of graphene-based devices in electronics, spintronics, and energy storage applications.

The polymer plays a very important role in the graphene transfer process. Without it, graphene would collapse during the substrate etching step due to the suface tension of the etching solution. However, since completely eliminating the polymer has not been accomplished yet, several works aimed at completely eliminating the use of a polymer in the transfer process by reducing the surface tension created by the etching solution, such as the work of Lin *et al.* [106]. In this work, they demonstrated a polymer-free graphene transfer to arbitrary substrates, using a graphite holder for the graphene/copper film to minimize any external force around graphene while the copper is etched using a chemical etchant. When the metal was completely etched, a mix of DI water and isopropyl alcohol (IPA) was injected into the beaker containing the etchant and the graphene on the holder. Simultaneously, the etchant was pumped at the same rate as the injection of DI water + IPA to control the surface tension. Finally, the graphene floating on the surface was lowered to the target substrate by slowly pulling out the remaining solution with a syringe pump. The use of IPA is critical in this process because it controls the surface tension of the etching solution, prohibiting the graphene from collapsing. The transfer process is described in figure 2.18 (c). Despite the residue-free transfer Lin *et al.* demonstrated, this technique has low yield since monolayer graphene tend to crack easily without a support layer, further proving how the transfer technique remains a challenging task.

Other transfer techniques include the use of metals as the support layer [107] but are not industrial-friendly since they are either costly or induce further defects in the graphene sheet.

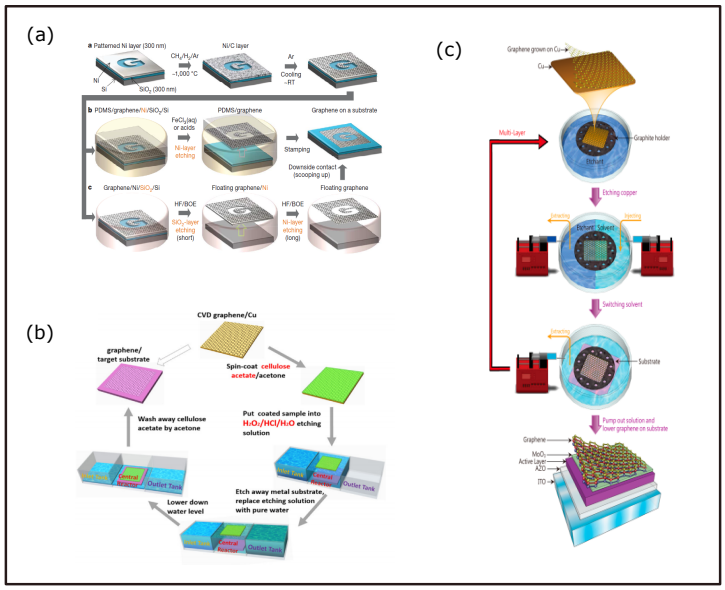

Figure 2.18: The transfer techniques using different methods: (a) The PDMS-assisted graphene (b) The green transfer using cellulose acetate and (c) The PDMS-assisted graphene transfer. Adapted respectively from [25], [105] and [106].

Figure 2.19 summarizes the properties of the graphene transferred via some of the most common transfer techniques.

Method	Growth substrate	Target substrate	[G cm^{-1}]	[2D cm^{-1}]	[D cm^{-1}]	I_{2D}/I_G	I_D/I_G	Sheet resistance	Field-effect mobility	No. layer
Wet transfer	Cu	SiO_2/Si	1560–1620	2660–2700	1300–1400	2.0			4050 $cm^2 v^{-1} s^{-1}$ (carrier-mobility)	95% one-layer
(polymer-assisted)	Cu	SiO_2/Si glass	1588	2690	1350	8.0–11.0	0.06–0.12	980 Ω sq^{-1}		one-layer
	Cu	SiO_2/Si PET	1583	2642	1320	3.1	0.06	255 Ω sq^{-1} (on glass)	5602 $cm^2 v^{-1} s^{-1}$ (hole-mobility)	one-layer
									4535 $cm^2 v^{-1} s^{-1}$ (electron mobility)	
Polymer-free	Cu	SiO_2/Si		2700				810 Ω sq^{-1}	6300 $cm^2 v^{-1} s^{-1}$ (on BN)	One-layer
Electrochemical	Pt	SiO_2/Si	1590	2685		2.0–3.0	<0.05		7100 $cm^2 v^{-1} s^{-1}$	Mostly one-layer
	Cu	PET	1582	2678				275 Ω sq^{-1}	350 $cm^2 v^{-1} s^{-1}$ (6 K)	>95% one-layer
Dry transfer	Cu	PDMS	1584	2681	1350	2.43	0.2			one-layer
	SiC	SiO_2/Si	1530	2700	1380		0.037 ± 0.008	175 Ω sq^{-1}	1348 $cm^2 v^{-1} s^{-1}$	one-layer
Face-to-face	Cu	SiO_2/Si	1560–1620	2690	1350				3800 $cm^2 v^{-1} s^{-1}$ (hole mobility)	one-layer
Transfer free	SiO_2/Si		1592	2685	1351	>2			667 $cm^2 v^{-1} s^{-1}$ (room temperature)	one-layer

Figure 2.19: (f) Table representing the properties of the transferred graphene film by different methods. Adapted from [93].

2.6 Raman spectropscopy for graphene characterization

Raman spectroscopy is a non-destructive characterization technique based on the inelastic interaction between the phonons (molecular vibrational modes) in a material and photons emitted from a monochromatic laser source. The basic concept of Raman spectroscopy states that when a material is excited with a light ray, its photons are absorbed by the sample and then re-emitted. If the incident photon has lost energy to a phonon, it is called Stokes scattering, thus the emitted photon will have a smaller frequency than the incident photon, and if the photon has gained energy from the phonon, it is called Anti-Stokes scattering, and the emitted photon will have a higher frequency than the incident photon as shown in figure 2.20. This frequency change is called the Raman Effect and it provides information on vibratory transitions, rotations and other low frequency transitions in molecules. The frequency differences between the incident v_0 and the dispersed inelastic v_v are determined by the properties of the molecules that constitute the material under study. In practice, only a tiny portion of the light sent undergoes inelastic scattering (approximately 1 in 10,000 photons). Much of the incident light is scattered exactly at the same frequency of the exciting light (Rayleigh elastic scattering). Identifying vibrational modes using only laser excitation, Raman spectroscopy has become a powerful, noninvasive method to characterize graphene and related materials. Characteristics such as disorder, strain, thickness, edge and grain boundaries, doping and thermal conductivity of graphene can be learned from Raman spectroscopy.

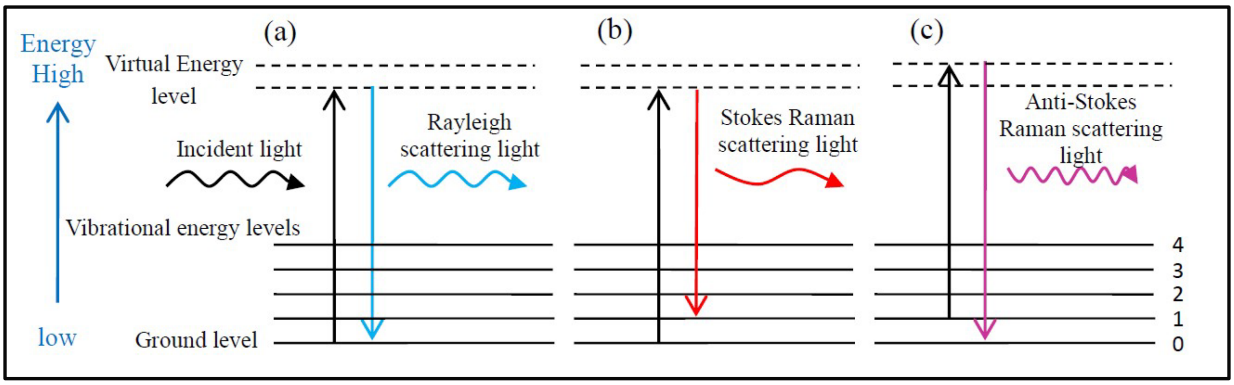

Figure 2.20: Schematic representation of Rayleigh scattering, Stokes Raman scattering and Anti-Stokes Raman scattering. Adapted from [108]

It has been shown that Raman spectroscopy can be used as a fingerprint tool for single, bi and few layer graphene [10, 109–112]. This characterization technique is particularly useful for graphene because of the semi-metal nature of this material that makes all wavelengths of incident radiation resonant, and therefore gives information about not only the atomic structure of graphene, but also its electronic properties. However, the relative simplicity of Raman measurements is balanced by the complicated data interpretation.

The Raman spectrum of single layer graphene consists of two main intense peaks (figure 2.21 (c)):

- The G band: Typically observed at 1585 cm^{-1} for a laser excitation energy of 532nm (2.33 eV), this peak is due to doubly degenerate high frequency E2g mode at the Brillouin centre Γ (figure 2.21 (e)). It is assigned to the in-plane optical vibration mode where each carbon atom vibrates in opposite direction to its three nearest neighbors (figure 2.21 (a)). This peak is present in the Raman spectroscopy of other carbon materials containing sp2 bonds such as carbon nanotubes and graphite since it corresponds to in-plane vibrations of sp2 carbon atoms.

- The 2D band: Also known as the G' band, this peak is observed at around 2680-2700 cm^{-1} for a laser excitation energy of 532nm (2.33 eV). It is a second-order double resonant process, that arises from the inter-valley scattering of the electrons by the Brillouin zone boundary phonons (figure 2.21 (f)). This peak always satisfies the Raman selection rule (q=0), thus it is always allowed.

For a defective graphene, a third band usually appears at around 1345 cm^{-1}. It is called the D band, and it is a defect-induced peak. The electron scattering process associated with the D peak involves both a Brillouin zone boundary phonon (TO phonons around the Brillouin zone corner K) and a defect state (figure 2.21 (d). The phonon mode responsible of this peak is related to the breathing modes of the sp2 six-atom rings and their excitation is forbidden for the Raman fundamental selection rules (figure 2.21 (b)), therefore, the D peak is absent in defect-free graphene. This peak is usually used as a measure of the quality of graphene flakes. Much like the 2D peak, the D peak is active by double resonance and is strongly dispersive with the excitation energy. A similar process to that of the D band is possible intra-valley. This activates phonons with a small q (wave vector), resulting in the so-called D' peak, which can be seen around 1620 cm^{-1} in defected graphite/graphene [10].

Since the 2D peak appear at twice the frequency of the D peak, it is thus considered as the second-order effect of the D band. Other secondary peaks exist, but they are not detailed in this work.

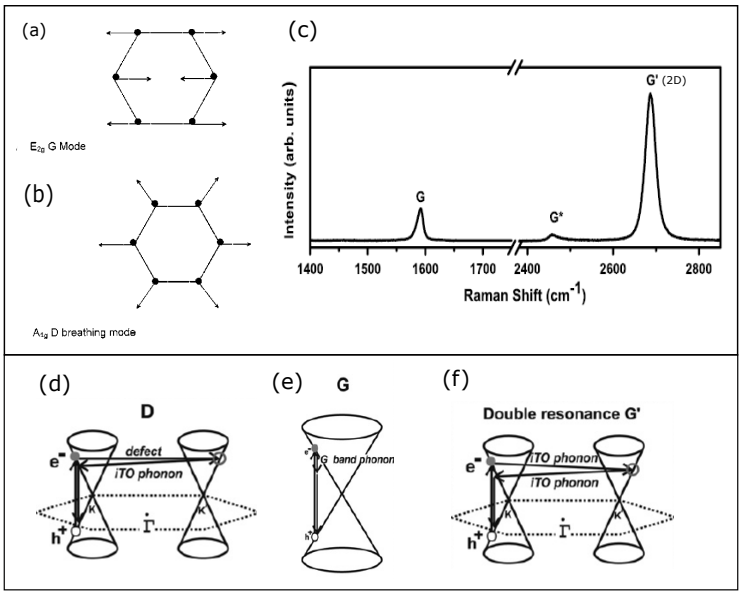

Figure 2.21: Graphical representations of examples of phonon scattering processes responsible for the significant graphene Raman peaks of (a) $E2_g$ mode of G lattice vibration and (b) $A1_g$ breathing mode of D peak. (c) Raman spectrum of monolayer graphene measured with a 2.41 eV laser excitation energy, showing the first-order Raman allowed G band and the very strong G' (or 2D) band described by one Lorentzian and a peak frequency of 2687 cm^{-1}. The G* band is also shown near 2450 cm^{-1}. (d) First-order G-band process (e) one-phonon second-order DR process for the D-band (intervalley process) (f) two-phonon second-order resonance Raman spectral processes for the double resonance 2D (G') process. Adapted from [109, 113]

Raman spectroscopy has also been shown to determine not only the graphene quality, but also the number of graphene layers. Figure 2.22 (a) shows the evolution of the Raman spectrum of graphene with increasing layer number (up to four). For more than five layers, the Raman spectrum of graphene and graphite become hard to distinguish [114]. The I_{2D}/I_G ratio decreases for an increasing number of layers and the 2D peak broadens, blue-shifts, and loses its Lorentzian shape. This is further confirmed in figure 2.22 (c), where the position of the 2D peak shifts towards higher frequencies with increased layer number for different excitation energies. As figure 2.22 (d) further demonstrates, single layer graphene presents a sharp Lorentzian 2D peak, while bilayer graphene presents a broader 2D peak, consisting of four components ($2D_{1B}, 2D_{1A}, 2D_{2B}$ and $2D_{2A}$). However, one should distinguish monolayer graphene from it turbostratic graphite, where the graphene layers are misoriented (i.e. without AB stacking) which also has a single 2D peak [115]. The evolution of the 2D peak originates from the multiple resonance modes present in the few-layer graphene that could be activated to give rise to the multi components of the 2D peak. This is further because the energy bands of the graphene with more than one layer split into several sub-bands due to the inter-layer

interaction. Thus, I_{2D}/I_G ratio provides a good correlation with the number of graphene layers.

The linewidth of the 2D peak is also an important indication of layer number. A FWHM(2D) around 30-35 cm^{-1} on silicon dioxide indicate a monolayer graphene, whereas a FWHM(2D) around 50 cm^{-1} indicates a bilayer graphene [38, 40, 87].

The linewidth of the 2D and G peaks are also correlated to the nanoscale-strain present in the sheet. According to Neumann *et al.* [116], a very narrow G line (lower than 22 cm^{-1} on silicon dioxide) and a broad 2D line (higher than 35 cm^{-1} on silicon dioxide) in the monolayer regime indicates the presence of nanoscale strain variations, a very important parameter affecting the charge carrier mobility of graphene.

The positions of the G and 2D bands are also affected by the level of charge doping in the graphene sheet. An indication of chemical doping is the upshifting of the G peak by 3-5 cm^{-1} which is consistent with hole doping [95, 114].

Thus, a high quality single layer graphene would be characterized in a spectrum containing no D-peak, indicating a very low density of lattice defects, a I_{2D}/I_G ratio around 2, a sharp Lorentzian 2D peak exhibiting a full-width-at-half-maximum (FWHM) of around 35 cm^{-1}.

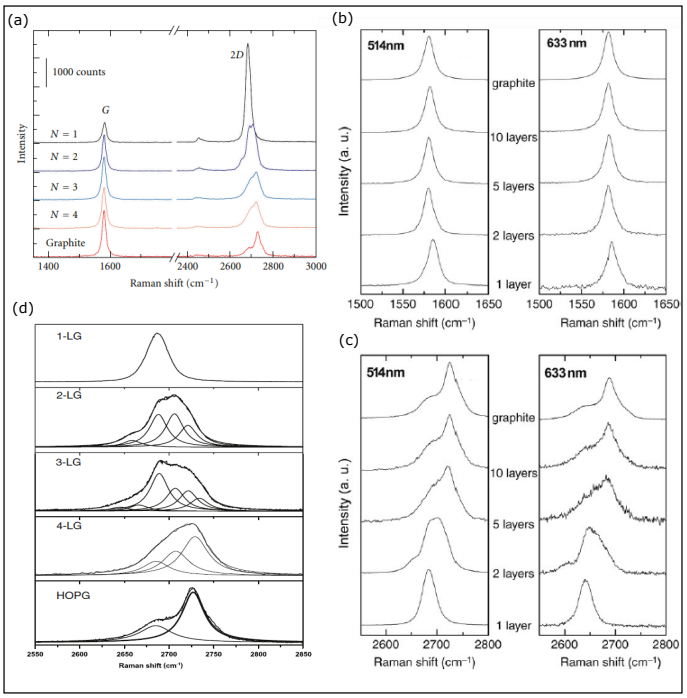

Figure 2.22: (a) Raman spectra of 1,2,3 and 4 layer graphene transferred onto SiO2/Si and of bulk graphite. (b) Evolution of the G peak with the layer number, respectively for 514 nm and 614 nm laser excitation energy. (c) Evolution of the 2D peak with the layer number, respectively for 514 nm and 614 nm laser excitation energy.(d) Evolution of the 2D line width with the layer number. Adapted from [10, 109, 117]

2.7 Graphene-based electronics and fexible electronics

2.7.1 Graphene-based electronics

Graphene has shown great potential in electronics, due to its unmatched combination of mechanical and electronic properties. For instance, graphene-based FETs have been widely demonstrated on arbitrary substrates such as SiO_2/Si, SiC [42,118,119] and hBN [120,121], with mobilities ranging from 1000 $cm^2/(V.s)$ for standard polycrystalline graphene on silicon dioxide to 60 000 $cm^2/(V.s)$ for CVD-graphene transferred on SiO_2/Si and encapsulated in hBN [122] using the standard wet transfer. These values highly surpass those of silicon-based FETs for the same channel lengths, making graphene amongst the candidate materials in post-silicon technologies. Graphene has also been implemented in radiofrequency applications such as low noise amplifiers and mixers thanks to its extremely high carrier velocity. Among all the type of graphene that can be used for RF devices, exfoliated graphene, epitaxial graphene and transferred CVD graphene usually come into focus. For instance, in 2010, devices based on exfoliated graphene using a nanowire as a top gate electrode achieved record cutoff frequencies higher than 300 GHz [123]. In 2011, by optimizing the gate dielectrics and the device dimensions, a record high output current and transconductance of 5 mA/μm and 2 mS/μm (respectively) in epitaxial graphene FETs and a cut-off frequency of 280 GHz was achieved for a 40-nm graphene FET [124]. In addition, the highest voltage gain of 10 dB has been achieved with an f_{max}/f_T ratio larger than 1 demonstrated consistently on different devices. It was for the first time that forward power gain $|S_{21}| > 1$ delivered into a 50 Ω load was demonstrated. When it comes to chemical vapor deposited graphene, the highest intrinsic cut-off frequency of 155 GHz has been achieved in 2011 for a device based on a transferred layer of graphene on top of a diamond-like carbon substrate with a 40 nm channel length [125].

The major obstacle of graphene in transistor applications, especially for integrated circuits as a potential Si replacement, is its zero bandgap. This property is responsible for the low I_{ON}/I_{OFF} ratio in GFETs due to a non-zero off state drain current, which leads to considerable static power dissipation [23].

Many techniques were developed in order to open a band gap in graphene, such as applying a uniaxial strain on graphene [126], large area hybrid films consisting of CVD-graphene and h-BN domains [127], quantum confinement (graphene nanoribbons [128,129] and graphene nanomesh [130]) and substrate induced band-gap opening [131]. Band-gap opening in graphene, both on h-BN and h-BN/Ni(111) with band gap up to 0.5 eV was also reported [132], and a bandgap for bilayer graphene grown on SiC was observed [133]. Other techniques include substitutional doping. For instance, nitrogen doping might be used to convert graphene into a p-type semiconductor [134]. However, opening a band gap remains one of the biggest challenges in electronics because usually, opening a band gap tends to induce defects into the graphene lattice, compromising graphene's other properties, such as charge carrier mobility and high field transport.

Among all these techniques, confinement of charge carriers by creating nanostructures like graphene nanoribbons (GNRs) or graphene nanomesh (GNMs) [130,135–138] seem to be the most promising for band gap opening. Although GNRs allow to open band gaps and have achieved an I_{ON}/I_{OFF} ratio of 10^7 at room temperature [139] and at 6K [140], there are several problems accompanied by the GNRs such as edge roughness induced localization effect and coulomb blockade effect [139, 141]. According to the scaling law, sub-10nm GNRs widths are required in order to achieve sufficiently large bandgaps for room temperature transistor operations, which is hard to fabricate. In addition, for the integration of GNRs in circuitry, precise placement of multiple GNRs into densely organized arrays is required [142]. Graphene nanomesh (GNM) seem capable to overcome these problems. By punching holes into a graphene sheet (by blockcopolymer lithography, nanoimprint lithography, nanoparticles local catalytic hydrogenation, etc), a high-density array of nanoscale-holes is created, as shown in figure 2.23. This structure can open a bandgap in graphene, and the bandgap depends on the neck width, the meshing orientation and the shape of holes [143,144], whereas a bandgap higher than 0.5 eV could be achieved. GNM-based transistors have been demonstrated to support driving currents nearly 100 times greater than that of individual GNRs devices with a comparable onoff ratio. Therefore, GNM has attracted increasing attention over the past couple of years.

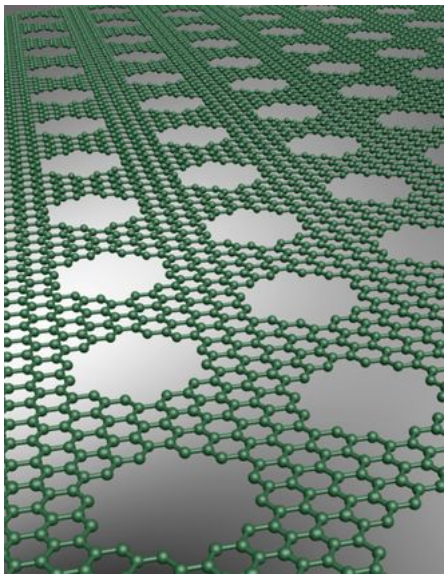

Figure 2.23: Schematic representation of a graphene nanomesh. Adapted from [145].

Opening a bandgap in graphene would open up a great number of new applications for graphene-based devices including high performance FETs, chemical sensing, supercapacitors, DNA sequencing, photothermal therapy, and a new generation of spintronics [23, 146–148].

2.7.2 Flexible electronics

Flexible electronics is the next generation universal platform for the electronics industry [23]. The realization of electronics with performance equal to that of established rigid technologies, but lighter, cheaper, more flexible, environmentally friendly, foldable, stretchable and more durable would enable numerous new and unforeseen applications in sectors including healthcare, the automotive industry, human/machine interfaces, mobile communications and computing platforms, and so on. Smaller and thinner electronic devices allow for higher performances, since a much higher number of devices can be implemented in integrated circuits for example, enabling a possible continuation of Moores law.

But why is it that the idea of flexible electronics have already existed for several years, but has not yet been commercialized?

In fact, a number of technological challenges still exist today. For instance, commercial flexible electronics should retain their mechanical and electrical properties even under mechanical deformation, and the materials used should meet performance criteria such as high conductivity or transparency, and eco-friendly. The incomparable flexibility, mechanical strength, optical transparency and thermal conductivity of graphene have led researchers to think about graphene as the ultimate solution to post-silicon technologies. Graphene-based flexible electronics might enable novel applications as well as enhanced performance not allowed by present technology [149, 150].

Flexible electronics started to become a very attractive active research in 2008 when Nokia first imagined a foldable and wearable mobile device named the Morph Concept [151]. From the beginning of the realization of flexible screens using organic materials [152], a wide range of applications have been developed such as flexible visual memory systems [153], lab-on-skin health monitoring [154], flexible batteries [155], flexible solar cells [156], *etc.*.

Flexible FETs have already been demonstrated with solution-based single-layer graphene yielding a 2.2 GHz cutoff frequency [157] and chemical vapor deposited graphene, where Lee *et al.* demonstrated a GFET with a 25-GHz cutoff frequency [158]. Yu *et al.* even broke the record for extrinsic cutoff frequency measuring 116 GHz in high frequency CVD-grown GFETs with gate length of 50 nm [159]. However, Petrone *et al.* still hold the record for highest intrinsic cutoff frequency of 198 GHz for CVD graphene transferred onto PEN substrates [160]. These advances in flexible RF electronics give hope for next generation graphene-based flexible electronics. In radiofrequency applications, the first flexible RF device based on graphene flakes on kapton was demonstrated by Sire *et al.* from the CEA Saclay laboratory in 2012 demonstrating cutoff frequency at 2.2 GHz and maximum frequency of 0.55 GHz [157]. The state of the art is recorded by Pallecchi *et al.* at the IEMN laboratory for demonstrating a cutoff frequency of 39 GHz and a 13.5 GHz maximum frequency [161] using a CVD graphene transferred onto a kapton substrate and a 180 nm gate length with an Al_2O_3 oxide layer.

Figure 2.24 summarizes the next-generation flexible electronics systems and their appropriate materials.

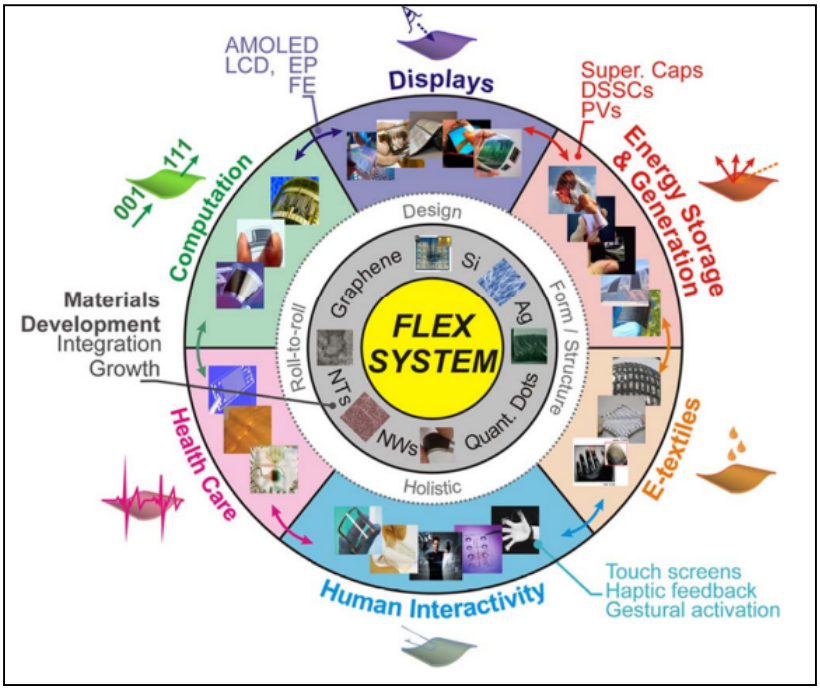

Figure 2.24: Next-generation flexible electronics systems and the underlying materials. Adapted from [150].

Chapter 3

Methodology

This chapter is divided into two sections. In the first section, surface characterization methods including atomic force microscopy, scanning electron microscopy, X-ray photoelectron microscopy and Resiscope mode are discussed. These techniques were used as part of this work for characterizing the copper surfaces before and after treatment, in terms of roughness, morphology and chemical composition, as well as identifying the presence and amount polymer residue on transferred graphene. These results are very important, as they identify the effects of copper treatment on the roughness and cleanliness of the copper as well as the concentration and effect of PMMA residue on the graphene sheet and subsequently electronic properties. In the second section, the fabrication steps that led from the CVD-transferred graphene to the graphene-based field effect transistors will be discussed. Electron beam lithography, reactive ion etching, electron beam physical vapor deposition and atomic layer deposition will be described.

In this work, the fabrication process was carried out at the C2N (Centre de Nanosciences et de Nanostructures) laboratory and the surface characterization and the electrical measurements of the devices were performed in the GeePs (Genie Electrique et Electromagnetique de Paris) and the L2E (Laboratoire d'Electronic et d'Electromagnetisme) laboratories. Raman spectroscopy was realized at the C2N and GeePs laboratories.

3.1 Surface characterization methods

3.1.1 Atomic force microscopy (AFM)

Atomic force microscopy (AFM) is a type of Scanning probe microscopy (SPM). It is designed to probe the surface topography of a sample by measuring the force between a probe and the sample. The probe is a sharp tip called a cantilever, typically made of silicon or silicon nitride, and it is a 3-6 μm tall pyramid with a radius of a few to tens of nm. The tip can be brought within atomic distances above the sample surface by moving either the sample with piezoelectric transducers or the scanning head of the AFM. This technique is based on the repulsive and attractive atomic forces experienced by the cantilever. In fact, there are two types of atomic forces: when the cantilever and the sample are distanced by about 0.1 nm, short range interactions occur, and are repulsive due to the proximity of the electron orbitals in the sample with those at the cantilever surface. Long range interactions however can be attractive and repulsive (electric, magnetic), or just attractive (van der Waals), and are present when there is a distance of about 1 nm between the tip and the sample. When the tip is approached to a sample surface, forces between the tip and the sample lead to a deflection of the cantilever. The deflection of the tip is measured using a laser spot reflected from the top surface of the cantilever into an array of photodiodes, as shown in figure 3.1.

There are three main operation modes for an AFM: contact, non-contact and tapping. In the contact mode, the tip scans the sample in close contact with the surface. The force on the tip is repulsive. This mode can damage the samples since the surface is scratched by the tip of the cantilever. In the non-contact mode, the cantilever oscillates a few nanometers (5-15 nm) above the surface of the sample. Attractive Van der Waals forces acting between the tip and the sample are detected, and topographic images are constructed by scanning the tip above the surface. The tapping mode allows high resolution topographic imaging of sample surfaces that are easily damaged. In this mode, the tip oscillates around 100-200 nm above the sample. Then, the tip is moved toward the surface until it begins to lightly touch, or tap the surface. The image is therefore produced by imaging the force of the intermittent contacts of the tip with the sample surface. This mode reduces the damage done to the surface and the tip compared to the amount done in contact mode [162, 163].

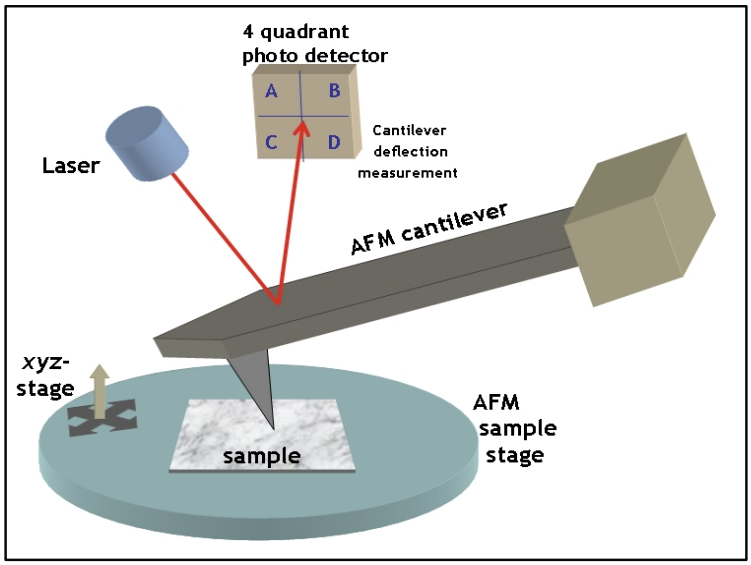

Figure 3.1: Schematic of the operation principle of an Atomic force microscope. Adapted from [164].

The AFM has the advantage of imaging almost any type of surface, including polymers, ceramics, composites, glass, and biological samples (unlike the STM for example, which can only characterize semiconducting and conducting surfaces).

In this thesis, both a Brucker Multimode and a Brucker Enviroscope AFMS were used at the Group of Electrical Engineering of Paris laboratory (GeePs) laboratory to characterize the roughness of the copper surface before and after treatment, as well as the field effect graphene channel topology, including the wrinkles, folds and PMMA residues on the graphene surface, as well as the thickness of the graphene.

3.1.2 Resiscope AFM mode

The use of conductive tips has paved the way for many new investigations combining the topography with electrical, magnetic and mechanical characteristics of the studied material. Electric modes include electric force microscopy, which allows the detection of electric charges [165] and kelvin force microscopy which detects surface potentials [166]. At the GeePs laboratory, a new electrical mode named Resiscope has been invented (patent number EP 2567245A1 (2013)) and is of particular interest for characterizing the conductive properties of materials [167]. The electronic system is showed in figure 3.2 and the principle is the following: similar to the AFM contact mode, the AFM tip is always in contact with the sample with a constant force. A fixed DC bias is then applied between the conductive tip and the sample. The current is amplified through a conversion module and sent to the AFM controller that will build an electrical image simultaneously with the topography of the surface sample. Every pixel of the image corresponds to the respective value of the resistance between the tip and the sample. The amplitude of detection ranges from 102 to 1012 Ω and the speed imaging can reach 5 kHz. Different kinds of AFM tips with different spring constant (expressed in N/m) can be used in order to take into account the hardness of the investigated materials.

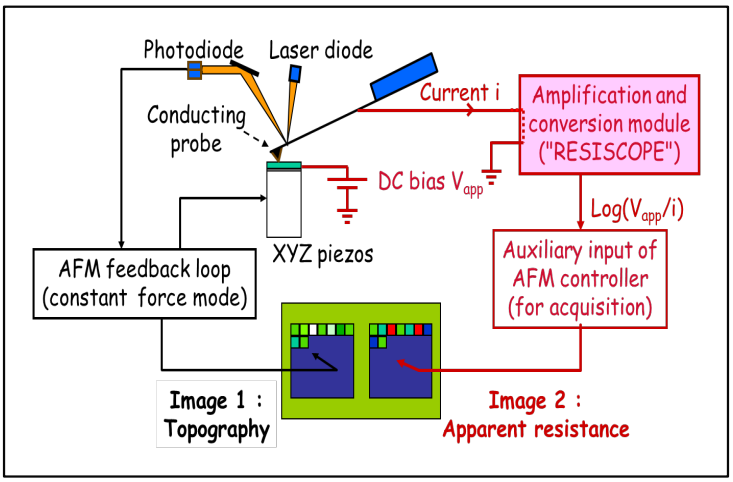

Figure 3.2: Schematic of the principle of the Resiscope mode. Image belongs to the GeePs laboratory.

3.1.3 Scanning electron microscopy (SEM)

Scanning Electron Microscopy (SEM) is a characterization technique extensively used to study the surface morphology of a sample. By scanning the sample surface with a focused beam of high energy electrons and collecting, via appropriate detectors, the secondary and backscattered electrons returning from the surface, an image of the morphology can be generated with very high resolution. SEM has the advantages of high resolution (under 100 nm), high contrast and high surface sensitivity. A scanning electron microscope is shown in figure 3.3 (left).

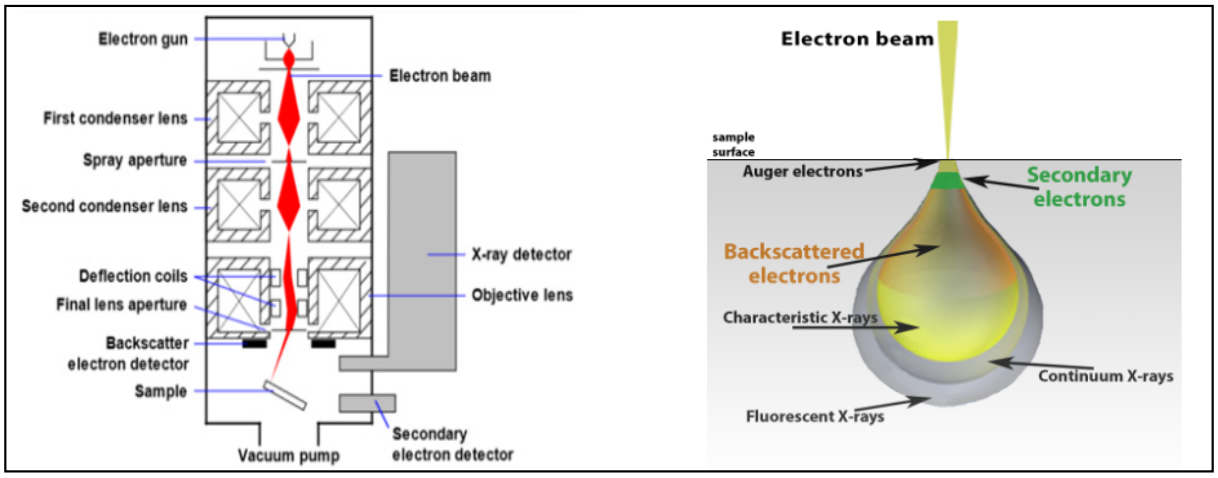

Figure 3.3: Left: Schematic representation of a Scanning Electron microscope. Right: Schematic representation of electron beam interaction. Adapted from [168].

A scanning electron microscope is composed of many components. The electron gun provides a stable beam of electrons. There are three main types of electron guns: Tungsten hairpin, Lanthanum hexaboride (LaB_6) and Field emission. The condenser and objective lenses control the diameter of the passing beam and focus the beam on the specimen. A series of apertures (micron-scale holes in a metal film) affect the properties of the beam, and finally, the beam interacts with the specimen, and the interaction generates several types of signals that can be detected and processed to produce an image. All this procedure is maintained at high vacuum levels [168].

The generated signals are the combination of the elastic and inelastic interactions which distributes the beam electrons over a three-dimensional ″interaction volume″ shown in figure 3.3 (right). These signals include secondary electrons, backscattered electrons, diffracted backscattered electrons, X-rays and visible light (cathodoluminescence). Secondary electrons and backscattered electrons are commonly used for SEM imaging samples [169].

In this thesis, a Magellan FEI electronic microscope was used to characterize the as-purchased copper

substrate (in its initial form) and the resulting surface after polishing and annealing. The measurements were done at the Centre de Nanosciences et de Nanostructures (C2N - Paris).

3.1.4 X-ray photoelectron microscopy (XPS)

X-ray photoelectron spectroscopy (XPS), also known as electron spectroscopy for chemical analysis (ESCA) is a quantitative spectroscopy technique that determines the chemical composition in the surface regions of a material, with an average analysis depth of 5 nm. XPS is typically accomplished by irradiating a sample with X-rays, exciting its atoms and causing photoelectrons to be emitted from the sample surface. The emitted photoelectrons are collected, and an electron energy analyzer is used to measure their energy (figure 3.4). From the binding energy (the energy they had before they left the atom) and intensity of a photoelectron peak, the elemental identity, chemical state, and quantity of a detected element can be determined. The resulting spectrum of the binding energy of the photoelectrons is specific to an atom.

XPS can can be applied to a broad range of materials and provides valuable quantitative and chemical state information from the surface of the material being studied. However, even with short analysis times, XPS damages the samples to a small extent [170].

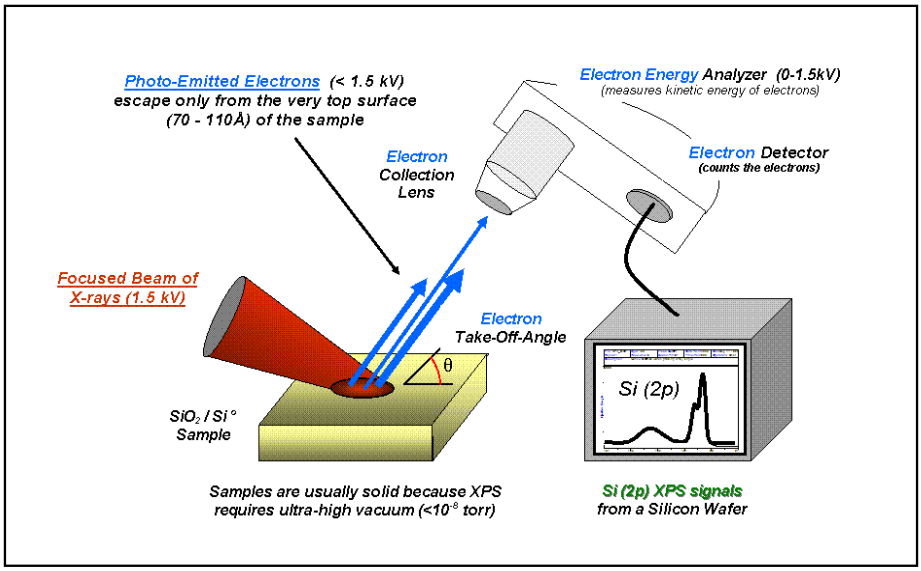

Figure 3.4: Schematic representation of X-Ray photoelectron spectroscopy. Adapted from [171].

In this PhD, an Omicron XPS system was used in order to determine the chemical composition of the chemical vapor deposition growth substrates, copper foils, before (as purchased) and after treatment (polishing and annealing). Various impurity particles were identified on the initial substrates due to their binding energies, along with their atomic concentration. Also, this XPS was used on transferred graphene

using different copper etching solutions (iron chloride and ammonium persulfate) in order to identify the PMMA residues and their amount left on the graphene sheet, as well as the amount of stuctural defects in the graphene lattice (sp3 bonds). The effect of the etching solution on the quality of the graphene was therefore discussed.

A Versaprobe 5000 phi/physical electronics was used on polymer substrates before and after oxide deposition in order to prove the presence of the oxide on the flexible substrates, since a relatively thin and transparent oxide sheet was deposited (20 nm) and an identification technique was required in order to not only identify the presence of the oxide, but to verify its thickness as well. Various oxide deposition techniques were used, and combined AFM and XPS measurements studied the effect of the oxide deposition technique on the roughness and final state of the polymer substrate.

3.2 Fabrication techniques

3.2.1 Electron beam lithography (EBL)

Electron beam lithography (EBL or e-beam lithography) is a direct writing technique mainly used for high resolution (sub-10 nm) lithography and the fabrication of masks for optical litography. Its principle is the following: an electron beam with less than 1 nm diameter scans a surface of a sample covered with an electro-sensitive resist (this resist could be negative or positive depending on the process), reproducing the required pattern with a high resolution of around 2.5 nm [172].

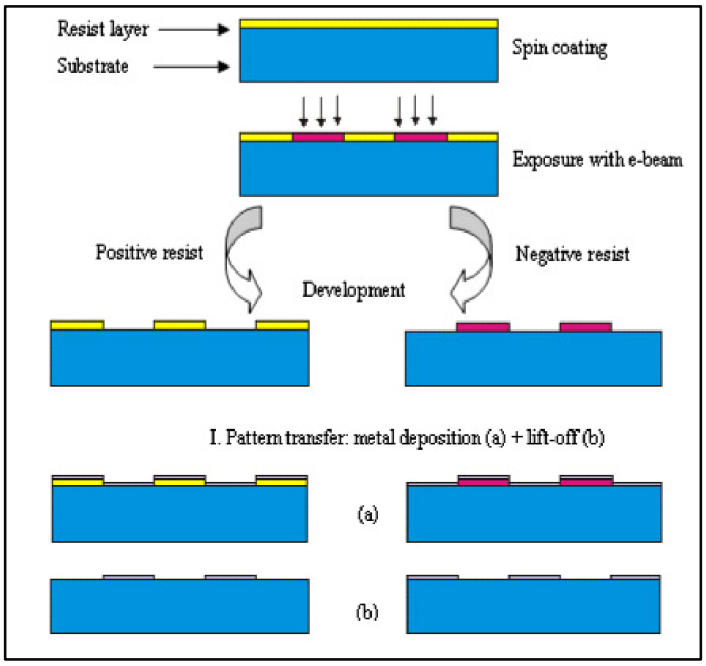

Figure 3.5: Illustration of a lithography process. Adapted from [173].

The process of EBL is described in figure 3.5 and operates in three stages:

1. An electro-sensitive resist is deposited on a sample by spin coating, and a specific time and speed of rotation and acceleration can be programmed in function of the required thickness of the resist.

2. The sample is then exposed to an electron beam with a certain dose. The trajectory of the electron beam follows, pixel by pixel (determined by the desired resolution), a drawing made with a specific lithography software.

3. The exposure to the electron beam changes the solubility of the resist, enabling selective removal of the resist by immersing it in a developer. The developer can selectively remove the exposed area

(positive resist) or the unexposed area (negative resist). The choice of the resist used makes it possible to achieve, from the same exposure, two complementary images of one another.

After the selective removal of the resist, metal deposition and lift off processes can be achieved in order to obtain the final result.

The exceptional resolution of this technique and its high versatility (since there is no mask, and the pattern can be modified at will on the computer), along with its capability of working with a variety of rigid and flexible materials make of it the instrument of choice for research and development. However, its high resolution is compromised by its slow writing time, which inhibits its utilization in the modern fast microelectronic production.

The Raith EBPG 5000+ (at the C2N laboratory) was used in this thesis to fabricate graphene-based field effect transistors. PMMA was used as a positive resist, and MaN (2405) was used as a negative resist.

3.2.2 Reactive ion etching (RIE)

Reactive ion etching (RIE) is a dry etching process that utilizes a chemically reactive plasma to remove materials on a sample surface. When the sample is placed inside the reactor, a low vacuum is created. Then, the feed gas is injected directly between two parallel electrodes while the chamber is maintained at a certain pressure. A radio frequency voltage is applied between the electrodes, ionizing the feed gas and generating a plasma [174] (figure 3.6 (left)). These ions are then accelerated to the surface of the sample, reacting with the sample and etching certain areas. A resist can be used to protect certain etching areas, exposing only the areas to be etched.

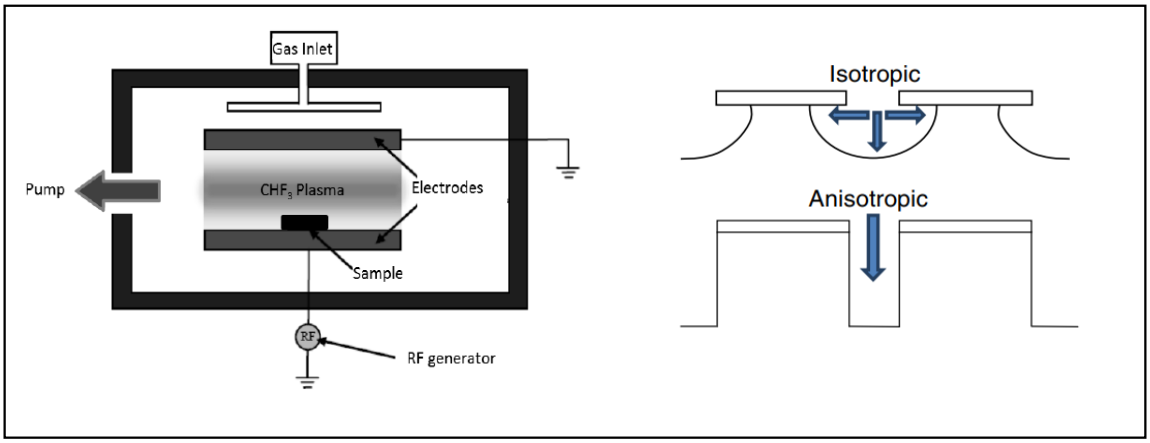

Figure 3.6: Schematic of a reactive ion etching process with CHF_3 as a feed gas example. Right: Schematic of isotropic versus anisotropic plasma etching. Adapted respectively from [175] and [174].

The process of etching by RIE is governed by both chemical and physical reactions:

- Chemical etching: in which the etching phenomenon is produced via chemical reactions between the feed gas and the etched surface. This mechanism leads to a high etch rate, but is isotropic.
- Physical etching: where the etching is due to a bombardment of ionized gas (plasma) and the etched material. This mechanism leads to a lower etch rate, but is anisotropic.

By varying the RIE parameters such as the pressure and power conditions, either the physical or the chemical etching process can be favored, and high quality patterns (i.e. a high aspect ratio and/or strong engraving) [176].

The advantage of dry etching is anisotropy (etching is unidirectional), which is critical for the transfer of high fidelity patterns. However, despite the fact that accelerated ions are indispensable for ion-driven etching, they also introduce damage to the sample.

A CCP RIE Nextral NE 100 was used in this thesis after e-beam lithography processes, and especially for the field effect channel definition step, where etching the graphene covering the entire substrate is necessary. Furthermore, it was used on arbitrary target substrates before the graphene transfer step in order to hydrophilize the surfaces for ultimate adhesion with the transferred graphene.

3.2.3 Electron beam physical vapor deposition (EBPVD)

Also known as e-beam evaporation, electron beam physical vapor deposition or simply EBPVD is a physical vapor deposition technique in which a current (5 to 10 kV) is sent through a tungsten filament and heats it to the point where thermionic emission of electrons takes place, generating by that an intense electron beam which is then steered via electric and magnetic fields to strike a source material (e.g. pellets of Au) and vaporize it within a vacuum environment. Only the surface of the source material is melted, while the source material in contact with the walls of the crucible stays solid. This eliminates the problems of contamination by the crucible and makes it possible to deposit layers of very high purity. Due to the energy transfer induced by the bombardment of the e-beam and the source material, the latter is heated and thus its surface atoms will have sufficient energy to leave the surface, traverse the vacuum chamber, and coat a substrate positioned above the evaporating material [177] (figure 3.7).)

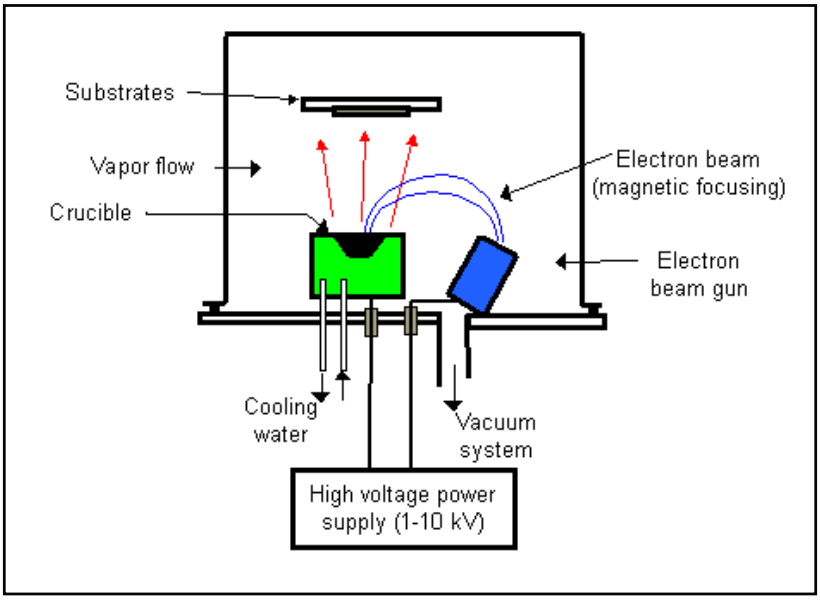

Figure 3.7: Schematic of an EBPVD. Adapted from [178].

High purity depositions is a huge advantage for the EBPVC, as well as the controlled thicknesses and the relatively high deposition rates. A MEB 550 was used in this thesis for various metal depositions such as gold, titanium, chromium and aluminum.

3.2.4 Atomic layer deposition (ALD)

Atomic layer deposition (ALD) is a vapor phase technique used to deposit thin films on a substrate. A general ALD process is illustrated in figure 3.8. The process involves the surface of a substrate being exposed to alternating precursors which are introduced sequentially, one at a time. In each alternate pulse, the chemical precursor reacts with the surface of the substrate in a self-limiting way that leaves no more than a single atomic sheet at the surface. Subsequently, the chamber is purged with an inert carrier gas (typically N_2 or Ar) to remove any unreacted precursor or by-products. Exposure to the separate precursors is repeated until the appropriate film thickness is achieved [179]. The process of ALD is often performed at relatively low temperatures (inferior to 350°C), which is beneficial when working with temperature-sensitive samples such as flexible substrates. This technique is capable of depositing a wide variety of thin film materials including oxides, metals, sulfides, and fluorides. Finally, the conformality of ALD-deposited films is often the main reason why ALD is almost always chosen over competing deposition techniques such as CVD or sputtering.

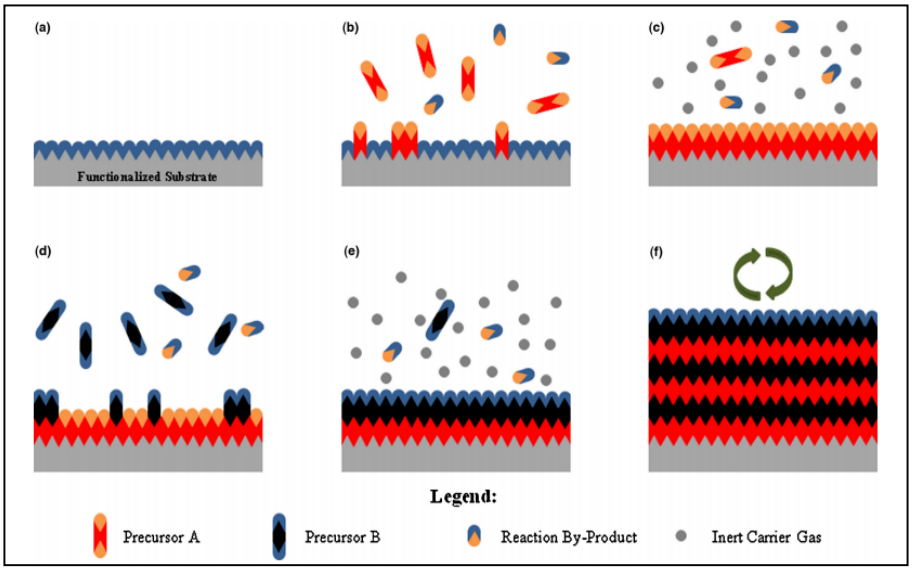

Figure 3.8: Schematic of ALD process. Adapted from [179].

In this thesis, a FIJI F200 was used to deposit thin films of aluminum oxide (Al_2O_3) on flexible substrates for further device fabrication. Al_2O_3 was used as a high-k dielectric for gate oxide, and the effects of depositing Al_2O_3 on polymer substrates via ALD was studied using combined XPS and AFM measurements in order to verify the presence of the oxide and the wanted thickness, as well as the impact of this technique on the roughness of the polymer substrate.

Chapter 4

Step-by-step characterization of large-scale graphene devices

4.1 Objectives of this study

The objective of this chapter is to study the properties of large-scale CVD graphene. For that, the chapter is divided into two sections. The first part consists of the fabrication process of graphene-based FET; from the polishing of the copper substrate, to the graphene synthesis and transfer onto dielectric substrates, to device fabrication. The second part deals with the structural and electrical characterization of the devices.

The fabrication of the GFETs consists of many steps. Before synthesizing graphene, the growth substrate must be treated, since its morphology greatly affects the graphene crystalline quality. Thus, we have carefully examined the copper substrate before and polishing and annealing via AFM, SEM and XPS measurements. Afterwards, the graphene transfer was thoroughly discussed, as the effect of the copper etchant ($FeCl_4$ and $(NH_4)_2S_2O_8$) on the PMMA residues is investigated. Then, Raman spectroscopy of graphene on copper is shown, and the device fabrication steps are detailed.

After the fabrication of the GFETs, Raman mappings on different GFETs are shown and discussed, and several electrical measurements were performed. The mobility extraction method used in this thesis is described in detail, and the effect of air exposure on the graphene's electrical properties is studied. Finally, preliminary electrical results on graphene nanomesh are demonstrated.

4.2 CVD growth catalytic substrate

In the first chapter, the choice of using copper as the catalytic substrate for graphene CVD growth has been discussed. In this section, we will further elaborate on our work with copper foils, pointing out the role of the copper morphology on graphene synthesis and graphene quality.

As-purchased Cu foils contain a high density of impurity particles and have very rough surfaces, which both play an important role in graphene quality and number of layers [180–184]. In fact, impurity particles and scratches on the as-purchased copper surface have been shown to act as nucleation seeds in the growth process [68, 185–189], increasing the density of graphene domains and thus decreasing graphene quality and carrier mobility, and also involuntarily increasing the graphene layer number. On the other hand, the roughness of the metal surface induces a none flat graphene which induces nanoscale strain variations in the sheet and therefore deteriorating the charge carrier mobility [116]. This is why obtaining a clean and flat copper surface is very important in our work and in the graphene technology.

Copper surface treatments have been proven to be extremely important prior to the graphene growth, and a plethora of polishing techniques have been introduced throughout the years. Some of the most common methods are electro-chemical polishing [68, 188, 189], chemical polishing using different chemical solutions such as nitric acid [187] and acetic acid [188], and mechanical chemical polishing [181].

In our study, we used the mechanical chemical polishing technique (CMP) first introduced by Han *et al.* [181] in 2011. It is a simple, fast and relatively cheap technique and can be used in the large-scale processing of devices. The principle of this method is unambiguous: 70 μm-thick Cu foils (Arcelormittal 99.99%, Luxembourg) are manually polished using a diluted $FeCl_3$ solution and microfiber cloth. Then, the foils are cleaned in DI water for about 20 minutes, and after that, in trichloroethylene, acetone and isopropanol respectively with ultra-sonication. Finally, the foils are dried using a nitrogen gun(N_2). The objective of the CMP technique is to eliminate all the impurity particles that are present on the surface of the copper. The next step is to have a flat copper surface. Therefore, the polished copper foils were annealed for an hour in the presence of an $Ar : H_2$ flow (800:200 sccm) under 1052°C. After the annealing step, the Cu surface becomes flat, the copper domains increase in size, and are therefore ready for graphene growth.

It is worth mentioning that in this work, we have chosen to work with scalable and low-cost methods, aiming to the industrialization of graphene-based devices. This polishing technique comes first among others. In fact, 70-100 μm-thick industrial copper is 1000 times cheaper than the standard 25 μm copper foil.

4.2.1 Structural characterization of the copper substrate

Figure 4.1 presents a comparison between the same copper foil before treatment (as purchased), after polishing and after annealing.

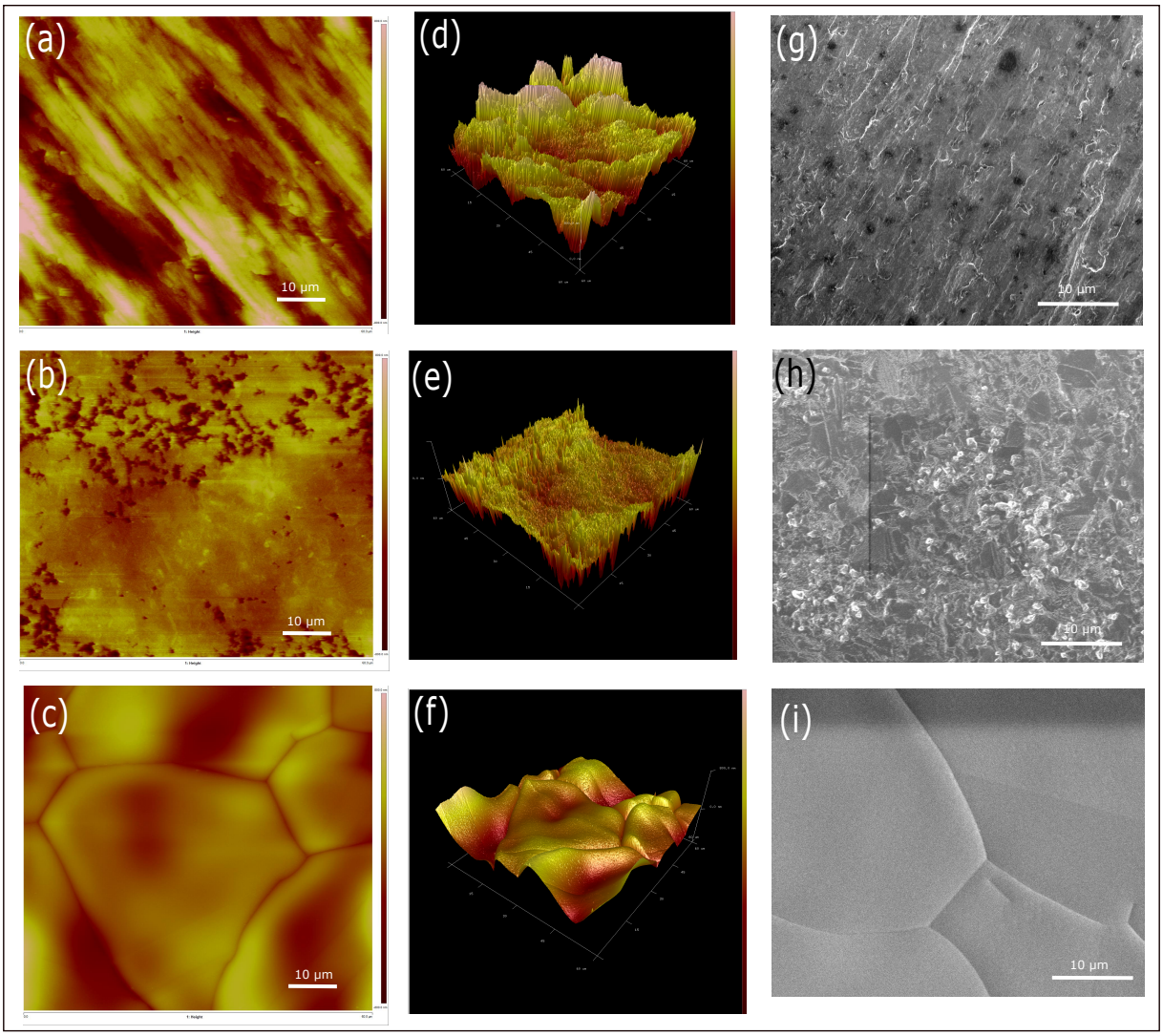

Figure 4.1: AFM images of 70 μm-thick copper foil (a) as-purchased (b) after polishing and (c) after polishing and annealing. 3D AFM images of the roughness of the copper foil: (d) as-purchased (e) polished, and (f) polished and annealed, respectively. SEM images of the copper foil (g) as-purchased (h) polished and (i) polished and annealead respectively.

Figure 4.1 (a), (d) and (g) shows AFM and SEM images of an as-purchased Cu foil. Surface scratches, holes and inhomogeneity of the surface are clearly observable, and a roughness of $\sim$ 200 nm was measured. Figure 4.1 (b), (e) and (h) shows AFM and SEM images of the foil after polishing. The copper grains are not visible yet, however, the surface roughness has decreased to $\sim$ 53 nm, and it can be seen that holes and scratches are no longer present on the surface. However, the surface appears to be inhomogeneous. After polishing and annealing of these foils, Figure 4.1 (c), (f) and (i) shows the effect of the annealing on Cu

grains, which are visible now. In addition, the surface is free of holes and scratches. AFM measurements showed a minimum roughness of $\sim$ 17 nm. Figure 4.1 (d), (e) and (f) demonstrates the 3D plotting of the copper surface at the exact place of the AFM images in the three stages of the copper foil. It is clear that the roughness has decreased drastically with treatment, and the surface has smoothed. This small surface roughness is critical to the graphene growth, since we need to obtain a flat graphene in order to avoid the presence of nanoscale strain variations in the graphene lattice, as well as cracks and wrinkles during the transfer process. This implies that our polishing-annealing process is very effective in reducing the surface roughness and obtaining a flat copper surface.

Furthermore, to show the effect of polishing on the copper morphology, as-purchased copper foil was annealed without polishing (figure 4.2 left) and another foil was polished and annealed (figure 4.2, right). The figure below represents the two cases:

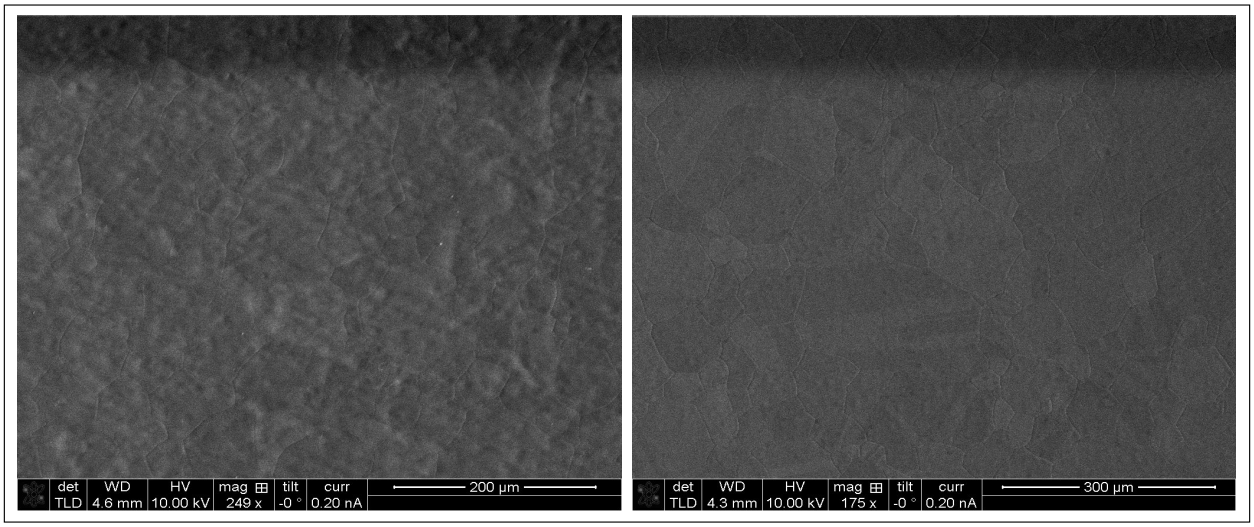

Figure 4.2: SEM images annealed copper (left) and polished + annealed copper (right). Difference in surface roughness is clearly visible, highlighting on the importance of the polishing step.

As it can be seen, the polishing plays a critical role not only in eliminating surface impurities but also in reducing the surface roughness and is therefore a very important step prior to graphene synthesis.

4.2.2 XPS measurements on the copper substrate

To further investigate the cleanliness of the metal surface, XPS measurements have been performed on the copper foil before and after treatment in order to examine the chemical composition of the copper and the effect of the treatment on the surface of the foil. Figure 4.3 shows XPS measurements on the same copper

foil (i) before treatment (as-purchased) (black), (ii) after chemical mechanical polishing (red) and (iii) after annealing (blue). The atomic concentrations of the particles found on the copper surface in each step is summarized in figure 4.4.

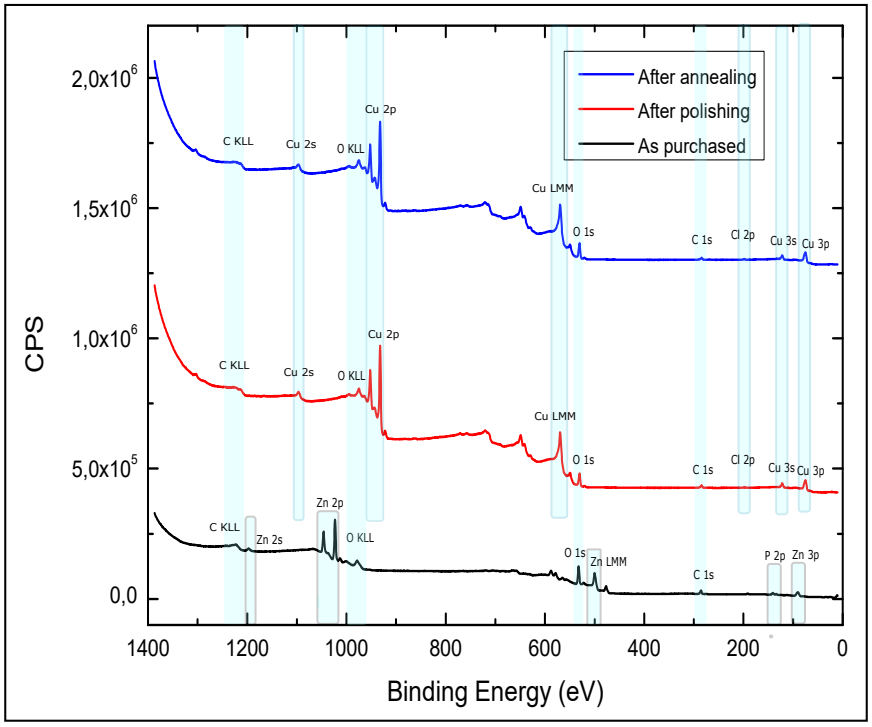

Figure 4.3: XPS measurements of the copper foil before treatment (black) after polishing (red) and after polishing and annealing (blue).

Particles on the surface	% At Conc As purchased Cu	% At Conc Polished Cu	% At Conc Polished + Annealed Cu
Cu	0	64.31	63.07
Zn	50.49	0	0
P	10.27	0	0
C	14.67	13.64	12.58
O	24.44	20.57	24.35
Cl	0.13	1	0
Fe	0	0	0

Figure 4.4: Table summarizing the atomic concentration of the particles found on the copper surface after each step (before treatment, after polishing and after polishing and annealing).

Unexpected results were found for the as-purchased Cu foil, as zero Cu was detected on the surface (to a 10 nm profundity). Instead, a continuous zinc layer covered the surface with an atomic concentration around 50.49 %. In addition, a significant phosphorus concentration (10.27 %) was present on the surface as well. Oxygen and carbon atoms were also found with concentrations around 24.44% and 14.67% respectively, which indicate a typical atmospheric contamination (C-C and C-O bonding). There is a possibility that oxygen atoms have combined with the zinc layer to form a continuous ZnO layer, however, we did not perform more detailed measurements on this subject. Traces of Cl were also detected on the surface with a very negligible concentration.

After the polishing step (red), the Zn and P contaminants disappeared completely and copper is detected on the surface with an atomic concentration around 64.31%. C and O particles remain present on the surface with concentrations around 13.64% and 20.57% respectively, however, the binding energies of C and O peaks are very different before and after CMP (polishing). In fact, before the polishing step, the C and O were considered as contaminants only since we did not detect any Cu particles on the surface. However, after polishing, atmospheric contamination remained on the surface since it is a very typical contamination for samples not conserved in vacuum, however, the oxygen reacted with the Cu to form copper oxide. These findings will be thoroughly discussed later. 1% of Cl is found on the surface, and this relatively low concentration is due to the polishing solution we have used ($FeCl_3$). However, no traces of Fe were detected on the surface of the Cu foil.

After annealing of the polished metal (blue), Cl particles disappeared with very light traces which could be due to the same tweezers we used with chlorinated materials discussed in chapter 4. Oxygen, copper and

carbon are the only remaining atoms present on the surface, with concentrations around 24.35%, 63.07% and 12.58% respectively. These XPS findings confirm the efficiency of our polishing + annealing step, which gives rise to a clean and Fe-free copper foil.

To understand more about the relationship between Cu and O, we have fitted the Cu2p and O1s peaks. The results are depicted in figures 4.5 and 4.6.

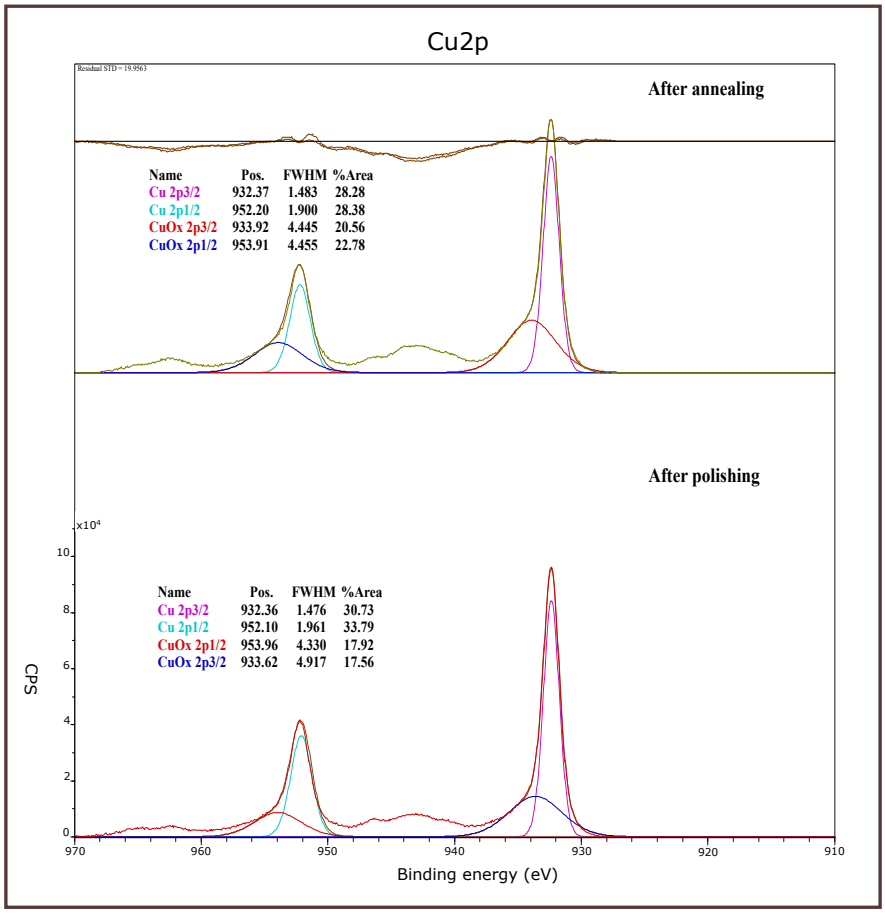

Figure 4.5: XPS spectra of the Cu2p3/2 and Cu2p1/2 peaks.

Figure 4.5 represents XPS measurements on the Cu2p peaks after polishing and after annealing (we could not compare to as-purchased copper since there was no copper on the surface of the as-purchased foil). Copper, or Cu(0) presents single XPS peaks around 1097 eV (Cu1s), 933 (Cu2p3/2), and 953 eV (Cu2p1/2). Cu also possess other peaks which are not studied here (Cu3s, Cu3p1/2 and Cu3p3/2) [190].

Cu2p peaks present only one component for copper. In our case, we notice after polishing of the copper foil that the Cu 2p3/2 and the Cu 2p1/2 peaks have broadened and were fitted into two components each, indicating the presence of copper oxide. The Cu 2p3/2 and the Cu 2p1/2 peaks of Cu(0) (copper) are observed at 932.36 eV and 952.10 eV respectively, whereas oxidized copper (CuOx for copper oxide) is detected for a Cu2p3/2 peak at around 933.62 eV and a Cu2p1/2 peak around 953.96 eV. We have found that approximately 36% of the copper concentration is Cu(II) oxide (CuO). The Cu (I) however (Cu_2O) is very hard to distinguish here from Cu(0) in our case since we did not perform detailed measurements on the Cu peaks. In fact, we are only interested in showing the chemical composition of the copper foil before and after treatment.

After annealing of the Cu, we observe the same two components for Cu2p3/2 and Cu2p1/2. The Cu(0) is observed for Cu2p3/2 around 932.37 eV and Cu2p1/2 around 952.20 eV, whereas oxidized copper is detected for the two components Cu2p3/2 around 933.92 eV and Cu2p1/2 around 952.20 eV. After the annealing step, we have found a concentration of around 43% of Cu(II) oxide (CuO).

To confirm these results, we have plotted and fitted the O1s peak represented in figure 4.6. As-purchased copper presented a single O1s peak at around 532.53 eV, which most probably indicates a typical atmospheric contamination with carbon atoms (C-O bonding). However, after polishing and annealing of the substrate, the O1s peak has broadened and could be fitted into three components. These three components are those of C-O contamination and copper oxidation (Cu(I) and Cu(II)).

After polishing of the Cu, the O1s C-O component is observed at 532.48 eV, the oxygen bonding with copper to form CuO is detected at 531.38 eV and the O-Cu bonding resulting in Cu_2O is found at 530.22 eV. Around 85% of the oxygen concentration on the polished Cu surface was found to come from the oxidation of copper. The rest is atmospheric contamination.

For the annealed substrate, the O1s C-O component is observed at 532.34 eV, the O-Cu resulting in CuO is detected at 531.4 eV and the O-Cu bonding corresponding to Cu_2O is found at 530.36 eV. After annealing, around 91% of the oxygen concentration was found to come from the oxidation of copper.

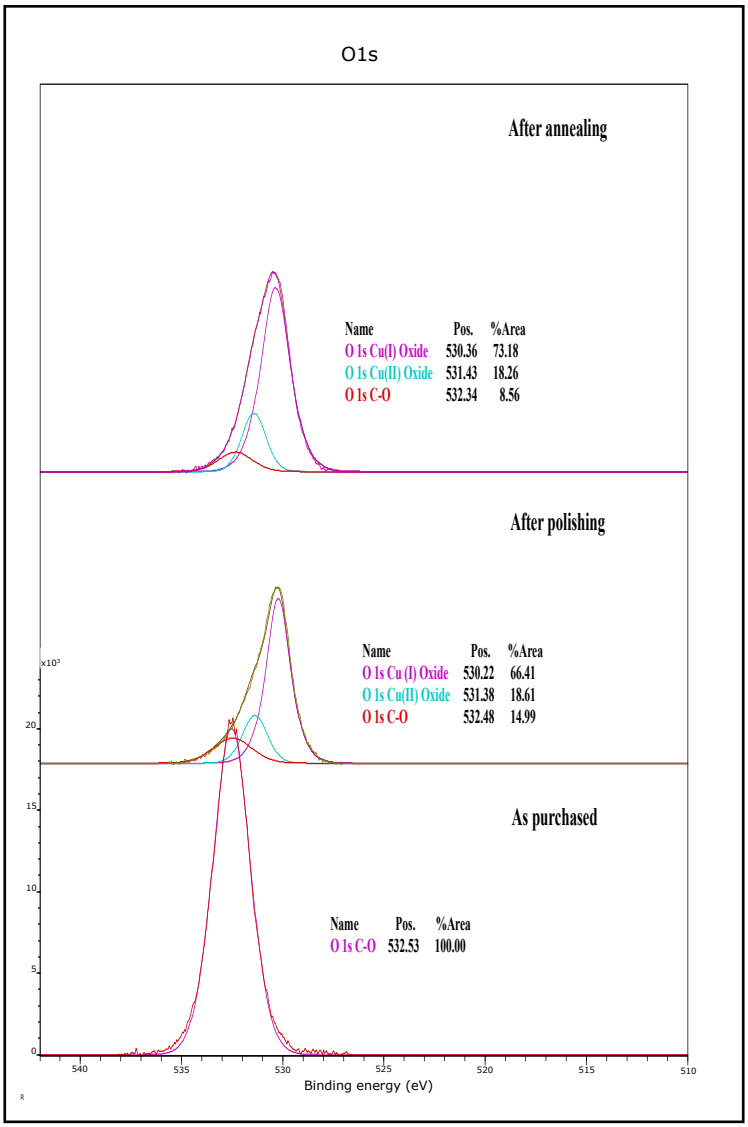

Figure 4.6: XPS spectra of the O1s core level.

In summary, XPS measurements performed on as purchased copper foils presented a zero concentration of copper on the surface, and a continuous layer of zinc. A significant phosphor concentration was also detected on the surface, as well as a typical atmospheric contamination (O and C atoms). This indicates that a graphene growth on untreated copper foils actually is a growth process on zinc alongside other significant concentrations of impurity particles. XPS results on polished copper demonstrated a total removal of the zinc layer and the phosphor particles, consequently revealing the underlying copper substrate, resulting in a clean surface containing only C and O particles on the foil. Further studies on the O1s and Cu2p peaks revealed that after polishing, oxygen atoms react with the copper to form an oxidized copper (CuO and

Cu_2O), while the standard atmospheric contamination remains through the C-O bondings. A very low concentration of Cl atoms (1%) was detected on the surface of the polished foil which is due to the polishing solution. After annealing of the Cu foil, the Cl disappeared completely and the only remaining particles on the Cu surface were C and O atoms. Oxygen atoms were found to slightly contribute more in the oxidation of the copper after annealing. These findings accentuate the importance of copper polishing and annealing prior to the graphene growth.

Combining SEM, XPS and AFM measurements, we can conclude that the CMP technique is very effective in eliminating impurity particles off the surface of the copper, thus decreasing the nucleation sites on the surface and limiting multi-layer growth. In addition, a defect-free copper surface is crucial to achieving a continuous and single graphene sheet. Furthermore, our annealing step has successfully eliminated Zn, P and Cl particles and has drastically reduced the surface roughness by a factor of 10, resulting in a flat and clean copper surface, critical to obtain high quality and single layer graphene sheets.

4.2.3 Resiscope AFM mode characterization of the copper substrate

For complementary information about the initial (as-purchased) and the treated (CMP + annealing) copper foil, we have performed Resiscope measurements shown in figure 4.7.

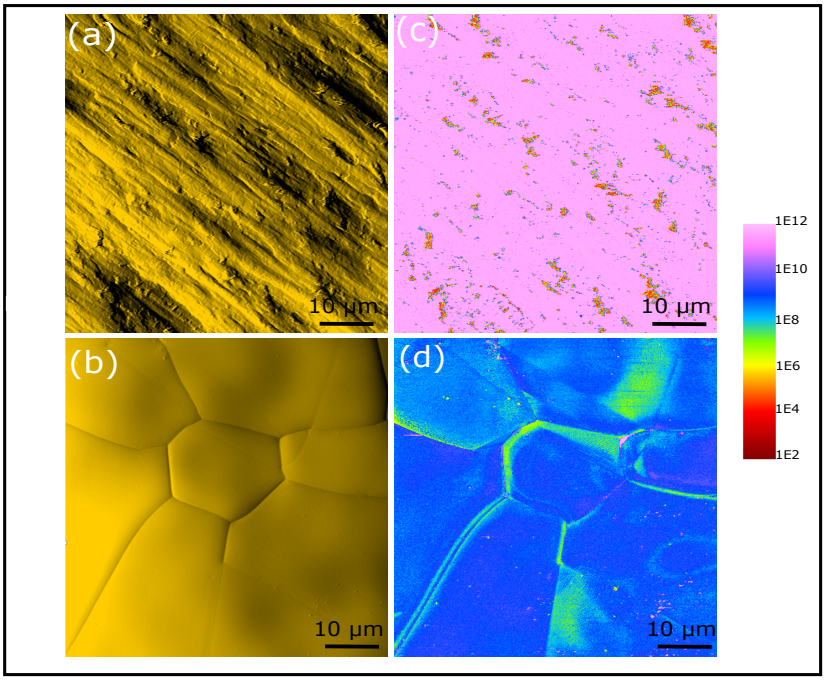

Figure 4.7: (a) AFM topography of as-purchased copper foil with its (b) electrical image in Resiscope Mode. (c) AFM topography of a chemically and mechanically polished and annealed copper foil with its (d) electrical image in Resiscope mode.

The Resiscope is a technique derived from AFM which allows dynamic resistance measurements over a wide range from 100 to 10^{12} Ω in normal conditions of scanning. The measured resistance is a sum of several resistances in series: (i) the resistance of the probe, (ii) the resistance of the tip-sample contact resistance and (iii) the sample resistance. If the applied force is strong enough, the tip-sample contact is severely reduced. In this work, we have used a doped-diamond tip NanoWorld with a spring constant of 72 N/m with a Digital Instruments Nanoscope IIIa Multimode. Figure 4.7 (a) and (c) respectively demonstrate the AFM topography and Resiscope imaging of as-purchased copper foil and the result is beyond expectations. Almost all of the Cu surface is highly resistive up to the limits of the resiscope mode at 10^{12} Ω. This high level of resistivity corroborates that insulating impurities are dominating the surface of the untreated foil. On the contrary, figure 4.7 (b) and (d) respectively show AFM topography and Resiscope imaging of the same copper foil after treatment (polishing and annealing) and the difference is visible at first sight. The roughness is highly decreased in figure 4.7 (b) compared to figure 4.7 (a) from 200 ± 20 nm to 17 ± 3 nm with a strong decrease in the resistance value down to 10^9 Ω. The resistance value drops to 10^7 Ω in the grain boundaries of the Cu foil. This could be a measurement artefact due to a better contact with the AFM tip at a fixed applied force. In conclusion, the difference of 4 decades in local resistances between an untreated and treated Cu foil clearly showed a Cu surface full of impurities completely disappearing after polishing and annealing, accentuating the need to treat the foils before graphene growth.

4.3 Graphene growth by pulsed chemical vapor deposition (P-CVD)

For the graphene-based electronic devices to be implemented in mass production, two criterion in the CVD process must be respected. First, the graphene sheet must be continuous over the entire Cu substrate in order to achieve maximum quantity of devices fabricated on the same graphene sheet, and second, the graphene must be of quality compared to that of exfoliated HOPG in order to obtain high carrier molibity, a crucial parameter in the electronic industry. Thus, the density of grain boundaries in the graphene sheet must be as low as possible. In recent years, centimeter-large single-crystal graphene has been obtained by several groups [68, 82, 189, 191–196], however, the graphene domains obtained are discontinuous and are therefore unsuitable for wafer-scale device fabrication.

In chapter 2, the standard CVD process was discussed. In this thesis, we have chosen to grow graphene using the so-called pulsed chemical vapor deposition (P-CVD), presented in 2012 and patented in 2016 by V. Bouchiat's group [197, 198]. The figure below shows the process of the P-CVD compared to that of the standard CVD.

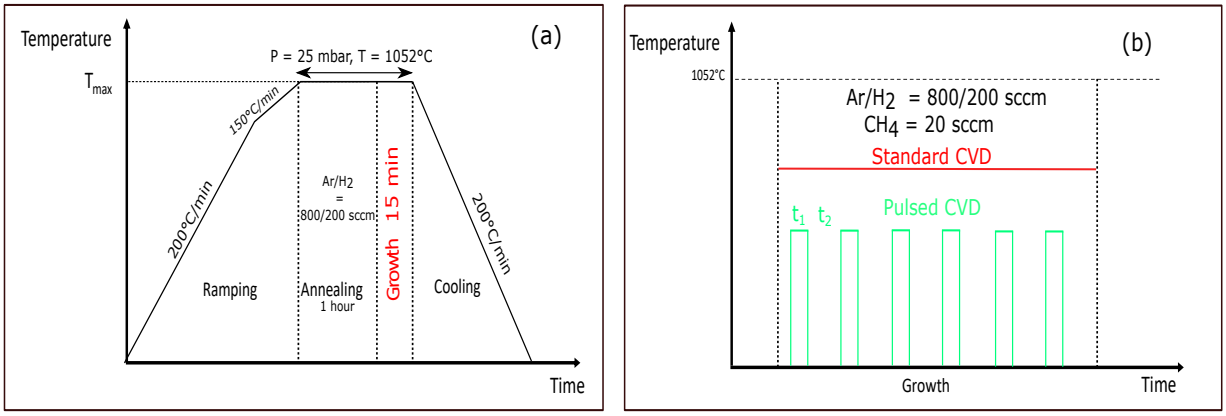

Figure 4.8: (a) Schematic illustration of our synthesis process. (b) the P-CVD growth (green) compared to that of standard CVD (red). t_1 is the injection time of CH_4 which is equal to 5s and t_2 is the ejection time equal to 55s in our case.

The principle of the P-CVD (green) is very close to that of the standard CVD (red). In fact, the only modification in the process is in the injection time of the hydrocarbon: instead of a continuous injection as in the case of standard CVD, the hydrocarbon is instead introduced into the reactor for a short period of time t_1 and is afterwards cut for a period of time t_2, in a repetitive manner until the end of growth.

This sequenced cut in the injection inhibits the formation of multi-layers, since the carbon adatom species on the surface of the substrate are given enough time to adsorb on the surface, to dehydrogenate and to be incorporated into the graphene lattice, but not enough time to dissolve in the defect sites which might still be present on the catalyst surface after polishing and annealing.

In this work, graphene was grown in a 4-inch Aixtron Blackmagic 4G cold wall reactor. For the cold-wall CVD, only the substrate holder is heated while the reactor walls are kept cool.

For the synthesis of graphene, we used 70 μm-thick polished and annealed copper foils. The growth parameters are shown in figure 4.8.

After the polishing of the copper foil, the substrate is introduced into the reactor and vacuum is reached. subsequently, the temperature rises at the ramping rate of 200°C/min until it reaches 850°C. Afterwards, the temperature ramps up at a rate of 150°C/min to reach a maximum value of 1052°C with a total pressure of 25 mbar. 800 standard cubic centimeter per min (sccm) of argon and 200 sccm of H_2 are then introduced into the chamber room and 1 hour of substrate annealing at 1052°C is performed. The growth of graphene is initiated when 20 sccm of CH_4 is added, along with the same Ar/H_2 mixture. The total growth time is 15 minutes: 5 seconds of injection followed by 55 seconds of incision of the hydrocarbon. As we have mentioned

before in chapter 2, this mechanism gives enough time for the CH_4 to adsorb on the copper surface and dehydrogenate, insuring by that a rapid and defect-free growth. Figure 4.9 shows an SEM image of a 2 μm graphene domain with a perfect compact hexagonal shape on copper grown using this recipe.

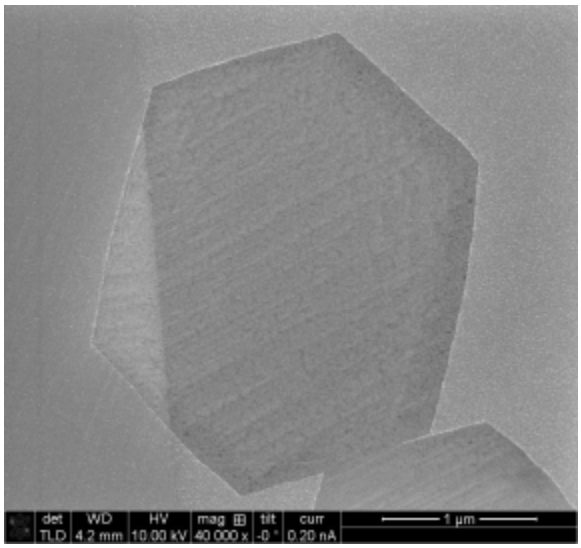

Figure 4.9: SEM image of a graphene domain on copper.

4.4 PMMA-assisted wet transfer of graphene

The PMMA-assisted wet transfer technique was chosen in this study due to its simplicity and high reproducibility. Centimeter-size continuous graphene sheets were transferred using this technique, and thus a huge number of devices was fabricated on the same substrate and from the same growth, highlighting the importance of this transfer method in wafer-scale technology. This method has been widely used in the graphene community and different transfer recipes exist under specific laboratory conditions and vary depending on the availability of each lab materials. Our transfer process is represented in figure 4.10 below.

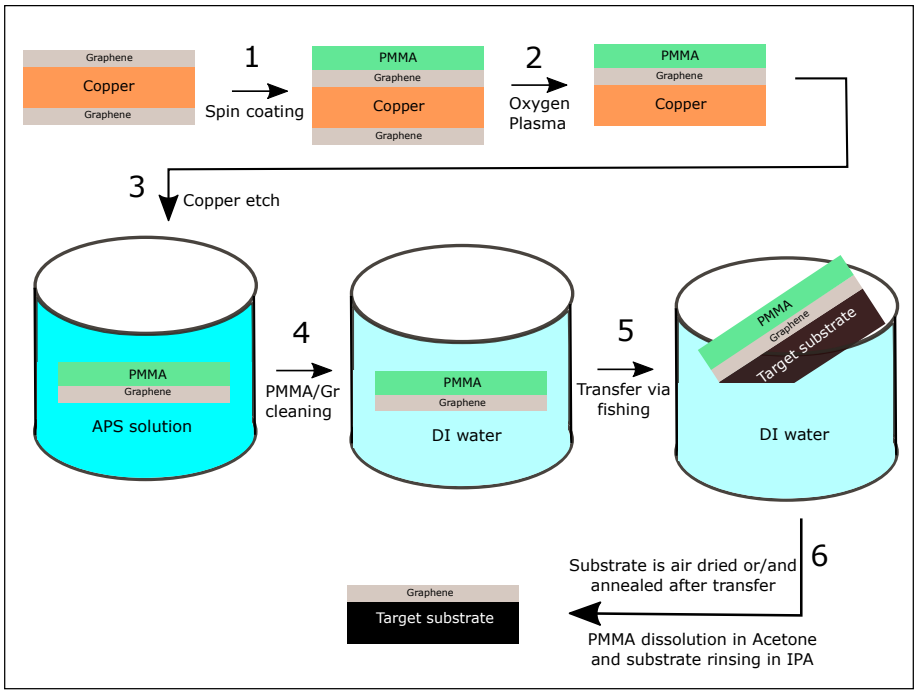

Figure 4.10: The PMMA-assisted wet transfer technique used in this work

First of all, the graphene is coated with a thin PMMA layer (950 000 molecular weight, 120 nm), which is afterwards annealed at 170°C for 7 minutes. Since graphene is grown on both copper sides, the graphene on the backside of the Cu is etched via oxygen plasma treatment (10s, 10W). This step is very important considering that graphene on the backside of the Cu can also be transferred onto the target substrate alongside the original sheet, resulting in wrinkles and bi or multi layers. The PMMA/Graphene/Copper stack is then placed in an ammonium persulfate solution (0.5M) pre-heated at 55°C. The etching time for our 70 μm-thick Cu foil is 1 hour. When the copper is completely etched, the PMMA/Graphene stack is transferred using a PET substrate, into a beaker containing DI water. The water is replaced several times for a total time of 30 minutes to insure a proper cleaning of the graphene. Subsequently, the PMMA/Graphene is transferred onto the final substrate and dried in cleanroom air. When the target substrate is dry, it is annealed for about 10 minutes under 110°C in order to obtain a strong adhesion between the graphene and the substrate. Finally, the PMMA is dissolved using acetone for two hours and the target substrate is rinsed in isopropanol and dried using a N_2 gun.

It is important to mention that the final substrate has to be hydrophilic enough in order to have a very good graphene/substrate adhesion. If the substrate is hydrophobic or slightly hydrophilic, the graphene layer is going to peel off after a short period of time (tested in our work). The hydrophilicity of the target substrates in our work is achieved by exposure to oxygen plasma. We must also mention that the substrates

here are cleaned in acetone and isopropanol respectively under ultrasonication before the transfer.

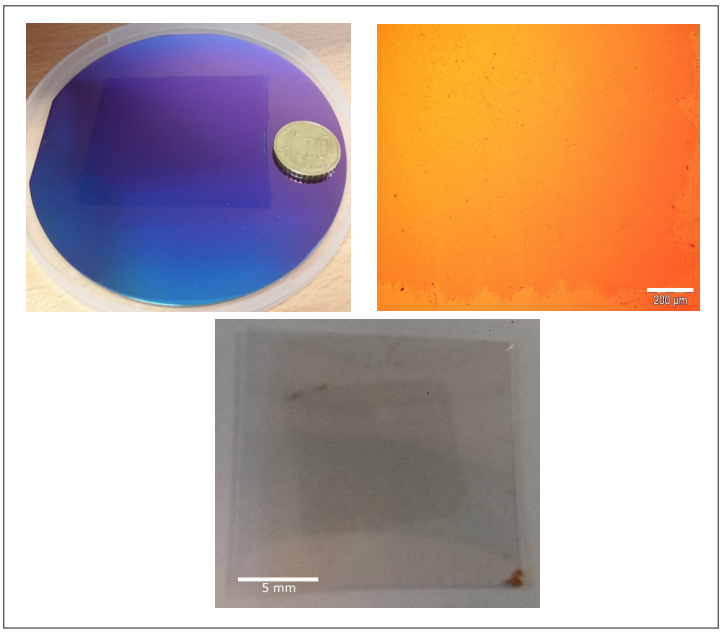

Figure 4.11: Wafer-scale transfer of graphene on a 4-inch rigid SiO_2 wafer (top) and on a flexible (PET) substrate (bottom).

4.4.1 Effect of the copper etchant on the transferred graphene

Among a considerable amount of etching solutions used to engrave the copper during the transfer process, two particular solutions have been more popular than others, mostly due to their etching simplicity and nonnecessity of preparation, iron chloride ($FeCl_3$) and ammonium persulfate ($(NH_4)_2S_2O_8$ or APS). $FeCl_3$ was found to dope the graphene with Fe atoms [199–201], resulting in the formation of iron oxides on the graphene surface, thus APS was considered as the better choice for etching copper. Nonetheless, the PMMA-assisted transfer of graphene has always yielded a graphene with PMMA residues, which were found to be very difficult to remove completely [100], especially when Lin *et al.* found that a 1-2 nm layer of PMMA residue adsorbs on the graphene surface upon contact with graphene [202]. Nevertheless, this transfer technique has continued to be the most popular for transferring large-area graphene sheets due to its simplicity and very high yield.

In this work, we have tested both etching solutions, and performed XPS measurements on both transferred graphene onto SiO_2 substrates in order to understand more about the effect of these solutions on the PMMA residues and the graphene crystal quality. Figures 4.12 and 4.13 depict the XPS spectra of $FeCl_3$ and APS transferred graphene respectively.

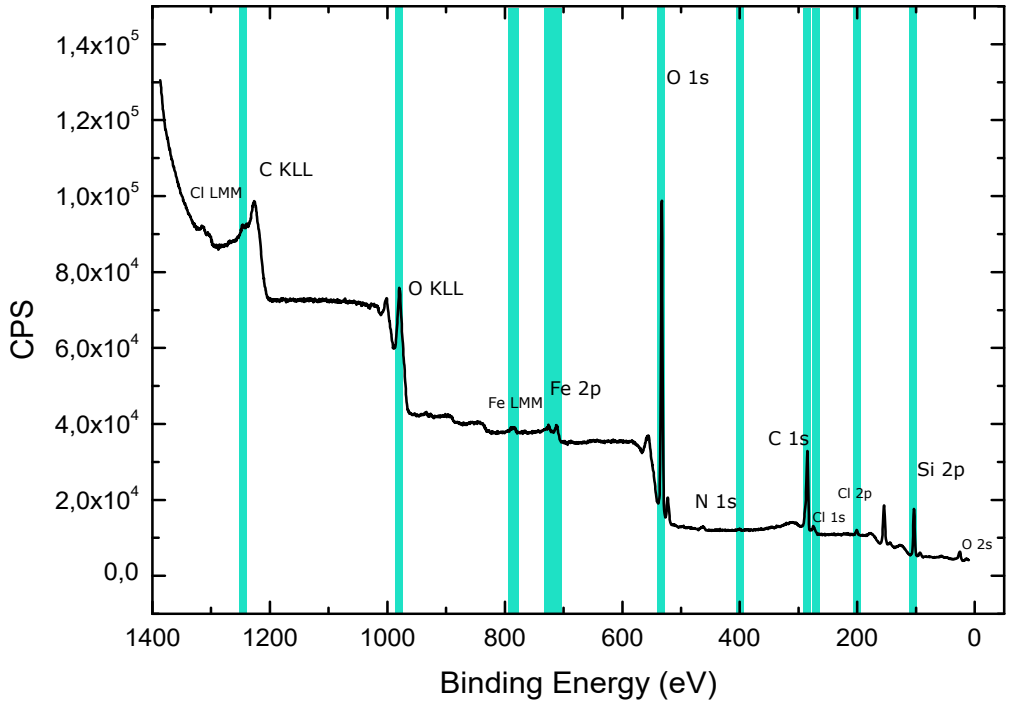

Figure 4.12: The X-ray photoelectron spectra of transferred graphene using an iron chloride solution to etch the underlying copper.

XPS measurements on the graphene transferred using $FeCl_3$ show Si, O and C species on the surface, which indicates the presence of SiO_2, as well as the typical atmospheric contamination (C-O bonding). However, the bonds between C and O play a huge role in determining the presence of polymer residue. We will later discuss this in detail. In terms of contamination, we have found traces of Fe and Cl, which certainly come from the etching solution. Although their atomic concentration is very low compared to other studies (<1% for both in our case compared to 12% in [199–201]), these contamination atoms may play a role in surface doping and scattering sites in the transferred graphene sheet. Extremely low traces of Cu were observed (0.06%), implying that the copper did not completely etch. A longer etching time would rid of these insignificant traces. We must also mention that traces of N were also observed (0.30%). This bizarre observation could be due to two things: the nitrogen gun we use during the transfer to dry the PMMA/graphene sheet and after the dissolution of PMMA, or the fact that we used the same tweezers to carry both samples ($FeCl_3$ and $(NH_4)_2S_2O_8$), which were also put in the same box.

In the case of the graphene transferred via $(NH_4)_2S_2O_8$, the XPS measurements are show in figure 4.13.

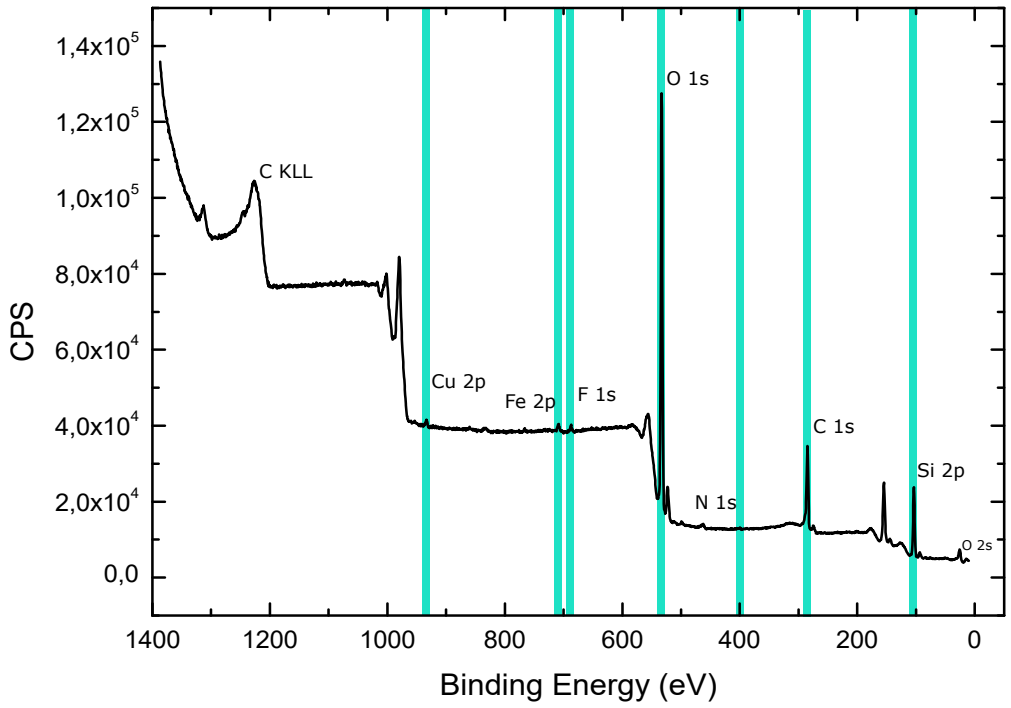

Figure 4.13: The X-ray photoelectron spectra of transferred graphene using an ammonium persulfate solution to etch the underlying copper.

Similarly to the first sample, we found C, O and Si species on the graphene transferred using APS. The bonds between C and O atoms will also be discussed later on. No S atoms are observed on the graphene surface, however, insignificant traces of N (0.10%) are detected, most likely originating from the etching solution. Similarly to the $FeCl_3$-transferred sample, low traces of Cu were observed (0.06%). However, in an unexpected manner, a relatively important amount of F atoms was detected on the APS-transferred graphene (0.62%).

In order to evaluate the presence of PMMA residues on the graphene, we need to examine the C 1s and the O 1s peaks carefully. For this, we consider the examples shown in figure 4.14, which represent the C1s peak of CVD graphene transferred via the standard PMMA-assisted transfer.

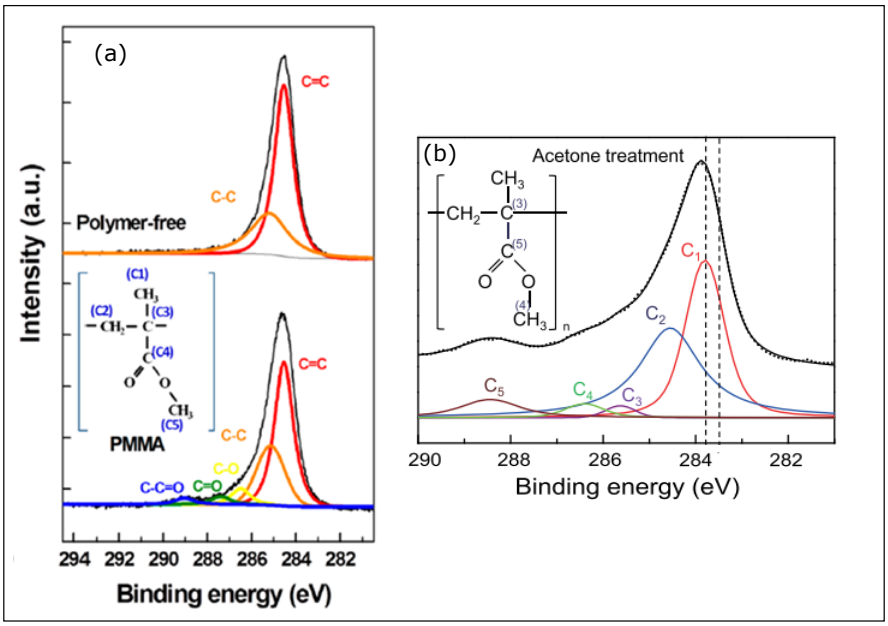

Figure 4.14: The C1s core level spectra of CVD graphene transferred via PMMA-assisted wet transfer. Adapted respectively from [106] and [100].

Figure 4.14 (a) compares a polymer-free transfer method and the typical PMMA-assisted technique. In the polymer-free transfer of graphene, the C1s spectrum can be deconvoluted into two components: an sp2-hybridized C=C peak at 284.4 V (±0.1 eV) and an sp3-hybridized C-C bond at 285.1 V (±0.1 eV). The sp3 hybridization is a result of amorphous graphitic carbon and defects. In the C1s spectrum of PMMA-transferred graphene, we notice the presence of three additional binding peaks, which are associated with the PMMA residues on the graphene surface. The peak at 286.5 eV (±0.1 eV) corresponds to the bonding of carbon atoms in polymer backbone (C3), the peak detected at 287.4 eV (±0.2 eV) is that of the carboxyl function group (C4), and lastly the peak observed at 289.1 eV (±0.2 eV) is the methoxy function group (C5) in the PMMA residues [106].

Similarly, figure 4.14 (b) represents the C1s core level spectra of PMMA-assisted transfer of CVD graphene after removal of the PMMA with acetone. We notice that the C1s spectra are composed of five components: the C1 and C2 components originates from the sp2 C-C bond of graphene and the sp3 C-C bond near defects of graphene respectively, whereas the C3, C4 and C5 components are associated with PMMA residues. In fact, the C3 component detected at $\sim$ 285.7 eV originates from the polymer backbone (C-C bond) of PMMA, the C4 component observed at $\sim$ 286.2 eV corresponds to the methoxy functional group (C-O bond) of PMMA, and the C5 component at 289.0 eV originates from the carboxyl functional group (O-C=O bond) of PMMA.

Note that both XPS spectra have found the same functional groups for PMMA, however the names are

different (for C4 and C5). Inset of each image is the corresponding name.

In our case, in order to analyze the residual impurities on the surface of the APS-transferred and the $FeCl_3$-transferred graphene, XPS scans of C1s and O1s core-levels are depicted in figures 4.15 and 4.16.

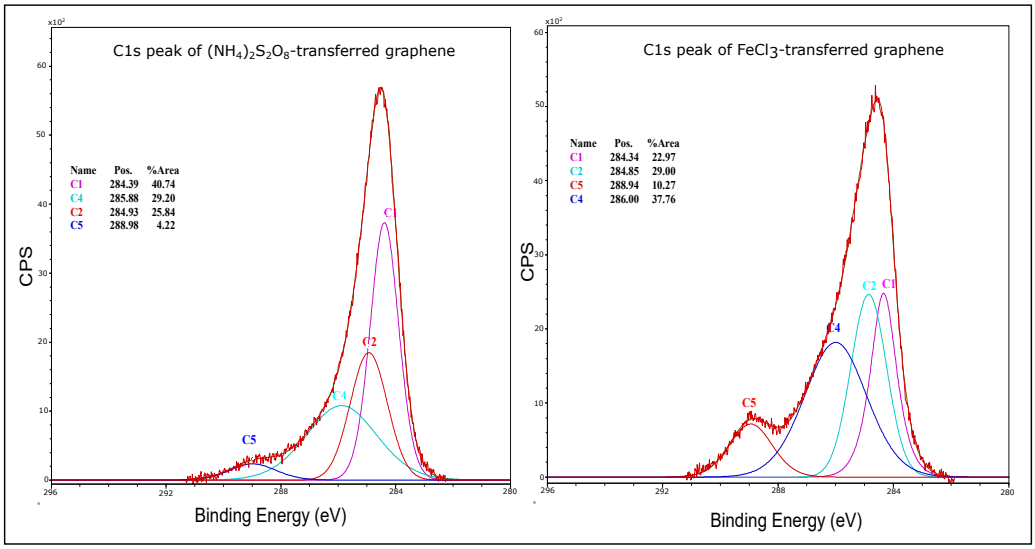

Figure 4.15: C1s core level spectra of APS transferred graphene (left) and $FeCl_3$ transferred graphene (right). Deconvoluted, the spectra show the different bondings present on the graphene after transfer.

For APS and $FeCl_3$ transferred graphene, the C1s peak shown in figure 4.15 can be deconvoluted into 4 components [91, 106, 203, 204]:

- The C1 component corresponding to the sp2-hybridized C=C peak attributed to graphene at bonding energies of 284.39 eV and 284.34 eV respectively for the APS-transferred and the $FeCl_3$-transferred sample.
- The C2 component corresponding to the sp3-hybridized C-C bond at 284.93 eV and 284.85 eV respectively, indicating defects and/or amorphous carbon in the graphene lattice.
- The C4 component originating from the methoxy functional group (C-O bond) of PMMA, at 285.88 eV and 286.0 eV respectively.
- The C5 component originating from the carboxyl functional group (O-C=O bond) of PMMA around 288.8 eV and 288.94 eV respectively.

The fact that we have only observed two PMMA bonds could be due to the atmospheric contamination (C-O bond) masking the PMMA.

These C1s core-level spectra indicate the presence of PMMA residues in both transfers, which is something expected in PMMA-assisted wet transferring of graphene using acetone as a solvent for the polymer [91,106, 203,204]. However, by comparing the intensities of the C4 and C5 bonds in the two samples, we can conclude that the polymer contribution in the APS-transferred graphene is lower than that of $FeCl_3$-transferred graphene, meaning that the residues are decreased when using $(NH_4)_2S_2O_8$ [203]. Similarly, the intensity of the C2 bond is higher in the $FeCl_3$-transferred graphene, which indicates a higher defect density in the graphene lattice. Along with the C1 peak having a high intensity in the APS transfer indicating a high density of sp2 bonded carbon atoms in the sample, we can conclude a lower residue and a higher graphene quality in the APS-transferred graphene. These findings are of utmost importance, since they show the effects of each solution on the graphene lattice.

Several points were measured on both samples, and C1s core level spectra were examined. The concentration of the PMMA is calculated from the atomic concentration of the components of the polymer. In this case, there are two PMMA components: the C-O and the O-C=O bonds. We have found that $\sim$ 39% of residue are found on the APS-transferred sample compared to $\sim$ 48% of PMMA residue on the $FeCl_3$-transferred graphene surface. These results are consistent with the XPS scans shown in figure 4.15. In addition, we have found that the density of sp3 bonded carbon atoms in the $FeCl_3$-transferred sample is much higher than that of the sp2 bonded C atoms, which indicates a highly defected graphene. However, this was not the case with the APS-transferred graphene, where the density of sp2 bonded C atoms was much higher than that of sp3 bonded C atoms. Another important observation is the concentration of the C-O and the O-C=O bonds. In fact, Hong *et al.* [204] have found that the carboxylic group O-C=O is related to the mechanical and chemical damage induced by the Cu etching during the transfer. In both samples, we have noticed that the O-C=O concentration is lower than that of C-O, indicating that there is more PMMA residues on the graphene than that of Cu etching induced chemical and mechanical damage. However, this damage is much higher in the $FeCl_3$-transferred graphene.

Figure 4.16 shows the XPS spectra of the O 1s core-level peak in APS-transferred graphene (right) and $FeCl_3$-transferred graphene (left).

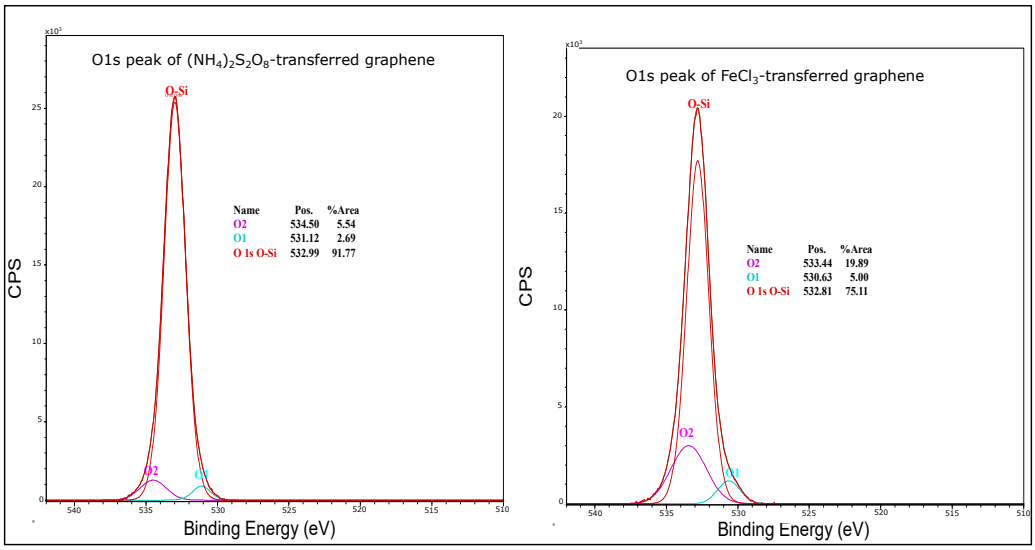

Figure 4.16: O1s core level spectra of APS transferred graphene (left) and $FeCl_3$ transferred graphene (right).

In the same manner, the O 1s peak can be deconvoluted into 3 peaks:

- The main O1s peak corresponding to the O-Si bond at 532.99 eV (532.81 eV) respectively, originating from the substrate.
- The O1 peak around 531.12 eV (530.63 eV) respectively corresponding to the O=C bond originating from the PMMA.
- The O2 peak corresponding to the C-O bond around 534.5 eV (533.4 eV) respectively, originating from the PMMA.

We note that for the $FeCl_3$-transferred sample, the peaks are shifted of about 0.5 to 1 eV towards lower binding energies. This energy shift is likely a result of doping in the graphene [203, 205] which confirms that the iron chloride solution dopes the graphene.

These findings indicate the presence of PMMA residues in both transfers, however, if we look at the intensities of the three peaks, we can conclude that the O1 and O2 peaks of the $FeCl_3$ transferred graphene have much higher intensities than those transferred using APS, and a lower intensity of the O1s peak, which means that the residue density is far higher in the $FeCl_3$ transferred graphene than in the APS transferred graphene.

Similarly to the C1s peak, we have performed multiple O1s core level measurements on different points of both samples. As expected, only 14% of residues were found to be related to the APS transfer compared to 22% for the $FeCl_3$ transferred sample, and more damage has been done to the graphene lattice transferred

using the iron chloride solution since a much larger O-C=O concentration was found on the $FeCl_3$ transferred graphene.

In conclusion, we have conducted XPS measurements on two graphene samples, transferred via the PMMA-assisted technique, using $FeCl_3$ and $(NH_4)_2S_2O_8$ to etch the copper. Both C1s and O1s core-level spectra of APS-transferred and $FeCl_3$ transferred graphene indicate the presence of PMMA residues on the surface of the graphene. However, further analysis of the intensity of the PMMA components in each spectrum have showed a higher residue density in the $FeCl_3$-transferred sample compared to that of the APS transferred graphene. In addition, by examining the O-C=O bonds resulting from the chemical and mechanical damage of the graphene during the etching step, we have found that the concentration of the carboxyl group is much higher in $FeCl_3$ transferred graphene, indicating that the iron chloride solution not only adsorbs more residues, but also induces more damage in the graphene lattice. The APS-transferred sample show less residues as well as higher graphene quality, indicated by a higher intensity of the sp2-hybridized C=C peak.

These XPS characterizations have helped us gain more insight about the effect of the copper etchant on the graphene quality. In this work, we have thus chosen to transfer the graphene using $(NH_4)_2S_2O_8$ to etch the underlying copper substrate.

4.5 Raman spectroscopy of graphene

In this work, the Raman spectra of graphene were obtained using a MicroRaman Confocal Renishaw inVia with a laser excitation of 532 nm (2.33 eV). This section is devided into three subsections. First, the baseline substraction of the Raman spectrum of graphene on copper will be briefly shown. Then, the Raman spectrum of graphene on copper grown by Pulsed CVD (P-CVD) for various temperatures will be discussed and the effect of the small temperature change will be evaluated. Finally, the Raman spectrum of graphene used for the fabrication of GFETs will be presented. The Raman spectra and maps of graphene channels of the transistors (transferred and processed graphene) will be discussed in details after the fabrication process.

4.6 Raman spectroscopy of P-CVD grown graphene on copper

Several spectra yielding similar results were taken at arbitrary points of the copper samples after the graphene growth. Although this approach does not give a complete idea about the graphene properties since we are only characterizing graphene locally, it does however give us a global idea about the graphene quality and number of layers, since we are collecting several spectra from different copper grains in the same sample.

The typical graphene growth occurs at temperatures above 1000°C [80]. In our case, previous works have found that the best growth temperature on thick (70 μm) copper foils is around 1052°C.

Figure 4.17 represents a Raman spectrum of P-CVD grown graphene on copper at 1052°C. The raw data is depicted on the left, where the background effect of the copper can be observed. The two main peaks of graphene (2D and G peaks) are observed, as well as a very small D peak. The Raman spectrum on the right is the result of the first spectrum after baseline substraction.

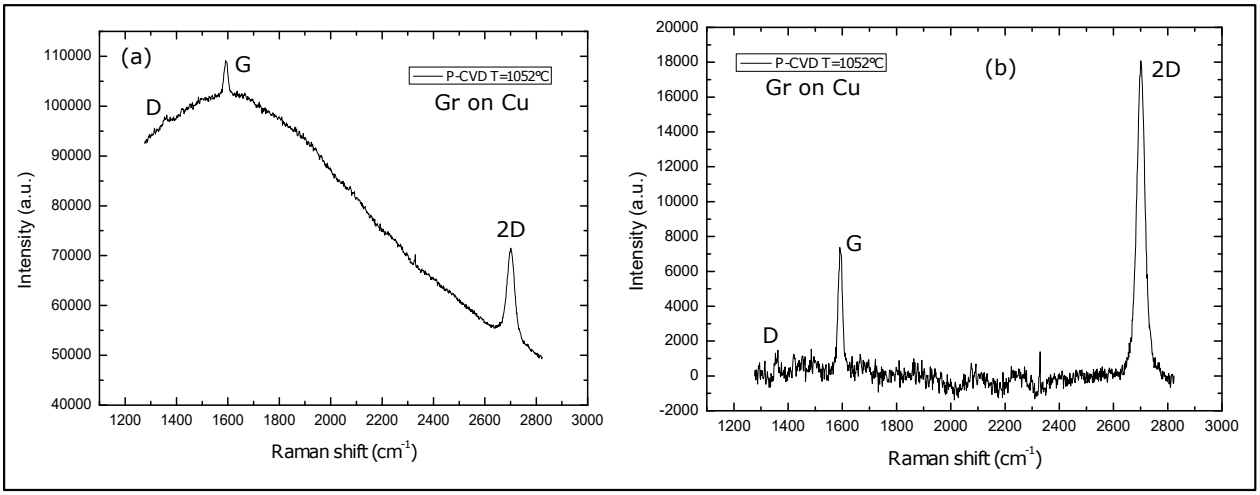

Figure 4.17: Raman spectrum of graphene on copper grown via pulsed CVD (P-CVD) (a) before and (b) after baseline substraction.

The $I(_D)/I(_G)$ intensity ratio evaluates the amount of defects present in the graphene lattice, and the The $I(_{2D})/I(_G)$ intensity ratio, as well as the linewidth of the 2D band (FWHM(2D)), estimate of the number of graphene layers. The peak position varies depending on the substrate (whether the graphene is on Cu or SiO_2). In figure 4.17 (b), the D peak is very low, indicating a high quality graphene with very low defects. The 2D peak at 2700 cm^{-1} is a single Lorentzian, 2.5 times more intense than the G peak with a FWHM (full width at half maximum) of 29 cm^{-1}. This indicates that the graphene is a single layer.

Figure 4.18 shows the average Raman spectrum of the graphene sheet we have used to fabricate our devices.

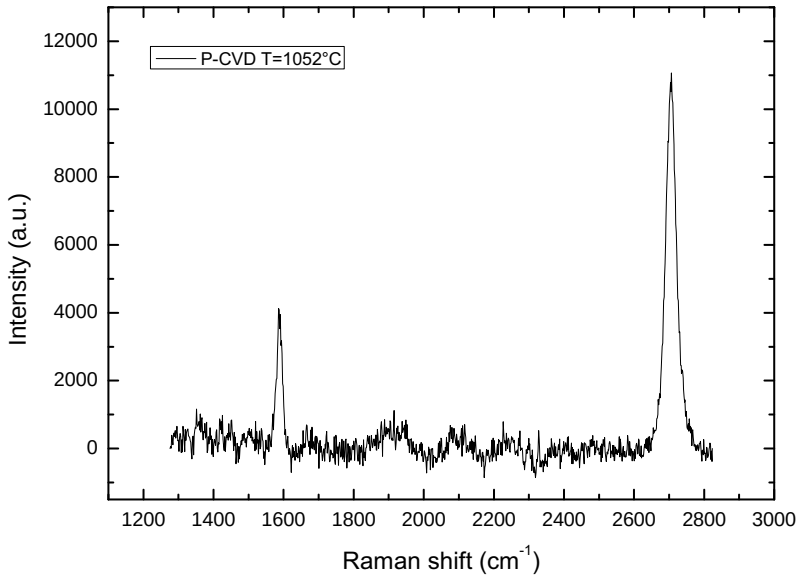

Figure 4.18: Raman spectrum of graphene on copper grown via pulsed CVD for T=1052°C.

In this spectrum, the D peak is absent, the $I(_{2D})/(_G)$ ratio is around 2.6 and the FWHM(2D) is $\sim$ 28.5 cm^{-1}. We have hence transferred this graphene sheet onto SiO_2/Si substrates for device fabrication.

4.7 Fabrication steps of graphene-based field effect transistors (GFETs)

Back-gated GFETs with square channels were fabricated in order to study the graphene's electronic properties such as the the Dirac point, the electron and hole mobility and the sheet resistance. Relatively large and square channels were chosen for an easier and quicker fabrication and characterization with less complications (cleanroom handling and mathematical analysis) as well as for a complete Raman characterization, since

channel lengths inferior to 1 μm are impossible to characterize using Raman spectroscopy because the laser spot is around 500 nm. The channel dimensions varied between 1x1 μm^2, 2x2 μm^2, 5x5 μm^2 and 10x10 μm^2. This variation helps us understand more about the nature of the correlation between the channel length and graphene electronic properties such as charge carrier mobility and sheet resistance. In order to observe the reproducibility of the GFETs performances and properties, we have fabricated a matrix of devices on the same substrate, which means that we are using the same graphene layer we have synthesized on the same copper foil and transferred on the same target substrate.

A model of the GFETs is shown in figure 4.19. The devices were designed using L-Edit, a software directly related to the E-beam lithography computer in the clean room.

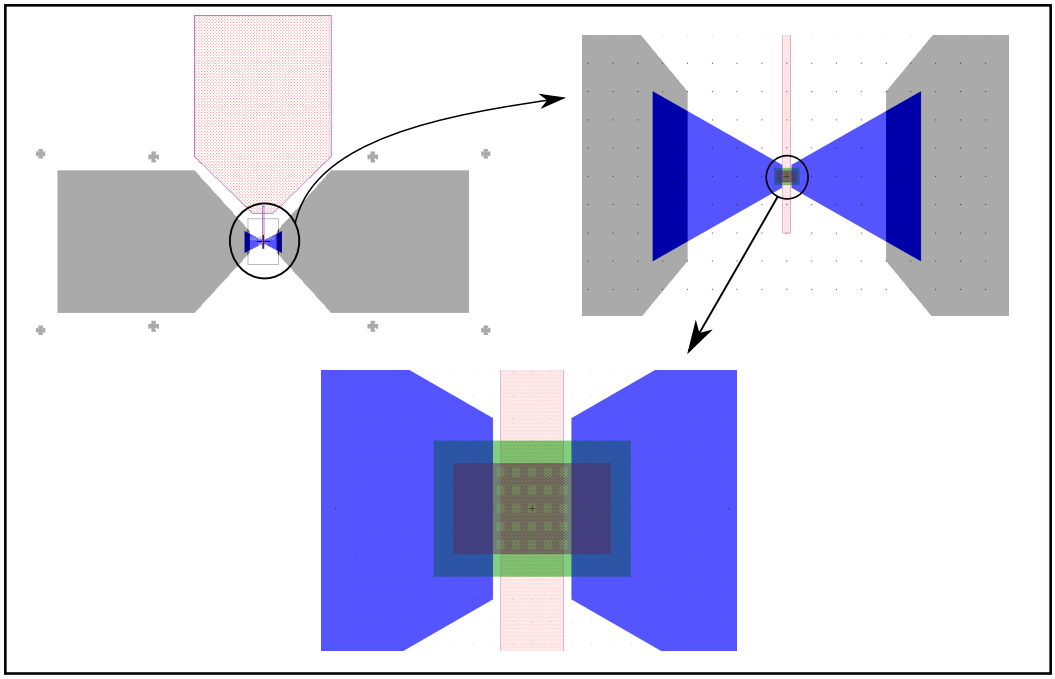

Figure 4.19: This work's GFET design. The circles are zoom ins.

The entire fabrication of the electronic devices was performed using electron-beam lithography (EBL). 950K PMMA was used (with different thicknesses according to the lithography step) as a positive resist, and MaN 2405 as a negative resist. Complementary fabrication processes such as reactive ion etching (RIE) and electron beam physical vapor deposition (EBPVD) were used to etch the excessive resist and graphene and to deposit various metals, respectively.

The fabrication steps (after the graphene transfer) are detailed as following:

1. The small drain and source electrodes (According to figure 4.19, the small electrodes are triangle-shaped and colored in blue) were patterned first. 950K PMMA with a thickness of 300 nm (A5, 4000

rpm, 400 rpm/s, 60s), baked at 170°C for 20 min prior to the lithography was used as the electro-sensitive resist. After the lithography, the PMMA was developed in an IPA:MIBK solution for 60s and then immersed in IPA for exactly 30s. Then, the sample was coated with Palladium/Gold (Pd/Au = 10/50 nm). Palladium was chosen as the contact metal with the graphene because palladium has been demonstrated to have the lowest contact resistance metal (185 ± 20 $\Omega.\mu m$ at 300k) [206]. More recently, Zhong *et al.* have demonstrated a palladium-graphene contact resistance of 69 $\Omega.\mu m$ [207]. After the metal deposition, the lift off was carried out in hot acetone to etch the PMMA and the metal layer on top. Finally, the sample was cleaned in IPA for a couple of minutes and dried using a N_2 gun.

2. The large drain and source electrodes (represented as the gray polygon in figure 4.19) were patterned using a 600 nm-thick PMMA resist (A7, 4000 rpm, 400 rpm/s, 30s), also baked at 170°C for 20 min prior to the lithography. After the patterning, the graphene underneath the large electrodes was etched away via oxygen plasma for a better contacts-substrate adhesion. Afterwards, Titanium/Gold (Ti/Au = 20/200 nm) was deposited and the lift off was once again carried out in hot acetone. The sample was further rinsed in IPA and dried using a N_2 gun.

3. The final step is the definition of the GFET channel (green rectangle in figure 4.19). MaN 2405 was spin coated (600 nm, 4000 rpm, 200 rpm/s, 30s) and baked on a hot plate at 90°C for 1 min. After the lithography, and since it is a negative resist, the graphene channels will be protected by the MaN. An oxygen plasma step etched away the entire graphene sheet not protected by the MaN, and finally, the resist was removed using acetone and the sample was cleaned in IPA and dried using a N_2 gun.

We must mention that the dimensions of the small electrodes and the channel lengths varied for each different GFET. In addition, the third pink electrode in figure 4.19 represents the gate electrode. However, back-gate GFETs are enough to give us the information we need on the graphene properties, thus the top gates were left as an extra option. The square "mesh" in the graphene channel represented in figure 4.19 is an extra lithography step we have performed on some transistors which will be explained later on.

A schematic of the final back-gated transistor is represented in figure 4.20:

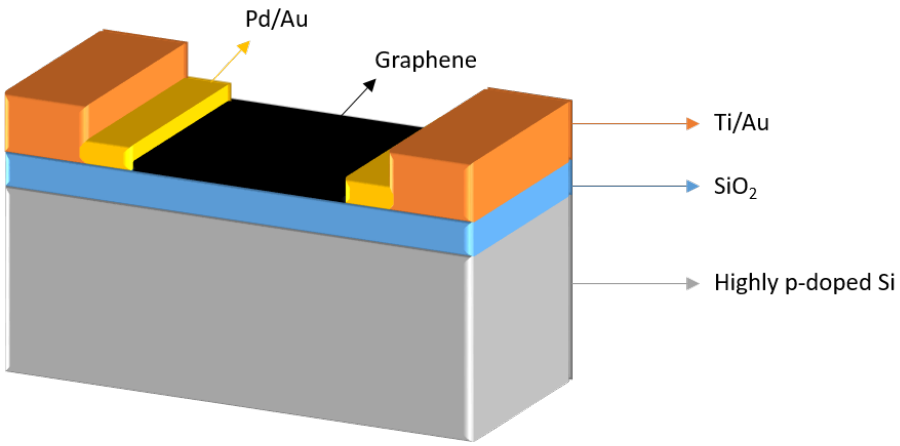

Figure 4.20: Representation of a back-gated graphene-based field effect transistor. The Si substrate is heavily p-doped and plays the role of gate electrode.

Figure 4.21 shows optical images of four GFETs with four different channel dimensions. Here, the graphene was not only transferred onto silicon dioxide substrates, but has also endured three lithography steps and oxygen plasma treatments, as well as metal deposition and lift off processes. These steps include sequenced coating and dissolution of PMMA on the graphene layer. This explains why PMMA residues from the fabrication process are observable in the optical images. However, around the channel area the graphene appears to be clean. We note that the gate electrodes are patterned along with the drain and source electrodes (to reduce the lithography steps), but are not connected to the graphene channel.

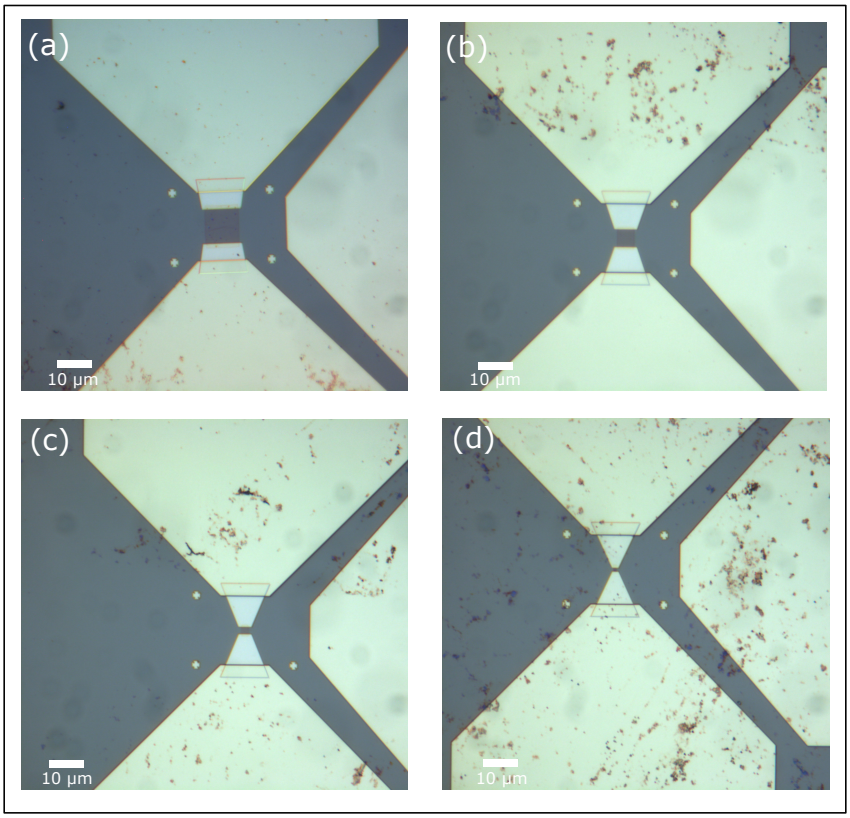

Figure 4.21: Optical images of GFETs with channel dimensions of (a) 10x10 μm^2 (b) 5x5 μm^2 (c) 2x2 μm^2 and (d) 1x1 μm^2.

4.8 Raman spectroscopy of GFETs

4.8.1 Raman spectra of GFETs

Raman spectra of four transistors with different channel dimensions were collected over the entire channels in ambient air and the average spectra are shown in figure 4.22.

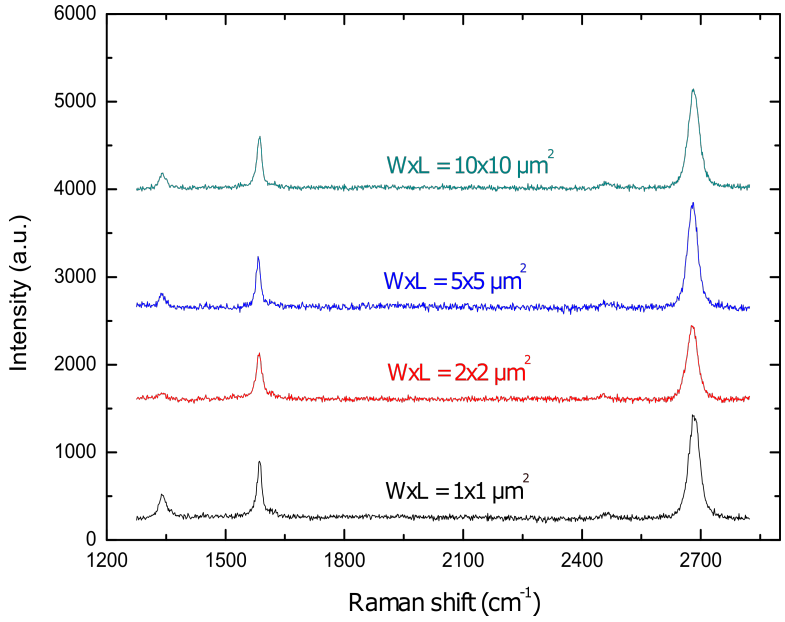

Figure 4.22: Raman spectra of four GFETs with four different channel dimensions (10x10 μm^2, 5x5 μm^2, 2x2 μm^2 and 1x1 μm^2).

In the Raman spectra of these GFETs, the D peak is visible around 1340 cm^{-1} for all four devices, which indicates the presence of defects induced by the transfer and the fabrication process. However, since the PMMA-assisted wet transfer is by far the easiest and most popular transfer method yielding almost always a complete transfer of the graphene sheet, and since the fabrication processes are all compatible with wafer-size device fabrication, it is then important to understand the consequences of these industrial processes on the graphene quality. We notice that the amount of defects for channel dimensions lower than 1 μm^2 is relatively small compared to a larger I_D peak for the smallest channel. This higher D peak intensity is due to the effect of the laser spot size (around 500 nm) on the small graphene channel, as the defects located on the edges of the channel could be taken into account when performing the Raman measurements.

Furthermore, the position of the 2D and G peaks should also be taken into account because these peak positions are correlated with the amount of doping in the graphene sheet [95, 114] as well as the presence of nanoscale strain variations in the graphene [116].

The G band is visible around 1585 cm^{-1} for all of these GFETs. The G peak position is sometimes

considered in order to estimate the presence of doping in the graphene, however without complementary characterization methods , it is not a reliable indicator of doping in the graphene since it is also influenced by other factors such as temperature. The position of the G peak here is consistent with other works which demonstrate the absence of doping in the graphene sheet. Nevertheless, we have fabricated a matrix of graphene devices on one graphene sheet, it is thus possible to find undoped graphene but also doped graphene. The doping is later discussed via electrical measurements performed on these devices.

The intensity ratio between the 2D band versus the G band ($I(_{2D})/(_G)$) is approximately 1.58, 1.4, 1.5 and 1.7 respectively for 2x2, 5x5 and 10x10 μm^2 channel size. The linewidth (FWHM) of the 2D band (G band) is around 29 cm^{-1} (14 cm^{-1}, 17 cm^{-1}) for the 1x1 and the 2x2 μm^2 channels (respectively), 27 cm^{-1} (13 cm^{-1}) for the 5x5 μm^2 channel and 30 cm^{-1} (14 cm^{-1}) for the 10x10 μm^2 channel. These values confirm the monolayer graphene characteristic.

4.8.2 Raman mappings of GFETs

Using Raman spectroscopy, one can easily distinguish monolayer from Bernal stacked bilayer (AB stacked) graphene to a few-layer graphene by simply looking at the 2D band. As we have seen in chapter 1, the 2D band of a normal AB-stacked bilayer (AB-BLG) graphene is much broader than that of monolayer graphene and can be fitted as four peaks (instead of one for single layer graphene), which originates from the splitting of the valence and conduction bands. Increasing the layer number decreases the intensity of the 2D peak and consequently changes its shape, and above 5 layers, the Raman spectrum becomes indistinguishable from that of bulk graphite, in which the 2D peak is comprised of two components. However, in turbostratic graphite, the graphene layers are randomly stacked. This weak interaction between the misoriented graphene planes results in a Raman spectrum similar to that of single layer graphene (sharp Lorentzian 2D band). Nevertheless, the linewidth of the 2D band in turbostratic graphite is broader than that of monolayer graphene, almost double (45-60 cm^{-1}), and the position of the 2D band (its frequency) is strongly upshifted. Thus, one can distinguish monolayer graphene from turbostratic graphite. A very challenging task lies in differentiating single layer graphene (SLG) from misoriented bilayer (BLG) graphene, also known as turbostratic BLG (T-BLG). This latter is not AB-stacked like normal bilayer graphene, but possesses two layers that are misoriented and the twisted angle is unknown. This turbostratic BLG also exhibits a single Raman 2D peak similar to that of SLG. Similarly to turbostratic graphite, in turbostratic BLG, the weak interlayer interaction does not split the electronic dispersion curve and hence only one component is observed, contrary to the case of a Bernal bilayer showing four components. [109, 110, 114, 208–210]

In this case, we ask ourselves, is Raman spectroscopy capable of distinguishing single layer graphene from misoriented bilayer graphene?

Multiple experimental and theoretical studies [208–211] have confirmed the resemblance of the linear energy dispersion and hence Raman spectrum between single layer graphene and misoriented bilayer graphene. For instance, Poncharal *et al.* [209] compared SLG to T-BLG (turbostratic BLG). They have found that in T-BLG, the 2D band is strongly blueshifted (9 cm^{-1}, 6 cm^{-1} and 2 cm^{-1} respectively for excitation energies of 633 nm, 514,5 nm and 488 nm) and interstingly narrower (by 7 cm^{-1}) than that of SLG. They have also recorded a very small redshift of the G peak for T-BLG (2.6 cm^{-1}). Ni *et al.* [210] have found similar results regarding the position shift and linewidth value of the 2D band for SLG and T-BLG, where the blueshifting of the 2D peak was not always strong. However, they did not find a change in the G peak position, and the linewidth of the 2D band was broader for T-BLG in 2 out of 6 samples they measured. Thus, one cannot depend on these parameters in order to distinguish between SLG and T-BLG. A very small blueshift in the 2D peak is not a reliable indication because the frequency of this peak varies with the excitation energy and does not have a precise reference value. Also, the G peak position varies with not only the number of layers, but with other effects such as doping. One observation for both studies came to be of use in order to distinguish SLG from T-BLG: the $I(_{2D})/I(_G)$ ratio. The intensity of the 2D peak is strongly increased in the case of T-BLG, where Poncharal *et al.* have found a ratio of 2.38 for T-BLG in contrast to 1.2 for SLG. Similarly, Ni *et al.* have observed an increased 2D and G (although much smaller than the 2D) intensity for turbostratic BLG. This is probably due to the different resonance conditions of misoriented BLG and monolayer graphene. Nonetheless, the $I(_{2D})/I(_G)$ ratio remains an uncertain parameter when we do not have a reference sample to compare with (in other words, if we have a random graphene sheet to characterize, how can one be sure its monolayer graphene and not turbostratic BLG ?). This emphasizes the need for complementary techniques such as AFM or STM (scanning tunneling microscope).

Figure 4.23 represents the Raman spectra of SLG, T-BLG and Bernal stacked BLG.

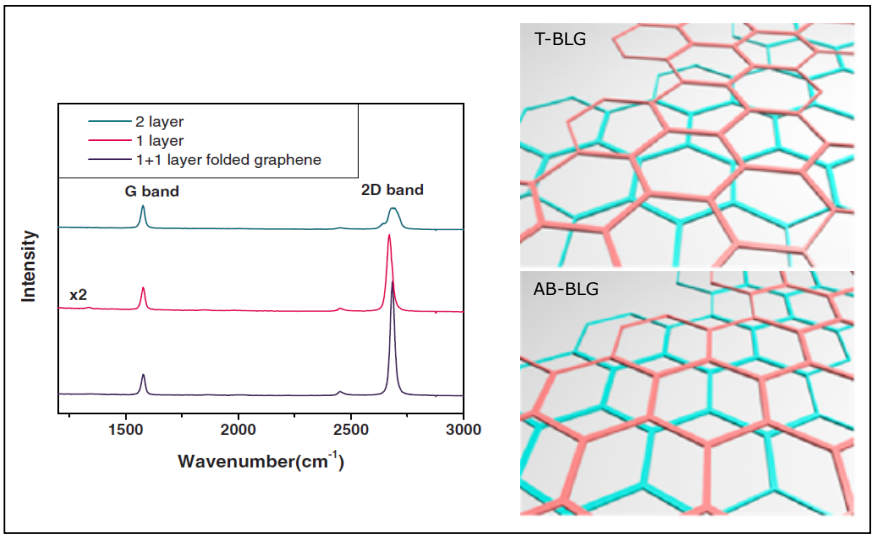

Figure 4.23: The Raman spectrum of BLG, SLG, and T-BLG (named 1+1 layer folded graphene here). The spectra are normalized to have similar G band intensity. The schematic representations of T-BLG and AB-BLG are viewed on the right. Adapted from [210] and [208].

As it can be seen in the Raman spectra in figure 4.23, it is very easy to distinguish AB-BLG from T-BLG and SLG (single layer graphene) by looking at the 2D peak. However, the Raman spectra of T-BLG and SLG are somewhat indistinguishable. The blueshift in the 2D peak and the increased $I(_{2D})/I(_G)$ ratio for T-BLG can be seen, but differentiating the two spectra remains a very hard task using only Raman spectroscopy.

In this section, we have performed Raman mappings on three GFETs with different channel dimensions, in order to study the graphene quality and number of layer. We have then correlated these findings with the electrical measurements of the GFETs.

Figure 4.24 represents Raman mappings of a 2x2 μm^2 channel device. Figure 4.24 (a2) shows the graphene channel connected to the source and drain electrodes, while Figure 4.24 (b2), (c2) and (d2) are the $I(_{2D})/I(_G)$ ratio, $I(_D)/I(_G)$ ratio and FWHM(2D), respectively.

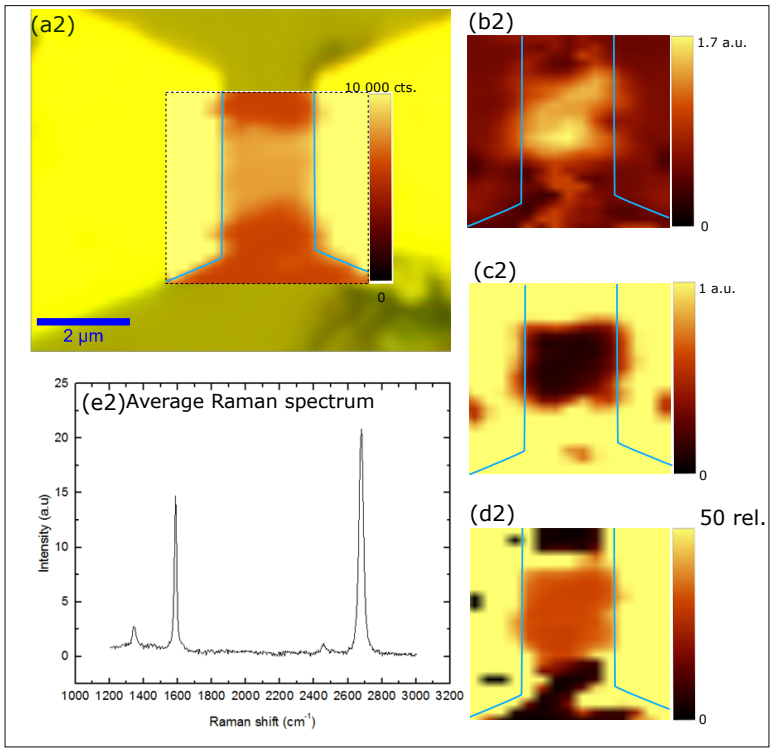

Figure 4.24: Raman maps of a GFET with 2x2 μm^2 channel.

The defects in the graphene lattice are estimated by looking at the $I(_D)/I(_G)$ ratio presented in Figure 4.24 (c2). We can conclude that the graphene is of excellent crystalline quality since the ratio is extremely low and homogeneous throughout the entire channel. The defects begin to appear at the palladium-graphene interface which is an expected result of lithography and fabrication processes.

Examining the $I(_{2D})/I(_G)$ ratio in Figure 4.24 (b2), we observe that it is around 1.6 and is homogeneous throughout the majority of the channel. The FWHM(2D) is homogeneous in the entire channel with a value around 30.6 cm^{-1}. These two results indicate the presence of a single layer graphene.

Figure 4.24 (e2) represents the average Raman spectrum of the entire graphene channel. The D peak is present because we have taken into account the edges of the channel and thus the metal-graphene contact. Although the averaged spectrum gives a global idea about the graphene in the channel, it is however not a representation of the entire channel since averaging the Raman spectra globalize the results and does not give a precise idea about the measured graphene in every single point of the channel. In this case, we can combine the Raman spectrum and the Raman mapping of the GFET and confirm that indeed we have a monolayer graphene in the channel.

In order to confirm the monolayer characteristic of the graphene channel, we have performed AFM measurements on the 2x2 μm^2 channel and the result is depicted in figure 4.25.

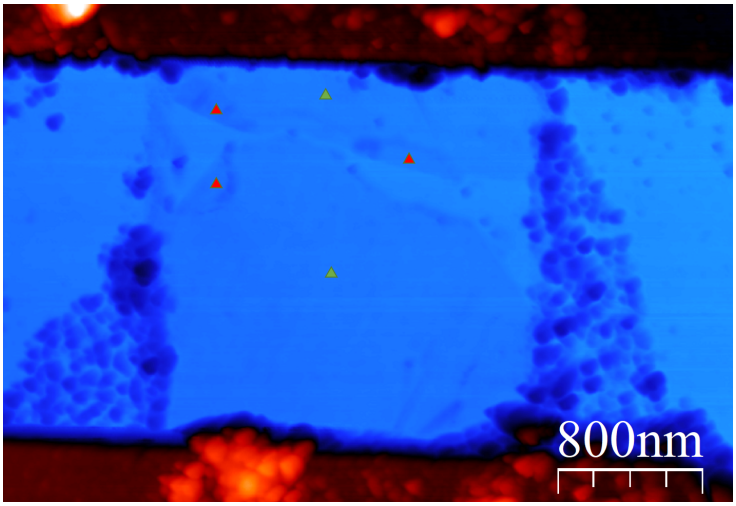

Figure 4.25: AFM image of the 2x2 μm^2 channel.

In figure 4.25, the channel can be seen in the middle, surrounded by the contacts where impurity particles have gathered. As it can be seen, the graphene sheet was torn after the electrical measurements. In regions where the graphene is broken, we notice that the torn graphene sheet has folded on the initial layer (red triangles). AFM measurements on the graphene sheet away from the tears (green triangles) have detected a thickness of $\sim$ 1 nm, whereas in regions of folded graphene (red triangles), the thickness was found to be $\pm$ 2.3 nm. Considering that the graphene layer contains water molecules and other impurities and residues, we can confirm the presence of a single graphene layer.

In figure 4.26 (a5), we have considered a 5x5 μm^2 graphene channel. As it can be seen, the electrode on the left is broken (during the fabrication process). The $I(_{2D})/I(_G)$ ratio in figure 4.26 (b5) is approximately 2 along the entire sheet. Considering the FWHM(2D) represented in figure 4.26 (d5), it is homogeneous in the entire sheet and its value is around 29.6 cm^{-1}. These findings indicate that the GFET channel is consisted of a single layer graphene.

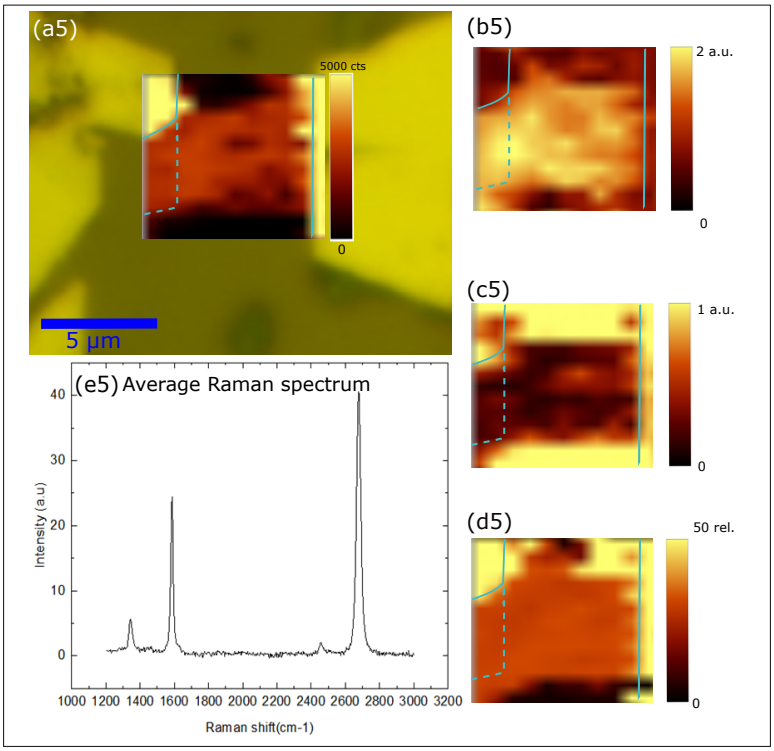

Figure 4.26: Raman maps of a GFET with 5x5 μm^2 channel.

The mapping of the defects is represented in figure 4.26 (c5). In general, the defect density is low in the majority of the channel. There are defects in some regions of the channel, which coincide with the black spots in the GFET channel in figure 4.26 (a5) and in regions where the $I(_{2D})/I(_G)$ ratio is delicately smaller than 2 in figure 4.26 (b5). These defects can arise from the graphene sheet itself during growth (sp3 bondings), or from folds or cracks induced in the sheet during the transfer and/or fabrication processes. These defects can also exist due to PMMA residues during the transfer and/or fabrication processes.

An interesting observation is in the region where the electrode is broken (figure 4.26 (a5)). In fact, during the fabrication of the GFETs, the graphene underneath the small Pd/Au electrodes was not etched away, thus we have a continuous graphene sheet under the small electrodes. If we examine closely figure 4.26 (b5-d5), we observe a constant $I(_{2D})/I(_G)$ ratio of 2, alongside a constant FWHM(2D) $\sim$ 29 cm^{-1}, identically to that of the graphene channel. What is even more intriguing is the very low $I(_D)/I(_G)$ ratio under the

broken electrode, which implies a high quality graphene layer. This remarkable event where the graphene sheet is still intact and of high quality even after the electrode broke indicates that the palladium metal contacts we used have conserved the intrinsic properties of the graphene layer. Thus, we can conclude that palladium is indeed a very good choice for contacting the graphene.

The average Raman spectrum of the 5x5 μm^2 channel is shown in figure 4.26 (e5). The D peak is present, mostly due to some of the defected regions of the channel. The sharp and thin Lorentzian 2D peak confirm, alongside the Raman mappings, a typical spectrum of single layer graphene.

As it is widely known, a major drawback in the PMMA-assisted wet transfer technique is the presence of PMMA residues on the graphene sheet which remain even after many removal techniques such as long acetone baths and annealing processes. Here, we have considered a 10x10 μm^2 GFET with PMMA residues on the sheet in order to correlate the presence of these residues with the quality of graphene. Figure 4.27 (a10) represents the graphene channel connected to the drain and source electrodes. PMMA residues can be seen on the graphene sheet and are pointed out in blue, red and green.

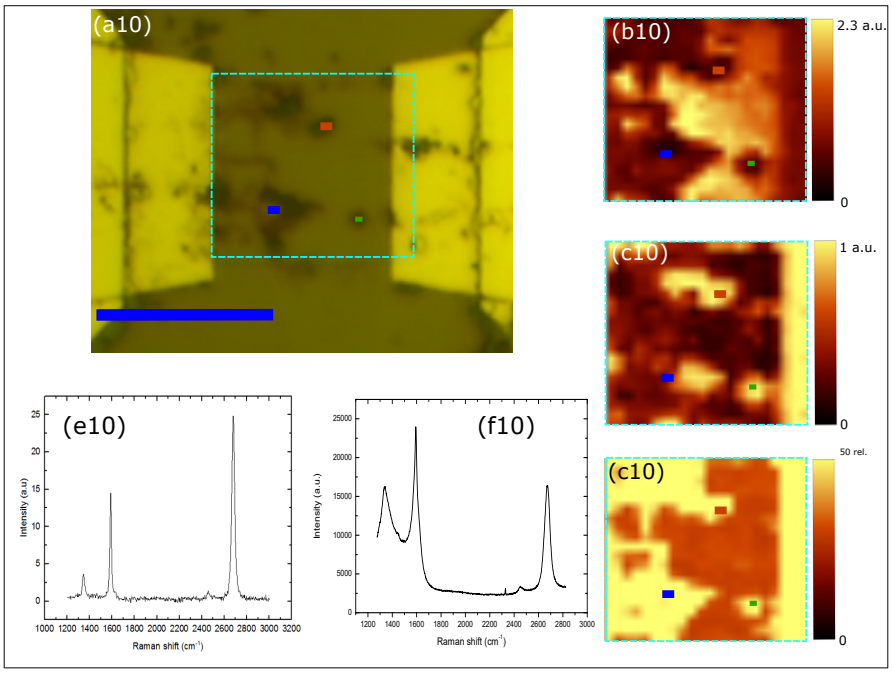

Figure 4.27: Raman maps of a GFET with 10x10 μm^2 channel. The scale bar is 10 μm.

Figure 4.27 (b10) shows the $I(_{2D})/I(_G)$ ratio across the channel. It can be seen that the ratio is higher than 2 in PMMA-free regions, whereas it strongly decreases for regions containing PMMA residues. Correlating these results with the defects in figure 4.27 (c10), the regions with PMMA residues have a very high defect density, while the residue-free regions contain a low defect density. The FWHM (2D) in figure 4.27

(d10) is also complementary to the two preceding maps, where the linewidth of the 2D peak is around 30 cm^{-1} across the channel, except the zones where polymer residues are present, where it increases for values higher than 50 cm^{-1}. These mappings illustrate the effect of PMMA residues on the graphene, where we conclude that residues have a very strong effect not only the quality of the graphene, but also on the 2D and G peaks, where the $I(_{2D})/I(_G)$ ratio decreases and the FWHM(2D) increases with the presence of PMMA. Figure 4.27 (e10) represents the average Raman spectrum of the channel taken in the region where the defects are low (thus not in the PMMA regions). Away from the PMMA residues, we can see that the $I(_D)/I(_G)$ ratio is relatively low considering the graphene edges. The average Raman spectrum away from the PMMA residues indicates a single layer graphene sheet with low defects. The Raman fingerprint of PMMA residues is shown in Figure 4.27 (f10). As it can be seen, the defects are very high ($I(_{2D})/I(_G) <$ 1) and the $I(_{2D})/I(_G)$ is very low. The 2D peak is also enlarged with a FWHM $> 50cm^{-1}$.

In summary, Raman mappings of three GFETs with different channel dimensions were discussed. The number of layer was correlated with a thin 2D peak and a $I(_{2D})/I(_G)$ ratio > 1.5, and a high graphene quality corresponded to a very low defect density in the sheet. Furthermore, the effect of PMMA residues on the $I(_D)/I(_G)$ ratio, $I(_{2D})/I(_G)$ ratio and FWHM(2D) of the graphene was shown. We concluded that the PMMA residues affected strongly these properties, where the density of defects was strongly increased in contaminated regions, and the 2D peak was doubly enlarged. The $I(_{2D})/I(_G) <$ has also strongly decreased due to polymer residues. This accentuates the importance of eliminating PMMA residues during the transfer of the graphene and the fabrication processes in order to conserve the high quality of graphene for further device applications.

4.9 Electrical characterization of GFETs

In this work, electrical measurements of GFETs were performed at the C2N and L2E laboratories using semiconductor analyzers (HP4155 and Agilent B1500 respectively). Typically, carrier mobility is extracted either via Hall measurements or field effect measurements. Hall measurements provide accurate measurements of carrier mobility, however, this requires a complicated fabrication process and measurement technique. Indeed, the Hall effect can be seen only when the device is placed into a magnetic field and with a specific design that allows the creation of a current and the measurement of a transverse voltage that is perpendicular to both the magnetic field and the created current. The principle is based on the Lorentz force. The major drawback of Hall measurements is that the devices are no longer used for applications, since they have already been patterned into a very precise architecture, implying that this technique of obtaining carrier mobility prohibits the use of the devices for any other application. It is for this reason that field effect measurements have become the most popular mean of estimating carrier mobility. In fact, these type of measurements do not require a specific design, and are simple to perform with a standard device geometry. The most widely

used carrier mobility extraction method is the direct transconductance method (DTM). In this technique, the transfer curve of a graphene device allows the extraction of the mobility. In fact, the transconductance (g_m) is used to calculate the mobility, and the effect of the contact resistance R_c is directly included. The latter leads to an underestimation of the mobility value at any gate voltage. However, the accuracy of the measurements can be improved by fabricating field effect transistors with low Schottky barriers at the contacts.

The back-gate capacitance is the capacitance of the SiO_2 layer, which is found to be:

$$C_{ox} = \frac{\varepsilon_0 \varepsilon_r}{t_{ox}} \tag{4.1}$$

where ε_0 is the permittivity of free space ($\varepsilon_0 \sim 8.856\ 10^{-12}$ F/m), ε_r is the permittivity of SiO_2 (for SiO_2, $\varepsilon_r = 3.9$) and t_{ox} is the oxide thickness which is 285 nm in our case. Since the quantum capacitance of graphene is much higher than the insulator capacitance, it has been neglected. In the DTM method, the carrier mobility is extracted according to the gate voltage dependent transconductance (g_m) which can be formulated as following:

$$g_m = \frac{\partial I_{DS}}{\partial V_{GS}} | V_{DS constant} \tag{4.2}$$

Hence, the charge carrier mobility can be calculated as following:

$$\mu = \frac{g_m L}{W V_{DS} C_{ox}} \tag{4.3}$$

L and W are the gate length and width respectively and V_{ds} is the drain source voltage.

If we take the example shown in figure 4.28, the DTM extraction process would be the following. The GFET is biased at a low V_{DS} voltage (between 10 and 50 mV) and a gate voltage is swept between -100 V and 100 V to record the hysteresis effect. According to the Drude model, by applying an external voltage, one can vary the carrier concentration in the graphene sheet and thus its conductance. The gate voltage induces then a surface charge density, according to the following equation:

$$n(V_{GS} - V_{Dirac}) = \sqrt{{n_0}^2 + \frac{C_{ox}(V_{GS} - V_{Dirac})}{e}} \tag{4.4}$$

With n_0 the residual carrier density at the Dirac point:

$$n_0 = \frac{C_{ox} V_{Dirac}}{e} = \alpha V_{Dirac} \tag{4.5}$$

With e the electron charge (e $\simeq$ 1.602 10^{19} C). After substituting the values we find the proportionality coefficient α between induced charge carriers and the measured V_{Dirac} to be approximately 7.56 $10^{10} cm^{-2}.V^{-1}$.

Figure 4.28(a) shows a typical electrical setup of a GFET with an example of an IV transfer characteristic depicted in figure 4.28(b). One single sweep from -90 V to 50 V of the gate bias is shown and implies a change in the channel current from 22 μA to 2.5 μA. The gate voltage where the current is at its minimum is called the charge point neutrality voltage also known as the Dirac Point (V_{Dirac}). In this example, the V_{Dirac} is measured at 31 V. For clarity, the IV curve has been plotted as a function of ($V_{GS} - V_{Dirac}$). Indeed, When $V_{GS} < V_{Dirac}$, the Fermi level is located in the valence band and holes are the majority carriers, whereas when $V_{GS} > V_{Dirac}$, the Fermi level is located in the conduction band and electrons are the majority carriers. Moreover, if V_{Dirac} is positive, it means that the graphene sheet is mainly p-doped whereas if V_{Dirac} is negative, the graphene sheet is mainly n-doped.

The carrier concentration at the charge neutrality point is found to be $n_0 = \alpha.V_{Dirac}$ = 31 x 7.56 x 10^{10} = 2.39 x $10^{12} cm^{-2}$. This value is quite similar to classical values recorded in previous works with CVD graphene. It is important to mention that 15 out of 50 devices in this thesis have demonstrated a n_0 close to 2.39 10^{11} which corresponds to the lowest carrier concentration at the Dirac Point for a transferred CVD graphene layer at room temperature [212].

The carrier mobility is depicted in figure 4.28(c) as a function of ($n - n_0$). The highest hole mobility recorded was 2550 $cm^2/V.s$ at ($n - n_0$) = -0.12 x $10^{12} cm^{-2}$ and the highest electron mobility was recorded at 1460 $cm^2/(V.s)$ at ($n - n_0$) = 0.44 x $10^{12} cm^{-2}$.

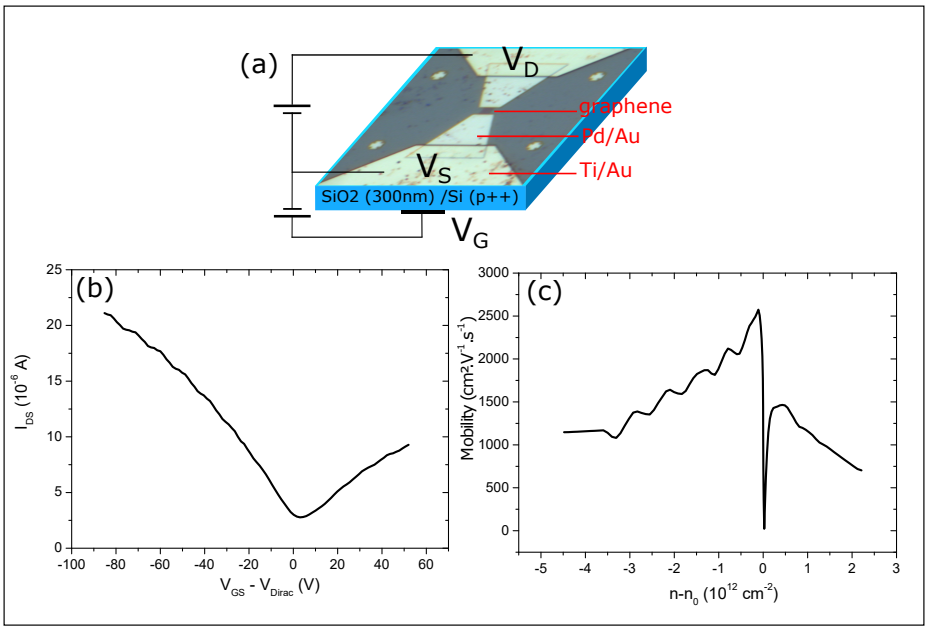

Figure 4.28: I_{ds} and carrier mobility versus V_{gs} plot (black and blue curves respectively).

Finally, in figure 4.28, the ambipolarity of the graphene layer is clearly visible. Indeed, for $V_{GS} > V_{Dirac}$, the current increases, demonstrating by that the electron transport in the channel. Almost 70% of the measured GFETs have shown ambipolarity in the conduction band, however electron mobility values have always been inferior to those of the holes in the valance band whereas the V-shaped of the dispersion relation should imply equal mobilities symmetrically to the Dirac point. To further illustrate the transfer characteristics measurements of the graphene sheet that has been synthesised in this thesis, we chose 3 different devices with gate dimensions (width x length) of 2x2 μm^2, 5x5 μm^2 and 10x10 μm^2. Figure 4.29 shows the resistance of the channel (calculated using Ohms law $R = V_{DS}/I_{DS}$) as a function of the gate voltage. Gate voltage sweeps are made in order to display the hysteresis effect in the GFETs. Previous studies have identified the water/oxygen redox couple present at the $graphene/SiO_2$ interface responsible for the presence of such hysteresis [213].

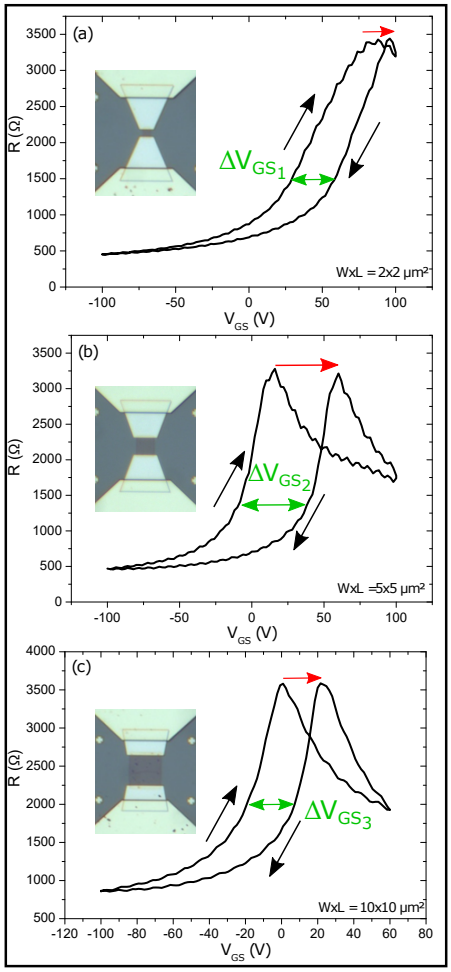

Figure 4.29: Plot of the channel resistance R_c in function of the gate voltage V_{gs} for a (a) 2x2 μm^2 (b) 5x5 μm^2 and (c) 10x10 μm^2.

In figure 4.29 (a), the 2x2 μm^2 channel resistance varies from 500 to 3300 Ω. The charge neutrality point is observed at the first gate sweep at V_{Dirac} = 88 V which implies a high carrier density of 7.56 $10^{12} cm^{-2}$ at the minimum conductance and thus, the presence of a large quantity of p-dopants in the graphene sheet. Moreover, when V_{GS} is swept back to negative voltages, a hysteresis is observed, consequently resulting in a shift in the V_{Dirac} from 88 V to 93 V and thus an increase in the channel current at constant gate voltage. This leads to a decrease in the channel resistance at constant gate voltage with a maximum $\triangle V_{GS1}$ = 30 V for a resistance value R = 1282 Ω. The maximum charges trapped in the water/oxygen molecules here is 2.27 $10^{12} cm^{-2}$ according to equation (1.4).

In the same manner, in figure 4.29 (b) and (c), for a 5x5 μm^2 and a 10x10 μm^2 channel, the resistance varies from 500 to 3300 Ω and from 800 to 3500 Ω respectively. The $\triangle V_{GS2}$ and $\triangle V_{GS3}$ are measured respectively at 45 V and 25 V which indicates the same dynamic of charge trapping of 3.4 $10^{12} cm^{-2}$ and 1.89 $10^{12} cm^{-2}$ according to equation (1.4).

These values are coherent with graphene field effect transistors fabricated on top of a SiO_2 surface and clearly highlight the necessity for a hydrophobic encapsulation such as parylene. Moreover, we note that the same minimum and maximum values of channel resistance here are random. The lowest resistance values at the Dirac point for all measured devices in this work were found to be between 450 and 1600 Ω whereas the highest resistance values were found between 2700 and 6200 Ω.

4.10 Effect of air exposure on the electrical properties of graphene

In the following paragraph, the effect of air exposure on the electrical properties of graphene will be detailed. Transfer characteristics have been recorded on the GFETs right after the fabrication, and after 8 months of air exposure. The devices were kept in a clean room atmosphere, i.e. not under vacuum. The electron and hole mobility of 14 GFETs is studied in function of time, as well as the charge neutrality point (Dirac point).

Firstly, the effect of time on the mobility values of four different channel dimensions is shown in figure 4.30. As we have mentioned before, in the DTM method, the mobility can be easily calculated by using the transconductance, which is the maximum slope of the transfer curve of the GFET away from the Dirac point. Here, we can have a global interpretation on the mobility changes after 8 months by simply comparing the slopes of the two curves (that is before and after 8 months). For instance, a very evident mobility decrease appears in figure 4.30 (c) for a 5x5 mum^2 graphene channel. The slope of the transfer curve after the fabrication (black) is clearly much higher than that of the red curve (after 8 months). Thus we can directly assume that the mobility has considerably dropped. In other cases, comparing the slopes can be useful, but if the mobility variation is small, one needs to calculate the values in order to precisely compare the two.

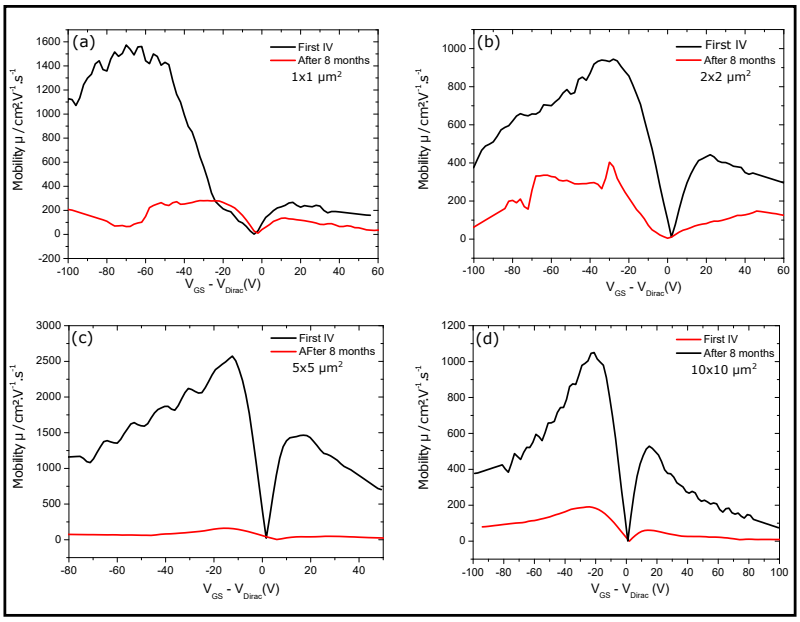

Figure 4.30: The effect of air exposure on the field effect mobility

In figure 4.30, the mobility of four different channel dimensions is plotted in function of V_{GS} - V_{Dirac}. We notice that the air exposure effect was the same on the four GFETs. A decrease in the carrier mobility is detected through the decrease of the maximum slope value of the red curves (that is the mobility after 8 months). For instance, for a 1x1 μm^2 (shown in (a)), the mobility value dropped from 1500 $cm^{-2}/V.s$ to 200 $cm^{-2}/V.s$. For the 2x2 μm^2 GFET, not only did the mobility value decrease, but we can also see that the graphene has lost some of its ambipolarity over time. This is the same case for the 5x5 and the 10x10 μm^2 GFETs. Note that we do not observe a shift in the Dirac point because we have plotted the mobility in function of (V_{GS} - V_{Dirac}) instead of V_{GS}.

In order to obtain a bigger picture on the effect of air exposure on the charge carrier mobility, we have plotted the electron and hole mobility values of 14 GFETs before (red) and after 8 months (green). The effect of air exposure on the electron mobility and hole mobility of the four gate dimensions can be seen in figure 4.31 and figure 4.32 respectively.

Although the effect of air exposure is much more visible on the hole mobility, we can conclude from these statistical measurements that both hole and electron mobility have degraded with time. A decrease in carrier mobility indicates a decrease in the charge carrier mean free path, which in turn is due to impurity particles such as water molecules adsorbing on the surface of the graphene throughout time. These particles impede the carrier transport in the graphene, resulting in a decrease in carrier mobility. In fact, these results highlight the properties of graphene as a gas sensor.

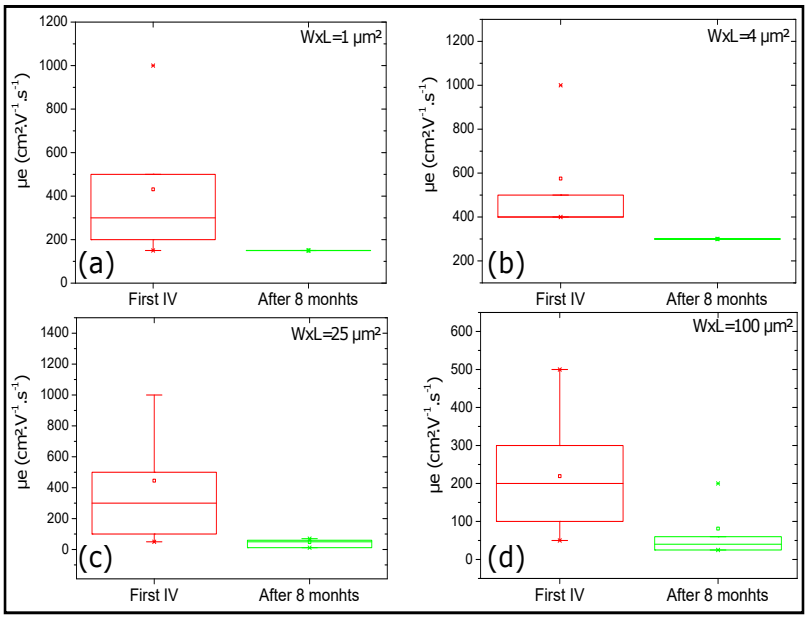

Figure 4.31: The effect of air exposure on the electron field effect mobility of 14 GFETs

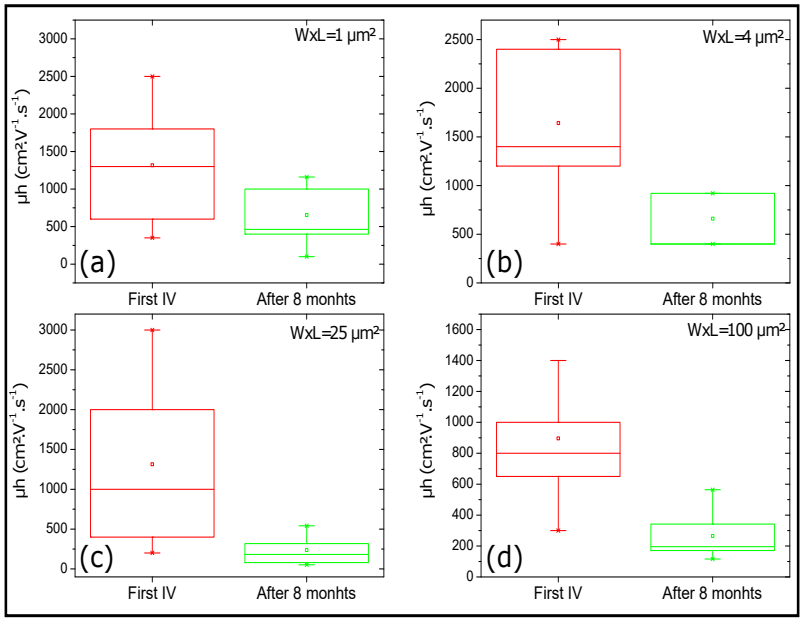

Figure 4.32: The effect of air exposure on the hole field effect mobility of 14 GFETs

In the case of the Dirac point, the effect of time on its position is depicted in figure 4.33.

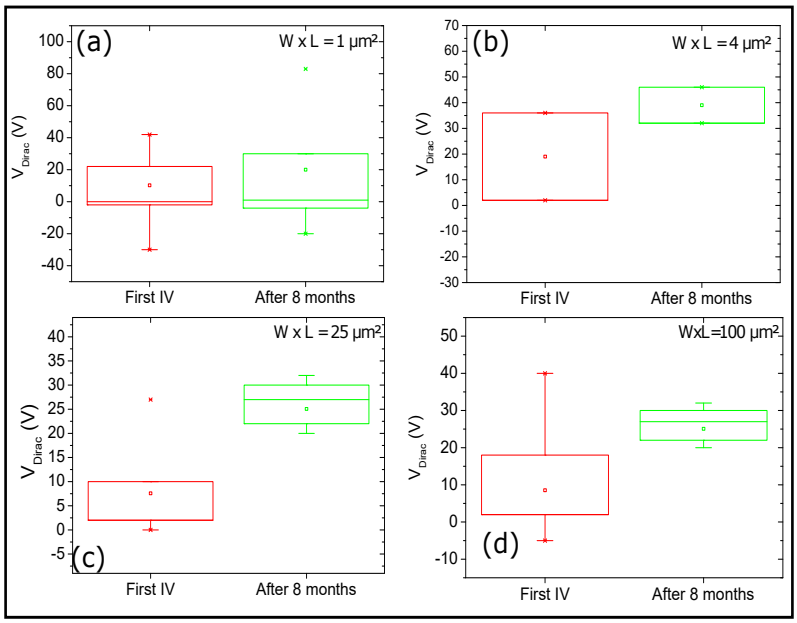

Figure 4.33: The effect of air exposure on the charge neutrality point of 14 GFETs

For channel dimensions of 2x2, 5x5 and 10x10 μm^2 shown respectively in figure 4.33 (b), (c) and (d), we can clearly observe an important shift of the Dirac point towards positive voltage. For instance, for a 2x2 μm^2 and a 5x5 μm^2 graphene channel, the Dirac point has shifted of 20 V in average, whereas it has shifted of 15 V for a 10x10 μm^2 channel. These result are consistent with the decrease of the mobility values throughout time discussed earlier. In fact, since mostly water particles (among other contamination) have adsorbed on the graphene sheet, these H_2O molecules act as p-type dopants, shifting the Dirac point towards positive bias, implying that the graphene layer is p-type doped.

A particular finding regards the 1x1 μm^2 graphene channels, where we do not see an important Dirac point shift after 8 months. This could be due to the fact that the graphene area is relatively small and thus the concentration of adsorbents on the sheet is much lower than that of larger sheets. This is considered as an advantage, since graphene devices in integrated circuits have typically acess lengths lower than 1 μm.

In conclusion, we have studied the influence of air exposure on the graphene electrical properties for 1x1, 2x2, 5x5 and 10x10 μm^2 graphene channels. We found that upon exposure to air, water particles and other contamination are adsorbed on the graphene layer, shifting by that the Dirac point towards positive voltage and lowering the carrier mobility values. These findings are especially significant, because they emphasize on the importance of encapsulating graphene devices in order to retain time-independent graphene properties. A choice of encapsulation could be parylene (discussed in chapter 4), since it is particularly beneficent for the hampering of water particles adsorbed on the graphene/substrate and graphene/air interface.

4.11 Graphene nanomesh

In this thesis, we have fabricated a graphene nanomesh (GNM) on four GFETs with four different channel dimensions (1x1, 2x2, 5x5 and 10x10 μm^2). The motivation behind this work was to study the effect of the GNM on the electrical properties of graphene, particularly the carrier mobility and Dirac point. In the literature, the role of GNMs is clear: to open a bandgap in graphene, allowing this 2D material to have semiconducting properties. Indeed, semiconducting properties are very important for both digital and analog electronics. For digital electronics, the presence of a bandgap is necessary in order to reach a high I_{ON}/I_{OFF} ratio. For analog electronics, a bandgap allows the decrease of the power consumption in the OFF state of the RF device. In addition, the cut-off frequency can be maximized by increasing the intrinsic transconductance g_m as much as possible and reducing the drain conductance g_{ds} and all capacitances and resistances as much as possible. This is expressed as following:

$$f_t = \frac{g_m}{2\pi} \frac{1}{(C_{GS} + C_{GD})[1 + g_{ds}(R_S + R_D)] + C_{GD} g_m (R_S + R_D)} \tag{4.6}$$

With C_{GS} gate source capacitance, C_{GD} the gate drain capacitance, R_S and R_D the source and drain series resistance respectively and g_{ds} the drain transconductance expressed by:

$$g_{ds} = \frac{dI_{DS}}{dV_{DS}} | V_{GS constant} \tag{4.7}$$

We have collaborated with our L2E colleagues Guido Valerio and Yi Zheng, as well as with Fernando Zanella of the University of Parana - Brazil in order to combine theoretical and experimental findings. Our collaborators have simulated a graphene nanomesh on a graphene FET using a full *abinitio* method and a semi-analytical compact approach based on the energy gap calculated with the $ab - initio$ method (article submitted). In their work, quantum wells were modeled by removing carbon atoms in a square pattern and filling in the edge of each well with hydrogen atoms. Similarly, we have patterned square holes into the graphene sheet via EBL, by protecting the graphene sheet with PMMA and etching the unwanted graphene in the square holes (via RIE) after the lithography.

The pitch distance (the distance between the edges of the square holes) for each channel dimension vary as following:

- For a 1x1 μm^2 channel, we have patterned 100 nm x 100 nm squares with a pitch distance of 100 nm.
- For a 2x2 μm^2 channel, we have patterned 150 nm x 150 nm squares with a pitch distance of 150 nm.
- For a 5x5 μm^2 channel, we have patterned 200 nm x 200 nm squares with a pitch distance of 200 nm.

- For a 10x10 μm^2 channel, we have patterned 250 nm x 250 nm squares with a pitch distance of 250 nm.

An optical image of a 10x10 μm^2 channel is shown in figure 4.34 (a) and AFM images of a 5x5 μm^2 channel are presented in figure 4.34 (b) and (c) (larger channel dimensions were shown for better clarity).

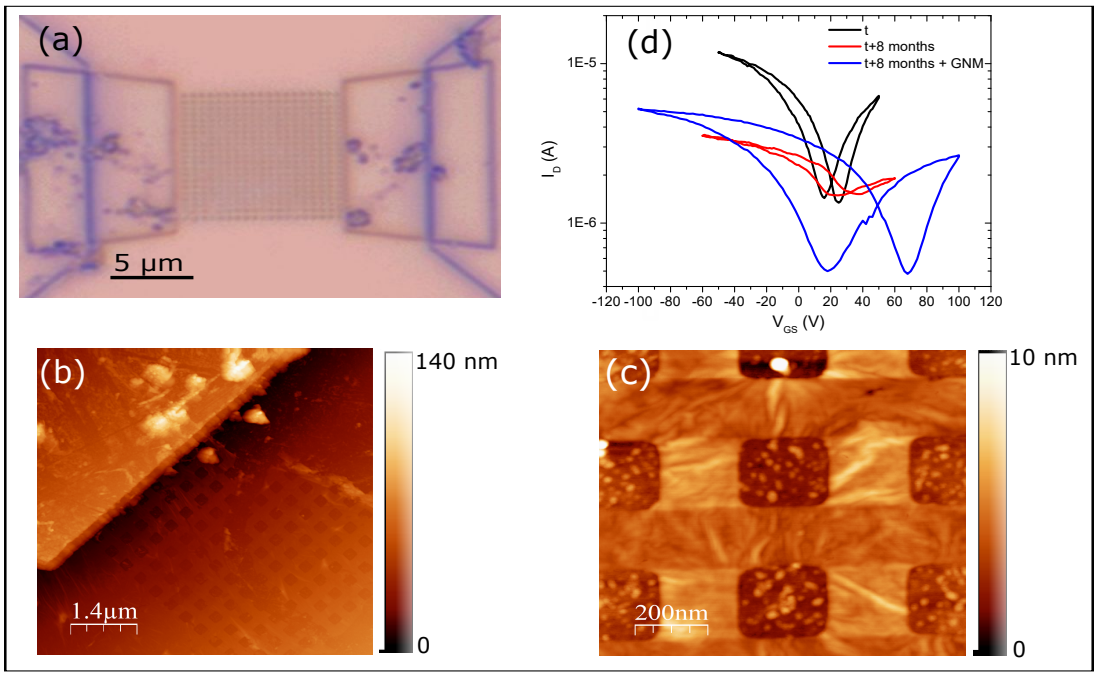

Figure 4.34: (a) Optical image of a graphene nanomesh (GNM) on a 10x10 μm^2 graphene channel. (b-c) AFM images on the same GFET showing the squared holes patterned into the graphene layer. (d) Transfer characteristics of a 1x1 μm^2 channel measured: in black: first IV in red: after 8 months and in blue: after GNM.

In figure 4.34 (c), the GNM can be clearly observed, with dark squares representing the holes "punched" into the graphene sheet. This AFM image indicates a strained graphene, since we can see wrinkles in the sheet induced by the patterning of the nanomesh. This result is expected, since by taking a relatively flat graphene sheet and perforating it, we induce defects into the graphene lattice. We must mention that the GNM did not have any effects on the electrical properties of the 2x2, 5x5 and 10x10 μm^2 channels. Thus, the electrical measurements of these devices were not shown here. However, on the 1x1 μm^2 channel, we note a very interesting observation. Figure 4.34 (d) shows the transfer characteristics of the same 1x1 μm^2 transistor, for three different cases: (i) in black we see the transfer curve of the initial GFET, measured after fabrication (and thus at a time t), (ii) in red we see the transfer curve of the same GFET after 8 months in clean room air and (iii) in blue we see the transfer curve after the patterning of the nanomesh.

If we look at the initial transfer characteristics of the GFET, (black curve) we observe a high ambipolarity and we calculate a carrier mobility of $\sim 1200\ cm^{-2}/(V.s)$ and an I_{ON}/I_{OFF} ratio of ~ 10. After 8 months of air exposure (red curve), the graphene loses its ambipolarity and carrier mobility with a slight shift in the Dirac point (an air exposure effect discussed earlier), and the new mobility is found to be $\sim 500\ cm^{-2}/(V.s)$. Similarly, the I_{ON}/I_{OFF} ratio decreased to ~ 2.3.

What is very odd and interesting in this study is the transfer curve obtained after the patterning of the graphene nanomesh (blue curve). In fact, a typical consequence of GNM is the degradation of carrier mobility, directly implying the decrease of the I_{ON}/I_{OFF} ratio. However, this is not the case here. In fact, by comparing the red curve and the blue curve, *i.e.* before and after the GNM, we observe an increase in the carrier mobility from ~ 500 to around $700\ cm^{-2}/(V.s)$ as well as an increase in the I_{ON}/I_{OFF} ratio, whose value is now equal to that of its initial value of 10. In addition, the graphene regained its ambipolarity. This unanticipated behavior could be due, as a hypothesis, to the fact that instead of inducing more defects into the graphene sheets, we have somehow created a larger mean free path for the carriers by eliminating structural defects in the sheet.

For instance, the exfoliation of carbon nanotubes (CNTs) on a target substrate creates a matrix of CNTs which are randomly distributed. It is known and confirmed through a plethora of experiments [214] that approximately 1/3 of these CNTs are semiconductor, while 2/3 are semi metal. Thus, by patterning these CNTs into ribbons connected to the contact metals, the probability of having semiconductor CNTs is 1. Much like CNTs, we assume for small channel lengths ($\leqslant 1\ \mu$m), GNM would faciliate the electron transport in the graphene sheet, which is confirmed via electrical measurements. Unfortunately, further studies on this device were not carried out for complementary findings.

Chapter 5

Towards 50 nm gate length RF GFET on parylene

5.1 Objectives of this study

As discussed in chapter 2, graphene is one of the most promising candidates for flexible electronics due to its combined high flexibility, mechanical strength, and electronic transport properties. Among plentiful of applications, high frequency electronics is considered to be a cornerstone of today's high tech economy. In this chapter, we present an investigation of the crucial steps in the fabrication of flexible radiofrequency (RF) graphene-based field effect transistors (RF GFETs). Parylene C was chosen as the flexible substrate due to its remarkable physical properties, including high flexibility and thermal and dielectric properties. The growth mechanism of parylene C as well as its properties will be presented in the first section of this chapter. Optical and structural characterization of our parylene C samples will be shown, and combined AFM and XPS measurements on Parylene C will be detailed in order to examine the topography and chemical composition of this polymer. These studies are of utmost importance since Parylene C is not much used in the electronic industry, but rather in the biomedical industry as a biocompatible and anti-corrosion material. However, it is an ideal flexible substrate for nanoscale devices as it can be simply deposited on SiO_2 substrate for e-beam lithography and fabrication processes, and easily detached from the SiO_2 by simply immersing it in DI water. Afterwards, the optimal RF design of the devices which was simulated during this thesis is discussed in details, and the fabrication process of the RF GFETs is described exhaustively, especially the gate electrode deposition since the channel lengths chosen for these microwave transistors vary from 50 to 500 nm. Later on, an intensive study on the effect of the oxide deposition method is presented, since we are working with a delicate polymer as a substrate, and many standard factors such as temperature used in the

silicon-based technology cannot be implemented here. Finally, the challenges of the fabrication of flexible devices are closely particularized.

5.2 Introduction to parylene C

In this section, a brief introduction on Parylene is presented. The chemical vapor deposition process of parylene C is described as well as some of its properties. Optical images, in addition to AFM and XPS measurements performed on parylene C substrates are carefully reviewed.

5.2.1 Parylene

Parylene, or poly(p-xylylene) is one of the most popular chemical vapor deposited thin film polymers. First discovered in 1947 by chemist Michael Mojzesz Szwarc, when he observed parylene as a product formed in the vacuum thermal decomposition (pyrolysis) of para-xylene, a common solvent. His method however only yielded a small percentage of the polymer film [215, 216]. A more efficient route was developed by William Franklin Gorham, who used a stable dimer, di-para-xylene (also known as [2,2] paracyclophane) as the base material in vacuum pyrolysis. At temperatures above 550°C and for pressures below 1 Torr, Gorham found that the dimer cleaves into two monomers, para-xylylene, which are adsorbed onto a surface at room temperature and polymerized to form a long chain of parylene thin films [217].

The principal member of the parylene family discovered by Szwarc is known as parylene N (poly(paraxylylene)). Throughout the years, many forms of parylene have branched out of parylene N such as parylene type-C,-D,-F, and -HT. These types have the same basic structure, but have replaced the aromatic or aliphatic hydrogen atoms with other atoms or chemical groups. Parylene C for example has one chlorine on the aromatic, whereas paryene D has two. The most common types of parylene are shown in figure 5.1.

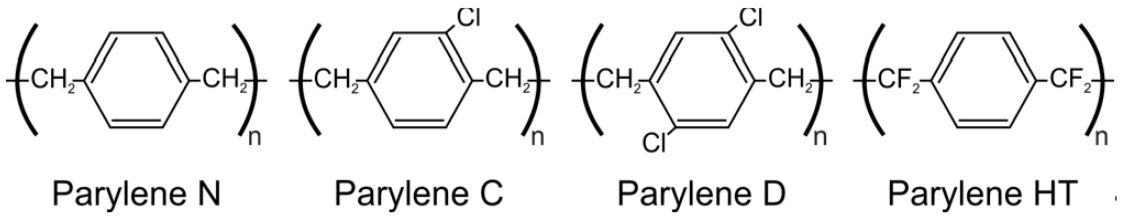

Figure 5.1: The most common types of parylene. Adapted from [218].

The exceptional interest of parylene arises from the fact that this family of polymers is the only class of polymeric hydrocarbon materials commercially produced via chemical vapour deposition (CVD) [219].

5.2.2 Chemical vapor deposition of parylene C

The schematic representation of parylene C deposition is shown in figure 5.2. Sublimation of the dimer (dichloro-di(p-xylylene) in the case of parylene C) occurs under vacuum at approximately 120°C. Then, the vaporized dimer is subjected to temperatures above 550°C and pressures lower than 1 Torr, resulting in the cleavage of the dimer into two chloro-p-xylylene monomer units. These monomers are extremely reactive, and immediately polymerize upon deposition onto a surface (SiO_2/Si in our case) at room temperature, forming parylene C.

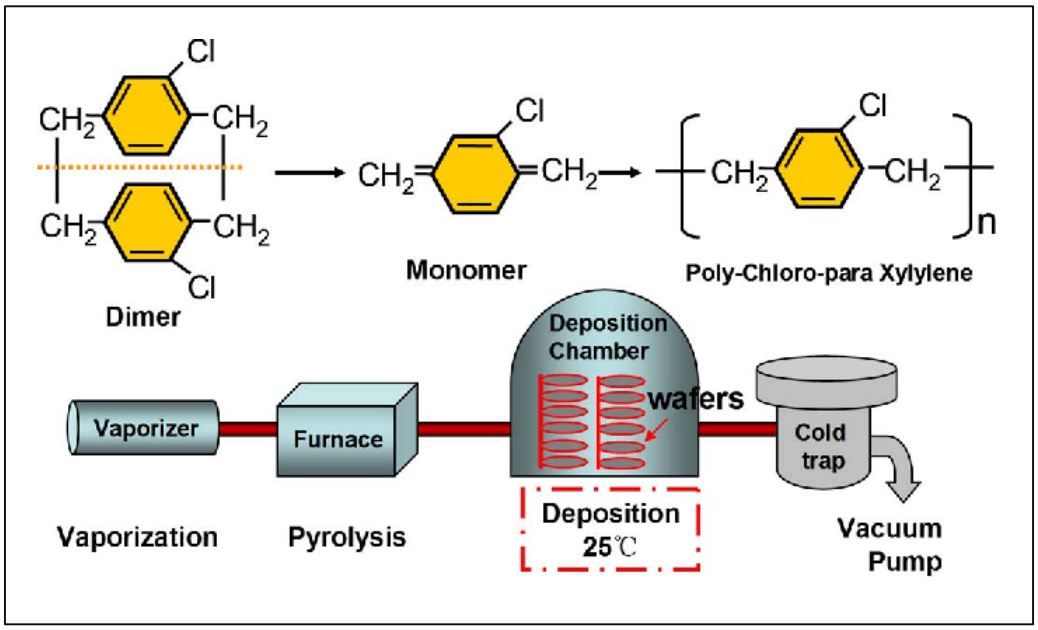

Figure 5.2: The chemical vapor deposition process of Parylene C. Adapted from [220].

5.2.3 Properties of parylene C

Parylene-C possesses many desirable properties, which make of it a very interesting material especially in the medical and electronic industries. For instance, parylene C aquires low chemical, moisture, and vapor permeability, making it particularly useful where protection is needed from corrosive gases [221]. Its chemical inertness and resistance to biological degradation allows it to be used in a variety of biomedical devices such as cardiovascular implants, wireless neural interfaces and catheters [216, 222, 223]. Designated by the United States Pharmacopeia as a Class IV polymer, parylene C possesses the highest level of biocompatibility for polymers, making it permissible for long-term implantation [216]. In addition to its biocompatibility; its biostability, low cytotoxicity and resistance against hydrolytic degradation [224, 225] have permitted the use of parylene C in micro- and nano-fabricated devices for microfluidic and bioMEMS applications [216]. When

it comes to electronic applications, parylene C have been used as a passive layer encapsulation of graphene-based field effect transistors (GFETs) [226, 227] as well as a substrate for GFETs for improved device stability [228]. Park et al [229] have used parylene C as a substrate for flexible RF electronics, whereas S. Sabri et al [230] and Levesque et al [213] from the same group have used parylene C as a gate dielectric for silicon dioxide-based GFETs, benefiting from the polymer's hydrophobicity to avoid the presence of water trapped between the SiO_2/Si substrate and the graphene flake, enhancing by that the electrical properties of the fabricated GFETs.

5.3 Structural and chemical characterization of Parylene C

In this work, 15 μm-thick parylene C was deposited onto SiO_2/Si substrates via chemical vapor deposition in the Ecole Normale Superieure - Paris (ENS Paris). The idea behind depositing a thick Parylene C film on silicon dioxide substrates is to facilitate the fabrication process, since the lithography step is very delicate and a flat substrate is critical in order to achieve the desired pattern. Since parylene C is hydrophobic, soaking the substrate for 3 to 4 hours in DI water is sufficient to delaminate the thick polymer film from the silicon dioxide substrate. In this section, structural and chemical characterization were performed on the polymer substrates to obtain a complete idea about the roughness and the chemical composition of chemical vapor deposited parylene C films.

AFM and XPS measurements were conducted at the Laboratoire de Genie Electrique et Electronique de Paris (GeePs - Gif-Sur-Yvette).

5.3.1 Optical and AFM images of parylene C substrates

Figure 5.3 (a) shows an optical image of the deposited parylene film on SiO_2/Si. bumps are observed on the surface, and their presence is due to the chemical vapor deposition process. In fact, thick films of parylene C (15 μm) are deposited in a sequence; in our case 3 μm are deposited five times in order to obtain the final film thickness. The total pressure plays an important role in the uniformity of the films, and a high pressure could induce bumps on the surface of the parylene, where strain in the film is created and is then released in the form of bumps.

AFM measurements performed on the surface of the parylene C allow us to estimate the roughness of the polymer film with a 10 to 20 % margin of error. Measurements were taken on the bumps, as shown in figure 5.3 (b), and away from the bumps as shown in figure 5.3 (c).

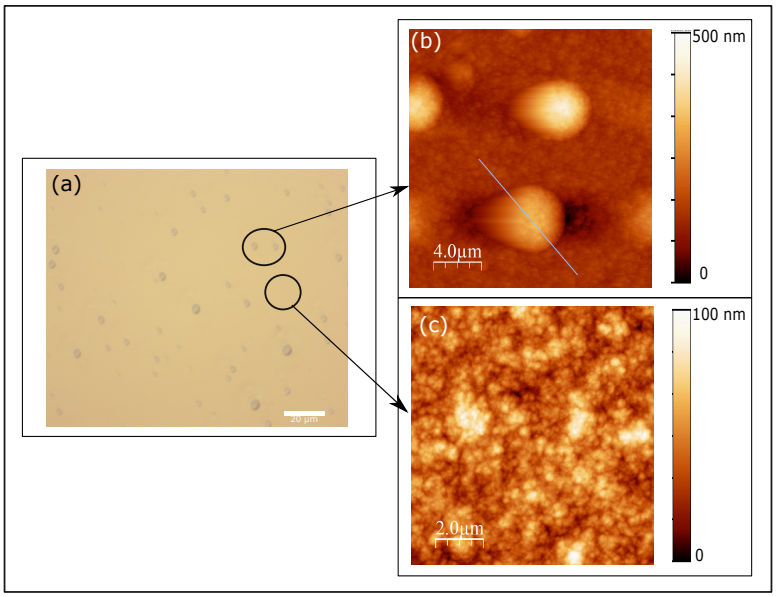

Figure 5.3: (a) Optical image of 15 μm-thick parylene C deposited on SiO_2/Si. The surface contains bumps as a result of the deposition process. (b) AFM image of a bump on parylene C and (c) AFM image of the parylene C surface away from a bump.

The bump on which we performed AFM measurements is about 250 nm high with a diameter of 6 μm, however, smaller bumps can be found on the surface. The roughness of the parylene film away from the bumps was found to be 10 nm on average.

The presence of the bumps can indeed obstruct the fabrication process, especially when depositing gate electrodes, considering that these electrodes are very thin in our case (sub 60 nm channel lengths). This subject will be detailed later on. These bumps can also complicate the transfer process, since graphene is a one-atom thick sheet and high roughness can induce cracks and folds in the graphene sheet. The graphene/substrate adhesion is also threatened by the presence of these bumps.

Furthermore, AFM measurements on parylene C substrates have showed a relatively low roughness averaging 10 nm. bumps of 250 nm height on average were also observed, potentially obstructing the fabrication steps.

These inconveniences are detailed later on.

5.3.2 Parylene C chemical composition via XPS

XPS measurements on parylene C (PC) allow us to investigate the chemical composition of the deposited polymer film, including surface contamination. Obtaining a clean polymer is very important for the conservation of the parylene's intrinsic properties. In this section, we have performed several XPS measurements in different regions on the surface of the polymer, as well as a few micrometer-deep in the surface of the film, where we intentionally scratched the surface of the polymer in order to eliminate the surface contamination as much as possible and to further examine the parylene C. The X-ray photoelectron spectrum of a $ParyleneC(PC)/SiO_2/Si$ sample is depicted in figure 5.4.

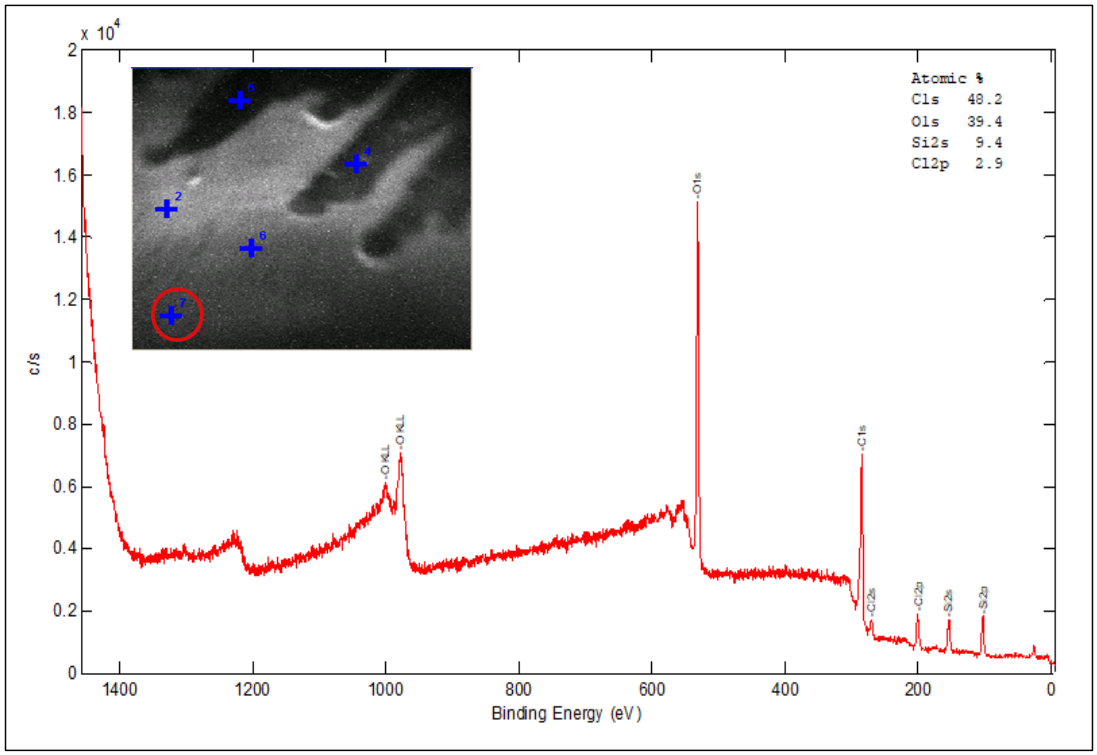

Figure 5.4: XPS spectrum of Parylene C on the surface as shown in the inset of the spectrum. The blue crosses are where different measurements were performed and the circled cross belongs to this specific XPS spectrum.

On the surface of the substrate, we observe several atomic species. C and Cl atoms belong to the parylene C, whereas O and Si atoms are clearly surface contamination. Approximately 40% of the total atomic concentration belongs to the oxygen atoms. Oxygen atoms are very abundant on the surface, and 20% of their atomic concentration can be attributed to the presence of silicon dioxide (SiO_2), since Si particles are also observed on the surface with an atomic concentration of around 10% (obtaining by that

the stoichiometry). Thus, Si and O atoms are bonded to form SiO_2. The other 20% of O atoms are C-O contamination, which can be in the form of hydroxyl groups (C-OH), carbonyl groups (C=O) or carboxyl groups (OH-C=O). This is concluded by the presence of $\sim$ 50% of C atoms, indicating that not all of the C atoms belong to the polymer, and that a % of C atoms is actually bonded to the remaining oxygen atoms in form of surface contamination. The carbon-oxygen surface contamination is typical and is due to the atmospheric environment of the samples. The Si atoms could come from the underlying substrate itself (SiO_2/Si) during the polymer deposition, or it can be due to the presence of several identical substrates in the same box, or to the handling of these samples which was conducted using the same tweezers for standard SiO_2/Si substrates. These measurements were repeated in several regions of the substrate, and we have obtained similar results in terms of atomic species and their respective atomic concentration, indicating a homogeneous deposition.

For a more specific measure of parylene C (away from surface contamination), XPS measurements were carried out on intentionally scratched areas of the PC shown in figure 5.5. The scratches were several micrometer deep. As we can see, the same species were observed (C, Cl, O and Si). However, their atomic concentration was different this time. Regarding Si and O atoms, half of the concentration was left (5% and 20% respectively) which means that there is less SiO_2 contamination in the "bulk" of the 15 μm-thick film. One possible explanation for the continuous observation of this type of contamination could be the scratching of the parylene itself, since it is a very soft material and it is very easy to scratch all the way to the underlying silicon substrate (which we have unintentionally done while scratching). The Cl atomic concentration has doubled (from 3 to 6 %), and the C atomic concentration has increased from 40 to 60 %. This means we are observing parylene C, where 1 chlorine atom possess 8 carbon atoms in a monomer (refer to figure 5.1). However, we still have a contamination coming from the C atoms. Multiple measurements were done on different scratched areas, and XPS results yielded identical results.

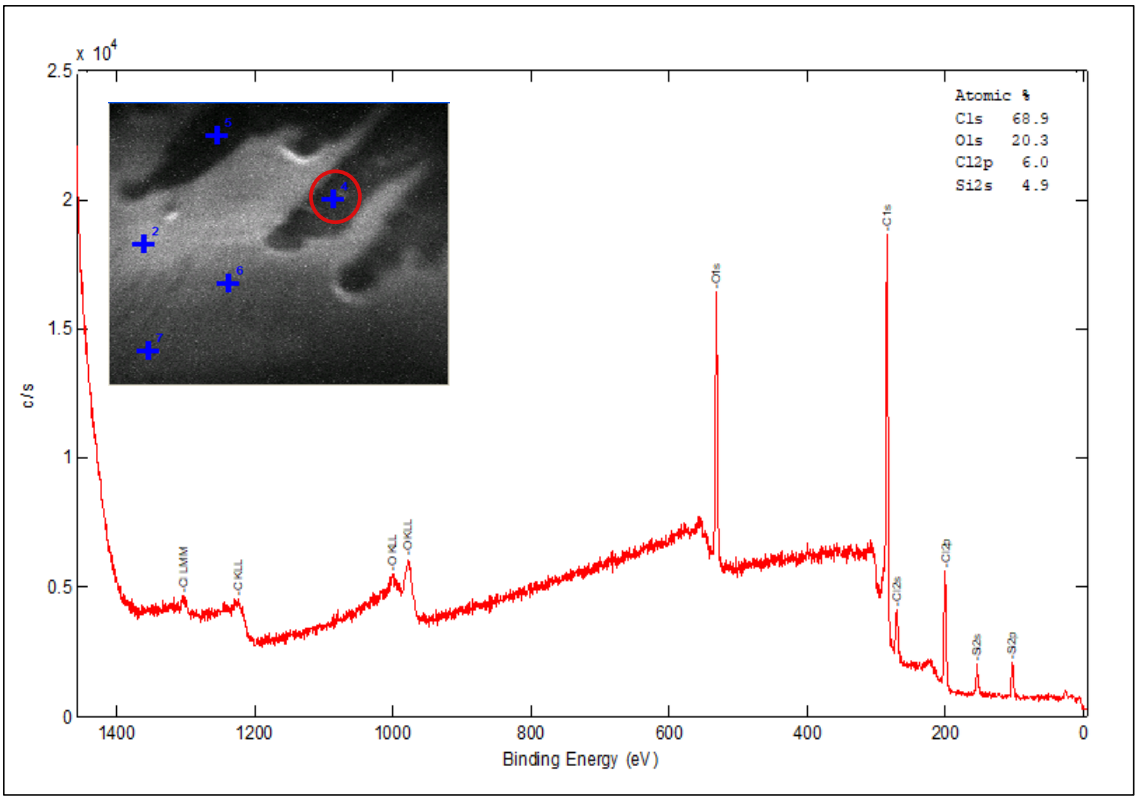

Figure 5.5: XPS measurements of Parylene C after a few scratches on the surface as shown in the inset of the graph. The circled cross is where the measurement was performed.

To conclude the XPS measurements, we have observed a relatively high SiO_2 and C-O contamination on the surface of the polymer. The carbon-oxygen surface contamination is a typical atmosphere-induced contamination, however, the SiO_2 is not standard, and could arise from the silicon dioxide substrate underneath the parylene C. This surface contamination is doubly decreased when we performed XPS measurements a few micrometer deep in the polymer film. This indicates that most of the contamination is superficial, however we still have non negligible contamination in the "bulk" of the thick parylene film.

5.4 RF devices: The design

In this work, our aim was to show the feasibility of fabricating high frequency transistors at large-scale. It is for this reason that we have not fabricated the devices directly on top of a flexible substrate, where the elasticity of the materials can hamper the industrial processes. Contrariwise, we have decided to fabricate RF devices based on CVD graphene on top of a 15 μm-thick parylene layer deposited on a SiO_2/Si wafer. Based on the study published by Park *et al.* [229] in which an easy way to detach parylene from a SiO_2 substrate

was demonstrated by immersing the hydrophobic polymer in DI water for a couple of hours, and based on the work of Sabri *et al.* [230] showing the enhancement of the ambipolarity of graphene devices deposited on top of a parylene layer, we have decided to use parylene C as a substrate for our large-scale graphene devices. In our lab (L2E), a probe station using Ground Signal Ground probes with a 100 μm pitch is available for high frequency characterization of S parameters in a coplanar waveguide with a Rohde and Schwarz ZVA67 Vectorial Network Analyzer up to 70 GHz. In order to design the correct coplanar waveguides, we performed simulations using the HP HFSS software with the great assistance of our colleagues Frederique Deshours and Georges Alquié. In order to have a 50 Ω impedance matching, the port 1 (In signal, gate side) waveguide has been designed following an online coplanar waveguide synthesis calculator. The simulations are shown in figure 5.6. The starting hypotheses were the following. The parylene C thickness is 13 μm (the reason will be stated in this paragraph) and its relative permittivity is 2.95 at 1 MHz (3.1 at 60 Hz) and loss tangent (tan δ) between 0.005 and 0.013.

In figure 5.7, the metal width W and spacing S are respectively 30 and 15 μm. These values are chosen so that the coplanar line impedance is between 49.72 Ω and 51.94 Ω respectively for a parylene thickness of 12 μm and 13 μm. Indeed, since the thickness of parylene depends on the etching of several microns from the initial 15 μm-thick layer in order to create C-OH bonds which render the polymer hydrophilic, we have decided to choose dimensions where the input impedance does not excessively vary.

In order to keep the best impedance match until the graphene layer where the metal width W dimension reaches 4 μm, a taper has to be designed. In this thesis, we have decided to study three different lengths shown in figure 5.6. The lengths are $L_1 = 50$ μm (figure 5.6 (a)), $L_2 = 25$ μm (figure 5.6 (b)) and $L_3 = 12.5$ μm (figure 5.6 (c)). For each of these three lengths, simulations were carried out on parylene C (figure 5.6 (d)) alone and on 13 μm parylene deposited on top of 260 nm-thick SiO_2 (figure 5.6 (e)). In the first case, a spacing of 5 μm between the metal width and the ground pads is calculated at the arrival of the three tapers on parylene and a spacing of 3 μm is calculated at the arrival of the three tapers on $parylene/SiO_2$.

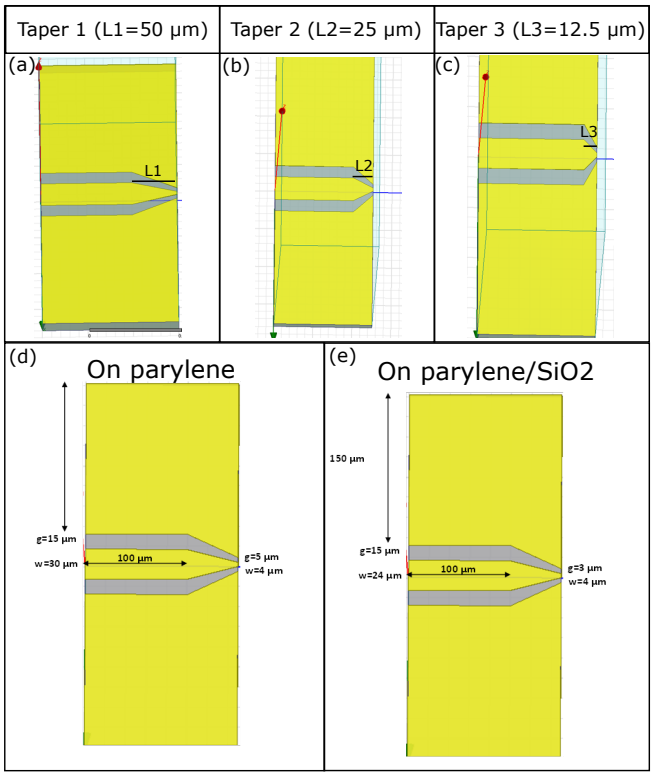

Figure 5.6: Coplanar waveguide simulations of (a) a taper length of 50 μm (b) a taper length of 25 μm (c) a taper length of 12.5 μm (d) a parylene substrate and (e) a parylene/SiO_2 substrate.

Simulations were performed for frequencies ranging from 1 to 10 GHz. Figure 5.7 (a-b) shows the reflection coefficients for the CPW (from left to the right of the design) on parylene and the CPW on $parylene/SiO_2$. All three results are highly satisfying since they are well below the -10 dB which is the characteristic value for impedance mismatch. On parylene, it can be seen that between 1 and 10 GHz, the reflection coefficient values vary from -37 dB to -30 dB for taper 1, from -40 dB to -32 dB for taper 2 and from -42 dB to -33 dB for taper 3. As the relative permittivity of parylene is slightly dependent on the frequency, we can estimate an increase of 8 dB per decade in the S_{11} reflection coefficient, leading to an impedance mismatch at around 40 GHz. In conclusion, taper number 3 is found to be the best geometry in order to reduce the reflection coefficient as much as possible in our coplanar waveguide. However, the differences are very slight between the three designs.

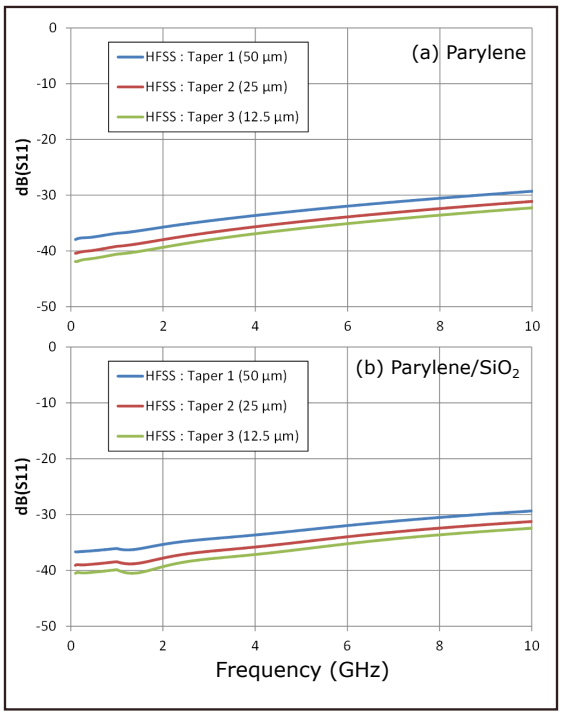

Figure 5.7: The reflection coefficients for the coplanar waveguides (a) on parylene and (b) on parylene/SiO_2.

We can now complete our coplanar waveguide between the gate input (G) and the drain output (D) as it is shown in figure 5.8 (1). The source of the transistor is chosen as the ground signal for designing a Ground Signal Ground geometry. Figure 5.8 (2) is a zoom in of the radio-frequency graphene field effect transistor. At the end of the taper, the gate input is divided in two parallel gate electrodes. We decided to implement a gate length varying from 50 nm to 500 nm, which we will be show later on in this chapter. We designed a dual-fingered device with total length between 20 μm and 50 μm. Indeed, using relation (1.1), we have calculated the total width for a classical FET operation with MOSFET technology with a graphene mobility and oxide layer of our choice. For instance, with a graphene mobility of 2700 $cm^{-2}/(V.s)$, $V_T = 1$ V, and for an Al_2O_3 oxide layer with $t_{ox} = 15$ nm and $(\varepsilon_r)_{Al_2O_3} = 9$, our GFET should provide a current of 15 mA at a source voltage of 0.6 V and a gate-source voltage of 5 V.

The relation (1) gives a value at around 24 μm for a gate length of 50 nm and 80 μm for a gate length of 100 nm. Then, the 2 x 12 μm is an example that can be done with a dual fingered device.

$$W = \frac{LI_D}{\mu_n C_{ox}(V_{GS} - V_T)V_{DS}} \tag{5.1}$$

For purposes of de-embedding high frequency data, standard “open” and “short” test devices have been designed.

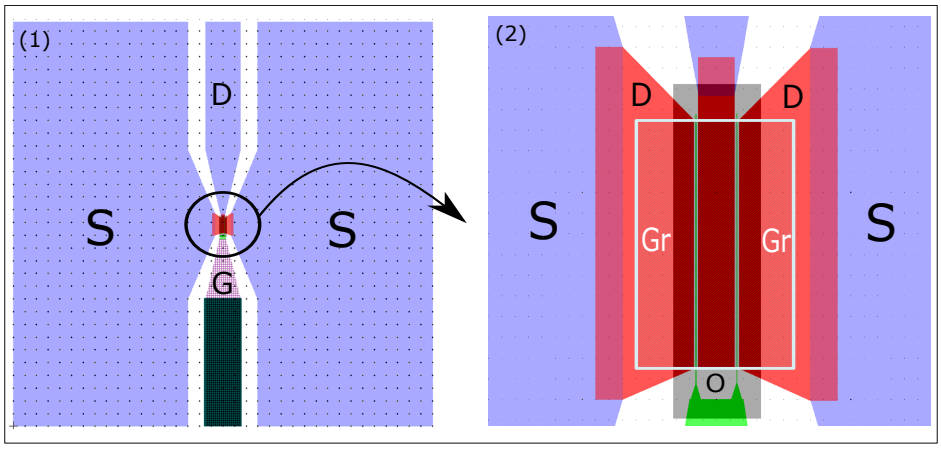

Figure 5.8: Schematic of the RF design (1) the entire RF transistor and (2) a zoom in on the channel area.

5.5 The fabrication process

Identically to the fabricated GFETs, the fabrication process of the RF devices was performed using electron-beam lithography (EBL). 950K PMMA was used as a positive resist, and MaN 2405 as a negative resist. Since the substrate is a thick polymer film, a 30 nm-film of aluminum (Al) is deposited on top of the resist before each lithography step in order to perform a correct lithography. Complementary fabrication processes (RIE, EBPVD) were also performed, as well as SEM characterization of the thin gates.

In this work, gate lengths varying between 50 and 500 nm were chosen (50, 100, 200, 300, 400 and 500 nm), with a constant gate width of 12 μm for all the devices.

The fabrication process thus comprises of 7 steps:

1. Small gate deposition: this part of the gate (shown in figure 5.8 in green) is patterned first, using a 190 nm-thick PMMA resist baked for 25 min at 170°C. 30 nm of Al is then deposited by EBPVD. After the lithography, the aluminum is dissolved using sodium hydroxide ($NaOH$, 10g/mL, 1min 30s) and then rinsed in DI water for 2 minutes. The resist is developed for 45s in a mix of MIBK and IPA and the substrate is subsequently rinsed in IPA for 30 seconds. Afterwards, 2/40 nm of chromium/gold (Cr/Au) is deposited and the lift off is carried out in acetone for 1 hour. Finally, the substrate is rinsed in IPA and dried using a $N2$ gun.

2. Large Gate deposition: since the dimensions of this segment of the gate is larger than that of the small gate (already deposited), we need thicker PMMA for the patterning and hence another lithography process. For this step, 600 nm-thick PMMA is spin coated and baked and Al is deposited prior to the lithography. After the patterning of the large gate and dissolving the aluminum film, the resist is

developed for 1 minute and Ti/Au (20/200 nm) is deposited as the large gate metal. We now have a complete gate electrode.

3. Oxide deposition: for this step, aluminum oxide (Al_2O_3) was chosen as the high-k gate dielectric with a thickness of 20 nm. This step is heavily discussed in the second part of this chapter, since the deposition technique (atomic layer deposition, ALD) had some effects on the parylene surface. The oxide was finally deposited by evaporation using a MEB 800 plassys system.

4. Graphene transfer: graphene was transferred on the Al_2O_3 by the PMMA-assisted wet transfer technique, and was characterized by Raman spectroscopy.

5. Channel definition: for this lithography step, MaN 2405 (600 nm, baked on a hot plate for 1 minute under 90°C) was used in order to protect the graphene channels of the devices. The unwanted graphene was etched away using oxygen plasma (10W, 40s).

6. Small drain and source deposition: the reason behind dividing the drain and source electrodes into two separate lithography processes is the metal choice for contacting graphene. In fact, we have found that palladium is a good choice of contact electrode with the graphene (refer to chapter 3). Thus, this step requires a Pd/Au deposition and therefore a precise lithography.

7. Large drain and source deposition: in this step, the metals chosen to cover the larger part of the source and drain electrodes were Ti/Au. This part of the electrodes will not be in contact with the graphene since it will be etched away via oxygen plasma before depositing the Ti/Au.

A schematic representation of an RF device is shown in figure 5.9.

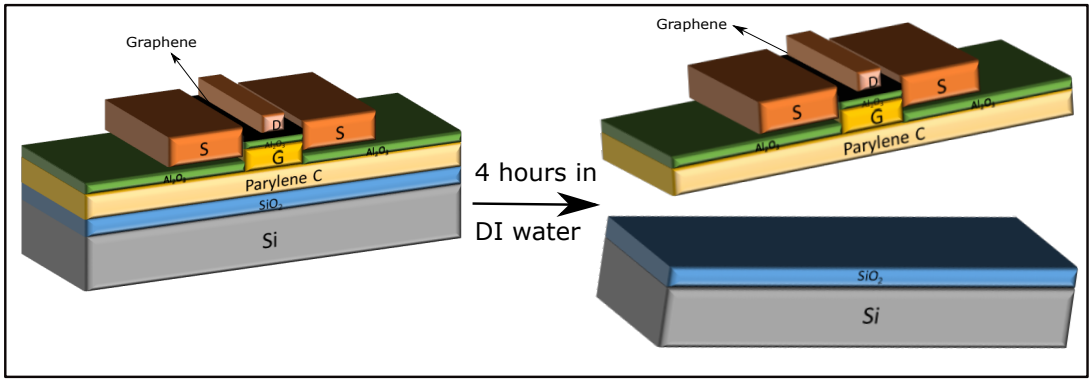

Figure 5.9: Schematic representation of an RF device on a parylene C substrate. The hydrophobic nature of parylene C allow us to easily delaminate the parylene C from the underlying SiO_2 by immersing in DI water.

5.6 Gate electrode deposition

5.6.1 Small gate electrode: dose test

In order to fabricate gate lengths of 50 nm, we carried out a dose test on a $PC/SiO_2/Si$ substrate by patterning a matrix of gates while varying the dose of the electron beam from 700 $\mu C/cm^2$ to 5650 $\mu C/cm^2$ with an increment of 50 $\mu C/cm^2$. This test will allow us to determine the optimum fabrication parameters (the e-beam dose, resist development time and lift off result) for obtaining a continuous gate with a uniform thickness. The SEM images of some of the gates is shown in figure 5.10. For 50 nm channel lengths, doses lower than 2000 $\mu C/cm^2$ did not give rise to the channels, and doses higher than 2700 $\mu C/cm^2$ resulted in enlarged channel lengths around 70 - 80 μm. For 100 nm channel lengths, the lowest dose resulting in a complete gate was 1650 $\mu C/cm^2$, whereas doses between 2300 $\mu C/cm^2$ and 5650 $\mu C/cm^2$ resulted in channel lengths of 110 nm to 160 nm (respectively). In summary, as the channel lengths increased from 50 to 500 nm, the required dose to obtain a complete gate decreased. The dose range for obtaining all the required channel lengths was between 2150 $\mu C/cm^2$ and 2300 $\mu C/cm^2$. Therefore, for the devices, we chose to operate with a dose of 2150 $\mu C/cm^2$.

In figure 5.10, we can see examples of some of the succeeded and failed channel lengths. Figure 5.10 (a-c) show channel lengths of 400, 300 and 100 nm respectively, whereas figure 5.10 (d) shows an example of a broken or discontinuous 50 nm channel. Figure 5.10 (e-f) show continuous channel lengths of $\sim$ 56 nm.

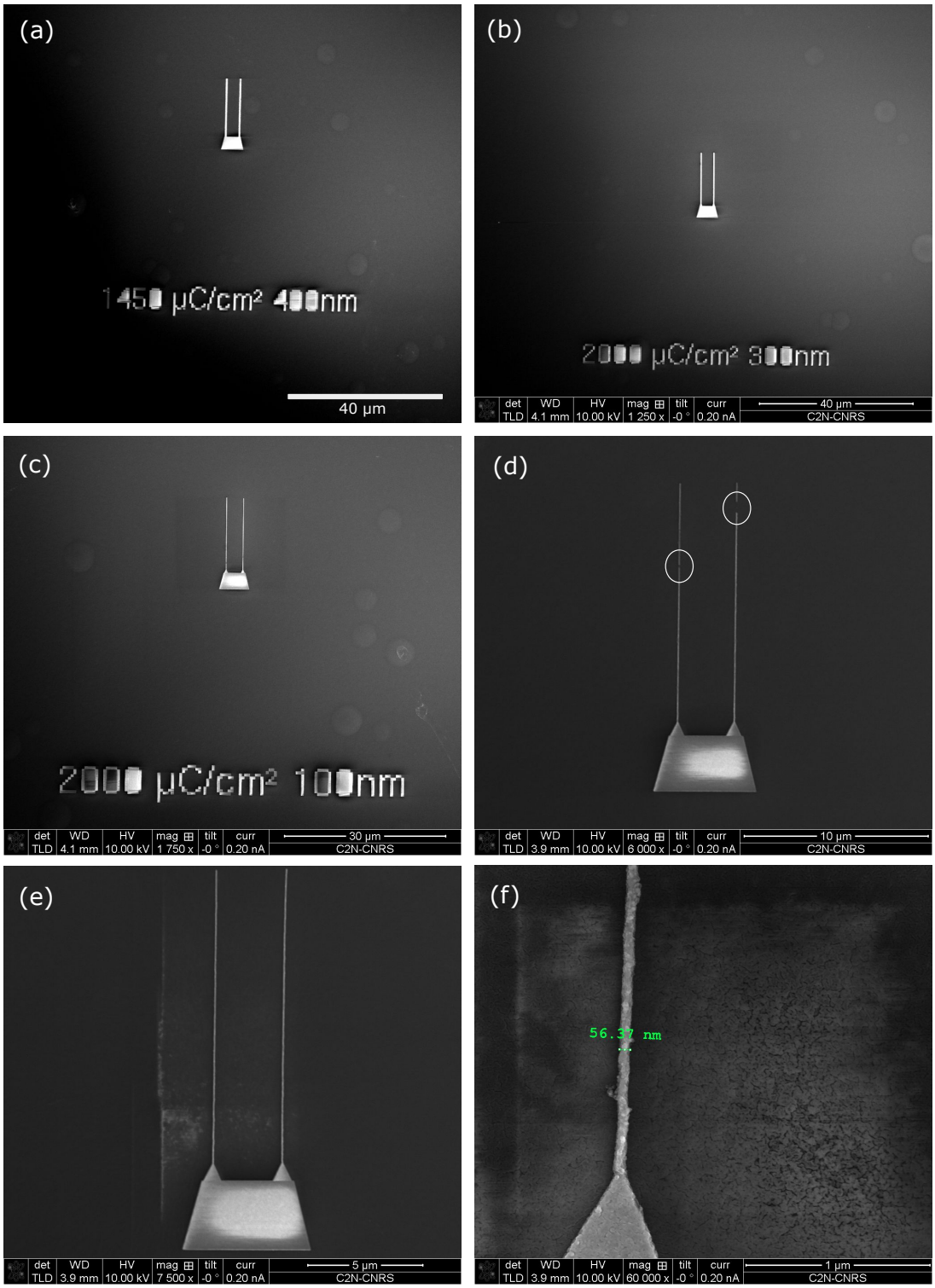

Figure 5.10: SEM images of the test dose carried out on $PC/SiO_2/Si$ for different channel lengths.

5.7 Small gate electrode

Now that we have determined the appropriate dose for the lithography, the small gates are patterned and the 50 and 100 nm channels are shown in figure 5.11.

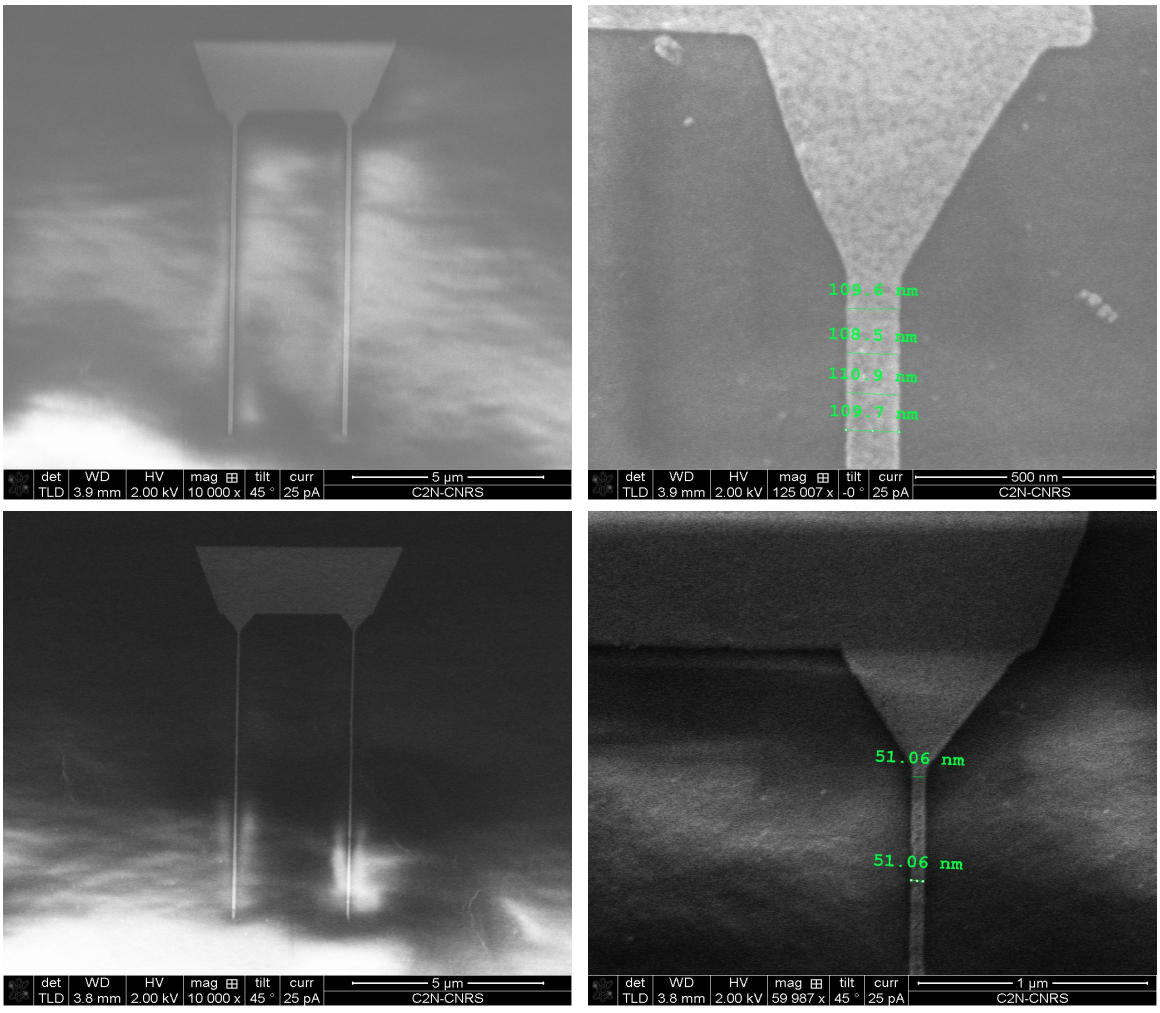

Figure 5.11: SEM images of 100 nm (top) and 50 nm (down) gate lengths on parylene C.

5.7.1 Large gate electrode

Figure 5.12 shows SEM images of complete gates. The bumps on the parylene C are clearly visible, however, it can be seen that there was no effect of those bumps on the channels, which can be seen smoothly crossing a bump.

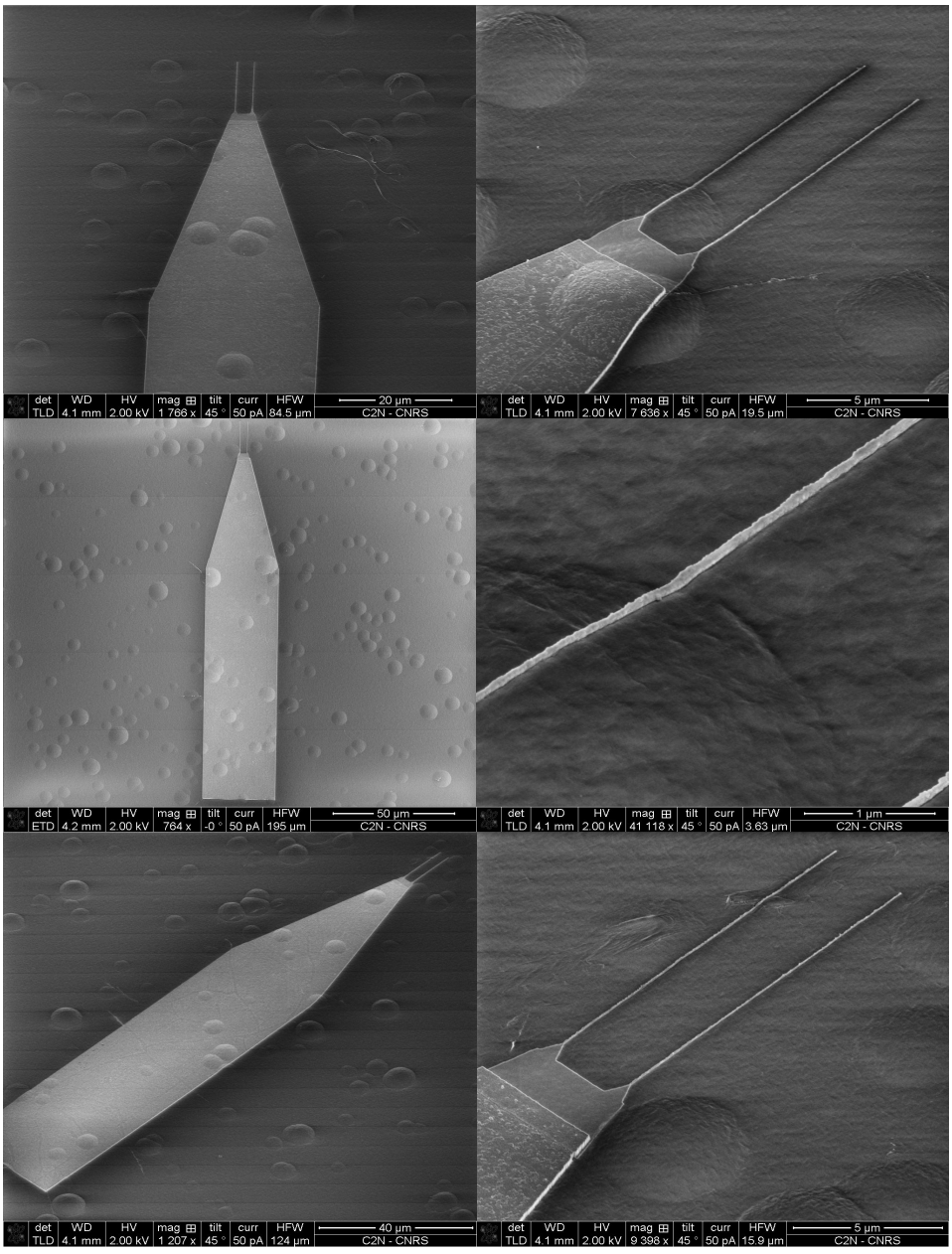

Figure 5.12: SEM images of complete gates on parylene C.

5.8 Atomic layer deposition of Al_2O_3 on parylene C

Atomic layer deposition (ALD) of Al_2O_3 on parylene C substrates was performed at 100°C under 10^{-1} Torr. The precursors used to deposit the oxide were trimethylaluminum (TMA) ($(Al_2(CH_3)_6$, which is a dimer) and H_2O. The deposition rate is 1 Å/cycle. Every cycle (60 seconds) is comprised of one pulse of TMA of 0.06 seconds followed by 30 seconds of purge, then 1 pulse (0.06 seconds) of H_2O followed by another 30 seconds of purge. During the purging, argon is pumped into the chamber to eliminate any by-products or unreacted gases. In addition, a duration of 20 minutes of thermalization is required before every deposition. For instance, it takes approximately 5 hours to deposit an oxide thickness of 30 nm.

5.9 XPS measurements of Al_2O_3 deposited on a reference sample

In order to calibrate the XPS measurements which will be performed on parylene C, we have deposited (using ALD) 26 nm of Al_2O_3 on $Au(200nm)/Ti(50nm)/PC/SiO_2/Si$ as a reference sample. In fact, since we do not know the etch rate, we cannot manipulate with the real samples. Thus, we use a reference sample with a known oxide thickness in order to find the etch rate and use it on the real samples. The exact thickness of the reference sample was confirmed to be 26 nm via ellipsometry. Figure 5.13 shows the XPS spectrum of Al_2O_3 on Au.

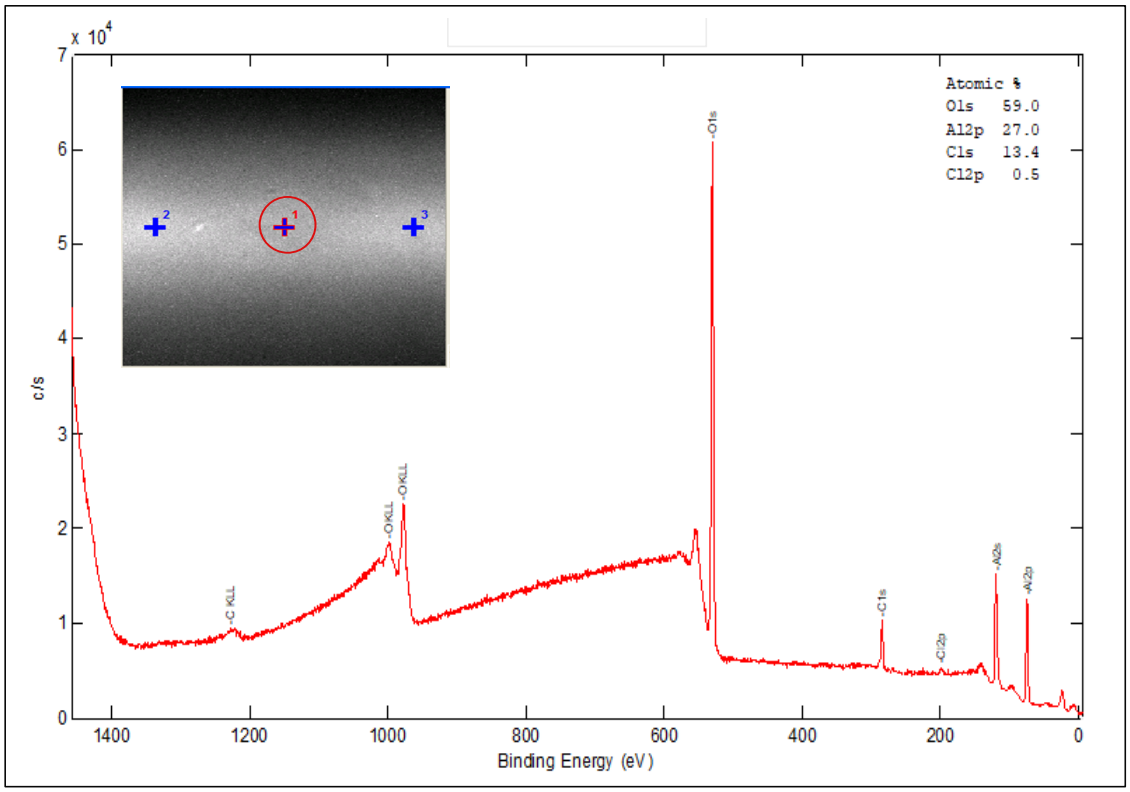

Figure 5.13: XPS spectrum of Al_2O_3 (26 nm) deposited on Au/Ti on Parylene C via ALD. Inset is a SEM image of the measurement region. The blue crosses indicate the different measurement zones and the red circle indicates the corresponding measurement of this spectrum.

The XPS spectrum confirm the presence of Al_2O_3 with a 27% atomic concentration of Al and a 70% atomic concentration of O. To obtain the stoichiometry of the oxide, we should have 40% of oxygen, which means we have an additional 20% acting as surface contamination. C atoms (13.4%) as well as Cl atoms (0.5%) are also observed on the surface. This indicates a typical atmospheric carbon-oxygen contamination. However, the presence of chlorine, although low, is not normal. It can be due to the tweezers or any other clean room handling of the samples. XPS measurements were taken in several regions of the sample (in the center of the sample and on the corners). All of them yielded similar results, indicating a homogeneous and continuous oxide along the surface of the test substrate.

To confirm the thickness of the deposited oxide, the XPS depth profile is shown in figure 5.14.

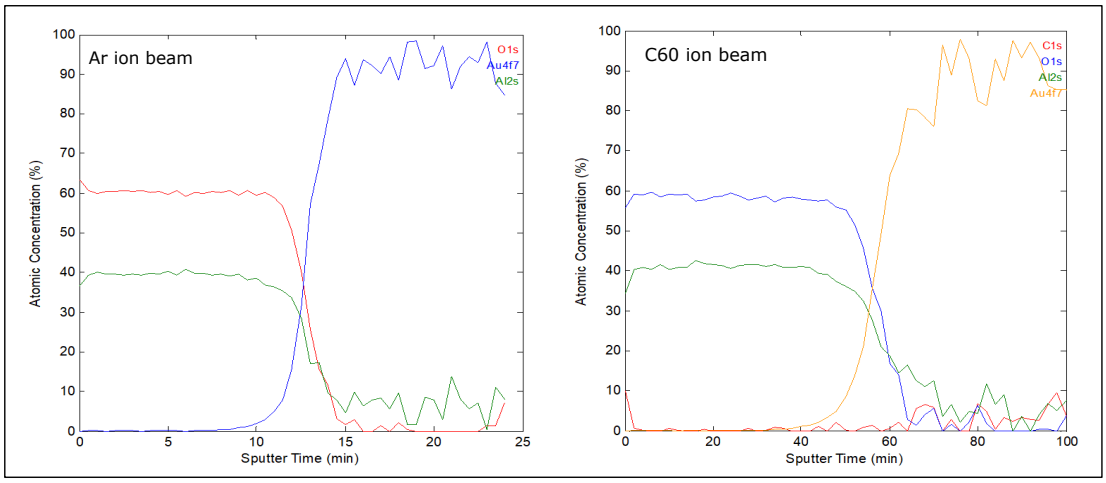

Figure 5.14: XPS depth profile of Al_2O_3 (26 nm) deposited on Au/Ti on Parylene C via ALD using Ar (left) and C60 (right) ion beams).

For the Ar sputtered region, we have obtained an average atomic concentration of $\sim 60.1\%$ of O in Al_2O_3 and $\sim 39.7\%$ of Al with a very low incertitude (less than 1%) which gives a O/Al ratio of ~ 1.51. The sputter time (also known as the sputter depth) is found to be $\simeq 12.9$ minutes (the inflection point) for an oxide thickness of 26 nm which indicates an etch rate of 2.02 nm/min.

For the C60 (fullerenes) sputtered region, we have found an average of 58.4% of O in Al_2O_3 and 41.2% of Al with an incertitude lower than 1%, which yields a O/Al ratio of ~ 1.42. The sputter time is $\simeq 58.08$ minutes for 26 nm thus the etch rate is $\simeq 0.448$ nm/min.

Now that we have determined the etch rate, we can perform XPS measurements on Al_2O_3 deposited on PC substrates. We should mention that the sputter time in the case of the C60 ion beam is much bigger than that of the Ar ion beam, and the reason for that is because the C60 beam is much softer than the Ar beam, which translates into a longer sputter time.

5.10 AFM and XPS measurements of ALD deposited Al_2O_3 on parylene C

5.10.1 AFM measurements of ALD deposited Al_2O_3 on parylene C

Now that we have calibrated the XPS measurements on a reference substrate, we have deposited 30 nm of Al_2O_3 on a $paryleneC/SiO_2/Si$ substrate via ALD. AFM measurements were performed on the deposited oxide, and are shown in figure 5.15 (a). Simultaneously, we have deposited Al_2O_3 on SiO_2/Si substrate as a reference sample. The AFM image of Al_2O_3 on SiO_2/Si is shown in figure 5.15 (b).

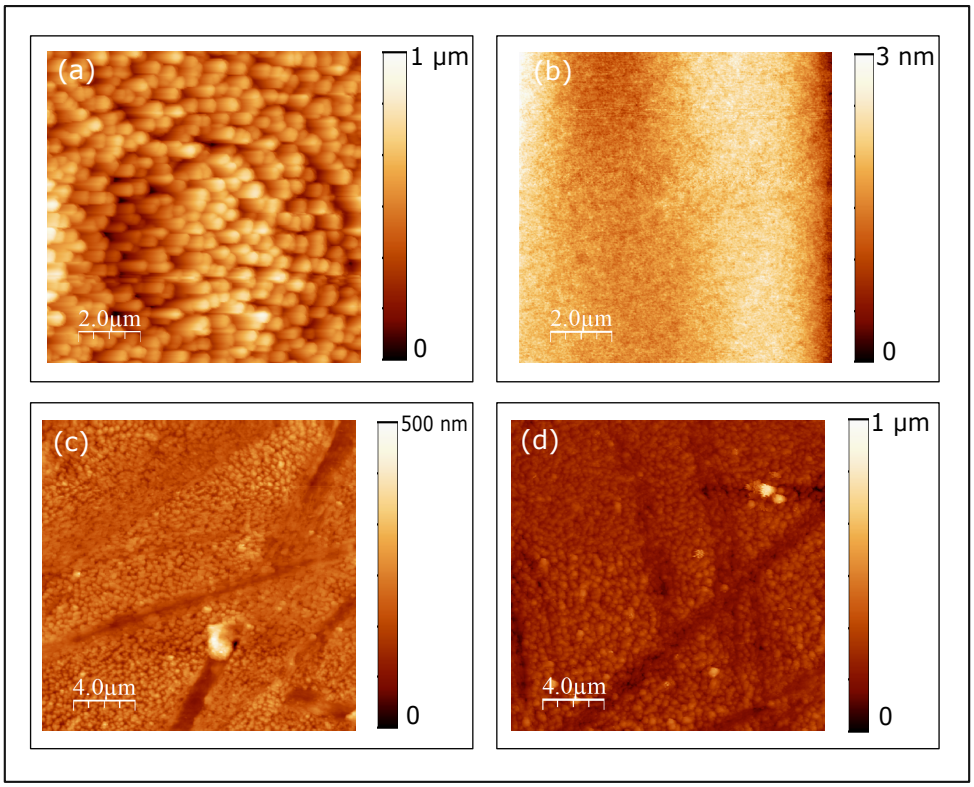

Figure 5.15: AFM images of (a) Al_2O_3 deposited on parylene C by ALD (b) Al_2O_3 deposited on SiO_2/Si by ALD (c) Parylene C annealing without actually depositing Al_2O_3 for the full deposition time ($\sim$ 5 hours) and (d) Parylene C annealing without actually depositing Al_2O_3 for half of the deposition time ($\sim$ 2.5 hours).

Figure 5.15 (a) represents the AFM image of $Al_2O_3/PC/SiO_2/Si$. As it can be seen, the atomic layer deposition of Al_2O_3 ($\sim$ 5 hours) on parylene C has strongly affected the morphology of the polymer. The surface of the parylene C has vigorously changed, and it seems the polymer has become porous and its surface is filled with "nanopillars". An average roughness of 110 nm was measured on the surface of the sample, which indicates the average depth of these nanopillars.

Figure 5.15 (b) shows the AFM image of Al_2O_3 deposited on SiO_2/Si via ALD. The very low measured roughness (0.3 nm) is that of the silicon dioxide substrate. This underlines the effect of the substrate on the deposition of the oxide. Indeed, these AFM measurements show a smooth deposition of aluminum oxide on silicon dioxide compared to a very rough polymer surface with nanopillar-shaped structures on the surface when manipulating with a temperature-sensitive soft polymer.

In order to understand more about this peculiar result, atomic layer deposition was carried out on two parylene C substrates without actual deposition of the oxide. Figure 5.15 (c) demonstrates the AFM image of the surface of the parylene C annealed for $\sim$ 5 hours (i.e. the entire ALD time for depositing 30 nm oxide)

without depositing the oxide, and figure 5.15 (d) shows the AFM image of the parylene C annealed for half of the deposition time ($\sim$ 2.5 hours). It is clear that the long-term temperature has its influence on the roughness of the parylene C, as it had increased its roughness to 40 nm for an annealing of 5 hours and to 30 nm for an annealing time of 2.5 hours (compared to its initial roughness of 10 nm). However, the nanopillars did not appear without the deposition of Al_2O_3. Thus, the oxide must have caused the appearance of such structures.

To verify if the oxide was deposited, and to interpret these AFM findings, we have conducted a series of XPS measurements on the Al_2O_3/parylene C sample.

5.10.2 XPS measurements on deposited Al_2O_3 on parylene C

XPS measurements of the Al_2O_3/parylene C sample were carried out in order to prove not only the presence of oxide on the polymer, but to also measure the deposited thickness. Figure 5.16 presents the XPS spectrum of $Al_2O_3/PC/SiO_2/Si$.

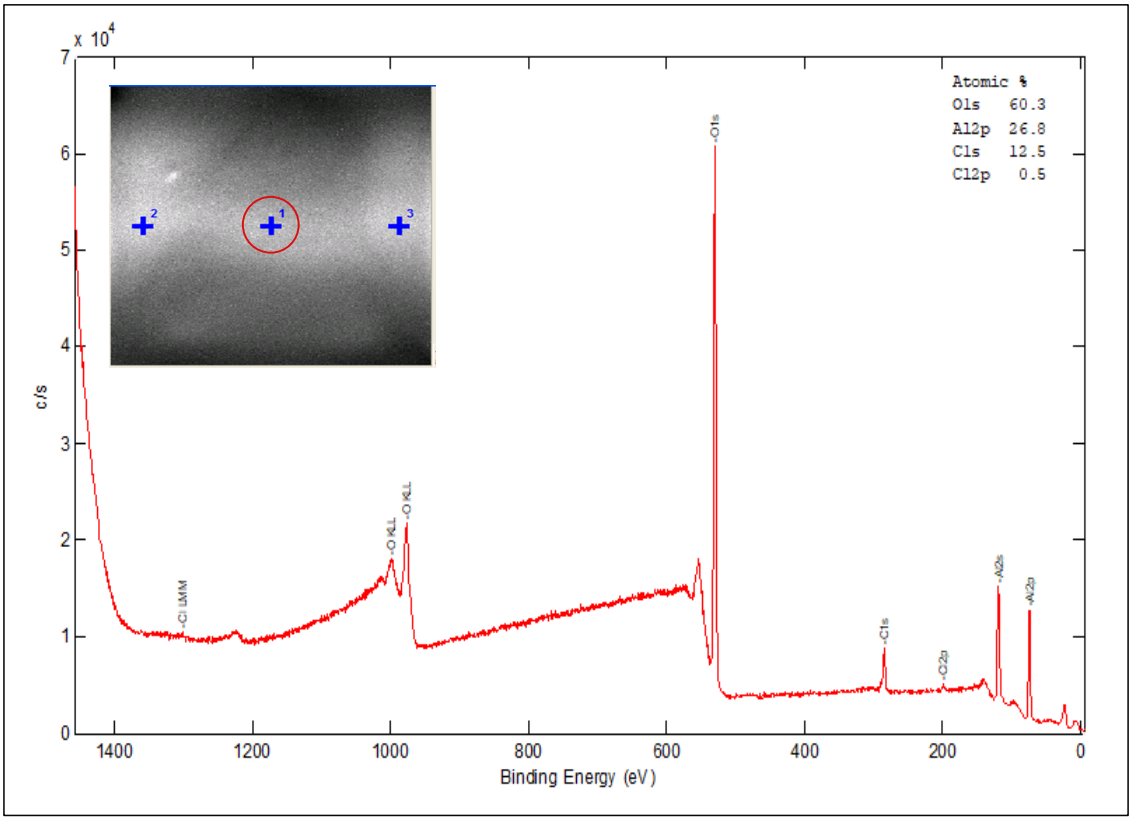

Figure 5.16: XPS spectrum of Al_2O_3 deposited on Parylene C via ALD. Inset is a SEM image of the measurement region. The blue crosses indicate the different measurement zones and the red circle indicates the corresponding measurement of this spectrum.

The presence of Al and O species in the XPS spectrum indicates the presence of Al_2O_3 on the PC. Carbon atoms are also present on the surface, showing once again the standard carbon-oxygen contamination originating from the atmospheric environment. Cl particles are also detected with a low atomic concentration. Since we have performed several XPS measurements in multiple regions on the sample, we are confident that the oxide is deposited homogeneously on the entire surface.

Considering we have a very low chlorine concentration on the surface, we can indeed consider the deposition of aluminum oxide to be very clean and uniform and the samples (the reference and the actual sample) to be clean and impurity-free. This highlights the main advantage of the ALD technique, which is a very clean and uniform deposition process.

To obtain the thickness of the oxide, the XPS depth profile using Ar ion beam is performed and shown in figure 5.17.

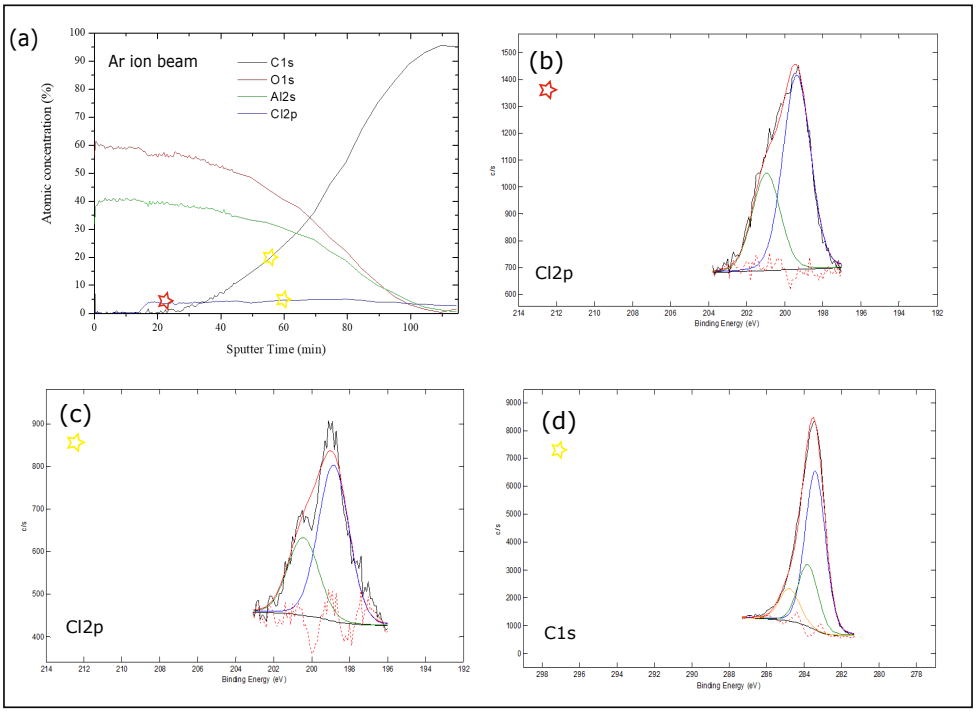

Figure 5.17: (a) XPS depth profile of $Al_2O_3/PC/SiO_2/Si$ using an Ar ion beam with a theoretical thickness of 30 nm. (b) and (c) XPS of the Cl2p peak measured (and fitted) at the red star and the yellow star in (a) respectively. (d) XPS spectrum of the C1s peak.

Figure 5.17 (a) shows the XPS depth profile of the Al_2O_3/PC sample performed using an Ar ion beam. We can see that the Al and O concentrations verify the redox equation. Nonetheless, the oxide remains detectable for a very long time ($\sim$ 100 minutes), resulting in a thickness of $\sim$ 144 nm, which is far beyond the theoretical deposited thickness (30 nm). Interestingly, the Cl species which normally belong to the parylene

C substrate, appear after 15.5 minutes of sputtering (which corresponds to 31 nm in thickness), however, the carbon layer appears after 27 minutes of sputtering, and strangely, its atomic concentration does not stabilize before 100 minutes of sputtering time. These findings are consistent with the AFM measurements performed on Al_2O_3/PC. In fact, during the deposition of Al_2O_3, the nanopillars were formed, and consequently, the oxide covered the surface of the nanopillars, resulting in the thickness of 30 nm (theoretical deposited thickness) confirmed via XPS by the presence of Cl at $\sim$ 30 nm. Simultaneously, the oxide covered the entire nanopillars in depth, which we have observed via XPS with the oxide thickness of $\sim$ 144 nm (when the oxide had disappeared after $\sim$ 100 minutes). This result is consistent with our previous AFM measurements where we found an average roughness (and thus nanopillar depth) of $\sim$ 110 nm.

Nonetheless, the carbon atoms did not appear simultaneously with the Cl particles as it was expected for parylene C since it is mainly comprised of C and Cl atoms. This finding is rather odd. We speculate that the oxide had reacted with the parylene C during the deposition. In order to verify this, we have plotted the Cl2p peak before the detection of C atoms (red star in figure 5.17 (a)) and after the detection of C atoms (yellow star in figure 5.17 (a)). The typical Cl2p peak is a double peak found at binding energies of 199 eV (Cl2p3/2) and 201 eV (Cl2p1/2) [190]. Interestingly, before the appearance of the carbon layer, the Cl2p peak was detected as a single peak, as it is shown in figure 5.17 (b). This single peak can be deconvoluted into two components with binding energies of 199.37 eV and 200.97 eV. The Cl2p double peak is found after the detection of carbon atoms, with binding energies of 198.84 eV and 200.44 eV, and is shown in figure 5.17 (c). Figure 5.17 (d) shows the carbon C1s peak measured at the yellow star in figure 5.17 (a). Typically, the C1s peak is a single peak with a binding energy of $\sim$ 285 eV [190]. In our case, the C1s peak is broadened and can be deconvoluted into three peaks with binding energies of 283.40 eV, 283.79 eV and 284.79 eV.

This change in the Cl2p and C1s peak shape and shift in binding energies imply that the Cl and C atoms (and hence the parylene C) have indeed reacted with the aluminum oxide during the ALD process.

In order to verify these results, we have performed similar measurements on the same sample using a C60 ion beam. The results are shown in figure 5.18. Figure 5.18 (a) presents the XPS depth profile of Al_2O_3 on parylene C. The Al_2O_3 layer disappears after 229.6 minutes of sputter time, which corresponds to a total oxide thickness of $\sim$ 103 nm. This is consistent with our AFM measurements and our previous XPS results. The Cl atoms appeared after 78.7 minutes of sputtering, which corresponds to a thickness of 35 nm.

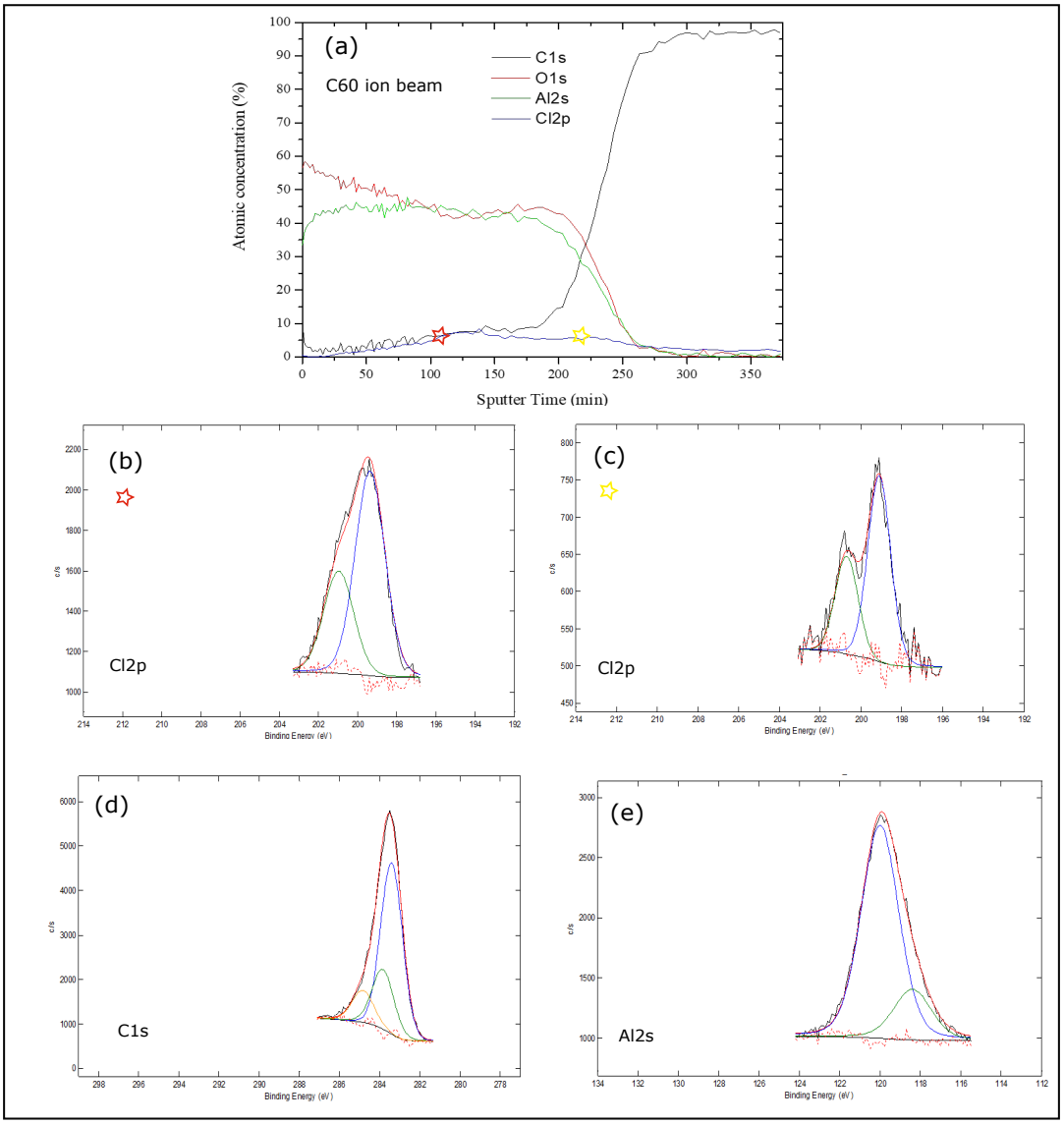

Figure 5.18: XPS depth profile of $Al_2O_3/PC/SiO_2/Si$ using a C60 ion beam with a theoretical thickness of 30 nm. (b) and (c) The Cl2p peak measured (and fitted) at the red star and the yellow star in (a) respectively. (d) XPS spectrum of the Al2s peak.

The carbon atoms appear at $\sim$ 100 minutes, and stabilize after $\sim$ 300 minutes (around 130 nm). The Cl2p peaks before (red star) and after (yellow star) the detection of C atoms are plotted and shown in figure 5.18 (b) and (c) respectively. As expected, and consistently with the previous XPS results obtained using an Ar ion beam, the Cl2p peak is detected (at the red star) as a single peak which can be deconvoluted into two components observed at 199.36 eV and 200.96 eV. However, after the detection of a significant

concentration of C atoms, the Cl2p peak measured (yellow star) was indeed a typical double peak, observed at 199.10 eV and 200.70 eV in our case. This change in peak shape and shift in binding energies of the Cl2p peak confirm the reaction between the Cl atoms with the aluminum oxide during deposition. The C1s peak is plotted in figure 5.18 (d). As expected, the single peak can be deconvoluted into three peaks of binding energies around 283.40 eV, 283.83 eV and 284.83 eV. This indicates that the carbon atoms are also reacting with the oxide, proving the reaction between parylene C and Al_2O_3.

To further verify this, we have measured the Al2s peak shown in figure 5.18 (d). A typical Al2s peak is a single peak found at $\sim$ 118 eV in Al_2O_3 [190]. In our case, this peak can be deconvoluted into two components, with binding energies of 118.40 eV and 120.00 eV. Thus, we assume that the Al had indeed reacted with the parylene C during the deposition process.

In summary, we have deposited Al_2O_3 on parylene C via ALD. AFM measurements have shown that the oxide deposition had strongly affected the topography of the polymer, on which we observed nanopillar-shaped structures which were absent prior to the ALD process, and were present only when the oxide deposition took place (not a temperature effect as we have seen via AFM measurements). XPS measurements have confirmed the presence of homogeneous and clean aluminum oxide on the surface of the parylene C. In addition, XPS depth profiles using Ar and C60 ion beams have found a thickness of $\sim$ 100-140 nm of Al_2O_3 on the polymer, which is consistent with the AFM measurements.

Since the ALD principle suggests that a thin film is deposited atom by atom on the target substrate, during the growth of the Al_2O_3, the nanopillars are shaped and the oxide is deposited simultaneously, covering the entire nanopillars in surface and in depth, creating by that different thicknesses ranging from 30 to 130 nm. These thicknesses depend on the profundity of the nanopillars.

Surprisingly, a significant concentration of chlorine was observed before the disappearance of the oxide, which normally indicates the presence of parylene C. However, no carbon concentration was found at that sputtering time. Complementary XPS measurements of Cl2p, C1s and Al2s peaks have shown that these peaks have changed in shape (change in FWHM) and their binding energies have also shifted, implying that the Cl and C atoms of parylene C had reacted with the oxide during the deposition.

5.11 XPS and AFM characterization of evaporated Al_2O_3 on parylene C

5.11.1 XPS measurements on evaporated Al_2O_3 on parylene C

As we have seen, the ALD-deposited Al_2O_3 on a parylene C have resulted in a strongly porous polymer film with an average depth of 110 nm. This particular result is not desirable since it would affect the next processing steps, especially the graphene transfer and the lithography process. In addition, this strong change in the polymer could alternate its properties and degrade its performances. Thus, we have resorted to another solution, that is depositing Al_2O_3 via electron beam evaporation.

We have deposited 15 nm of Al_2O_3 on parylene C and performed XPS measurements to determine the chemical composition of the sample and confirm the deposited thickness. Afterwards, we have performed AFM measurements in order to observe the resulted morphology of the polymer and examine the effect of the evaporation method on the parylene C morphology.

Figure 5.19 shows the XPS spectrum of a $Al_2O_3/PC/SiO_2/Si$ sample. Inset is an image of the measured zone on the sample.

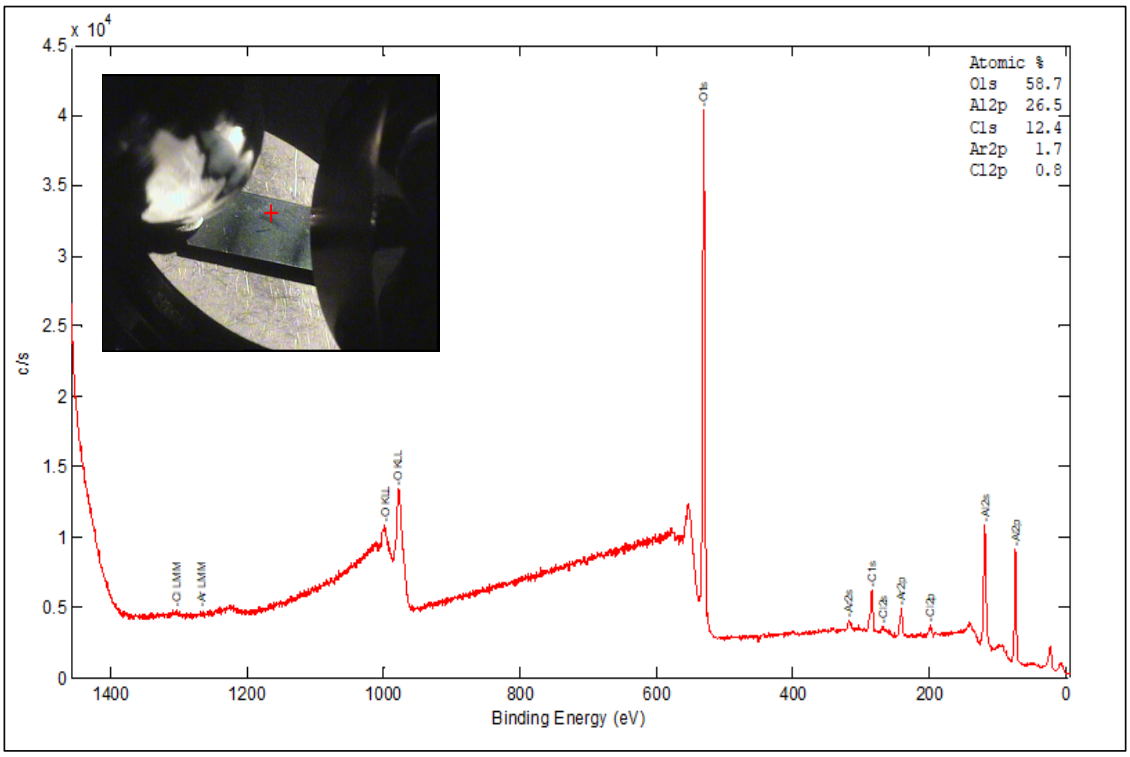

Figure 5.19: XPS spectrum of Al_2O_3 deposited on parylene C via E-beam evaporation. Inset is an optical image of the substrate and the red cross indicates the measurement zone.

This spectrum confirms the presence of Al_2O_3 on the polymer, since Al and O are detected on the surface. Surface contamination such as C-O bonds, Cl particles and Ar particles are also observed. In comparison to ALD-deposited Al_2O_3, the evaporated oxide has an extra Ar particles. This is most probably due to the evaporation method itself, where argon flux is used in order to return to the atmospheric pressure after the deposition process.

To verify the thickness we have deposited, the XPS depth profile is plotted and shown in figure 5.20 (a).

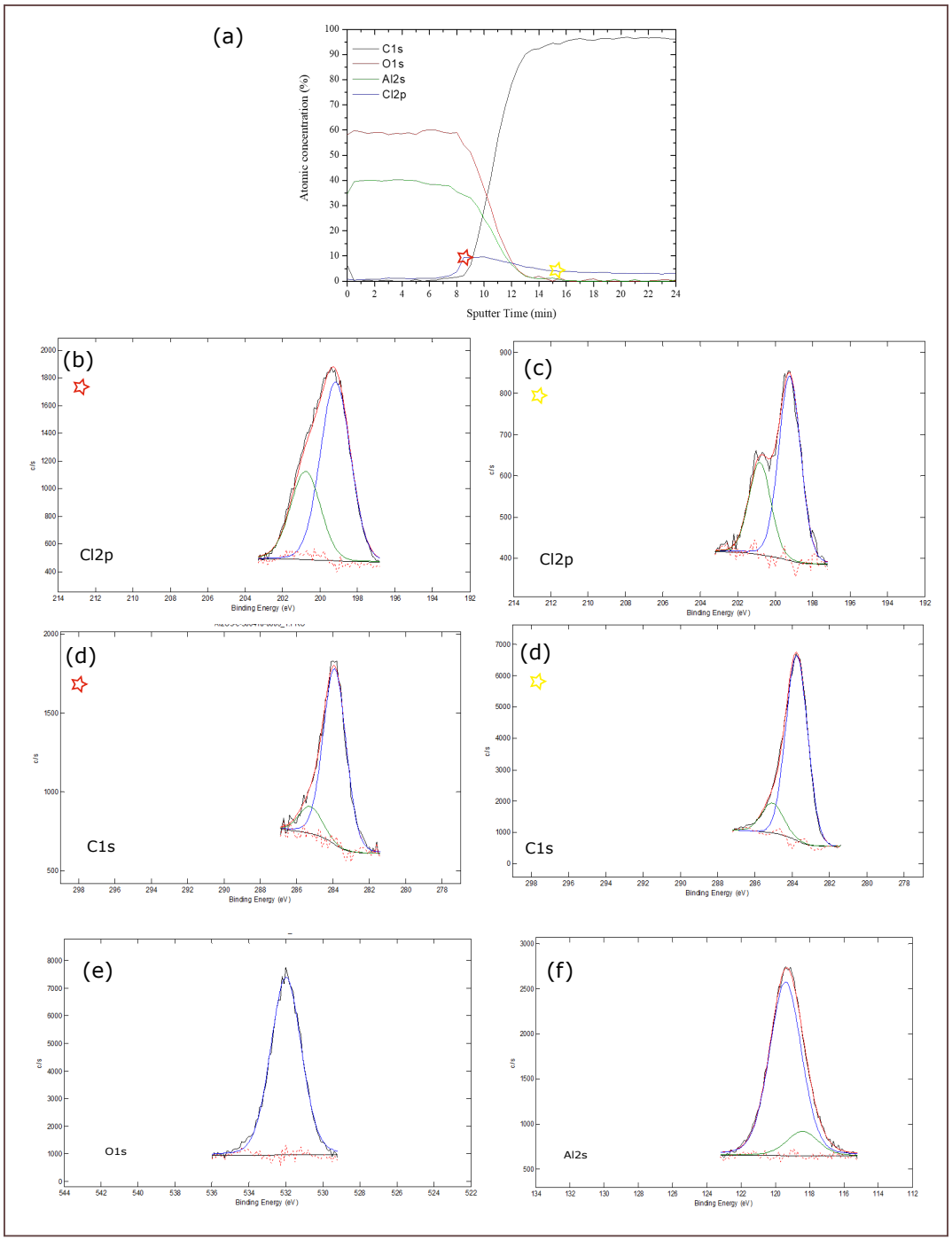

Figure 5.20: XPS depth profile of Al_2O_3 deposited on parylene C via evaporation. (b),(c) The XPS spectra of Cl2p peaks measured (and fitted) at the red star and the yellow star in (a) respectively. (d),(e) The XPS spectra of C1s peaks measured (and fitted) at the red star and the yellow star in (a) respectively. (e) The XPS spectrum of O1s and (f) The XPS spectrum of Al2s.

In figure 5.20 (a), we have found a sputtering time of $\sim$ 10.5 minutes for an etch rate of $\sim$ 1.61 nm/min, which corresponds to an average atomic concentration of 59% of O in Al_2O_3 and 39.9% of Al, indicating an O/al ratio $\simeq$ 1.48. This means that the oxide deposited via evaporation confirms the redox equation.

Furthermore, a sputter time of 10.5 minutes corresponds to an oxide thickness of $\sim$ 17 nm, which is very close to that of the theoretical deposited thickness (15 nm), showing the uniformity of the evaporation deposition process. Similarly to the ALD deposited Al_2O_3, we notice in figure 5.20 (a) that the Cl particles appear at a sputtering time of 8 minutes, before the disappearance of the oxide. The C atoms however are detected at $\sim$ 9 minutes of sputtering time but are not stable before the complete disappearance of Al_2O_3. For this reason, we have decided to plot the XPS depth profile of Cl2p, C1s, O1s and Al2s in order to verify whether the reaction between Al_2O_3 and parylene C is a result of ALD deposition or a typical reaction between the oxide and the polymer.

Figure 5.20 (b) and (c) represents the XPS spectra of the Cl2p peak measured before and after the stabilization of the carbon layer, and consequently before and after the disappearance of the oxide, as indicated with the red and yellow stars (respectively). The single peak of Cl2p detected while the oxide is still present can be deconvoluted into two components with binding energies measured at 199.17 eV and 200.77 eV. For the Cl2p peak detected after the disappearance of Al_2O_3, we find the typical double peak shape at 199.21 eV and 200.81 eV. This change in peak shape and shift in the binding energies is consistent with the XPS measurements on Al_2O_3 deposited via ALD. The C1s peaks depicted in Figure 5.20 (d) and (e) show similar peak shapes, where we can deconvolute both into two components. For the C1s peak measured at the red star (in the presence of oxide), we find binding energies around 283.90 eV and 285.25 eV whereas for the C1s peak measured at the yellow star (in the absence of oxide) we find two components at $\sim$ 283.76 eV and 285.07 eV. This confirms that the carbon layer reacts with the oxide, which is consistent with the previous XPS results of the C1s peak measured for Al_2O_3 deposited by ALD. However, the broadened C1s peak in the parylene C layer (yellow star) also shows the C-Al_2O_3 reaction. We suspect that the measurements were not enough deep in the parylene C surface, which explains the two components of the C1s peak. Finally, the spectra of O1s and Al2s are shown in figure 5.20 (e) and (f) respectively. The O1s peak in Al_2O_3 is a single peak observed at 531 eV [190]. In our case, the peak is detected at $\sim$ 531.99 eV. This shift of $\sim$ 0.99 eV indicates the reaction between the oxygen in Al_2O_3 and the parylene C. The Al2s peak is deconvoluted into two components with binding energies of 118.40 eV and 119.40 eV which is consistent with the previous XPS measurements on Al_2O_3 deposited via ALD. These findings further confirm the reaction between parylene C and Al_2O_3. Thus, we can conclude that the Al_2O_3 and the parylene C react during the oxide deposition via ALD and E-beam evaporation. The effect of this reaction on the properties of Al_2O_3 and the underlying parylene C must be thoroughly understood in order to obtain a complete idea about RF and other electronic devices fabricated on parylene C.

5.11.2 AFM measurements on evaporated Al_2O_3 on parylene C

Finally, to verify the effect of evaporation-deposited Al_2O_3 on the morphology of the parylene C, AFM measurements were carried out and the result is depicted in figure 5.21.

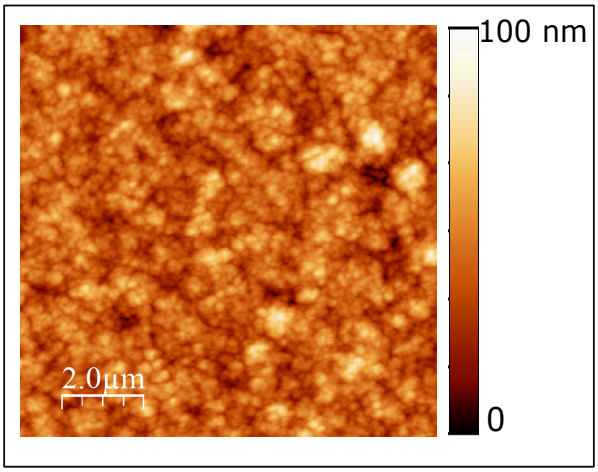

Figure 5.21: AFM image of Al_2O_3 deposited on parylene C by evaporation.

The AFM measurements reveal an average roughness of $\sim$ 9 nm of the parylene C, indicating that, as confirmed by XPS measurements, the evaporation technique did not affect the surface morphology of the parylene C.

5.12 ALD Versus Evaporation of oxide on Parylene C

In conclusion, we compared two Al_2O_3 deposition techniques and thoroughly studied their effect on the parylene C. We have found that depositing Al_2O_3 by atomic layer deposition had strongly affected the morphology of the parylene C, where we have observed via AFM measurements $\sim$ 110 nm-deep nanopillar-shaped structures. This resulted in a non-uniform deposition of Al_2O_3, leading to a $\sim$ 30 nm thick oxide on the surface of the nanopillars, and a $\sim$ 100 nm thickness of oxide inside the nanopillars for what it seems as the oxide trying to fill the holes in the parylene C caused by the deposition process itself. We speculate that the precursor responsible for the donation of oxygen is mainly responsible for the strong modification in the parylene C roughness, since the polymer is extremely hydrophobic. However, the deposition is very clean and the resulting oxide is pure and contamination-free as confirmed by XPS measurements. XPS results also detected the presence of Cl particles before the disappearance of the oxide and the appearance of carbon. This finding is odd since Cl and C atoms are supposed to be detected together as a sign of parylene C. XPS depth profiles have shown that the Cl2p and C1s peaks change in shape and their corresponding binding energies shift before and after the disappearance of the oxide, indicating that the parylene C had

reacted with the oxide during deposition. Complementary XPS measurements on the Al2s and O1s peaks have confirmed the parylene C-Al_2O_3 reaction. In addition to these findings, the ALD deposition time is very long and incompatible with parylene-based devices since AFM measurements have shown an increase of polymer roughness by a factor of 4 induced by the relatively low deposition temperature. This roughness could have a negative impact on the transfer process of the graphene.

Nevertheless, by using E-beam evaporation to deposit Al_2O_3 on parylene C, we have found additional Ar impurity particles on the oxide surface compared to ALD deposited Al_2O_3, which are due to the deposition process itself. However, the theoretical deposited thickness was respected, and the deposition process had zero effect on the polymer roughness as confirmed by AFM measurements. Interestingly, we have also found that the polymer substrate had reacted with the oxide during the short deposition time. More research on this subject is needed in order to understand the effect of this reaction on the properties of the deposited oxide and the underlying parylene C substrate.

In summary, the evaporation technique was found to be the most convenient mean of depositing uniform Al_2O_3 on parylene C substrates. Another advantage of this technique is its deposition time, where 15 nm of oxide are deposited in 11 minutes and at a temperature close to that of room temperature.

5.13 Approach toward flexible RF electronics

In this chapter, we have demonstrated our approach towards the fabrication of flexible RF devices. As we have seen, there are many challenges remaining in order to cross the industrialization step of graphene flexible devices, especially when the basis of current research is that of silicon technology. Parylene C-based graphene RF FETs are not well known in the electronics industry, although many devices have been fabricated, but only for proof of concept. Nonetheless, given the right amount of research and attention, this subject could be very valuable since parylene C has been proven to be very beneficial for graphene and as a great encapsulation material. A very important factor in the industry is time-dependency of the electronics devices, and parylene C could solve this challenge. In addition, the superior biocompatibility of parylene C renders this material very compelling in bioelectronics .

According to Ferrari *et al.* [23], we should expect to see flexible electronics more frequently around 2020. The timeline is shown in figure 5.22.

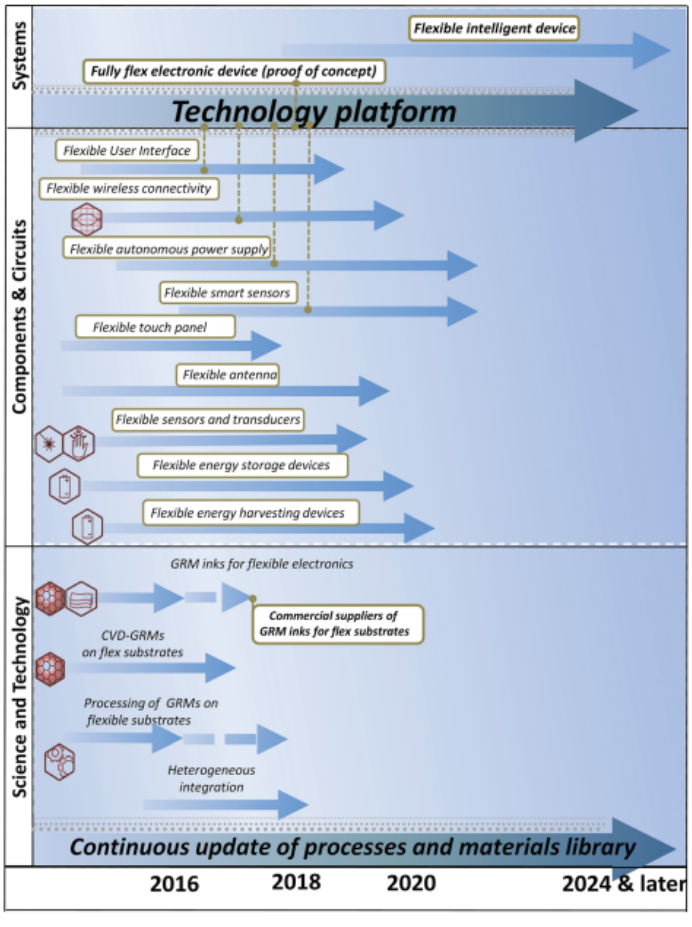

Figure 5.22: Flexible electronics timeline. Adapted from [23].

Chapter 6

Conclusion and perspectives

6.1 Conclusions

This research was intended to obtain a complete idea on the fabrication steps of chemical vapor deposited graphene for large-scale electronics applications and to advance the parylene C-based radiofrequency graphene devices.

The first part of this thesis has established the fabrication and step-by-step characterization of large-scale graphene-based field effect transistors. The chemical mechanical polishing and the annealing of the copper CVD substrate has proven to be very effective via AFM and SEM measurements, which have shown a reduction of Cu surface roughness by a factor of 10, as well as via XPS measurements which have presented the chemical composition of the Cu foil before and after the treatment. While as-purchased Cu foils presented zero copper concentration and a continuous zinc layer among many other impurity particles such as phosphorus, the XPS results have demonstrated the effectiveness of our polishing + annealing step on the Cu surface, where impurity particles were completely removed and the Cu surface was proved to be impurity-free. After achieving a clean and flat copper substrate, the graphene growth was carried out via pulsed chemical vapor deposition (P-CVD). This technique is derived of the standard CVD. The only difference is the injection time of the hydrocarbon (methane here). In the standard CVD process, the methane is continuously injected throughout the entire growth time, whereas in the P-CVD , the methane is injected for 5 seconds and then cut for 55 seconds. This sequenced injection limits the multi-layer formation. In fact, upon adsorbing to the surface of the copper, the CH_x molecules dehydrogenate until the only species left on the surface are carbon atoms, which will coalesce to form graphene. The P-CVD gives enough time for the dehydrogenation to be completed without depositing more CH_4 molecules on the Cu surface. As confirmed by Raman spectroscopy, the graphene grown on copper was of high crystalline quality and single layered. The transfer of the graphene was carried out via the PMMA-assisted graphene transfer since it is the most common

technique for transferring large-area graphene onto arbitrary substrates. Two etching solutions were used, $FeCl_3$ and $(NH_4)_2S_2O_8$, and the effect of these etchants on the graphene quality and PMMA residues was exhaustively studied via XPS measurements performed on two different samples. XPS results showed that the $FeCl_3$-transferred graphene not only had more PMMA residues, but also more defects in the graphene lattice. In addition, more impurity particles were found on the graphene transferred with iron chloride. Thus, $(NH_4)_2S_2O_8$ was chosen as the etching solution in this work. Graphene-based field effect transistors (GFETs) were fabricated via E-beam lithography. Four different channel dimensions were chosen for the GFETs, 1x1, 2x2, 5x5 and 10x10 μm^2. These relatively large channels were chosen firstly to facilitate the lithography and other fabrication processes, and secondly in order to characterize these graphene channels via Raman spectroscopy. Raman spectra and mappings on different GFETs were conducted. The monolayer characteristics of the graphene were observed, as well as the effect of PMMA residues on the graphene quality and consequently on the corresponding Raman spectrum was discussed. The graphene contact metal chosen was palladium (Pd), and Raman spectra revealed that the pd had conserved the graphene's high quality. Electrical measurements were performed on 16 devices, and the charge carrier mobility was extracted using the direct transconductance method (DTM). The highest hole mobility calculated was 2700 $cm^2/(V.s)$, which fits very well in the mobility range of polycrystalline small grain graphene layers. Large-scale fabrication of GFETs has shown that the reproducibility of the GFETs performance is still a fundamental challenge, since the graphene possesses different qualities from one area to another of the same sheet, resulting in hundreds of GFETs fabricated on the same sheet having different electrical properties. The effect of air exposure on the electrical properties of graphene (hole and electron carrier mobility and Dirac point) was studied, and results have shown that air exposure has strongly degraded the graphene's mobility and ambipolarity, accentuating on the need to encapsulate graphene-based devices for long term use. Preliminary results on graphene nanomesh were also presented in this work. Unexpected results showed that structuring the graphene into "connected" nanoribbons had conserved (and slightly increased) the carrier mobility for gate length = 1 μm, and had increased the I_{ON}/I_{OFF} ratio.

In the second part of this research, an approach toward fabricating sub 60 nm flexible RF GFETs was presented. The chosen substrate was parylene C due to its remarkable mechanical, thermal and dielectric properties. Parylene C had been demonstrated to improve the ambipolarity of graphene, as well as to prohibit the hysteresis which is due to the water molecules trapped at the graphene/substrate interface. In addition, this polymer is widely used in the medical industry as an encapsulation material, thus, this characteristic would be very beneficial for obstructing the degradation of the graphene's properties under air exposure. 15 μm of parylene C was deposited on SiO_2 substrates via CVD, and characterized by AFM and XPS. The parylene roughness was found to be 10 nm, however, bumps were observed on the surface with an average height of 250 nm. An optimum RF device design on parylene C was simulated in this work, and a

fabrication process was proposed. The idea behind depositing parylene C on SiO_2 substrates was to facilitate the fabrication process, since the delamination of the hydrophobic parylene C could be achieved by simply immersing the sample in DI water. Sub-60 nm gate electrodes were patterned on parylene C, and SEM images showed no effect of the bumps on the thin gates. An intense study on the oxide deposition method was presented. ALD-deposited Al_2O_3 was compared to E-beam evaporated Al_2O_3. AFM measurements have shown that the ALD deposition of Al_2O_3 had vigorously changed the polymer's topography, where nanopillar-shaped structures were observed on the entire surface of the parylene. However, XPS measurements have demonstrated a very clean and homogeneous oxide deposition, and further XPS measurements have confirmed a reaction between the deposited Al_2O_3 and the parylene C. Contrariwise, AFM measurements on e-beam evaporated Al_2O_3 have shown no effects of the deposition technique on the roughness of the parylene C. However, XPS measurements have indicated the presence of Ar impurity particles on the surface of the oxide, which are due to the deposition process itself. Further XPS measurements have confirmed the Al_2O_3 and parylene C reaction during the deposition. The e-beam evaporation method was found to be the most convenient mean of depositing Al_2O_3 on parylene C.

6.2 Future work

50 nm gate length RF GFETs with cut-off frequencies of a few tens of GHz can be achieved by carefully studying each step of the fabrication process. This thesis contributed to the choice of flexible substrate and encapsulation for long term applications, as well as the realization of sub 60 nm gate lengths. Unfortunately, the graphene channel definition lithography step had failed because of an accidental dose error, and with the C2N-Marcoussis closing to re-open at Palaiseau, we were not able to continue this work despite the fact that only two relatively simple lithography processes were left. Based on this work, parylene-based RF devices could be fabricated in a short period of time and the RF properties could be characterized at the L2E laboratory.

To preserve the high quality of graphene, the transfer must be further improved in order to prohibit the PMMA residue on the graphene layer, as well as cracks and fold that can occur during the transfer. Another challenge lays in conserving the graphene's intrinsic properties throughout the fabrication process. Various studies have suggested coating the graphene with the oxide, however, this still leaves one or two lithography steps with graphene unprotected.

Profounder studies on graphene nanomesh are required as well, as we have seen here that the carrier mobility and ambipolarity of the graphene were improved after structuring the graphene nanomesh. In addition, the I_{ON}/I_{OFF} ratio was found to increase after the graphene nanomesh. Smaller pitch widths can be patterned on channel lengths $< 1\ \mu m$ in order to obtain a higher I_{ON}/I_{OFF} ratio. With proper attention to this subject, a gap can indeed be opened in the graphene layer without inducing more defects. Once the device

is fabricated, a parylene C encapsulation is required in order to preserve the graphene quality and electrical properties.

The knowledge acquired in the field of graphene can also be implemented for other 2D materials such as MoS_2 and black phosphorus. The first is expected to bring new insights in digital electronics and the latter in analog electronics.

Bibliography

[1] G. E. Moore, "Cramming more components onto integrated circuits, reprinted from electronics, volume 38, number 8, april 19, 1965, pp. 114 ff." *IEEE Solid-State Circuits Society Newsletter*, vol. 11, no. 3, pp. 33–35, 2006.

[2] J. A. Del Alamo, "Nanometre-scale electronics with iii–v compound semiconductors," *Nature*, vol. 479, no. 7373, p. 317, 2011.

[3] M. M. S. Aly, M. Gao, G. Hills, C.-S. Lee, G. Pitner, M. M. Shulaker, T. F. Wu, M. Asheghi, J. Bokor, F. Franchetti *et al.*, "Energy-efficient abundant-data computing: The n3xt 1,000 x," *Computer*, vol. 48, no. 12, pp. 24–33, 2015.

[4] K. S. Novoselov, A. K. Geim, S. V. Morozov, D. Jiang, Y. Zhang, S. V. Dubonos, I. V. Grigorieva, and A. A. Firsov, "Electric field effect in atomically thin carbon films," *science*, vol. 306, no. 5696, pp. 666–669, 2004.

[5] A. Geim and K. Novoselov, "The rise of graphene. naturematerials, 6: 183–191," 2007.

[6] C. Corbella Roca, *Thin film structures of diamond-like carbon prepared by pulsed plasma techniques.* Universitat de Barcelona, 2006.

[7] Benjah-bmm27, "s-p-Orbitals," https://commons.wikimedia.org/wiki/File:S-p-Orbitals.svg, 2006, [Online; accessed 16-September-2018].

[8] LibreTexts, "Sigma and Pi Bonds," https://chem.libretexts.org/Textbook_Maps/Introductory_Chemistry/Book%3A_Introductory_Chemistry_(CK-12)/09%3A_Covalent_Bonding/9.20%3A_Sigma_and_Pi_Bonds, 2016, [Online; accessed 07-October-2018].

[9] Mstroeck, "Allotropes of carbon," https://en.wikipedia.org/wiki/Allotropes_of_carbon, 2006, [Online; accessed 07-October-2018].

[10] A. C. Ferrari, "Raman spectroscopy of graphene and graphite: disorder, electron–phonon coupling, doping and nonadiabatic effects," *Solid state communications*, vol. 143, no. 1-2, pp. 47–57, 2007.

[11] A. K. Geim and K. S. Novoselov, "The rise of graphene," in *Nanoscience and Technology: A Collection of Reviews from Nature Journals*. World Scientific, 2010, pp. 11–19.

[12] H. Zhu, *Graphene: Fabrication, Characterizations, Properties and Applications*. Academic Press, 2017.

[13] S. Milovanović, "Electronic transport properties in nano-and micro-engineered graphene structures," Ph.D. dissertation, University of Antwerp, 2017.

[14] F. Xia, D. B. Farmer, Y.-m. Lin, and P. Avouris, "Graphene field-effect transistors with high on/off current ratio and large transport band gap at room temperature," *Nano letters*, vol. 10, no. 2, pp. 715–718, 2010.

[15] A. A. Balandin, S. Ghosh, W. Bao, I. Calizo, D. Teweldebrhan, F. Miao, and C. N. Lau, "Superior thermal conductivity of single-layer graphene," *Nano letters*, vol. 8, no. 3, pp. 902–907, 2008.

[16] C. Lee, X. Wei, J. W. Kysar, and J. Hone, "Measurement of the elastic properties and intrinsic strength of monolayer graphene," *science*, vol. 321, no. 5887, pp. 385–388, 2008.

[17] P. R. Wallace, "Erratum: The band theory of graphite [phys. rev. 71, 622 (1947)]," *Phys. Rev.*, vol. 72, pp. 258–258, Aug 1947. [Online]. Available: https://link.aps.org/doi/10.1103/PhysRev.72.258

[18] M. Ray, "The Spacecraft That Requires no Fuel: Graphene Photoelectric Solar Sails," http://muonray.blogspot.com/2016/06/the-spacecraft-that-requires-no-fuel.html, 2016, [Online; accessed 07-October-2018].

[19] R. R. Nair, P. Blake, A. N. Grigorenko, K. S. Novoselov, T. J. Booth, T. Stauber, N. M. Peres, and A. K. Geim, "Fine structure constant defines visual transparency of graphene," *Science*, vol. 320, no. 5881, pp. 1308–1308, 2008.

[20] X. Li, Y. Zhu, W. Cai, M. Borysiak, B. Han, D. Chen, R. D. Piner, L. Colombo, and R. S. Ruoff, "Transfer of large-area graphene films for high-performance transparent conductive electrodes," *Nano letters*, vol. 9, no. 12, pp. 4359–4363, 2009.

[21] S. Watcharotone, D. A. Dikin, S. Stankovich, R. Piner, I. Jung, G. H. Dommett, G. Evmenenko, S.-E. Wu, S.-F. Chen, C.-P. Liu *et al.*, "Graphene- silica composite thin films as transparent conductors," *Nano letters*, vol. 7, no. 7, pp. 1888–1892, 2007.

[22] P. Blake, P. D. Brimicombe, R. R. Nair, T. J. Booth, D. Jiang, F. Schedin, L. A. Ponomarenko, S. V. Morozov, H. F. Gleeson, E. W. Hill *et al.*, "Graphene-based liquid crystal device," *Nano letters*, vol. 8, no. 6, pp. 1704–1708, 2008.

[23] A. C. Ferrari, F. Bonaccorso, V. Fal'Ko, K. S. Novoselov, S. Roche, P. Bøggild, S. Borini, F. H. Koppens, V. Palermo, N. Pugno *et al.*, "Science and technology roadmap for graphene, related two-dimensional crystals, and hybrid systems," *Nanoscale*, vol. 7, no. 11, pp. 4598–4810, 2015.

[24] X. Wang, L. Zhi, and K. Müllen, "Transparent, conductive graphene electrodes for dye-sensitized solar cells," *Nano letters*, vol. 8, no. 1, pp. 323–327, 2008.

[25] K. S. Kim, Y. Zhao, H. Jang, S. Y. Lee, J. M. Kim, K. S. Kim, J.-H. Ahn, P. Kim, J.-Y. Choi, and B. H. Hong, "Large-scale pattern growth of graphene films for stretchable transparent electrodes," *nature*, vol. 457, no. 7230, p. 706, 2009.

[26] S. Bae, H. Kim, Y. Lee, X. Xu, J.-S. Park, Y. Zheng, J. Balakrishnan, T. Lei, H. R. Kim, Y. I. Song *et al.*, "Roll-to-roll production of 30-inch graphene films for transparent electrodes," *Nature nanotechnology*, vol. 5, no. 8, p. 574, 2010.

[27] L. D'Arsié, S. Esconjauregui, R. Weatherup, Y. Guo, S. Bhardwaj, A. Centeno, A. Zurutuza, C. Cepek, and J. Robertson, "Stability of graphene doping with moo3 and i2," *Applied Physics Letters*, vol. 105, no. 10, p. 103103, 2014.

[28] L. D'Arsié, S. Esconjauregui, R. S. Weatherup, X. Wu, W. E. Arter, H. Sugime, C. Cepek, and J. Robertson, "Stable, efficient p-type doping of graphene by nitric acid," *RSC Advances*, vol. 6, no. 114, pp. 113 185–113 192, 2016.

[29] K. M. Shahil and A. A. Balandin, "Thermal properties of graphene and multilayer graphene: Applications in thermal interface materials," *Solid State Communications*, vol. 152, no. 15, pp. 1331–1340, 2012.

[30] X. Zhang, L. Wang, Q. Lu, and D. L. Kaplan, "Mass production of biocompatible graphene using silk nanofibers," *ACS applied materials & interfaces*, 2018.

[31] H. Chen, M. B. Müller, K. J. Gilmore, G. G. Wallace, and D. Li, "Mechanically strong, electrically conductive, and biocompatible graphene paper," *Advanced Materials*, vol. 20, no. 18, pp. 3557–3561, 2008.

[32] C. Berger, Z. Song, T. Li, X. Li, A. Y. Ogbazghi, R. Feng, Z. Dai, A. N. Marchenkov, E. H. Conrad, P. N. First *et al.*, "Ultrathin epitaxial graphite: 2d electron gas properties and a route toward graphene-based nanoelectronics," *The Journal of Physical Chemistry B*, vol. 108, no. 52, pp. 19 912–19 916, 2004.

[33] C. Berger, Z. Song, X. Li, X. Wu, N. Brown, C. Naud, D. Mayou, T. Li, J. Hass, A. N. Marchenkov *et al.*, "Electronic confinement and coherence in patterned epitaxial graphene," *Science*, vol. 312, no. 5777, pp. 1191–1196, 2006.

[34] P. W. Sutter, J.-I. Flege, and E. A. Sutter, "Epitaxial graphene on ruthenium," *Nature materials*, vol. 7, no. 5, p. 406, 2008.

[35] A. Obraztsov, E. Obraztsova, A. Tyurnina, and A. Zolotukhin, "Chemical vapor deposition of thin graphite films of nanometer thickness," *Carbon*, vol. 45, no. 10, pp. 2017–2021, 2007.

[36] J. Coraux, A. T. N Diaye, C. Busse, and T. Michely, "Structural coherency of graphene on ir (111)," *Nano letters*, vol. 8, no. 2, pp. 565–570, 2008.

[37] E. Rutkov, A. Y. Tontegode *et al.*, "Interaction of silver atoms with iridium and with a two-dimensional graphite film on iridium: Adsorption, desorption, and dissolution," *Physics of the Solid State*, vol. 46, no. 2, pp. 371–377, 2004.

[38] A. Reina, X. Jia, J. Ho, D. Nezich, H. Son, V. Bulovic, M. S. Dresselhaus, and J. Kong, "Large area, few-layer graphene films on arbitrary substrates by chemical vapor deposition," *Nano letters*, vol. 9, no. 1, pp. 30–35, 2008.

[39] Q. Yu, J. Lian, S. Siriponglert, H. Li, Y. P. Chen, and S.-S. Pei, "Graphene segregated on ni surfaces and transferred to insulators," *Applied Physics Letters*, vol. 93, no. 11, p. 113103, 2008.

[40] X. Li, W. Cai, J. An, S. Kim, J. Nah, D. Yang, R. Piner, A. Velamakanni, I. Jung, E. Tutuc *et al.*, "Large-area synthesis of high-quality and uniform graphene films on copper foils," *Science*, vol. 324, no. 5932, pp. 1312–1314, 2009.

[41] A. K. Geim, "Graphene: status and prospects," *science*, vol. 324, no. 5934, pp. 1530–1534, 2009.

[42] Y.-M. Lin, C. Dimitrakopoulos, K. A. Jenkins, D. B. Farmer, H.-Y. Chiu, A. Grill, and P. Avouris, "100-ghz transistors from wafer-scale epitaxial graphene," *Science*, vol. 327, no. 5966, pp. 662–662, 2010.

[43] R. Cheng, J. Bai, L. Liao, H. Zhou, Y. Chen, L. Liu, Y.-C. Lin, S. Jiang, Y. Huang, and X. Duan, "High-frequency self-aligned graphene transistors with transferred gate stacks," *Proceedings of the National Academy of Sciences*, vol. 109, no. 29, pp. 11 588–11 592, 2012.

[44] C. Yu, Z. He, X. Song, Q. Liu, T. Han, S. Dun, J. Wang, C. Zhou, J. Guo, Y. Lv *et al.*, "Improvement of the frequency characteristics of graphene field-effect transistors on sic substrate," *IEEE Electron Device Letters*, vol. 38, no. 9, pp. 1339–1342, 2017.

[45] J. Kedzierski, P.-L. Hsu, P. Healey, P. W. Wyatt, C. L. Keast, M. Sprinkle, C. Berger, and W. A. De Heer, "Epitaxial graphene transistors on sic substrates," *IEEE Transactions on Electron Devices*, vol. 55, no. 8, pp. 2078–2085, 2008.

[46] J. Jobst, D. Waldmann, F. Speck, R. Hirner, D. K. Maude, T. Seyller, and H. B. Weber, "Quantum oscillations and quantum hall effect in epitaxial graphene," *Physical Review B*, vol. 81, no. 19, p. 195434, 2010.

[47] E. Pallecchi, F. Lafont, V. Cavaliere, F. Schopfer, D. Mailly, W. Poirier, and A. Ouerghi, "High electron mobility in epitaxial graphene on 4h-sic (0001) via post-growth annealing under hydrogen," *Scientific reports*, vol. 4, p. 4558, 2014.

[48] H. Hibino, S. Tanabe, S. Mizuno, and H. Kageshima, "Growth and electronic transport properties of epitaxial graphene on sic," *Journal of physics D: Applied physics*, vol. 45, no. 15, p. 154008, 2012.

[49] J. Hass, W. De Heer, and E. Conrad, "The growth and morphology of epitaxial multilayer graphene," *Journal of Physics: Condensed Matter*, vol. 20, no. 32, p. 323202, 2008.

[50] S. Stankovich, D. A. Dikin, G. H. Dommett, K. M. Kohlhaas, E. J. Zimney, E. A. Stach, R. D. Piner, S. T. Nguyen, and R. S. Ruoff, "Graphene-based composite materials," *nature*, vol. 442, no. 7100, p. 282, 2006.

[51] T. Hasan, F. Torrisi, Z. Sun, D. Popa, V. Nicolosi, G. Privitera, F. Bonaccorso, and A. Ferrari, "Solution-phase exfoliation of graphite for ultrafast photonics," *physica status solidi (b)*, vol. 247, no. 11-12, pp. 2953–2957, 2010.

[52] S. Park, D. A. Dikin, S. T. Nguyen, and R. S. Ruoff, "Graphene oxide sheets chemically cross-linked by polyallylamine," *The Journal of Physical Chemistry C*, vol. 113, no. 36, pp. 15 801–15 804, 2009.

[53] J. Hassoun, F. Bonaccorso, M. Agostini, M. Angelucci, M. G. Betti, R. Cingolani, M. Gemmi, C. Mariani, S. Panero, V. Pellegrini *et al.*, "An advanced lithium-ion battery based on a graphene anode and a lithium iron phosphate cathode," *Nano letters*, vol. 14, no. 8, pp. 4901–4906, 2014.

[54] K. Parvez, Z.-S. Wu, R. Li, X. Liu, R. Graf, X. Feng, and K. Mullen, "Exfoliation of graphite into graphene in aqueous solutions of inorganic salts," *Journal of the American Chemical Society*, vol. 136, no. 16, pp. 6083–6091, 2014.

[55] A. M. Dimiev, G. Ceriotti, A. Metzger, N. D. Kim, and J. M. Tour, "Chemical mass production of graphene nanoplatelets in 100% yield," *ACS nano*, vol. 10, no. 1, pp. 274–279, 2015.

[56] M. Liu, X. Zhang, W. Wu, T. Liu, Y. Liu, B. Guo, and R. Zhang, "One-step chemical exfoliation of graphite to 100% few-layer graphene with high quality and large size at ambient temperature," *Chemical Engineering Journal*, vol. 355, pp. 181–185, 2019.

[57] F. Torrisi, T. Hasan, W. Wu, Z. Sun, A. Lombardo, T. S. Kulmala, G.-W. Hsieh, S. Jung, F. Bonaccorso, P. J. Paul *et al.*, "Inkjet-printed graphene electronics," *ACS nano*, vol. 6, no. 4, pp. 2992–3006, 2012.

[58] M. Lotya, Y. Hernandez, P. J. King, R. J. Smith, V. Nicolosi, L. S. Karlsson, F. M. Blighe, S. De, Z. Wang, I. McGovern *et al.*, "Liquid phase production of graphene by exfoliation of graphite in surfactant/water solutions," *Journal of the American Chemical Society*, vol. 131, no. 10, pp. 3611–3620, 2009.

[59] M. Xu, D. Fujita, K. Sagisaka, E. Watanabe, and N. Hanagata, "Production of extended single-layer graphene," *Acs Nano*, vol. 5, no. 2, pp. 1522–1528, 2011.

[60] K. Yamamoto, M. Fukushima, T. Osaka, and C. Oshima, "Charge-transfer mechanism for the (monolayer graphite)/ni (111) system," *Physical Review B*, vol. 45, no. 19, p. 11358, 1992.

[61] J. Lahiri, T. Miller, L. Adamska, I. I. Oleynik, and M. Batzill, "Graphene growth on ni (111) by transformation of a surface carbide," *Nano letters*, vol. 11, no. 2, pp. 518–522, 2010.

[62] H. J. Park, J. Meyer, S. Roth, and V. Skákalová, "Growth and properties of few-layer graphene prepared by chemical vapor deposition," *Carbon*, vol. 48, no. 4, pp. 1088–1094, 2010.

[63] X. Li, W. Cai, L. Colombo, and R. S. Ruoff, "Evolution of graphene growth on ni and cu by carbon isotope labeling," *Nano letters*, vol. 9, no. 12, pp. 4268–4272, 2009.

[64] X. Li, L. Colombo, and R. S. Ruoff, "Synthesis of graphene films on copper foils by chemical vapor deposition," *Advanced Materials*, vol. 28, no. 29, pp. 6247–6252, 2016.

[65] H. I. Rasool, E. B. Song, M. J. Allen, J. K. Wassei, R. B. Kaner, K. L. Wang, B. H. Weiller, and J. K. Gimzewski, "Continuity of graphene on polycrystalline copper," *Nano letters*, vol. 11, no. 1, pp. 251–256, 2010.

[66] Z. Sun, Z. Yan, J. Yao, E. Beitler, Y. Zhu, and J. M. Tour, "Growth of graphene from solid carbon sources," *Nature*, vol. 468, no. 7323, p. 549, 2010.

[67] L. Gao, J. R. Guest, and N. P. Guisinger, "Epitaxial graphene on cu (111)," *Nano letters*, vol. 10, no. 9, pp. 3512–3516, 2010.

[68] V. Miseikis, D. Convertino, N. Mishra, M. Gemmi, T. Mashoff, S. Heun, N. Haghighian, F. Bisio, M. Canepa, V. Piazza *et al.*, "Rapid cvd growth of millimetre-sized single crystal graphene using a cold-wall reactor," *2D Materials*, vol. 2, no. 1, p. 014006, 2015.

[69] E. Loginova, N. Bartelt, P. Feibelman, and K. McCarty, "Factors influencing graphene growth on metal surfaces," *New Journal of Physics*, vol. 11, no. 6, p. 063046, 2009.

[70] E. Loginova, N. C. Bartelt, P. J. Feibelman, and K. F. McCarty, "Evidence for graphene growth by c cluster attachment," *New Journal of Physics*, vol. 10, no. 9, p. 093026, 2008.

[71] O. Rader, A. Varykhalov, J. Sánchez-Barriga, D. Marchenko, A. Rybkin, and A. Shikin, "Is there a rashba effect in graphene on 3 d ferromagnets?" *Physical review letters*, vol. 102, no. 5, p. 057602, 2009.

[72] D. Eom, D. Prezzi, K. T. Rim, H. Zhou, M. Lefenfeld, S. Xiao, C. Nuckolls, M. S. Hybertsen, T. F. Heinz, and G. W. Flynn, "Structure and electronic properties of graphene nanoislands on co (0001)," *Nano letters*, vol. 9, no. 8, pp. 2844–2848, 2009.

[73] J. Coraux, M. Engler, C. Busse, D. Wall, N. Buckanie, F.-J. M. Zu Heringdorf, R. Van Gastel, B. Poelsema, T. Michely *et al.*, "Growth of graphene on ir (111)," *New Journal of Physics*, vol. 11, no. 2, p. 023006, 2009.

[74] E. Loginova, S. Nie, K. Thürmer, N. C. Bartelt, and K. F. McCarty, "Defects of graphene on ir (111): Rotational domains and ridges," *Physical Review B*, vol. 80, no. 8, p. 085430, 2009.

[75] N. A. Vinogradov, A. Zakharov, V. Kocevski, J. Rusz, K. Simonov, O. Eriksson, A. Mikkelsen, E. Lundgren, A. Vinogradov, N. Mårtensson *et al.*, "Formation and structure of graphene waves on fe (110)," *Physical review letters*, vol. 109, no. 2, p. 026101, 2012.

[76] S. Nie, N. C. Bartelt, J. M. Wofford, O. D. Dubon, K. F. McCarty, and K. Thürmer, "Scanning tunneling microscopy study of graphene on au (111): Growth mechanisms and substrate interactions," *Physical Review B*, vol. 85, no. 20, p. 205406, 2012.

[77] E. N. Voloshina, Y. S. Dedkov, S. Torbrügge, A. Thissen, and M. Fonin, "Graphene on rh (111): Scanning tunneling and atomic force microscopies studies," *Applied Physics Letters*, vol. 100, no. 24, p. 241606, 2012.

[78] P. Sutter, J. T. Sadowski, and E. Sutter, "Graphene on pt (111): Growth and substrate interaction," *Physical Review B*, vol. 80, no. 24, p. 245411, 2009.

[79] X. Feng, J. Wu, A. T. Bell, and M. Salmeron, "An atomic-scale view of the nucleation and growth of graphene islands on pt surfaces," *The Journal of Physical Chemistry C*, vol. 119, no. 13, pp. 7124–7129, 2015.

[80] M. R. Habib, T. Liang, X. Yu, X. Pi, Y. Liu, and M. Xu, "A review of theoretical study of graphene chemical vapor deposition synthesis on metals: nucleation, growth, and the role of hydrogen and oxygen," *Reports on Progress in Physics*, vol. 81, no. 3, p. 036501, 2018.

[81] K. Wang, "Chemical vapour deposition of large-area high-quality graphene films for electronic applications," 2014.

[82] Y. Hao, M. Bharathi, L. Wang, Y. Liu, H. Chen, S. Nie, X. Wang, H. Chou, C. Tan, B. Fallahazad *et al.*, "The role of surface oxygen in the growth of large single-crystal graphene on copper," *Science*, p. 1243879, 2013.

[83] H. Kim, C. Mattevi, M. R. Calvo, J. C. Oberg, L. Artiglia, S. Agnoli, C. F. Hirjibehedin, M. Chhowalla, and E. Saiz, "Activation energy paths for graphene nucleation and growth on cu," *ACS nano*, vol. 6, no. 4, pp. 3614–3623, 2012.

[84] W. Zhang, P. Wu, Z. Li, and J. Yang, "First-principles thermodynamics of graphene growth on cu surfaces," *The Journal of Physical Chemistry C*, vol. 115, no. 36, pp. 17 782–17 787, 2011.

[85] N. Bartelt and K. McCarty, "Graphene growth on metal surfaces," *MRS bulletin*, vol. 37, no. 12, pp. 1158–1165, 2012.

[86] V. I. Artyukhov, Y. Liu, and B. I. Yakobson, "Equilibrium at the edge and atomistic mechanisms of graphene growth," *Proceedings of the National Academy of Sciences*, 2012.

[87] A. Reina, H. Son, L. Jiao, B. Fan, M. S. Dresselhaus, Z. Liu, and J. Kong, "Transferring and identification of single-and few-layer graphene on arbitrary substrates," *The Journal of Physical Chemistry C*, vol. 112, no. 46, pp. 17 741–17 744, 2008.

[88] L. Jiao, B. Fan, X. Xian, Z. Wu, J. Zhang, and Z. Liu, "Creation of nanostructures with poly (methyl methacrylate)-mediated nanotransfer printing," *Journal of the American Chemical Society*, vol. 130, no. 38, pp. 12 612–12 613, 2008.

[89] Z. Han, "Graphène pour la nanoélectronique: de la croissance cvd jusqu'à la suparconductivité de proximité à deux dimensions," Ph.D. dissertation, Grenoble, 2013.

[90] H. C. Lee, W.-W. Liu, S.-P. Chai, A. R. Mohamed, A. Aziz, C.-S. Khe, N. M. Hidayah, and U. Hashim, "Review of the synthesis, transfer, characterization and growth mechanisms of single and multilayer graphene," *RSC Advances*, vol. 7, no. 26, pp. 15 644–15 693, 2017.

[91] G. Deokar, J. Avila, I. Razado-Colambo, J.-L. Codron, C. Boyaval, E. Galopin, M.-C. Asensio, and D. Vignaud, "Towards high quality cvd graphene growth and transfer," *Carbon*, vol. 89, pp. 82–92, 2015.

[92] M. Chen, R. C. Haddon, R. Yan, and E. Bekyarova, "Advances in transferring chemical vapour deposition graphene: a review," *Materials Horizons*, vol. 4, no. 6, pp. 1054–1063, 2017.

[93] Y. Chen, X.-L. Gong, and J.-G. Gai, "Progress and challenges in transfer of large-area graphene films," *Advanced Science*, vol. 3, no. 8, 2016.

[94] J. Chen, Y. Wen, Y. Guo, B. Wu, L. Huang, Y. Xue, D. Geng, D. Wang, G. Yu, and Y. Liu, "Oxygen-aided synthesis of polycrystalline graphene on silicon dioxide substrates," *Journal of the American Chemical Society*, vol. 133, no. 44, pp. 17 548–17 551, 2011, pMID: 21988639. [Online]. Available: https://doi.org/10.1021/ja2063633

[95] G. B. Barin, Y. Song, I. de Fátima Gimenez, A. G. Souza Filho, L. S. Barreto, and J. Kong, "Optimized graphene transfer: Influence of polymethylmethacrylate (pmma) layer concentration and baking time on graphene final performance," *Carbon*, vol. 84, pp. 82–90, 2015.

[96] S. Kim, S. Shin, T. Kim, H. Du, M. Song, C. Lee, K. Kim, S. Cho, D. H. Seo, and S. Seo, "Robust graphene wet transfer process through low molecular weight polymethylmethacrylate," *Carbon*, vol. 98, pp. 352–357, 2016.

[97] S. Gorantla, A. Bachmatiuk, J. Hwang, H. A. Alsalman, J. Y. Kwak, T. Seyller, J. Eckert, M. G. Spencer, and M. H. Rümmeli, "A universal transfer route for graphene," *Nanoscale*, vol. 6, no. 2, pp. 889–896, 2014.

[98] M. Ohtomo, Y. Sekine, S. Wang, H. Hibino, and H. Yamamoto, "Etchant-free graphene transfer using facile intercalation of alkanethiol self-assembled molecules at graphene/metal interfaces," *Nanoscale*, vol. 8, no. 22, pp. 11 503–11 510, 2016.

[99] L. Gao, G.-X. Ni, Y. Liu, B. Liu, A. H. C. Neto, and K. P. Loh, "Face-to-face transfer of wafer-scale graphene films," *Nature*, vol. 505, no. 7482, p. 190, 2014.

[100] Y.-C. Lin, C.-C. Lu, C.-H. Yeh, C. Jin, K. Suenaga, and P.-W. Chiu, "Graphene annealing: how clean can it be?" *Nano letters*, vol. 12, no. 1, pp. 414–419, 2011.

[101] H. Park, P. R. Brown, V. Bulovic, and J. Kong, "Graphene as transparent conducting electrodes in organic photovoltaics: studies in graphene morphology, hole transporting layers, and counter electrodes," *Nano letters*, vol. 12, no. 1, pp. 133–140, 2011.

[102] Y. Jia, X. Gong, P. Peng, Z. Wang, Z. Tian, L. Ren, Y. Fu, and H. Zhang, "Toward high carrier mobility and low contact resistance: laser cleaning of pmma residues on graphene surfaces," *Nano-Micro Letters*, vol. 8, no. 4, pp. 336–346, 2016.

[103] J. Sun, H. O. Finklea, and Y. Liu, "Characterization and electrolytic cleaning of poly (methyl methacrylate) residues on transferred chemical vapor deposited graphene," *Nanotechnology*, vol. 28, no. 12, p. 125703, 2017.

[104] X.-D. Chen, Z.-B. Liu, C.-Y. Zheng, F. Xing, X.-Q. Yan, Y. Chen, and J.-G. Tian, "High-quality and efficient transfer of large-area graphene films onto different substrates," *Carbon*, vol. 56, pp. 271–278, 2013.

[105] M. Chen, G. Li, W. Li, D. Stekovic, B. Arkook, M. E. Itkis, A. Pekker, E. Bekyarova, and R. C. Haddon, "Large-scale cellulose-assisted transfer of graphene toward industrial applications," *Carbon*, vol. 110, pp. 286–291, 2016.

[106] W.-H. Lin, T.-H. Chen, J.-K. Chang, J.-I. Taur, Y.-Y. Lo, W.-L. Lee, C.-S. Chang, W.-B. Su, and C.-I. Wu, "A direct and polymer-free method for transferring graphene grown by chemical vapor deposition to any substrate," *ACS nano*, vol. 8, no. 2, pp. 1784–1791, 2014.

[107] A. Matruglio, S. Nappini, D. Naumenko, E. Magnano, F. Bondino, M. Lazzarino, and S. Dal Zilio, "Contamination-free suspended graphene structures by a ti-based transfer method," *Carbon*, vol. 103, pp. 305–310, 2016.

[108] Z. Xu, Z. He, Y. Song, X. Fu, M. Rommel, X. Luo, A. Hartmaier, J. Zhang, and F. Fang, "Topic review: Application of raman spectroscopy characterization in micro/nano-machining," *Micromachines*, vol. 9, no. 7, 2018.

[109] L. Malard, M. Pimenta, G. Dresselhaus, and M. Dresselhaus, "Raman spectroscopy in graphene," *Physics Reports*, vol. 473, no. 5-6, pp. 51–87, 2009.

[110] A. C. Ferrari and D. M. Basko, "Raman spectroscopy as a versatile tool for studying the properties of graphene," *Nature nanotechnology*, vol. 8, no. 4, p. 235, 2013.

[111] D. Graf, F. Molitor, K. Ensslin, C. Stampfer, A. Jungen, C. Hierold, and L. Wirtz, "Spatially resolved raman spectroscopy of single- and few-layer graphene," *Nano Letters*, vol. 7, no. 2, pp. 238–242, 2007, pMID: 17297984. [Online]. Available: https://doi.org/10.1021/nl061702a

[112] A. Gupta, G. Chen, P. Joshi, S. Tadigadapa, and P. Eklund, "Raman scattering from high-frequency phonons in supported n-graphene layer films," *Nano letters*, vol. 6, no. 12, pp. 2667–2673, 2006.

[113] A. C. Ferrari and J. Robertson, "Interpretation of raman spectra of disordered and amorphous carbon," *Physical review B*, vol. 61, no. 20, p. 14095, 2000.

[114] A. C. Ferrari, J. Meyer, V. Scardaci, C. Casiraghi, M. Lazzeri, F. Mauri, S. Piscanec, D. Jiang, K. Novoselov, S. Roth *et al.*, "Raman spectrum of graphene and graphene layers," *Physical review letters*, vol. 97, no. 18, p. 187401, 2006.

[115] P. Lespade, A. Marchand, M. Couzi, and F. Cruege, "Caracterisation de materiaux carbones par microspectrometrie raman," *Carbon*, vol. 22, no. 4-5, pp. 375–385, 1984.

[116] C. Neumann, S. Reichardt, P. Venezuela, M. Drögeler, L. Banszerus, M. Schmitz, K. Watanabe, T. Taniguchi, F. Mauri, B. Beschoten *et al.*, "Raman spectroscopy as probe of nanometre-scale strain variations in graphene," *Nature communications*, vol. 6, p. 8429, 2015.

[117] D. R. Cooper, B. DAnjou, N. Ghattamaneni, B. Harack, M. Hilke, A. Horth, N. Majlis, M. Massicotte, L. Vandsburger, E. Whiteway *et al.*, "Experimental review of graphene," *ISRN Condensed Matter Physics*, vol. 2012, 2012.

[118] J. Moon, D. Curtis, M. Hu, D. Wong, C. McGuire, P. Campbell, G. Jernigan, J. Tedesco, B. VanMil, R. Myers-Ward *et al.*, "Epitaxial-graphene rf field-effect transistors on si-face 6h-sic substrates," *IEEE Electron Device Letters*, vol. 30, no. 6, pp. 650–652, 2009.

[119] J. Moon, D. Curtis, S. Bui, M. Hu, D. Gaskill, J. Tedesco, P. Asbeck, G. Jernigan, B. VanMil, R. Myers-Ward *et al.*, "Top-gated epitaxial graphene fets on si-face sic wafers with a peak transconductance of 600 ms/mm," *IEEE Electron Device Letters*, vol. 31, no. 4, pp. 260–262, 2010.

[120] I. Meric, C. R. Dean, N. Petrone, L. Wang, J. Hone, P. Kim, and K. L. Shepard, "Graphene field-effect transistors based on boron–nitride dielectrics," *Proceedings of the IEEE*, vol. 101, no. 7, pp. 1609–1619, 2013.

[121] N. Petrone, T. Chari, I. Meric, L. Wang, K. L. Shepard, and J. Hone, "Flexible graphene field-effect transistors encapsulated in hexagonal boron nitride," *ACS nano*, vol. 9, no. 9, pp. 8953–8959, 2015.

[122] D. De Fazio, D. Purdie, A. Ott, P. Braeuninger-Weimer, S. Hofmann, I. Goykhman, A. Ferrari, and A. Lombardo, "High mobility from wet-transferred encapsulated cvd graphene," *Bulletin of the American Physical Society*, 2018.

[123] L. Liao, Y.-C. Lin, M. Bao, R. Cheng, J. Bai, Y. Liu, Y. Qu, K. L. Wang, Y. Huang, and X. Duan, "High-speed graphene transistors with a self-aligned nanowire gate," *Nature*, vol. 467, no. 7313, p. 305, 2010.

[124] Y. Wu, D. Farmer, A. Valdes-Garcia, W. Zhu, K. Jenkins, C. Dimitrakopoulos, P. Avouris, and Y.-M. Lin, "Record high rf performance for epitaxial graphene transistors," in *Electron Devices Meeting (IEDM), 2011 IEEE International*. IEEE, 2011, pp. 23–8.

[125] Y. Wu, Y.-m. Lin, A. A. Bol, K. A. Jenkins, F. Xia, D. B. Farmer, Y. Zhu, and P. Avouris, "High-frequency, scaled graphene transistors on diamond-like carbon," *Nature*, vol. 472, no. 7341, p. 74, 2011.

[126] Z. H. Ni, T. Yu, Y. H. Lu, Y. Y. Wang, Y. P. Feng, and Z. X. Shen, "Uniaxial strain on graphene: Raman spectroscopy study and band-gap opening," *ACS nano*, vol. 2, no. 11, pp. 2301–2305, 2008.

[127] L. Ci, L. Song, C. Jin, D. Jariwala, D. Wu, Y. Li, A. Srivastava, Z. Wang, K. Storr, L. Balicas *et al.*, "Atomic layers of hybridized boron nitride and graphene domains," *Nature materials*, vol. 9, no. 5, p. 430, 2010.

[128] P. Shemella, Y. Zhang, M. Mailman, P. M. Ajayan, and S. K. Nayak, "Energy gaps in zero-dimensional graphene nanoribbons," *Applied Physics Letters*, vol. 91, no. 4, p. 042101, 2007.

[129] X. Wang, Y. Ouyang, X. Li, H. Wang, J. Guo, and H. Dai, "Room-temperature all-semiconducting sub-10-nm graphene nanoribbon field-effect transistors," *Physical review letters*, vol. 100, no. 20, p. 206803, 2008.

[130] J. Bai, X. Zhong, S. Jiang, Y. Huang, and X. Duan, "Graphene nanomesh," *Nature nanotechnology*, vol. 5, no. 3, p. 190, 2010.

[131] S. Y. Zhou, G.-H. Gweon, A. Fedorov, d. First, PN, W. De Heer, D.-H. Lee, F. Guinea, A. C. Neto, and A. Lanzara, "Substrate-induced bandgap opening in epitaxial graphene," *Nature materials*, vol. 6, no. 10, p. 770, 2007.

[132] T. Kawasaki, T. Ichimura, H. Kishimoto, A. A. Akbar, T. Ogawa, and C. Oshima, "Double atomic layers of graphene/monolayer h-bn on ni (111) studied by scanning tunneling microscopy and scanning tunneling spectroscopy," *Surface Review and Letters*, vol. 9, no. 03n04, pp. 1459–1464, 2002.

[133] X. Peng and R. Ahuja, "Symmetry breaking induced bandgap in epitaxial graphene layers on sic," *Nano letters*, vol. 8, no. 12, pp. 4464–4468, 2008.

[134] D. Wei, Y. Liu, Y. Wang, H. Zhang, L. Huang, and G. Yu, "Synthesis of n-doped graphene by chemical vapor deposition and its electrical properties," *Nano letters*, vol. 9, no. 5, pp. 1752–1758, 2009.

[135] L. Zhang, S. Diao, Y. Nie, K. Yan, N. Liu, B. Dai, Q. Xie, A. Reina, J. Kong, and Z. Liu, "Photocatalytic patterning and modification of graphene," *Journal of the American Chemical Society*, vol. 133, no. 8, pp. 2706–2713, 2011.

[136] M. Wang, L. Fu, L. Gan, C. Zhang, M. Rümmeli, A. Bachmatiuk, K. Huang, Y. Fang, and Z. Liu, "Cvd growth of large area smooth-edged graphene nanomesh by nanosphere lithography," *Scientific reports*, vol. 3, p. 1238, 2013.

[137] M. Kim, N. S. Safron, E. Han, M. S. Arnold, and P. Gopalan, "Fabrication and characterization of large-area, semiconducting nanoperforated graphene materials," *Nano letters*, vol. 10, no. 4, pp. 1125–1131, 2010.

[138] A. Sinitskii and J. M. Tour, "Patterning graphene through the self-assembled templates: toward periodic two-dimensional graphene nanostructures with semiconductor properties," *Journal of the American Chemical Society*, vol. 132, no. 42, pp. 14 730–14 732, 2010.

[139] X. Li, X. Wang, L. Zhang, S. Lee, and H. Dai, "Chemically derived, ultrasmooth graphene nanoribbon semiconductors," *science*, vol. 319, no. 5867, pp. 1229–1232, 2008.

[140] P. Jangid, D. Pathan, and A. Kottantharayil, "Graphene nanoribbon transistors with high ion/ioff ratio and mobility," *Carbon*, vol. 132, pp. 65–70, 2018.

[141] G. Schubert, J. Schleede, and H. Fehske, "Anderson disorder in graphene nanoribbons: A local distribution approach," *Physical Review B*, vol. 79, no. 23, p. 235116, 2009.

[142] J. Yang, M. Ma, L. Li, Y. Zhang, W. Huang, and X. Dong, "Graphene nanomesh: new versatile materials," *Nanoscale*, vol. 6, no. 22, pp. 13 301–13 313, 2014.

[143] W. Oswald and Z. Wu, "Energy gaps in graphene nanomeshes," *Physical Review B*, vol. 85, no. 11, p. 115431, 2012.

[144] K. Lopata, R. Thorpe, S. Pistinner, X. Duan, and D. Neuhauser, "Graphene nanomeshes: Onset of conduction band gaps," *Chemical Physics Letters*, vol. 498, no. 4-6, pp. 334–337, 2010.

[145] M. Chin and W. W. Kromhout, "Young innovators take research in new directions ," http://newsroom.ucla.edu/stories/young-science-innovators-take-176874, 2010, [Online; accessed 07-October-2018].

[146] P. Xu, J. Yang, K. Wang, Z. Zhou, and P. Shen, "Porous graphene: properties, preparation, and potential applications," *Chinese science bulletin*, vol. 57, no. 23, pp. 2948–2955, 2012.

[147] A. Girdhar, C. Sathe, K. Schulten, and J.-P. Leburton, "Graphene quantum point contact transistor for dna sensing," *Proceedings of the National Academy of Sciences*, vol. 110, no. 42, pp. 16 748–16 753, 2013.

[148] J. Liu, Y. Xue, M. Zhang, and L. Dai, "Graphene-based materials for energy applications," *MRS bulletin*, vol. 37, no. 12, pp. 1265–1272, 2012.

[149] G. Fiori, F. Bonaccorso, G. Iannaccone, T. Palacios, D. Neumaier, A. Seabaugh, S. K. Banerjee, and L. Colombo, "Electronics based on two-dimensional materials," *Nature nanotechnology*, vol. 9, no. 10, p. 768, 2014.

[150] A. Nathan, A. Ahnood, M. T. Cole, S. Lee, Y. Suzuki, P. Hiralal, F. Bonaccorso, T. Hasan, L. Garcia-Gancedo, A. Dyadyusha *et al.*, "Flexible electronics: the next ubiquitous platform," *Proceedings of the IEEE*, vol. 100, no. Special Centennial Issue, pp. 1486–1517, 2012.

[151] J. Gozalvez, "The european union backs he dvb-h standard [mobile radio]," *IEEE Vehicular Technology Magazine*, vol. 3, no. 2, pp. 3–12, 2008.

[152] C. Gray, J. Wang, G. Duthaler, A. Ritenour, and P. S. Drzaic, "Screen printed organic thin film transistors (otfts) on a flexible substrate," in *Organic Field Effect Transistors*, vol. 4466. International Society for Optics and Photonics, 2001, pp. 89–95.

[153] S. Chen, Z. Lou, D. Chen, and G. Shen, "An artificial flexible visual memory system based on an uv-motivated memristor," *Advanced Materials*, vol. 30, no. 7, p. 1705400, 2018.

[154] Y. Liu, M. Pharr, and G. A. Salvatore, "Lab-on-skin: a review of flexible and stretchable electronics for wearable health monitoring," *ACS nano*, vol. 11, no. 10, pp. 9614–9635, 2017.

[155] Y. Huang, J. Liu, Q. Huang, Z. Zheng, P. Hiralal, F. Zheng, D. Ozgit, S. Su, S. Chen, P.-H. Tan *et al.*, "Flexible high energy density zinc-ion batteries enabled by binder-free mno 2/reduced graphene oxide electrode," *npj Flexible Electronics*, vol. 2, no. 1, p. 21, 2018.

[156] Y.-B. Cheng, A. Pascoe, F. Huang, and Y. Peng, "Print flexible solar cells," *Nature News*, vol. 539, no. 7630, p. 488, 2016.

[157] C. Sire, F. Ardiaca, S. Lepilliet, J.-W. T. Seo, M. C. Hersam, G. Dambrine, H. Happy, and V. Derycke, "Flexible gigahertz transistors derived from solution-based single-layer graphene," *Nano letters*, vol. 12, no. 3, pp. 1184–1188, 2012.

[158] J. Lee, T.-J. Ha, H. Li, K. N. Parrish, M. Holt, A. Dodabalapur, R. S. Ruoff, and D. Akinwande, "25 ghz embedded-gate graphene transistors with high-k dielectrics on extremely flexible plastic sheets," *ACS nano*, vol. 7, no. 9, pp. 7744–7750, 2013.

[159] C. Yu, Z. He, X. Song, Q. Liu, L. Gao, B. Yao, T. Han, X. Gao, Y. Lv, Z. Feng *et al.*, "High-frequency flexible graphene field-effect transistors with short gate length of 50 nm and record extrinsic cut-off frequency," *physica status solidi (RRL)–Rapid Research Letters*, vol. 12, no. 5, p. 1700435, 2018.

[160] N. Petrone, I. Meric, T. Chari, K. L. Shepard, and J. Hone, "Graphene field-effect transistors for radio-frequency flexible electronics," *IEEE Journal of the Electron Devices Society*, vol. 3, no. 1, pp. 44–48, 2015.

[161] W. Wei, E. Pallecchi, S. Haque, S. Borini, V. Avramovic, A. Centeno, Z. Amaia, and H. Happy, "Mechanically robust 39 ghz cut-off frequency graphene field effect transistors on flexible substrates," *Nanoscale*, vol. 8, no. 29, pp. 14 097–14 103, 2016.

[162] H.-Q. Li, "The Common AFM Modes," http://www.chembio.uoguelph.ca/educmat/chm729/afm/details.htm#summary, 1997, [Online; accessed 16-September-2018].

[163] N. Instruments, "Atomic Force Microscopy," https://www.nanoscience.com/techniques/atomic-force-microscopy/, -, [Online; accessed 16-September-2018].

[164] Yashvant, O. H. of Nanoscience, and Nanotechnology, "Atomic Force Microscope," https://simple.wikipedia.org/wiki/Atomic_force_microscope, 2013, [Online; accessed 16-September-2018].

[165] M. Zdrojek, T. Heim, D. Brunel, A. Mayer, and T. Mélin, "Inner-shell charging of multiwalled carbon nanotubes," *Phys. Rev. B*, vol. 77, p. 033404, Jan 2008. [Online]. Available: https://link.aps.org/doi/10.1103/PhysRevB.77.033404

[166] D. Brunel, A. Mayer, and T. Mlin, "Imaging the operation of a carbon nanotube charge sensor at the nanoscale," *ACS Nano*, vol. 4, no. 10, pp. 5978–5984, 2010. [Online]. Available: https://doi.org/10.1021/nn1012435

[167] N. Jamond, P. Chrétien, F. Houzé, L. Lu, L. Largeau, O. Maugain, L. Travers, J. Harmand, F. Glas, E. Lefeuvre *et al.*, "Piezo-generator integrating a vertical array of gan nanowires," *Nanotechnology*, vol. 27, no. 32, p. 325403, 2016.

[168] N. Instruments, "Scanning Electron Microscopy," https://www.nanoscience.com/techniques/scanning-electron-microscopy/, -, [Online; accessed 16-September-2018].

[169] B. Hafner, "Scanning Electron Microscopy Primer," http://www.charfac.umn.edu/instruments/sem_primer.pdf, 2015, [Online; accessed 16-September-2018].

[170] C. Causserand and P. Aimar, "1.15–characterization of filtration membranes," *Comprehensive Membrane Science and Engineering*, vol. 1, p. 311, 2010.

[171] L. C. d. Bvcrist (talk); transferred to Commons by Lauro Chieza de Carvalho (Carvalho, "X-ray photoelectron spectroscopy," https://en.wikipedia.org/wiki/Xray_photoelectron_spectroscopy, 2009, [Online; accessed 16-September-2018].

[172] M. Lahmani, C. Dupas, and P. Houdy, *Les nanosciences*. Springer, 2004.

[173] A. Grigorescu and C. Hagen, "Resists for sub-20-nm electron beam lithography with a focus on hsq: state of the art," *Nanotechnology*, vol. 20, no. 29, p. 292001, 2009.

[174] F. Karouta, "A practical approach to reactive ion etching," *Journal of Physics D: Applied Physics*, vol. 47, no. 23, p. 233501, 2014.

[175] S. Naureen, "Top-down fabrication technologies for high quality iii-v nanostructures," Ph.D. dissertation, KTH Royal Institute of Technology, 2013.

[176] T. S. Le, M. Cretin, P. Huguet, P. Sistat, and F. Pichot, "Effect of coating and plasma treatments on the induced coupled plasma-reactive ionic etching of boron-doped diamond for microelectromechanical systems (mems) applications," *Nanoscience Methods*, vol. 3, no. 1, pp. 1–10, 2014.

[177] A. I. INC, "What is Electron beam (E-beam) evaporation?" http://www.ajaint.com/what-is-e-beam-evaporation.html, -, [Online; accessed 16-September-2018].

[178] Adhikaprasangi, "RVCE Thin Films," https://rvcethinfilms.wordpress.com/2016/08/09/unit-2/, 2016, [Online; accessed 16-September-2018].

[179] R. W. Johnson, A. Hultqvist, and S. F. Bent, "A brief review of atomic layer deposition: from fundamentals to applications," *Materials today*, vol. 17, no. 5, pp. 236–246, 2014.

[180] S. Dhingra, J.-F. Hsu, I. Vlassiouk, and B. DUrso, "Chemical vapor deposition of graphene on large-domain ultra-flat copper," *Carbon*, vol. 69, pp. 188–193, 2014.

[181] G. H. Han, F. Gunes, J. J. Bae, E. S. Kim, S. J. Chae, H.-J. Shin, J.-Y. Choi, D. Pribat, and Y. H. Lee, "Influence of copper morphology in forming nucleation seeds for graphene growth," *Nano letters*, vol. 11, no. 10, pp. 4144–4148, 2011.

[182] Z. Luo, Y. Lu, D. W. Singer, M. E. Berck, L. A. Somers, B. R. Goldsmith, and A. C. Johnson, "Effect of substrate roughness and feedstock concentration on growth of wafer-scale graphene at atmospheric pressure," *Chemistry of Materials*, vol. 23, no. 6, pp. 1441–1447, 2011.

[183] T. Fan, C. Yan, J. Lu, L. Zhang, and J. Cai, "The effect of copper substrates roughness on graphene growth process via pecvd," *Materials Research Express*, vol. 5, no. 4, p. 045604, 2018.

[184] Y. Xiao, H. Kim, C. Mattevi, M. Chhowalla, R. C. Maher, and L. F. Cohen, "Influence of cu substrate topography on the growth morphology of chemical vapour deposited graphene," *Carbon*, vol. 65, pp. 7–12, 2013.

[185] X. Ge, Y. Zhang, Z. Chen, Y. Liang, S. Hu, Y. Sui, G. Yu, S. Peng, Z. Jin, and X. Liu, "Effects of carbon-based impurities on graphene growth," *Physical Chemistry Chemical Physics*, 2018.

[186] J. M. Wofford, S. Nie, K. F. McCarty, N. C. Bartelt, and O. D. Dubon, "Graphene islands on cu foils: the interplay between shape, orientation, and defects," *Nano letters*, vol. 10, no. 12, pp. 4890–4896, 2010.

[187] S. M. Kim, A. Hsu, Y.-H. Lee, M. Dresselhaus, T. Palacios, K. K. Kim, and J. Kong, "The effect of copper pre-cleaning on graphene synthesis," *Nanotechnology*, vol. 24, no. 36, p. 365602, 2013.

[188] T. J. Gnanaprakasa, Y. Gu, S. K. Eddy, Z. Han, W. J. Beck, K. Muralidharan, and S. Raghavan, "The role of copper pretreatment on the morphology of graphene grown by chemical vapor deposition," *Microelectronic Engineering*, vol. 131, pp. 1–7, 2015.

[189] S. Chen, H. Ji, H. Chou, Q. Li, H. Li, J. W. Suk, R. Piner, L. Liao, W. Cai, and R. S. Ruoff, "Millimeter-size single-crystal graphene by suppressing evaporative loss of cu during low pressure chemical vapor deposition," *Advanced Materials*, vol. 25, no. 14, pp. 2062–2065, 2013.

[190] P. E. Jolm F. Moulder, William F. Stickle and K. D. Bomben, "Handbook of X-Ray Photoelectron Spectroscopy ," https://www.cnyn.unam.mx/~wencel/XPS/MANXPS.pdf, 1992, [Online; accessed 13-october-2018].

[191] Z. Yan, J. Lin, Z. Peng, Z. Sun, Y. Zhu, L. Li, C. Xiang, E. L. Samuel, C. Kittrell, and J. M. Tour, "Toward the synthesis of wafer-scale single-crystal graphene on copper foils," *ACS nano*, vol. 6, no. 10, pp. 9110–9117, 2012.

[192] X. Xu, Z. Zhang, L. Qiu, J. Zhuang, L. Zhang, H. Wang, C. Liao, H. Song, R. Qiao, P. Gao *et al.*, "Ultrafast growth of single-crystal graphene assisted by a continuous oxygen supply," *Nature nanotechnology*, vol. 11, no. 11, p. 930, 2016.

[193] L. Gan and Z. Luo, "Turning off hydrogen to realize seeded growth of subcentimeter single-crystal graphene grains on copper," *Acs Nano*, vol. 7, no. 10, pp. 9480–9488, 2013.

[194] A. Mohsin, L. Liu, P. Liu, W. Deng, I. N. Ivanov, G. Li, O. E. Dyck, G. Duscher, J. R. Dunlap, K. Xiao *et al.*, "Synthesis of millimeter-size hexagon-shaped graphene single crystals on resolidified copper," *ACS nano*, vol. 7, no. 10, pp. 8924–8931, 2013.

[195] H. Zhou, W. J. Yu, L. Liu, R. Cheng, Y. Chen, X. Huang, Y. Liu, Y. Wang, Y. Huang, and X. Duan, "Chemical vapour deposition growth of large single crystals of monolayer and bilayer graphene," *Nature communications*, vol. 4, p. 2096, 2013.

[196] J. Li, X.-Y. Wang, X.-R. Liu, Z. Jin, D. Wang, and L.-J. Wan, "Facile growth of centimeter-sized single-crystal graphene on copper foil at atmospheric pressure," *Journal of Materials Chemistry C*, vol. 3, no. 15, pp. 3530–3535, 2015.

[197] Z. Han, A. Kimouche, A. Allain, H. Arjmandi-Tash, A. Reserbat-Plantey, S. Pairis, V. Reita, N. Bendiab, J. Coraux, and V. Bouchiat, "Suppression of multilayer graphene patches during cvd graphene growth on copper," *arXiv preprint arXiv:1205.1337*, 2012.

[198] V. Bouchiat, J. Coraux, and Z. Han, "Process and device for forming a graphene layer," Feb. 16 2017, uS Patent App. 15/258,983.

[199] B. Alemán, W. Regan, S. Aloni, V. Altoe, N. Alem, C. Girit, B. Geng, L. Maserati, M. Crommie, F. Wang *et al.*, "Transfer-free batch fabrication of large-area suspended graphene membranes," *ACS nano*, vol. 4, no. 8, pp. 4762–4768, 2010.

[200] S. Bhaviripudi, X. Jia, M. S. Dresselhaus, and J. Kong, "Role of kinetic factors in chemical vapor deposition synthesis of uniform large area graphene using copper catalyst," *Nano letters*, vol. 10, no. 10, pp. 4128–4133, 2010.

[201] M. Regmi, M. F. Chisholm, and G. Eres, "The effect of growth parameters on the intrinsic properties of large-area single layer graphene grown by chemical vapor deposition on cu," *Carbon*, vol. 50, no. 1, pp. 134–141, 2012.

[202] Y.-C. Lin, C. Jin, J.-C. Lee, S.-F. Jen, K. Suenaga, and P.-W. Chiu, "Clean transfer of graphene for isolation and suspension," *ACS nano*, vol. 5, no. 3, pp. 2362–2368, 2011.

[203] J.-H. Park, W. Jung, D. Cho, J.-T. Seo, Y. Moon, S. Woo, C. Lee, C.-Y. Park, and J. R. Ahn, "Simple, green, and clean removal of a poly (methyl methacrylate) film on chemical vapor deposited graphene," *Applied Physics Letters*, vol. 103, no. 17, p. 171609, 2013.

[204] S. K. Hong, S. M. Song, O. Sul, and B. J. Cho, "Carboxylic group as the origin of electrical performance degradation during the transfer process of cvd growth graphene," *Journal of The Electrochemical Society*, vol. 159, no. 4, pp. K107–K109, 2012.

[205] A. Pirkle, J. Chan, A. Venugopal, D. Hinojos, C. Magnuson, S. McDonnell, L. Colombo, E. Vogel, R. Ruoff, and R. Wallace, "The effect of chemical residues on the physical and electrical properties of chemical vapor deposited graphene transferred to sio2," *Applied Physics Letters*, vol. 99, no. 12, p. 122108, 2011.

[206] F. Xia, V. Perebeinos, Y.-m. Lin, Y. Wu, and P. Avouris, "The origins and limits of metal–graphene junction resistance," *Nature nanotechnology*, vol. 6, no. 3, p. 179, 2011.

[207] H. Zhong, Z. Zhang, B. Chen, H. Xu, D. Yu, L. Huang, and L. Peng, "Realization of low contact resistance close to theoretical limit in graphene transistors," *Nano Research*, vol. 8, no. 5, pp. 1669–1679, 2015.

[208] W. Fang, A. L. Hsu, R. Caudillo, Y. Song, A. G. Birdwell, E. Zakar, M. Kalbac, M. Dubey, T. Palacios, M. S. Dresselhaus *et al.*, "Rapid identification of stacking orientation in isotopically labeled chemical-vapor grown bilayer graphene by raman spectroscopy," *Nano letters*, vol. 13, no. 4, pp. 1541–1548, 2013.

[209] P. Poncharal, A. Ayari, T. Michel, and J.-L. Sauvajol, "Raman spectra of misoriented bilayer graphene," *Physical Review B*, vol. 78, no. 11, p. 113407, 2008.

[210] Z. Ni, Y. Wang, T. Yu, Y. You, and Z. Shen, "Reduction of fermi velocity in folded graphene observed by resonance raman spectroscopy," *Physical Review B*, vol. 77, no. 23, p. 235403, 2008.

[211] J. L. Dos Santos, N. Peres, and A. C. Neto, "Graphene bilayer with a twist: Electronic structure," *Physical review letters*, vol. 99, no. 25, p. 256802, 2007.

[212] H. Zhong, Z. Zhang, H. Xu, C. Qiu, and L.-M. Peng, "Comparison of mobility extraction methods based on field-effect measurements for graphene," *Aip Advances*, vol. 5, no. 5, p. 057136, 2015.

[213] P. L. Levesque, S. S. Sabri, C. M. Aguirre, J. Guillemette, M. Siaj, P. Desjardins, T. Szkopek, and R. Martel, "Probing charge transfer at surfaces using graphene transistors," *Nano letters*, vol. 11, no. 1, pp. 132–137, 2010.

[214] W. Zhao, G. Agnus, V. Derycke, A. Filoramo, J. Bourgoin, and C. Gamrat, "Nanotube devices based crossbar architecture: toward neuromorphic computing," *Nanotechnology*, vol. 21, no. 17, p. 175202, 2010.

[215] J. B. Fortin and T.-M. Lu, *Chemical vapor deposition polymerization: the growth and properties of parylene thin films*. Springer Science & Business Media, 2003.

[216] E. Meng, P.-Y. Li, and Y.-C. Tai, "Plasma removal of parylene c," *Journal of Micromechanics and Microengineering*, vol. 18, no. 4, p. 045004, 2008.

[217] W. F. Beach, "A model for the vapor deposition polymerization of p-xylylene," *Macromolecules*, vol. 11, no. 1, pp. 72–76, 1978. [Online]. Available: https://doi.org/10.1021/ma60061a014

[218] J. Ortigoza-Diaz, K. Scholten, C. Larson, A. Cobo, T. Hudson, J. Yoo, A. Baldwin, A. Weltman Hirschberg, and E. Meng, "Techniques and considerations in the microfabrication of parylene c microelectromechanical systems," *Micromachines*, vol. 9, no. 9, p. 422, 2018.

[219] M. Kamińska, W. Okrój, W. Szymański, W. Jakubowski, P. Komorowski, A. Nosal, H. Szymanowski, M. Gazicki-Lipman, H. Jerczyńska, Z. Pawłowska *et al.*, "Interaction of parylene c with biological objects," *Acta of bioengineering and biomechanics*, vol. 11, no. 3, pp. 19–25, 2009.

[220] R. Huang, Y. Tang, Y. Kuang, W. Ding, L. Zhang, and Y. Wang, "Resistive switching in organic memory device based on parylene-c with highly compatible process for high-density and low-cost memory applications," *IEEE Transactions on Electron Devices*, vol. 59, no. 12, pp. 3578–3582, 2012.

[221] J. S. Song, S. Lee, S. H. Jung, G. C. Cha, and M. S. Mun, "Improved biocompatibility of parylene-c films prepared by chemical vapor deposition and the subsequent plasma treatment," *Journal of Applied Polymer Science*, vol. 112, no. 6, pp. 3677–3685, 2009.

[222] A. Sharma, L. Rieth, P. Tathireddy, R. Harrison, H. Oppermann, M. Klein, M. Töpper, E. Jung, R. Normann, G. Clark *et al.*, "Long term in vitro functional stability and recording longevity of fully integrated wireless neural interfaces based on the utah slant electrode array," *Journal of neural engineering*, vol. 8, no. 4, p. 045004, 2011.

[223] T. Y. Chang, V. G. Yadav, S. De Leo, A. Mohedas, B. Rajalingam, C.-L. Chen, S. Selvarasah, M. R. Dokmeci, and A. Khademhosseini, "Cell and protein compatibility of parylene-c surfaces," *Langmuir*, vol. 23, no. 23, pp. 11 718–11 725, 2007.

[224] B. A. Weisenberg and D. L. Mooradian, "Hemocompatibility of materials used in microelectromechanical systems: platelet adhesion and morphology in vitro," *Journal of Biomedical Materials Research: An Official Journal of The Society for Biomaterials, The Japanese Society for Biomaterials, and The Australian Society for Biomaterials and the Korean Society for Biomaterials*, vol. 60, no. 2, pp. 283–291, 2002.

[225] J. Lahann, "Vapor-based polymer coatings for potential biomedical applications," *Polymer international*, vol. 55, no. 12, pp. 1361–1370, 2006.

[226] K. Alexandrou, F. Farmakis, A. Arapis, N. Georgoulas, Y. Hao, J. Hone, and I. Kymissis, "Effect of vacuum thermal annealing to encapsulated graphene field effect transistors," *Journal of Vacuum Science & Technology B, Nanotechnology and Microelectronics: Materials, Processing, Measurement, and Phenomena*, vol. 34, no. 4, p. 041805, 2016.

[227] K. Alexandrou, N. Petrone, J. Hone, and I. Kymissis, "Encapsulated graphene field-effect transistors for air stable operation," *Applied Physics Letters*, vol. 106, no. 11, p. 113104, 2015.

[228] S. S. Sabri, J. Guillemette, A. Guermoune, M. Siaj, and T. Szkopek, "Enhancing gas induced charge doping in graphene field effect transistors by non-covalent functionalization with polyethyleneimine," *Applied Physics Letters*, vol. 100, no. 11, p. 113106, 2012.

[229] D.-W. Park, H. Kim, J. Bong, S. Mikael, T. J. Kim, J. C. Williams, and Z. Ma, "Flexible bottom-gate graphene transistors on parylene c substrate and the effect of current annealing," *Applied physics letters*, vol. 109, no. 15, p. 152105, 2016.

[230] S. Sabri, P. Levesque, C. Aguirre, J. Guillemette, R. Martel, and T. Szkopek, "Graphene field effect transistors with parylene gate dielectric," *Applied Physics Letters*, vol. 95, no. 24, p. 242104, 2009.